Cardiac Imaging for Regenerative Therapy and Tissue Engineering

---

Laurence H. Jackson BSc. MRes.

December 2016

For the degree of Doctor of Philosophy

University College London, UK

Centre for Advanced Biomedical Imaging (CABI)

Paul O'Gorman Building

72 Huntley Street

London, WC1E 6DD

Declaration

I, Laurence H. Jackson, confirm that the worked presented in this thesis is my own. Where information has been derived from other sources, I confirm that this has been indicated in the thesis. The work is based on research that was conducted by me during the period from October 2012 to August 2016 at the Centre for Advanced Biomedical Imaging (CABI) within University College London.

Laurence H. Jackson

15 April 2017

Abstract

Cardiovascular disease remains the number 1 cause of death worldwide. Over the past 20 years, therapies for treating cardiac disease have come of age and coronary heart disease in particular has seen a revolution in new treatments such as statins, stents and beta blockers. These therapies have slowed death rates and have shown potential to minimise ischemia induced atrophy following myocardial infarction. Crucially however, they are unable to recover lost heart function due to cardiomyocyte death, resulting in poor prognosis for patients. Myocardial regeneration therapy is a new strategy towards treating cardiac disease that engrafts regenerative cells and biomaterials to the myocardium to stimulate repair of tissue and restore contractile function. Cardiac regeneration therapy has made a rapid translation from preclinical research to clinical trials with the first trial in humans published in 2001. Clinical trials in the years since however have produced underwhelming results and there is a general consensus that further preclinical optimisation with powerful non-invasive imaging data will be key to the future success of regenerative medicine in humans.

Magnetic resonance imaging is unparalleled in providing non-invasive multiparametric imaging of both global and regional cardiac structure and function. MRI provides high spatiotemporal resolution and multiple contrast mechanisms revealing information about molecular changes in the myocardium. These imaging abilities make MRI a versatile and powerful tool in the preclinical optimisation of cardiac regeneration therapies. Over the chapters presented in this thesis I have established a set of MR imaging techniques that enable valuable in vivo characterisation of cardiac function and structure in for use in studies of regenerative therapy. It is hoped that the methods developed over the course of this thesis aid in the uptake of imaging applications in studies of regenerative medicine and that the wide range of imaging tools demonstrated help to bring regenerative medicine closer to practical clinical therapy.

Acknowledgements

Working within an environment like CABI makes it impossible not to form friendships with those around you and the contribution these people make to this work cannot be understated.

I would like to thank first and foremost Dr Daniel Stuckey who has guided and supported me since he joined us and brought with him incredible knowledge of cardiovascular disease and imaging. Professor Mark Lythgoe has somehow cultured an atmosphere in the lab of academic excellence but made sure it never feels like I'm coming to work. I am indebted to him for his experience and guidance in my first years in academia.

I would like to thank all my external collaborators including Adrienne Campbell-Washburn, Andrew Cook, Anna David, John Porter, Panicos Shangaris, Elina Koumoutsea Vlachodimitropoulou and Panos Sofokleous. These people have helped me with technical expertise, bringing me opportunities and enabling research contained within this thesis.

I would like to thank the UK Medical Research Council for funding me during my time at UCL whose sponsorship I am extremely grateful for.

I would like to thank the whole of CABI for their support during my time with them, without the incredible range of knowledge possessed by these people I would surely be worse off. Specifically, I would like to thank Tom for showing me what an MRI scanner is and for beating me at ping pong without gloating. Arun for his attention to detail and losing to me at ping pong without minding me gloating. Angela for being the best desk buddy I could have asked for. Yanan for her kindness and support. I would like to specially mention Oz, Morium and Rupi for helping me with literally everything. CABI is full of people I cannot thank enough for their time, knowledge and camaraderie I am eternally grateful to (in order of distance from my desk) Ben, Jack, Simon, Heather, Bernard, Adam, Giulia, Tammy, Yolanda, Ian, John, Pete, Hannah, Izzy, Matin, Stephen, Miguel, Patrick, MZT, Yichao, Tim, Holly, Alicia, Jed, Nur, Eoin, Payam, Nick, Raul, Jennifer, Ana, Da Ma, JBN and Xiao Xiao.

I want to thank the Jacksons, my Mum, Dad and siblings who have supported me since forever and motivated me with their own achievements. Finally, I want to thank Zeynep for being a limitless source of encouragement and inspiration.

Publications and awards arising from this PhD

Peer-reviewed journal articles

Laurence H. Jackson, Evangelia Vlachodimitropoulou, Panicos Shangaris, Thomas A. Roberts, Thomas M. Ryan, Adrienne E. Campbell-Washburn, Anna L. David, John B. Porter, Mark F. Lythgoe, Daniel J. Stuckey. **Non-invasive MRI biomarkers for the early assessment of iron overload in a humanized mouse model of β-thalassemia**. (under review)

Thomas. A. Roberts, PhD; Anthony N. Price, PhD; **Laurence H. Jackson**; Valerie Taylor; Anna L. David, PhD; Mark F. Lythgoe, PhD; Daniel J. Stuckey, PhD**. High temporal resolution CINE MRI at 9.4T vs. ultrasound: assessment of diastolic dysfunction in mice**. (under review)

Alessondra T. Speidel, Daniel J. Stuckey, Lesley W. Chow, **Laurence H. Jackson**, Michela Noseda, Marta Abreu Paiva, Michael D. Schneider and Molly M. Stevens. **Multi-modal hydrogel platform to enhance and monitor cardiac progenitor/stem cell engraftment**. (under review)

Book Chapters

Laurence H. Jackson, Mark F. Lythgoe, Daniel J. Stuckey (2016); Chapter 15: **MRI tools for assessment of cardiovascular tissue Engineering, Magnetic Resonance in Tissue Engineering**. Wiley.

Published Abstracts

2013

Jackson LH, d'Esposito A, Siow B, Stuckey DJ, Lythgoe MF, **Ex-Vivo Cardiac Fibre Imaging using Diffusion MRI and Optical Projection Tomography**. British Chapter ISMRM annual meeting (2013).

2014

Jackson LH, d'Esposito A, Siow B, Stuckey DJ, Lythgoe MF. **Ex-Vivo Cardiac Fibre Imaging using Diffusion Tensor MRI and Optical Projection Tomography**. Proceedings of the ISMRM annual meeting 22(2014): 2442

Jackson LH, Georgiadis V, Habib J, Siow B, Stuckey DJ, Lythgoe MF. **In-vivo and ex-vivo assessment of myocardial regeneration therapies using magnetic resonance and optical projection tomography**. British Chapter ISMRM annual meeting (2014).

2015

Jackson LH, Roberts TA, Taylor V, Habib J, Stuckey DJ, Lythgoe MF. **MRI visible bioscaffold for stem cell-mediated repair and improved cardiac function**. Proceedings of the ISMRM annual meeting 23(2015): 2602

Stuckey DJ, Roberts TA, Jackson LH, Ramasawmy R, Taylor V, David AL, Siow B, Lythgoe MF. **Can we rely on the new 1T "benchtop" systems for investigating cardiac function and viability?** Proceedings of the ISMRM annual meeting 23(2015): 4481

Jackson LH, Habib J, Stuckey D, Lythgoe M. **MRI visible bioscaffold for stem cell-mediated repair and improved cardiac function**. InProceedings of The Physiological Society 2015. The Physiological Society.

Jackson LH, Georgiadis V, Habib J, Roberts TA, Stuckey DJ, Lythgoe MF. **Regional assessment of myocardial regeneration therapies in rats using magnetic resonance tagging**. Journal of Cardiovascular Magnetic Resonance. 2015;17(1):1.

2016

Jackson LH, Vlachodimitropoulou EK, Shangaris P, Ryan TM, David AL, Porter J, Stuckey DJ, Lythgoe MF. **MRI characterisation of iron overload in a humanised mouse model of β-thalassemia major**. Proceedings of the ISMRM annual meeting 24(2016): 2534

Awards

December 2013	**Research Images as Art- 1st place, UCL** *Image: Muscle Fibres of the Heart (Appendix A.1)*
November 2014	**Images with Impact: The Great British Bioscience Image Competition- Runner up, BBSRC** *Image: Muscle Fibres of the Heart (Appendix A.1)*
September 2015	**British Chapter Prize- Runner up, British Chapter ISMRM**

Awarded for innovative in vivo MRI imaging or MR spectroscopy research with potential utility in medicine

Title: MRI characterisation of mouse models of β-thalassemia major and iron overload

Table of Contents

List of figures

List of tables

Abbreviations

AAR	Area At Risk
ACE	Angiotensin Converting Enzyme
ASTAMI	Autologous Stem Cell Transplantation in Acute Myocardial Infarction
ATP	Adenosine Triphosphate
AV	Atrioventricular
BABB	Benzyl Alcohol Benzyl Benzoate
bFGF	Basic Fibroblast Growth Factor
BLI	Bioluminescence Imaging
BMSC	Bone Marrow Stem Cell
CABI	Centre for Advanced Biomedical Imaging
CAD	Computer Aided Design
CADUCEUS	CArdiosphere-Derived aUtologous stem CElls to reverse ventricULar dySfunction
CANSEL	Cosine and Sine Modulation to Eliminate artefacts
CCW	Counter Clockwise
cDENSE	Complimentary DENSE
CEST	Chemical Exchange Saturation Transfer
CHD	Coronary Heart Disease
CO	Cardiac Output
CSC	Cardiac Stem Cell
CSPAMM	Complementary Spatial Modulation of Magnetisation
CT	Computed Tomoraphy (X-ray)
CVD	Cardiovascular Disease
DANTE	Delay Alternating with Nutations for Tailored Excitation
DCM	Dilated Cardiomyopathy
DENSE	Displacement ENcoding using Stimulated Echoes
DHF	Diastolic Heart Failure
DMSO	Dimethyl Sulfoxide
DT	Distance Transform
Ecc	Circumferential Strain
ECG	Electrocardiogram
ECM	Extracellular Matrix
EDD	End Diastolic Diameter
EDV	End Diastolic Volume
EF	Ejection Fraction
EHT	Engineered Heart Tissue
Ell	Longitudinal Strain
EPI	Echo Planar Imaging
Err	Radial Strain
ESD	End Systolic Diameter

ESV	End Systolic Volume
EWA	Expectation maximisation, Weighted, A priori information
FBP	Filtered Back Projection
FDG	Fludeoxyglucose
FS	Fractional Shortening
FSE	Fast Spin Echo
Gd	Gadolinium
Gd-DTPA	Gadolinium diethylenetriaminepentaacetic acid (chelated Gd)
GEMS	Gradient Echo Multi Slice
Gpe	Phase Encode Gradient
GRE	Gradient Echo
Gro	Readout (Frequency encoding) Gradient
Gss	Slice Select Gradient
HARP	Harmonic Phase
Hb	Hemoglobin
HbA	Adult Hemoglobin
HbF	Fetal Hemoglobin
HBP	Heparin Binding Peptide
HCM	Hypertropic Cardiomyopathy
HF	Heart Failure
HGF	Hepatocyte Growth Factor
hMSC	human mesenchymal stem cell
HPFH	Hereditary Presistance of Fetal Hemoglobin
HSC	Hematopoietic Stem Cell
ICI	Intracoronary Infusion
IMI	Intramyocardial Injection
IR	Inversion Recovery
LA	Long Axis
LAD	Left Anterior Descending coronary artery
LGE	Late Gadolinium Enhancement
LVEF	Left Ventricular Ejection Fraction
LVM	Left Ventricular Mass
MAGIC	Myoblast Autologous Grafting in Ischemic Cardiomyopathy
mBMC	Mononuclear Bone Marrow Cell
MI	Myocardial Infarction
MRI	Magnetic Resonance Imaging
MSC	Mesenchymal Stem Cell
NIH	National Institute of Health
NMR	Nuclear Magnetic Resonance
NTBI	Non-Transferrin Bound Iron
OPT	Optical Projection Tomography
PBS	Phosphate Buffered Saline
PCI	Percutaneous Coronary Intervention

PDF	Projection onto Dipole Fields
PE	Phase Encoding
PEG	Polyethylene Glycol
PENIR	Phase Encoded Noise-Based Image Removal
PET	Positron Emission Tomography
PFA	Paraformaldehyde
PIPAAm	Poly(N-isopropylacrylamide)
PROMETHEUS	Prospective Randomized Study of Mesenchymal Stem Cell Therapy in Patients Undergoing Cardiac Surgery
QSM	Qunatitative Susceptability Imaging
RBC	Red Blood Cell
RF	Radiofrequency
RO	Readout
ROI	Region of Interest
RR	Interval between two R waves in ECG
SA	Short Axis
SEMSE	Spin Echo Multi Slice
SENC	Strain Encoding
SERVO	Servomechanism
SHF	Systolic Heart Failure
SM	Skeletal Myoblast
SNR	Signal to Noise Ratio
SOD	Superoxide dismutase
SPAMM	SPatial Modulation of Magnetisation
SPECT	Single Photon Emission Computed Tomography
SPION	Superparamagnetic Iron Oxide Nanoparticle
STE	Speckle Tracking Echocardiography
SV	Stroke Volume
SVF	Systemic Venous Infusion
T1	Longitudinal Relaxation Contant
T2	Transverse Relaxation Constant
*T2**	Effective Transverse Relaxation Constant
TDI	Tissue Doppler Imaging
TE	Echo Time
TI	Inversion Time
TM	Mixing Time
TPD	Through Plane Dephasing
TR	Repetition Time
TTL	Transistor-Transitor Logic
UCL	University College London
US	Ultrasound
VDA	Vascular Disrupting Agent
VEGF	Vascular Endothelial Growth Factor
VF	Ventricular Fibrillation

WBC	White Blood Cell
WTHK	Wall Thickening
βT	Beta Thalassemia

Chapter 1

Introduction I – Cardiac disease, regenerative medicine and tissue engineering

1.1 Introduction

1.1.1 Research aims

Cardiovascular disease represents the leading cause of death globally. Coronary artery disease (CAD) in particular resulted in an estimated 7.4 million deaths in 2012.[1] The high oxygen requirements of the heart mean that CAD induced ischemia is highly damaging to the myocardium resulting in rapid onset of apoptosis and adverse ventricular remodelling.[2] The ability of the heart to regenerate following injury is extremely limited due to the low populations of resident cardiac stem cells and the hostile cellular environment in myocardial ischemia. Over the last decade cardiac regeneration therapy has emerged as a potential treatment for producing functional repair in cardiac disease. Cell therapy and tissue engineering have produced promising preclinical evidence for regenerating the myocardium and has great potential for patients. However, clinical trials have shown only modest improvements in heart function and a return to preclinical optimisation of therapy is now key to successful clinical translation. This thesis aims to develop non-invasive and in-vivo MRI imaging techniques for assessing cardiac structure and function and apply them to studies of regenerative medicine in preclinical models of myocardial infarction. The aims of this work are summarised as the following four objectives, ultimately leading towards the development of a complete MRI imaging toolset for assessment of cardiac disease and regeneration:

1. Establish quantitative MRI techniques for assessing cardiac function and structure in preclinical models of cardiac disease
2. Implement, optimise and develop the current reference standard technique for imaging regional heart function with spatial modulation of magnetisation.
3. Implement, optimise and develop a novel high resolution imaging technique for imaging regional heart function using displacement encoding using stimulated echoes
4. Test the developed imaging toolset in preclinical models of cardiac regeneration

Development of these goals is seen as key enabling technology to accelerate the development and optimisation of myocardial regeneration therapy aiding in the translation from bench to bedside.

1.1.2 Structure of thesis

This thesis is structured into 8 chapters. Each chapter has a specific role within the body of work as a whole in describing a project, or series of projects that have a common theme.

Chapter 1 provides broad background information about cardiovascular disease worldwide, regenerative medicine and tissue engineering. This introduction provides the physiological context underpinning the work presented in this thesis.

Chapter 2 is a second introduction that describes the theory behind the imaging techniques used for cardiac imaging in general practice and those that are specific to this work. Magnetic resonance imaging (MRI) is discussed in detail as this forms a significant part of this thesis. Other imaging modalities that are used less frequently are also introduced including bioluminescence imaging (BLI), ultrasound (US) and optical projection tomography (OPT).

Chapter 3 describes the development of a multiparametric preclinical imaging platform for the assessment of cardiac disease. The imaging techniques are applied to a novel model of β thalassemia using quantitative assessment of cardiac function, structure and NMR relaxometry. These techniques are presented in the context of β thalassemia but the techniques developed are applicable to the wider field of cardiac imaging. The methodologies presented here are applied in later chapters to studies of cardiac regeneration.

In chapter 4 the assessment of regional myocardial function is introduced. A large component of this work focuses on the development of imaging techniques for assessment regional heart function using MRI. In this section the literature is reviewed and a brief study on the effects of myocardial infarction on the regional structure of the left ventricle from cine MRI images is presented.

In chapter 5 the first advanced cardiac MR imaging technique is presented. Here, my work in developing and implementing a preclinical spatial modulation of magnetisation (SPAMM) sequence for tagging the myocardium and enabling the spatiotemporal tracking heart tissue through time is presented. This sequence is validated with a motion phantom and processed using the harmonic phase technique.

In chapter 6 another regional assessment technique is developed that offers improved spatial and temporal resolution information about myocardial contraction relative to SPAMM. Displacement encoding using stimulated echoes (DENSE) is an advanced phase based myocardial imaging technique that can be used to quantify myocardial mechanics in fine detail. This chapter describes my work on developing, optimising and accelerating this sequence in terms of both the acquisition and post processing of data.

Chapter 7 describes three studies I performed in which preclinical models of myocardial regeneration therapy were assessed using advanced imaging techniques. During these pilot studies ultrasound, optical projection tomography and bioluminescence imaging are

implemented to support the MRI imaging platform that is developed in previous chapters in a multimodal approach to imaging.

Finally, chapter 8 provides a summary of the work presented as well as the findings of this thesis, offering a discussion of future developments that would be beneficial to the work. This is followed by a discussion of the future directions for myocardial regeneration therapy and the role imaging has within its translation to clinical practise.

1.2 Cardiac disease and regeneration

1.2.1 Cardiovascular disease worldwide

Cardiovascular diseases (CVDs) are a group of disorders affecting the heart and blood vessels, they represent the largest cause of deaths worldwide and attribute to a third of all deaths globally.[3] CVD is a broad term for a range of diseases that affect the heart and blood vessels and can be broadly split into the 6 categories described in Table 1.1.

Table 1.1 Overview of categories of cardiovascular disease including a description and example of each major category.

Category	Description	Example
Coronary heart disease (CHD)	Diseases effecting blood vessels supplying the myocardium	Myocardial infarction
Cerebrovascular disease	Effects blood vessels supplying the brain	Stroke
Peripheral arterial disease	Effects blood vessels in the arms and legs	Atherosclerosis
Rheumatic heart disease	Bacterial infection damaging the heart muscle and valves	Rheumatic fever
Congenital heart disease	Abnormalities of the heart existing from birth	Atrial septal defect
Venous thromboembolism	Blood clot (thrombus) that forms in veins and can occlude vessels	Deep vein thrombosis

Coronary heart disease (CHD) and cerebrovascular disease are the most severe forms of CVD and account for 40 and 25% of CVD deaths respectively.[4] Global deaths due to CVD is projected to increase year on year to 23.3m by 2030, compared to 16.7m in 2002, an increase of 40% over 28 years.[5,6] Incredibly, by 2030, 40.5% of the population of the USA is predicted to have some form of cardiovascular disease by current projections.[7]

The huge economic cost of CVD is reflective of its position as the leading contributor to global disease burden. Contributions from primary healthcare treatment, prevention and lost productivity due to illness are estimated to total €169bn(2008) annually in Europe.[4] In the USA this estimate is €286bn(2008) of which €70bn can be directly attributed to CHD.[7] The wide prevalence and high cost of CVD has led to a great amount of investment in research and development from basic science through to clinical therapy. In 2015 the national institute of health (NIH) received a total of $3.7bn to support research into CVDs.[8]

Myocardial infarction (MI) in particular is a devastating consequence of CHD. Regional ischemia in MI causes regions of the heart to form non-contractile scar tissue. These scars result in cardiac dysfunction, leading to heart failure and death. This thesis focuses on assessment of targeted therapies for treating MI and produces imaging tools for the assessment of disease and therapy.

1.2.2 Anatomy and physiology of the heart

The cardiovascular system can be separated into two networks, the pulmonary circulation and the systemic circulation.[9] The function of the heart is to pump blood through these two networks. The systemic circulation is supplied by the left side of the heart and provides oxygenated blood flow to the body and coronary blood vessels through the aorta. The pulmonary circulation is supplied by the right side of the heart and pumps deoxygenated blood received from the systemic circulation via the pulmonary artery to the lungs where it becomes oxygenated before being passed back into the systemic circulation, this process is illustrated in Figure 1.1. Both sides are connected to the body by large veins and arteries known as the great vessels. Each side of the mammalian heart consists of two chambers, an atrium and a ventricle giving the heart four chambers in total. Each pair of atria and ventricles are isolated from the other in normal physiology and so can be thought of as two pumps connected in series via the pulmonary and systemic vasculature.

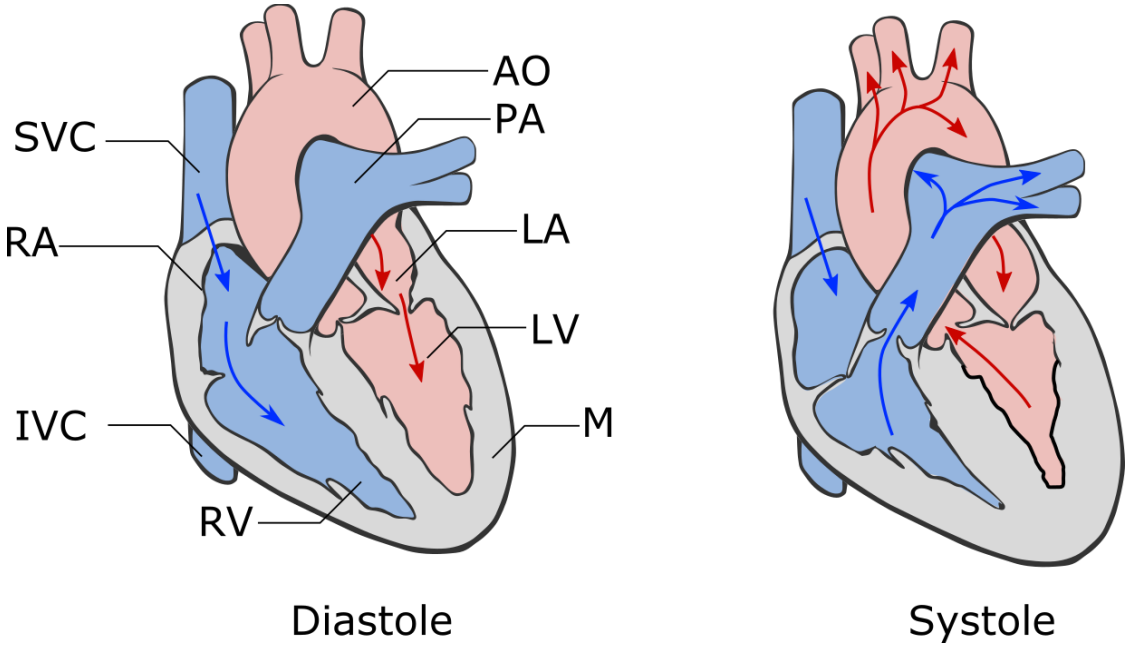

Figure 1.1 Anterior cross section of the heart at diastole and systole. Arrows show direction of blood flow in each phase. Red and blue regions indicate components of the systemic and pulmonary circulation respectively. SVC: Superior vena cava; RA right atrium; IVC inferior vena

cava; RV right ventricle; M myocardium; LV left ventricle; LA left atrium; PA pulmonary artery; AO aorta.

The ventricles serve as the main pumping elements of the heart. They are surrounded by muscular myocardium that rhythmically contracts to reduce the volume of the chamber and pump the blood. Full relaxation of the ventricular myocardium when the ventricles are at peak volume is called end diastole, full contraction when their volume is smallest is called end systole.

For efficient cardiac function the contraction of the atria, ventricles and valves must be carefully timed to produce the least resistance to flow. The contraction of the heart is paced and controlled by a network of conductive cells and impeding bundles that propagate an electrical impulse (action potential) that causes regular waves of depolarisation in cardiac muscle cells (cardiomyocytes) making them contract. This cycle produces electrical signals that can be detected by electrodes remote to the heart. The detection of these signals is called an electrocardiogram (ECG) that can provide information about the function or instantaneous contraction phase of the heart, this signal is illustrated in Figure 1.2.

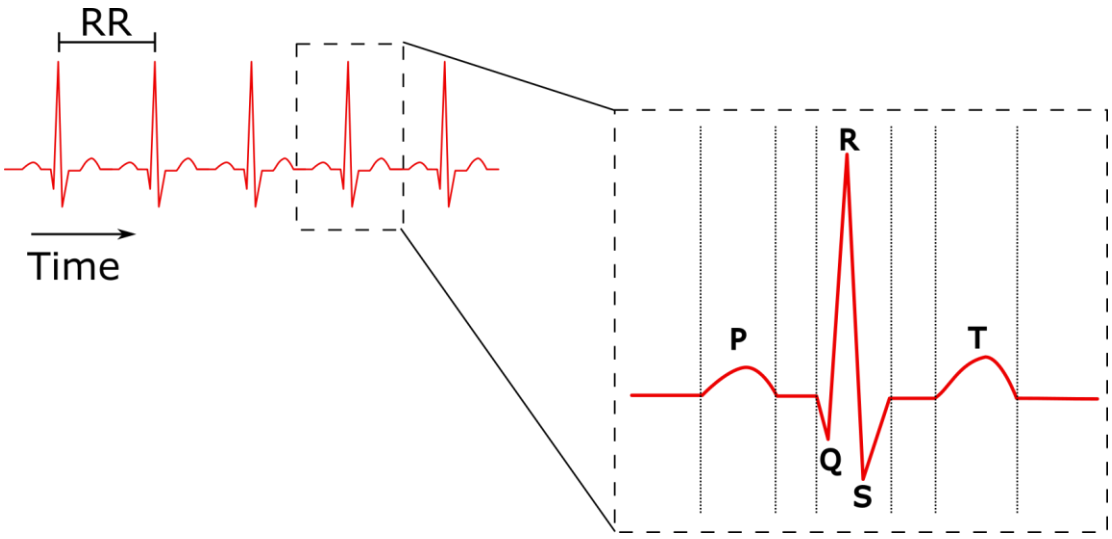

Figure 1.2 The ECG signal in sinus rhythm is a regular repeating waveform composed of three parts. The P wave caused by depolarisation of the atria, the large amplitude QRS complex caused by depolarisation of the ventricular myocardium and the T wave produced by ventricular repolarisation. The heartrate is normally described by the RR interval.

The impulse originates in the sinoatrial node, a bundle of specialised cells located in the top wall of the right atrium. The regular spontaneous depolarisation of the sinoatrial node acts as the hearts pacemaker and initiates each contraction cycle, the normal rhythm of the heart by this process is called sinus rhythm. After the sinoatrial node fires the depolarisation wave propagates through the atria before slowing in the slowly conducting atrioventricular (AV) node. This movement causes the P wave in the ECG signal, during this delay the atria pump blood into the ventricles. The depolarisation then propagates quickly down through the septum through the AV

bundle and splits into left and right branches, before spreading into the ventricular myocardium through the His-Purkinje system. This rapid depolarisation leads to the QRS complex in the ECG signal that signals the initiation of ventricular contraction.

1.2.3 Coronary vessels and myocardial infarction

1.2.3.1 Coronary vasculature

The coronary vasculature is the dense network of blood vessels that supply blood to the myocardium. This includes an arterial network that connects to the systemic circulation at the base of aorta and a venous network that drains into the right atrium.

The arterial system stems from the aorta in 2 major coronary arteries, the left main and the right coronary artery. The left main splits to form the left anterior descending (LAD) and circumflex and the right coronary forms the posterior descending artery. These 5 vessels supply all of the oxygenated blood to the myocardium and occlusion or narrowing (stenosis) of these vessels can cause significant and rapid damage to the regions of muscle they perfuse. The major coronary arteries frequently branch into smaller arteries and capillaries creating a dense vascular network that is able to meet the perfusion requirements of the myocardium.

The heart has one of the highest oxygen requirements in the body (5.6 ml/min/100g at rest and increasing up to 10.6 ml/min/100g during exercise).[10] Interruption of myocardial perfusion as a result of coronary heart disease can have severe and rapid consequences. Coronary occlusion has been shown to reduce regional metabolism and impair systolic function within just a few heartbeats.[11] The hypoxic environment rapidly leads to cell death with regions of the heart irreversibly damaged in a process called myocardial infarction.

1.2.3.2 Myocardial infarction

Myocardial infarction (MI) is the death of myocardial cells that occurs when an artery supplying oxygenated blood to the myocardium become narrowed or blocked. The high energy demand of the heart requires an uninterrupted supply of oxygen and restriction of blood flow leads to the rapid onset of cell death and loss of function. MI is normally a result of coronary occlusion, of which the most common cause is coronary atherosclerosis.[9] Atherosclerosis is the formation of a plaque within the wall of an artery composed of accumulated white blood cells (WBCs), smooth muscle and the remnants of dead cells. Plaques with high infiltration of WBCs are unstable and

prone to rupture whereupon the inner thrombogenic core is exposed to the bloodstream. The resulting thrombus can then occlude the vessel (Figure 1.3) or enter the circulation resulting in remote thromboembolism.[12] Other causes of MI include aortic stenosis[13,14], non-obstructive diseases such as coronary artery vasospasms[15] and changes in the oxygen supply/demand such as anaemia or hypertension.[16]

Regional myocardial cell death due to ischemia begins at the subendocardium where energy demand is highest and spreads outwards to the subepicardium over a period of hours, this process is termed the wavefront phenomenon.[17] The region of tissue supplied by the blocked vessel is bordered by regions where tissue is perfused by multiple or collateral vessels. This region is known as the area at risk (AAR) or border zone and represents tissue that can be salvaged if the blocked artery is cleared and tissue reperfused quickly. The proportion of the AAR that can be recovered depends on multiple factors including time from infarct to reperfusion, ischemic preconditioning and collateral perfusion.[18]

Cardiac electrophysiology is altered in infarcted myocardium due to the abnormal conductance in infarcted tissue and the accurately timed contraction cycle described in 1.2.2 loses coherence.[19] In the worst case scenario immediately following infarction the patient can develop ventricular fibrillation (VF) where the ventricles cannot contract rhythmically resulting in a fluttering motion in which very little or no blood is pumped. The abnormal conductance in infarcts is known to predispose patients to future arrhythmia with the surviving AAR thought to be the primary arrhythmogenic source.[20,21] VF as a result of conduction failure is the most common cause of death during the acute phase of MI.[22,23]

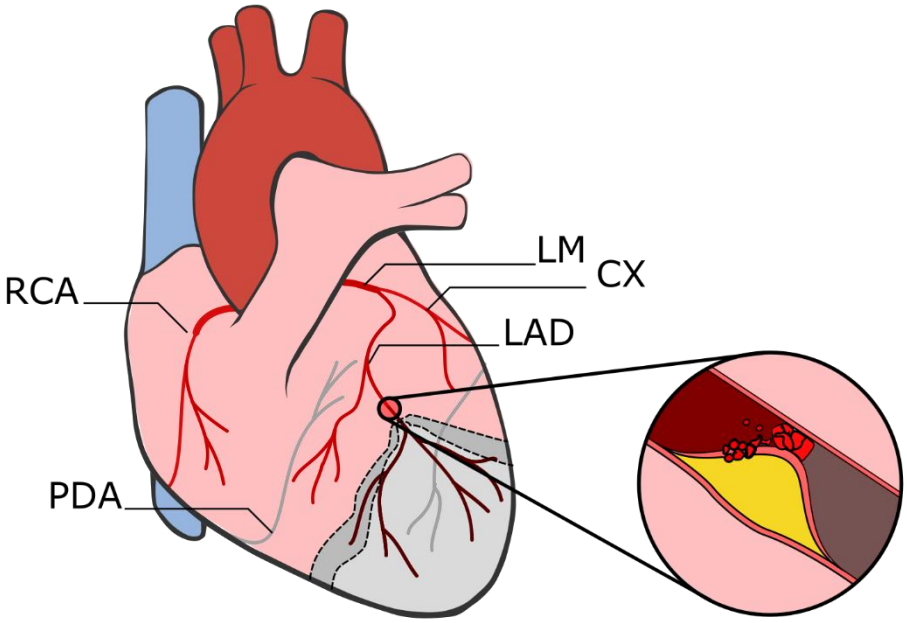

Figure 1.3 Myocardial infarction occurs when the blood supply to the heart is restricted. The most common cause of myocardial infarct is a ruptured atherosclerotic plaque and resulting thrombotic occlusion (inset). The myocardium supplied by the blocked vessel becomes infarcted (light grey) but is bordered by salvageable tissue (dark grey). RCA; right coronary artery, PDA; posterior coronary artery, LAD; left anterior descending coronary artery, CX; circumflex, LM; left main coronary artery.

Following the ischemic event, the heart begins a remodelling process, in which it undergoes changes in size, shape and contractility, in an attempt to adapt to the damaged myocardium. The onset and extent of this remodelling process is dependent on the severity of the initial injury as well as factors such as haemodynamic load and secondary MI events.[24] This remodelling process begins within the first few hours of coronary occlusion.[25] A major feature of remodelling is the formation of a region of non-contractile collagen-rich scar tissue that replaces the ischemic tissue. This scar helps prevent myocardial rupture and keeps the structure of the heart intact but is not able to contribute to cardiac output. Other major features of cardiac remodelling include ventricular dilation, delayed infarct expansion and myocyte hypertrophy.[26-28]

Extensive cardiac remodelling eventually leads to chronic heart failure (HF), this occurs when the heart loses its ability to adequately pump blood to sustain the body's needs. HF can be the result of severe MI, arrhythmia, disease and hypertension. The transition from adaptive remodelling to cope with changes induced by infarction to maladaptive remodelling leading to HF occurs as the heart overcompensates for damage.[29] In clinical practice the remodelling process following MI is typically pharmacologically constrained to limit the extent of remodelling and provide a better prognosis for the patient.

1.2.3.3 Clinical management of myocardial infarction

Atherosclerosis and the resulting MI, is a chronic condition and plaques take many years to form with patients asymptomatic before plaque rupture with little warning before an ischemic event. Early diagnosis is therefore extremely difficult and consequently clinical management tends towards damage limitation following MI rather than intervention before the event.

Pharmacological treatments for MI include the administration of a combination of aspirin, β-adrenergic blockers and angiotensin-converting-enzyme (ACE) inhibitors.[30] These drugs are able to manage the major symptoms of MI by antithrombotic, antiarrhythmic and antihypertensive properties respectively. Coronary reperfusion therapy can be given either pharmacologically or mechanically via percutaneous coronary intervention (PCI) in which a balloon catheter is inflated to clear occluded vessels.[31,32] Infarct size and functional recovery is strongly dependent on the severity of occlusion and time to reperfusion therapy, so in cases where coronary occlusion is ongoing, reperfusion therapy will be performed as quickly as possible in centres that possess the capability. In the case of major heart failure, the only current clinical treatment is heart transplant where donor availability, organ rejection and surgical risk present significant complications.

Although current clinical therapy has provided reductions in infarct size, mortality and adverse cardiac remodelling, significant ventricular dysfunction remains in the vast majority of patients.[33-36] Therefore there is a need for the development of therapies able to stimulate growth of new contracting heart tissue or to replace damaged tissue with artificial myocardium grown in-vitro in a new regenerative approach to therapy.

1.2.3.4 Animal Models of myocardial infarction

Accurate animal models of myocardial infarction are important enabler to the study of myocardial infarction physiology and the development of effective therapies. Producing an animal model of myocardial infarction requires artificially inducing changes to coronary blood flow. This has been done using surgical ligation, cauterisation/cryoinjury, balloon occlusion and pharmacological methods.[37] Balloon occlusion uses a surgically implanted inflatable balloon catheter to occlude a coronary artery. This is performed in large animals by inflating the balloon following transluminal implantation. The balloon occlusion method has been adapted to small animals (rabbit) by using an inflatable balloon catheter that encircles a superficial coronary artery.[38] This method is reliable and reproducible in the case that the balloon is positioned accurately. This procedure requires a high level of surgical expertise and is impractical in small

rodent models of disease, especially mice where the major coronary vessels have an average diameter of 0.16mm.[39] Pharmacologically induced infarction aims to create an ischemic region in the myocardium by either increasing the oxygen requirements of the muscle above what the coronary circulation is capable of delivering (e.g. Isoproterenol[40]) or inducing coronary artery spasms (e.g. Doxorubicin[41]). Although these methods offer an easy route to creating myocardial ischemia, they offer little control over the location of the infarcted region or degree of damage and is limited by to drug toxicity. An electrocoagulation knife or cryoprobe can be used to induce cauterisation/cryoinjury respectively in the target coronary artery. This has two effects, local tissue damage and cell necrosis due to the thermal injury and myocardial ischemia distal to the region of damage. MI caused by this type of injury is easy to produce but has limited reproducibility and the damage caused at the site of the injury is not physiologically similar to pathological MI.[42,43] For this reason surgical ligation of the coronary arteries was chosen to produce animal models of MI for research undertaken in this work. Surgical ligation ties off a coronary artery using suture ligation. It is the most similar model of MI to pathological MI caused by atherosclerosis or coronary thrombosis and causes reliable myocardial infarction. However, the procedure can result in infarcts of variable sizes and requires a high degree of surgical skill to implement successfully, especially in mouse models due to the small dimensions of the coronary arteries.[44]

1.2.4 Regenerative medicine

Artificially inducing regeneration in organs and tissues that would not normally have the capability is a promising and feasible approach to therapy that has the potential to alleviate humans from diseases that have not yet been cured.[45] Regeneration occurs in nature, and the regrowth of organs and limbs is a characteristic of certain species such as the salamander, zebrafish and gecko (Figure 1.4). The regrowth organs in these species originates from a cluster of undifferentiated cells called a blastema that accumulates at the site of injury. Most mammals, including humans, lack the ability to produce a blastema and so require some other mechanism to deliver cells to the regenerating region either through cell signalling to recruit endogenous stem cells or through cell transplantation.

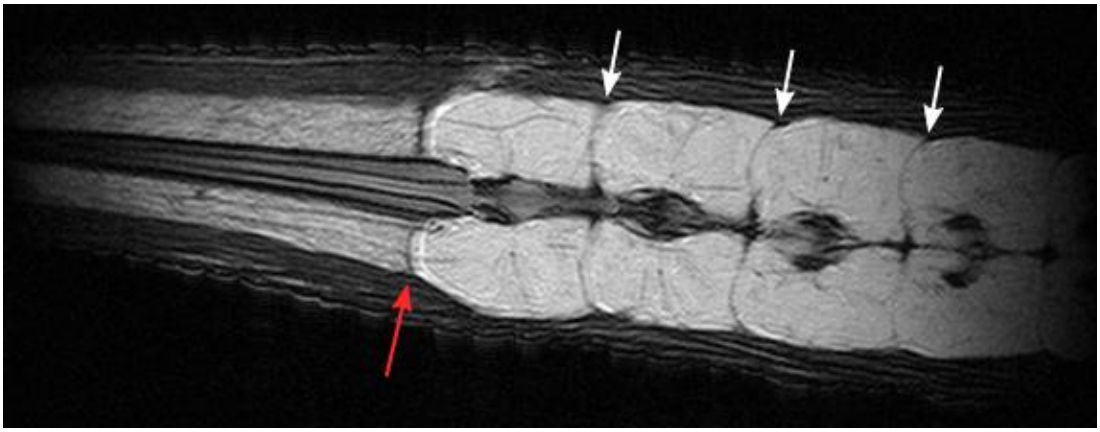

Figure 1.4 Some species of gecko are able to shed their tails as a defence to regenerate the lost appendage. This MRI image of a regenerated gecko tail shows the original tail to the right and the regrown tail to the left. This species is unable to fully regenerate the tail and cannot re-shed the tail from below the original severance point (red) note lack of vertebra and new fracture planes (white) in the regenerated tail.

The aim of regeneration therapy is to stimulate new growth in tissue, where damaged cells and structures are replaced and functionality of the organ restored. Approaches to regeneration therapy can take two approaches, 1) stimulating growth or recovery through the activation of endogenous regenerative ability or 2) transplanting cells or structures that have been cultured in-vitro to replace damaged tissue.[46]

1.2.4.1 Overview of cardiac cell therapy

Although the regenerative properties of organs such as skeletal muscle and the liver are well known, it was thought until recently that the heart lacks this inherent capability.[47] In a breakthrough study by Beltrami et al. (2001) it was shown that a subpopulation of cardiomyocytes undergo mitosis in response to myocardial infarction.[48] A later study by Bergmann et al. (2009) used radioactive carbon-14 fallout from cold war era nuclear tests to radiometrically determine the age of in-vivo cardiomyocyte populations and provide evidence for post-natal cellular renewal in normal physiology.[49] This report showed that approximately 1% of cardiomyocytes regenerate annually in early adulthood and that this turnover decreases with age, in an average human lifespan less than half of all myocytes are regenerated. These discoveries challenged the traditional view of the terminally differentiated heart and introduced the field of myocardial regeneration and the existence of autologous cardiac stem cells (CSCs). This limited regenerative ability suggests that the integration of new cardiomyocytes to the heart, although barely perceptible in adults, is possible and consequently that the growth or transplantation of new cardiomyocytes is a feasible therapeutic goal.

The cell therapy approach to cardiac regeneration typically transplants cells by infusion or injection of isolated proregenerative cells in liquid suspension. Cardiac cell therapy offers an attractive solution to treating heart failure patients by offering a highly targeted and tailored therapy without the risk of donor rejection since cell grafts can be cultured from autologous adult stem cells.[50] However, the question remains that if the heart possesses a dormant regenerative ability as shown by Beltrami et al. (2001) and Bergmann et al. (2009) what factors are preventing the total regeneration of large areas of damaged tissue without external intervention. One commonly considered obstacle is the hostile cellular environment present in many forms of CVD such as infarction where adverse mechanisms such as inflammation and ischemia may be preventing the activation of endogenous cardiac stem cells.[51] An additional barrier to native regeneration is the physical impedance caused by fibrotic and scar tissue following injury, this response mechanism is necessary to maintain the structural integrity of the heart but poses a barrier to the growth of new cardiomyocytes in the region.[52] Finding effective and safe ways to circumvent or remove these growth-limiting factors will be vital to the development of regenerative medicine.

1.2.4.2 Cell types

A wide range of stem and progenitor cell types have been proposed for regeneration therapy.[53] The potential of these cells for regeneration comes from their ability to differentiate into a range of different mature cells depending on their growth environment. Autologous stem cells can be sourced from adipose tissue, blood, bone marrow and heart tissue. Blood derived stem cells such as circulating endothelial progenitor cells have undergone clinical trials where they were chosen for their angiogenic properties.[54] Cells extracted from adipose tissue have been shown to differentiate into cardiomyocyte-like cells that exhibit pacemaker activity and beating action.[55-57] Bone marrow is a rich source for regenerative cells including hematopoietic stem cells (HSCs) and mesenchymal stem cells (MSCs) and is the most common cell source used in current clinical trials.[58] Stem cells sourced from cardiac tissue (CSCs) offer an exciting prospective cell type for regeneration in the heart.[59] Furthering our understanding of CSCs and their role in cell renewal in the native myocardium may profoundly change the potential of regenerative medicine in the heart over the next decade.[60] Due to the small autologous populations of all these cells, they must be isolated and amplified in-vitro before transplantation into damaged myocardium.

The first trials for myocardial regeneration in humans extracted skeletal myoblasts (SM) via intramuscular biopsy and cultured populations in-vitro before intramyocardial injection.[61] Skeletal myoblasts are the cell precursors to skeletal myocytes and their similarity to

cardiomyocytes makes them a good candidate for cardiac regeneration. Results from a long term investigation into the safety and efficacy of myoblast transplantation found that ejection fraction was improved in MI patients treated with direct infusion of myoblast as measured by echocardiography and Fluorodeoxyglucose (FDG) positron emission tomography (PET). PET imaging revealed new regions of glucose uptake in scar tissue suggesting new regions of viable tissue.[62] However a subsequent and more rigorous study using data from the Myoblast Autologous Grafting in Ischemic Cardiomyopathy (MAGIC) trial has since found that SM transplantation can also result in arrhythmogenesis and produces no significant changes in global or regional heart function in cell treated patients.[63]

There is a growing body of evidence that the beneficial effects of transplanted stem cells to the myocardium and other organs is not directly through the integration and proliferation of the cells but due to paracrine signalling effects.[64] Stem cells are known to secrete cytokines, chemokines and growth factors that have been shown to be beneficial in the ischemic myocardium.[65-67] The paracrine signalling model of cardiac regeneration regards the transplanted stem cells as analogous to proregenerative molecule factories secreting bioactive molecules to the benefit the surrounding tissue without fully integrating with it. These paracrine effects are thought to modulate the physiological response of the body to the infarcted myocardium, attenuating the inflammatory response to myocardial infarction, resulting in reduced cell death and reduced adverse remodelling.

This view of stem cell therapy as beneficial only through paracrine effects has led to studies that focus on the release of paracrine signalling molecules by delivering cells with little regenerative potential such as fibroblasts and macrophages.[68] Other studies have genetically altered stem cells to overexpress the genes that produce these proregenerative paracrine molecules theoretically maximising the effect. For example, Duan et al. (2003) produced a genetically modified bone marrow derived mesenchymal stem cell line that overexpressed the hepatocyte growth factor(HGF).[69] The authors demonstrated improved contraction, denser capillary networks, smaller scar size and reduced collagen content in ischemic myocardium treated with the cells, attributing these improvements to the high persistence of HGF in the infarcted tissue. Another important bioactive molecule in cardiac regeneration is vascular endothelial growth factor (VEGF) thought to be key in the development of new vasculature and improving tissue perfusion following infarction.[70] A study by Ye et al. (2007) transfected skeletal myoblasts with the human gene for producing VEGF and transplanted the cells into rats following myocardial infarction.[71] Based on ultrasound measurements, ejection fraction was improved in animals

treated with the VEGF expressing cells. Molecular and histological studies were performed to demonstrate improved regional blood flow and blood vessel density in the VEGF group.

The relative roles of cell differentiation, integration and paracrine effects in the regeneration of tissue is an ongoing field of research. The overall consensus of these studies is an acceptance that although myocardial regeneration is a feasible goal, optimization of cell type, delivery strategy, cell survival and graft integration is still required and is key to producing a successful therapy.

1.2.4.3 Delivery routes

The delivery route chosen for cardiac cell therapy can make a significant difference to the therapeutic outcome. An important factor dictating delivery strategy is the invasiveness of the procedure, with open chest injections unlikely to gain clinical acceptance unless performed in conjunction with necessary invasive surgery. For this reason catheter and infusion based delivery routes are preferred.[72]

Currently there are 3 common delivery routes that are used in clinical trials, systemic venous infusion (SVI), intracoronary infusion (ICI) and intramyocardial injection (IMI). The choice of delivery strategy aims to maximise the number of cells retained, efficacy of the treatment and minimise complexity and invasiveness of the procedure. SVI is the simplest delivery method and does not require anaesthetic or specialised equipment but delivery is indirect and has been shown to deposit a high proportion of transplant cells in the lungs and non-target organs such as the liver and spleen.[73,74] ICI is currently the preferred method for clinical trials, and has the advantage that cells are only delivered to perfused tissues in MI, ensuring they settle where oxygen and nutrient flow are preserved and there is a favourable environment for cell survival. However, this is a non-specific delivery technique and cell retention in the heart is low.[75] IMI injections can be delivered via catheter to the LV where the cells are delivered via the endocardium, this route has shown the best retention of cells in the myocardium but a significant number is still deposited to other organs. In a study by Hou et al. (2005) radiolabelled blood mononuclear cells were injected by ICI and IMI routes and their distributions at 1 hour post engraftment showed that up to 47% of cells were located in the lungs and all injection routes showed significant loss of cells from the heart.[76]

Low cell retention in the target area following engraftment is a common issue seen throughout cell therapy studies.[77] Reports suggest that integration of therapeutic cells is a transient process with the vast majority of donor cells lost from the heart within hours of delivery.[78] This has been reported in the case of SM cells, bone marrow cells, cardiac stem cells (CSCs), c-kit+/cardiospheres

and embryonic stem cells suggesting that cell choice is unlikely to be the sole cause. Although a high cell rejection fraction still has the potential to improve heart function through paracrine effects it is only a partial solution for cardiac regeneration. This has necessitated the development of a more refined concept of cell therapy in tissue engineering.[79] Advanced tissue engineering techniques are now at the forefront of regenerative medicine, and an array of technologies under development aim to protect and nurture grafted cells and improve the post infarct environment.

1.2.5 Tissue engineering

Tissue engineering aims to supplement cell therapy for improving outcome in regenerative medicine. The aim is to produce functional 3D constructs that are able to stimulate regeneration or directly replace damaged tissue. These constructs are produced in-vitro where they can be tailored in size, shape and function before engraftment.[80] The major difference from standard cell therapy and tissue engineered solutions is the movement from liquid suspension of treatment cells to the combination of cells with a supporting structure and microenvironment that can be tailored to aid cell survival and host integration.

1.2.5.1 Overview of cardiac tissue engineering

When engineering 3D biomaterials for cardiac regeneration several considerations need to be made regarding the mechanical properties and cellular microstructure required to create a suitable environment for contractile cells, these requirements are outlined in Figure 1.5. Creating artificial force-producing cardiac muscle tissue for engraftment to the damaged myocardium is a complex problem and producing a structure that is able to meet all these requirements is a significant challenge and will rely on a great deal of cross disciplinary expertise.

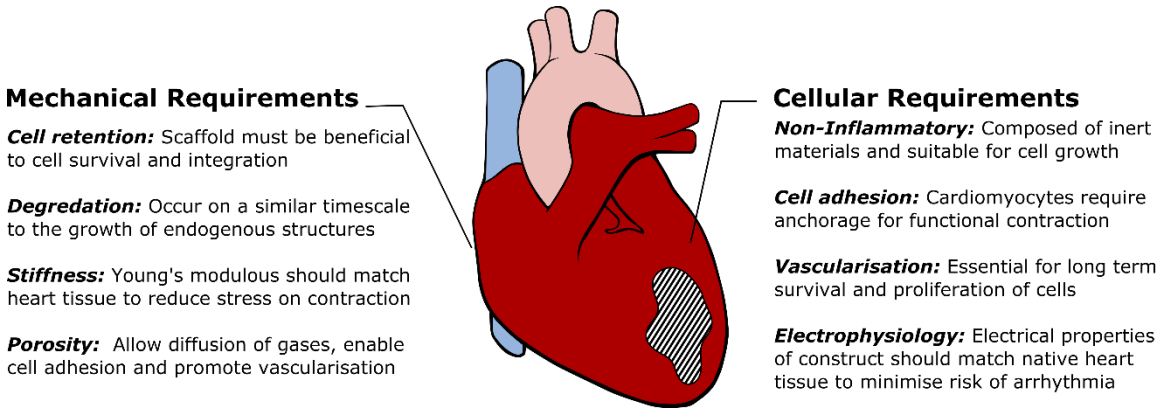

Figure 1.5 The ideal scaffold for engineered heart tissue would meet all of these requirements. Due to complex interactions between the host tissue and the engineered construct this represents a major challenge for cardiac tissue engineering.

Cardiac tissue engineering aims to replicate the native environment of the myocardium, requiring a combination of cellular and extracellular structures. More advanced materials may also incorporate sources of bioactive molecules, perfusion and oxygen transport.[78] The extracellular structure is usually referred to as a matrix or scaffold and is seeded with cells in culture or bioreactor to create engineered tissue with specific properties. For example, a bioreactor in which cells are cultured under mechanical stimulation is able to induce orientation in myofibers seeded on a scaffold.[81] Cardiac tissue engineering can also be approached without cell seeding. In this approach it is hoped that the scaffold will promote in-situ regeneration either through mechanical support of the damaged myocardium or through controlled release of bioactive molecules or drugs as the scaffold material breaks down.[82] Alternatively cells can be cultured to form artificial tissue without the use of an artificial scaffold, this approach is discussed in depth in Chapter 7.

1.2.5.2 Extracellular biomaterials

The choice of material with which the engineered extracellular structure is constructed affects all stages of development and integration. At the cell culture stage the chosen material must allow cell adhesion, promote cell proliferation and allow for cell survival by permitting oxygen and nutrient transport. At the engraftment stage the biomaterial must be biocompatible-inducing a minimal immune response whilst also being biodegradable and maintaining a preregenerative cellular environment.

In general, there are 2 broad classes of material currently used as a base for creating an artificial extracellular matrix (ECM) in engineered heart tissue; natural polymers and synthetic polymers.

These ECM materials can be used singularly or they may be combined to create hybrid natural/synthetic materials to take advantage of certain characteristics of each.

Natural polymers currently utilised for cardiac tissue engineering include collagen I, alginate, fibrin, Matrigel, glycosaminoglycan's, gelatin, chitosan and decellularised natural extracellular matrix.[83-87] Natural polymers are inherently biodegradable in regenerative timescales and biocompatible due to their similarities to internal extracellular matrix. Importantly they are also highly permissive to enzyme transport and cell signalling making them good candidates for promoting regenerative therapy. However, these advantageous biomolecular properties are offset by comparatively weak mechanical properties in comparison to synthetic materials. Synthetic polymers currently in use include poly(lactic-*co*-glycolic acid), poly(glycerol sebacate), poly(N-isopropylacrylamide), polycaprolactone, polyurethane and polyethylene glycol (PEG).[88-92] Synthetic polymers are much more versatile in terms of mechanical characteristics such as stiffness, degradation and microstructure however they are less permissive to chemical signalling making them susceptible to immunological rejection.

There is a strong case for mechanical support being one of the key influences in minimising adverse cardiac remodelling. Restoration of the mechanical support lost through tissue apoptosis following infarction may be highly beneficial to patients following acute MI. For example, ventricular restraint therapy is a surgical treatment for major heart failure in which a supporting structure is wrapped around the ventricles to provide passive end-diastolic support reducing the severity of ventricular dilation.[93] The presence of this support has been shown to reduce end systolic and diastolic volumes as well as maintain the shape of the heart in a 300 patient cohort from the ACORN trial.[94] However, although cardiac morphology was preserved, LV ejection fraction showed no significant improvement. This suggests that mechanical support alone is not sufficient to regenerate the myocardium and that additional therapeutic agents are needed such as integration with cell therapy or incorporation of growth factors.

1.2.5.3 Functionalisation of constructs

An exciting advantage of implanting a cell loaded biomaterial, as opposed to direct cell injection, is that the biomaterial can be more than an inert cell structure for supporting cells. The biomaterial can be 'functionalised' with a multitude of different properties to make it more effective for different applications. Key functionalisation can include incorporating bioactive molecules, electromechanical stimulation and imaging contrast agents.

The incorporation of bioactive molecules in the structure of biomaterials for regeneration such as growth factors and pharmacological agents has been shown to produce therapeutic effects. The targeted delivery of VEGF to the infarct border zone for example has been shown by Rosano et al. (2012) to significantly improve perfusion and LV function in rats.[95] Incorporating growth factors such as VEGF within a biomaterial has the advantage that the biomaterial can be tuned to a specific degradation profile resulting in the controlled release of the stored growth factors over time. This has the potential to significantly improve the uptake of the growth factor within the target region and provide long term regional therapy. A study by Silva et al. (2007) injected VEGF loaded hydrogels into ischemic hind limbs to demonstrate this concept.[96] The authors were able to show significantly greater angiogenesis in the treated hind limbs compared to a one-time bolus of VEGF. A recent study by Rodness et al. (2016) delivered VEGF to the infarcted epicardium in rats via a patch composed of calcium-alginate microspheres with a known degradation profile engrafted with a restraining chitosan sheet.[97] The authors showed that the microspheres with or without VEGF showed improved cardiac function assessed by MRI but that the rats treated with VEGF positive microspheres had reduced wall thinning and smaller infarct areas at 4 weeks. Regenerative application of microspheres are discussed in more detail in chapter 7.

This delivery approach is not limited to VEGF and can be beneficial in any pharmacological therapy for myocardial infarction where spatial and temporal control of drug action can aid efficacy. Other studies have been performed with encapsulated superoxide dismutase (SOD) encapsulated in polymer microparticles.[98,99] SOD scavenges the damaging superoxide radical $O2^{\cdot-}$, following MI it has been shown that there is a significant increase in superoxide levels along with a reduced presence of native SOD due to saturation of the clearance system. Regulation of SOD levels following MI has therefore been proposed as a potential mechanism for therapy following MI.[100] However, this approach has led to mixed results and remains an active area of research.[101,102]

Electromechanical functionalisation of biomaterials has been pioneered by Zimmerman et al. with the development of engineered heart tissue (EHT).[103] EHT are small loops of collagen/Matrigel based scaffold that are cultured with neonatal heart cells while under continuous cyclic mechanical stretching. The result is a loop of self-contracting engineered tissue that can be transplanted singularly or in a patch onto the epicardium to improve contraction in regions of lost function. The first example of EHT was produced by Eschenhagen et al. (1997).[104] The authors developed the EHT as a testbed for cardiac research and proposed it would be beneficial to streamlining genetic and pharmacological studies in the heart. The EHT constructs

were first transplanted into the infarcted myocardium as a therapy in 2002 by Zimmerman et al. who showed that despite the contractile function of the EHT being maintained following transplantation there was no significant improvement in left ventricular ejection fraction (LVEF) measured using echocardiography. The authors did show however that the EHT was heavily vascularised and retained well-ordered muscle structure suggesting that the graft could survive and optimisation of the therapy may provide better functional improvements.

The addition of contrast agents to a biomaterial allows the use of non-invasive imaging modalities to observe the location of the engraftment. With an appropriate imaging modality the volume and structure of the material can be visualised in situ (see imaging theory 2.1). Contrast agents can be bound to the therapeutic cells or molecules within the biomaterial that enables tracking the migration of the therapy. This has been used to shown the migration of native stem cells to infarcted tissue following an ischemic injury as well as the localisation of explanted cells that were labelled with the CxCR4 gene to induce homing to the ischemic myocardium.[105,106] Contrast agents can also be bound directly to the supporting extracellular biomaterial to allow tracking of biomaterial retention that can allow quantification of in vivo material degradation. In an example of this Shkand et al. (2016) introduced viscosity sensitive fluorescent dyes in an alginate hydrogel. This was used to optically track alginate implants in shallow tissue to measure the half-life of hydrogel retention under physiological conditions.[107]

The importance of imaging in the assessment of cardiac regeneration therapies is acknowledged as key to demonstrating that regenerative medicine is effective and safe. Imaging enables the means to optimise therapies and identify which components of tissue engineering or cell therapy produce the greatest benefits for the patient and most effective functional repair of the myocardium. The regional nature of cardiac disease and the localised therapies described here require specialised techniques for tracking regional tissue and assessment of function. Clinically, heart function is traditionally quantified using global function measurements such as left ventricular ejection fraction (LVEF). There is a requirement for effective imaging tools for locating engrafted cells and biomaterials and for quantifying regional heart function. This thesis works to develop tools for regional heart assessment with the goal of translating them to the assessment of regenerative therapies. Imaging technologies with valuable applications in assessment of cardiac disease are introduced in the following chapter.

1.3 Summary

This chapter has introduced the devastating effects of cardiovascular disease worldwide and the way in which coronary artery disease and the resulting myocardial infarction leads to heart failure and death. The potential benefits of myocardial regeneration therapy are significant and the development and optimisation of these techniques offers hope for a better prognosis in patients with CVD. Later chapters in this thesis will discuss in detail, specific techniques for regenerative therapy and discuss the imaging tools developed for assessing therapeutic outcome. The importance of imaging in the assessment of cardiac regeneration therapies is acknowledged as key to demonstrating that regenerative medicine is effective and safe as well as providing the means to optimise therapies and identify what components of tissue engineering and cell therapy produces the maximum benefit for the patient and most effective functional repair of the myocardium.

Chapter 2

Introduction II - Imaging background and theory

2.1 Introduction

This chapter describes the principles behind the biomedical imaging modalities used for this research. This thesis primarily focuses on developing advanced preclinical MRI techniques and so MRI is discussed in detail. Also introduced are optical projection tomography (OPT), Ultrasound (US) and bioluminescence imaging (BLI) that are used in a multimodal approach to imaging cardiac regeneration in Chapter 7. Since OPT, US and BLI represent comparatively smaller components of the project they are briefly summarised. Descriptions of these techniques will include short explanations of the origin of the relevant signal, how images are acquired and reconstructed and notable applications.

In vivo imaging is an essential tool for assessing the efficacy of therapy and is utilised in the vast majority of studies reporting on regenerative therapies.[108] The efficacy of cardiac regeneration therapies remains controversial, with the majority of studies reporting little to no improvements of standard measures of cardiac health such as left ventricular ejection fraction (LVEF). Therefore, there is ongoing discussion concerning whether this regenerative medicine strategy is beneficial to patients and worth pursuing.[109] With no definitive evidence of major functional improvement, cell therapy and tissue engineering will not be preferred to standard techniques such as beta blockers and revascularisation therapy that have proven improvements in LVEF. Although LVEF has traditionally provided valuable quantification of overall heart function, the possible beneficial effects of cell therapy on specific regions of myocardium may not be captured using this measurement. Advanced regional assessment techniques such as the MRI techniques developed in Chapter 5 and Chapter 6 are therefore required.

When investigating regeneration, it is valuable to be able to track and monitor cell and biomaterial retention following engraftment to the heart. Without this knowledge it is difficult to attribute any functional change to the presence of the therapeutic cells or material. Cell tracking is typically performed using molecular imaging techniques based on nuclear, fluorescent or bioluminescent emissions. Tracking biomaterials can be performed in the same way, the objective being the introduction of imaging contrast to the transplanted material that makes it valuable using a non-invasive in-vivo imaging modality. The work described in this thesis takes a multi-modal imaging approach, allowing each imaging modality to be used for a specific optimised purpose.

2.2 Cardiac imaging overview

By far the most common imaging modality used for cardiac imaging is ultrasound echocardiography. This is mainly due to the convenience offered by an ultrasound examination thanks to the imaging device being portable and widely available. However, the improved tissue contrast and spatial resolution of MRI has led to it being the gold standard imaging modality for assessing heart function where available.[110] In preclinical imaging studies it has been shown that cine-MRI is more sensitive to functional change that standard 2D echocardiography.[111] However, the high temporal resolution and real time imaging of ultrasound has made it the ideal tool for image guided procedures. This has found frequent use in myocardial regeneration therapy as an aid to cell and biomaterial injections. For cell tracking, nuclear imaging systems such as PET and SPECT are regarded as the gold standard for tracking cells in vivo. However, the cost and complexity introduced by adding nuclear imaging to a study makes it unappealing for many studies. Alternative and more convenient cell tracking systems such as bioluminescence imaging are available that are also able to offer another layer of information by imaging only viable cells. This study makes use of magnetic resonance imaging in Chapter 3, 4, 5, 6 and 7 for its ability to offer high quality and versatile assessment of cardiac structure and function, ultrasound is used for image guided delivery of treatment material to the heart and BLI is used of cell tracking since it is the most suited modality for tracking both the spatial distribution of cells and their viability.

The following sections will discuss in more detail the inner workings of each of these chosen imaging modalities describing the mechanisms by which they produce image contrast and how they form an image. The therapeutic biomaterial imaging studies described in Chapter 7 make use of the imaging techniques described in this section.

2.3 Magnetic Resonance Imaging

A large fraction of this thesis is focused on developing and using MRI acquisition techniques. It is therefore helpful for the reader to have a basic understanding of fundamental MRI principles. Since MRI has been described extensively in previous works this section will aim to briefly describe the major concepts. For a full description of physical principles and MRI theory readers are directed to Haacke et al. (1999).[112] This section will begin with an explanation of nuclear magnetic resonance and its origin this is followed by a description of the essential components of an MRI system and how radiofrequency (RF) energy can be used to manipulate nuclear spins. Next, the concept of image formation from these RF signals will be described and the gradient echo and spin echo imaging pulse sequences described. Finally, the necessary modifications to

adapt MRI to cardiac imaging are introduced including frequently used pulse sequences for measuring global heart function with cine MRI, T1 mapping, MRI contrast agents and late gadolinium enhancement imaging for mapping myocardial viability.

2.3.1 Nuclear magnetic resonance

Nuclear magnetic resonance (NMR) refers to the phenomenon of specific atomic nuclei absorbing and reemitting radiation of specific frequencies when experiencing an external magnetic field. NMR refers to 'nuclear' as the process occurs within atomic nuclei, it requires the application of a series of 'magnetic' fields and these fields must oscillate at the specific precession frequency of the nucleus in 'resonance'.

Protons and neutrons are fermions and possess a half integer spin value. Spin is an intrinsic property within the quantum mechanical description of matter and is a quantised form of angular momentum. For the purposes of this description spin can be thought of as a particle spinning about its own axis. Any nuclei with an odd number of protons/neutrons will have nonzero spin and possess a magnetic moment along the direction of their spin. Stern and Gerlach showed in 1922 that spin was quantised by passing a beam of silver ions through a magnetic field gradient. They found that each silver ion in the beam was deflected into one of two discrete paths corresponding the spin 'up' or spin 'down' state of the nuclei. This quantisation of states is a fundamental principle of MRI. Following our previous description of a spinning magnetic moment, a proton, such as those constituting the nuclei of hydrogen atoms in physiological water and fat molecules can be described using classical physics as a spinning bar magnet that can point up or down. Manipulation of these magnetic moments using external magnetic fields is utilised in MRI to produce an image. The term spin, proton and nuclei are used interchangeably within this work and all terms refer to any particle with spin and a magnetic moment that produces MRI signal.

Figure 2.1 illustrates the spin up/down states of a proton within an external magnetic field B_0. When there is no external field i.e. $B_0 = 0$, the two spin states are equally populated and possess equivalent energy. When the spin population is placed within an external magnetic field ($B_0 > 0$) the spin state in which the magnetic moment is aligned to the magnetic field has a lower energy than the anti-aligned state. Therefore, it is energetically favourable for spins to align with the magnetic field resulting in a small excess of spins aligning with the field. The reason that only a small excess, rather than all spins align with the field is due to the thermal motion of particles forcing local interaction that equalises the two states. The small excess is

therefore temperature dependent and follows the Boltzmann distribution. At physiological temperatures this results in a small net magnetisation vector aligned with the B_0 field.

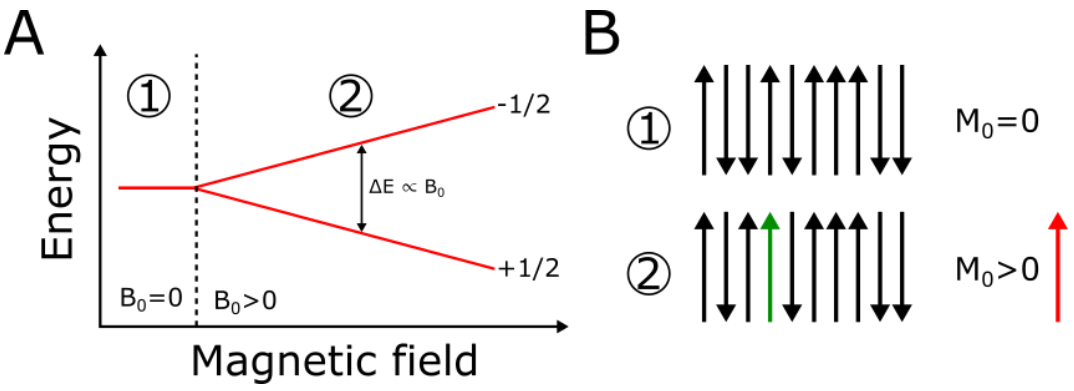

Figure 2.1 Ordering of spin states in a magnetic field. (A) When the external field (B_0) is zero the population of spins in each state is approximately equal As B_0 increases the state aligned with the magnetic field has a lower associated energy (+1/2) resulting in a small excess of spins (green) taking this state (B). This splitting of states allows spins to absorb energy ΔE in resonance.

The spin excess ΔN is equal to the number of additional of spins occupying the aligned state ($\uparrow$) relative to the anti-aligned ($\downarrow$) state, described by the Boltzmann distribution, Equation 2.1.

$$\Delta N = N(\uparrow) - N(\downarrow) = \frac{1}{2}N\left(e^{\frac{\hbar\omega}{kT}}\right) = \frac{1}{2}N\left(e^{\frac{\Delta E}{kT}}\right) \qquad \text{Equation 2.1}$$

Where N is the number of spins, $\hbar$ is the reduced Planck constant, ω is the Larmor frequency (see below), k is Boltzmann's constant and T is temperature. The spins are able to absorb energy equal to the energy gap between these two states. The relative proportions of these two states becomes higher at increasing field strengths. A higher main B_0 field therefore produces a larger magnetic moment as more spins align with the field, producing a correspondingly higher signal due to increased interaction with detection coils (see 2.3.3).

The external field exerts a torque or turning force on the spinning magnetic moment of the protons within the field. This torque causes them to precess about the axis to which they align. The angular frequency of this precession (Larmor frequency) was described by Joseph Larmor in the early 1900s by Equation 2.2.

$$\omega = -\gamma B_0 \qquad \text{Equation 2.2}$$

Where B_0 is the main magnetic field strength, γ is the gyromagnetic ratio – a constant determined by the nuclei being imaged and ω is the precessional Larmor frequency. Hydrogen is the most abundant element in the body and as such is the main target for MRI imaging providing the highest signal. Hydrogen precesses at a frequency of 42.6 MHz/T, in a modern clinical system ($B_0 = 3T$) this results in resonant absorption occurring at 127.8MHz in a preclinical 9.4T system such as that used throughout this work resonance occurs at 400.4MHz. These frequencies fall within the radio frequency (RF) spectrum. RF energy can be used to perturb the physical state described above and produce image data, this process will be described below following a brief introduction to the key components in an MR imaging system.

2.3.2 The components of an MRI system

This section will describe the hardware required for MRI imaging, how these systems are used to create an image will be described in the following section (2.3.3). The basic components of an MRI system can be split into 3 subsystems, these are the magnet, equipment and control systems. Figure 2.2 illustrates how these components are connected. The magnet is the system that performs the imaging and produces the various magnetic fields and RF energy transmission/detections to/from the body being imaged. The magnet system is stored within a room where walls often have magnetic, acoustic and RF shielding to minimise external sources of interference. The magnet is housed adjacent to an equipment room that stores the electrical amplifiers required to produce the rapid gradient and RF switching with timing provided by the MRI console. This room also houses the cooling equipment that maintains the temperature of the gradients to maintain electrical performance. From Equation 2.1 we can see that the population of spins in the aligned state increases with field strength B_0, more spins in this state produces a larger net magnetisation vector that can induce higher signals within detecting electronics. Modern MRI systems will have main field strengths in excess of 1.5T. Creating this high field requires many loops of wire carrying a high current. The heating induced by resistance in these wires at these high currents means that the main field electromagnet is constructed with superconducting wires with a critical temperature of around 4K requiring cryogen cooling. The equipment room stores the cryogen compressor that circulates liquid helium within the magnet to maintain the critical temperature of the superconducting wire. The final room is the control room where the MRI system operator controls the magnet using a computer running specialised software produced by the magnet manufacturer as well as physiological monitoring systems.

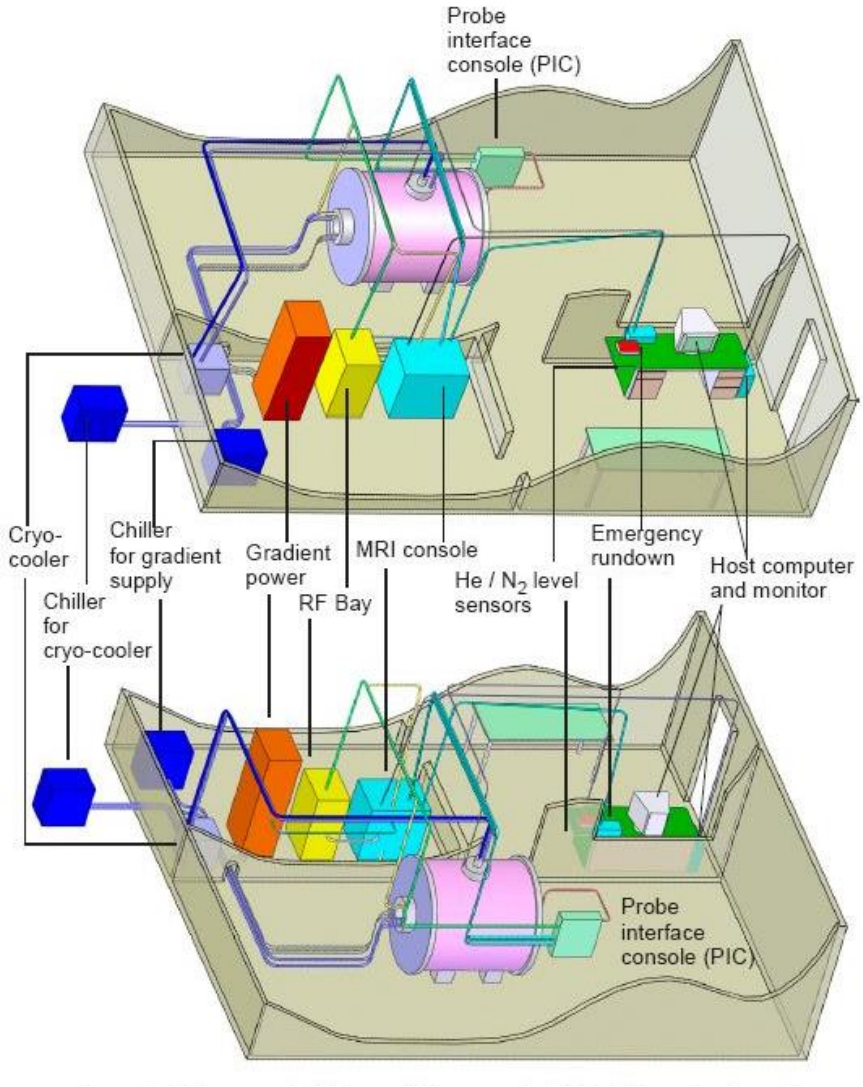

Figure 2.2 Complete MRI system. The system is spread over 3 rooms- the magnet room, the equipment room and the control room. Image credit Agilent 9.4T manual.

For the following sections it is necessary to look in more detail at the magnet system, specifically magnetic gradients used for image formation (2.3.4) and RF coils for signal excitation and detection (2.3.3).

The gradients are additional resistive electromagnets built within the main magnet body that are used to modulate the main field creating spatial dependence in precession frequency. Three gradient systems are used to modulate the field in the x, y and z directions respectively. These gradient systems may also be referred to as the phase encoding, frequency encoding and slice select gradients depending on the orientation of the imaging plane. The approximate configuration of these coils is shown in Figure 2.3. The z gradient by convention induces magnetic fields that superimpose with the main field in the axis of the scanner these coils are produced in a circular Maxwell coil configuration. The x and y gradients induce fields that

superimpose on the main field in the x and y directions perpendicular to the main field. The x and y directions are typically arranged in a Golay coil configuration.

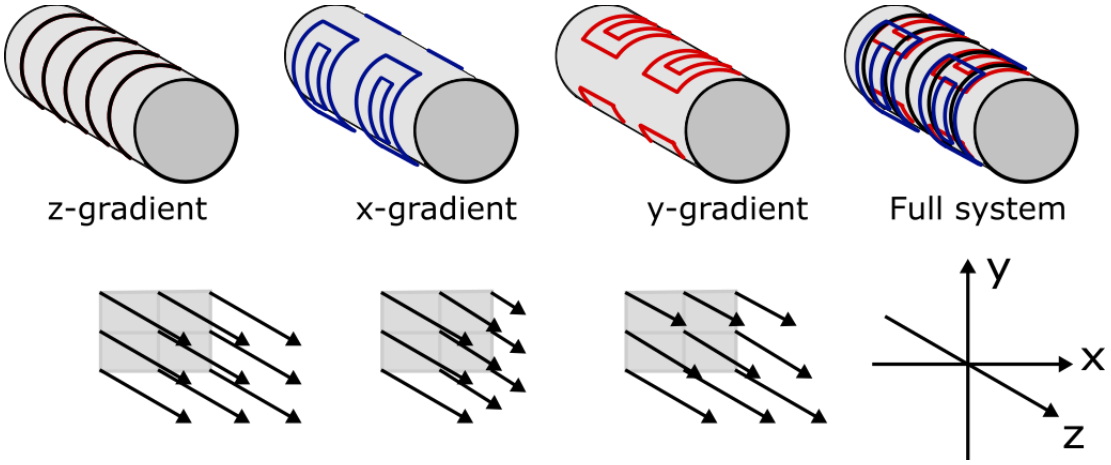

Figure 2.3 MRI gradient systems. The z gradient modulates the field in the direction of the main field. The x and y gradients modulate the field in the perpendicular directions. Vector plot below each gradient shows the resulting magnetic field when each gradient is turned on. Note that the x and y gradient act only on the z components of B_0.

RF coils are the components that transmit and detect RF frequency energy for manipulating the spins within the system. In the most basic sense the RF coils are loops of conducting wire that produce an additional magnetic field denoted B_1 that is discussed further below. The majority of RF coils used for this work operate as both RF transmitter and receivers, however it is sometimes preferable to use a larger volume transmit coil with a separate detection coil close to the organ being imaged. The voltage induced in the coil by the precession of the magnetisation has a distance dependence and placing the receive coil as close to the organ as possible allows for higher signal detection.

2.3.3 Excitation, relaxation and detection

In the above sections the manipulation of the net magnetisation vector has been described as fundamental to the imaging process in MRI, this section will elaborate on that and describe how M_0 can undergo excitation and relaxation to produce measurable signals.

The excitation process is induced by the application of a B_1 field produced by current in the RF coil as described above. The B_1 field is a rotating magnetic field applied perpendicular to the main B_0 field. The frequency of the rotation is matched to the Larmor frequency meaning that spins within the B_1 field absorb the RF energy transmitted by the coil. As they absorb RF energy the spins rotate to align with the B_1 field offsetting the net magnetisation vector M_0. These

rotating B_1 magnetic fields are switched on briefly in what is termed an RF pulse. The duration and magnitude of the RF pulse determines the angle to which M_0 is tipped relative to the main B_0 field.

The excitation process is illustrated in Figure 2.4. The net magnetisation M_0 initially points along the main field typically defined as the z axis. The application of the perpendicular B_1 field oscillating at the Larmor frequency induces a reorientation of M_0 so that it lies in the transverse plane. When the RF pulse is switched off and B_1 returns to zero, M_0 is in an unstable state and attempts to return to equilibrium along the z-axis. In the lab (stationary) reference frame this relaxation process occurs as a dense spiralling precession about B_0 where M_0 spins at the Larmor frequency while undergoing both longitudinal (along z) recovery and transverse (xy plane) relaxation. If we view the process from a reference frame rotating at the Larmor frequency, then the process is greatly simplified and M_0 returns to equilibrium along a linear path where both longitudinal and transverse relaxation occur exponentially.

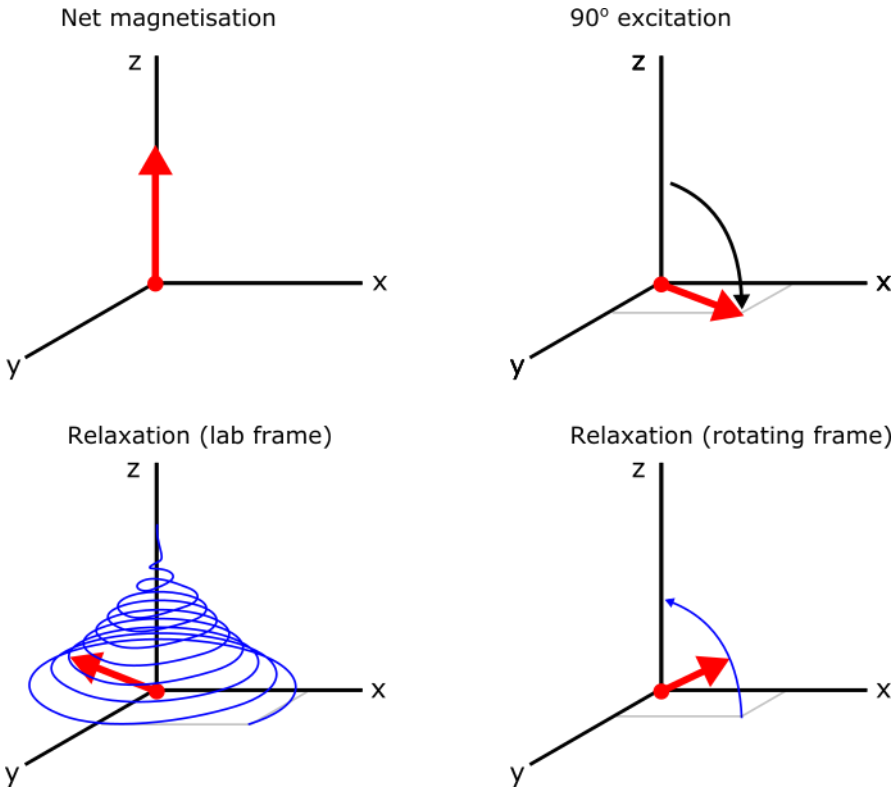

Figure 2.4 Relaxation of M_0 in the lab and rotating frames of reference. The red vector shows the NMV and the blue lines show the trajectory of the tip of the NMV. This illustrates the relaxation in the transverse (xy plane) and longitudinal (z) recovery of the magnetic vector. The lab view is the stationary reference frame and shows the rapid precession of the NVM, the rotating frame is an aid to visualising the spin relaxation in a reference frame rotating at the Larmor frequency.

The longitudinal and transverse recovery times are governed by the local magnetic environment that can be altered by the presence of molecules indicating disease or dysfunction. The longitudinal recovery is due to the exchange of energy with surrounding nuclei, atoms and molecules through physical collisions or electromagnetic interaction. These interactions create small fluctuations in the local magnetic field and these fluctuations occur at a frequency called the tumbling rate, related to properties of the molecule. When the tumbling rate of molecule is close to the Larmor frequency, the energy exchange is more efficient resulting in faster longitudinal recovery. The energy input to the system through the B_1 field is dissipated to the surrounding molecules as heat and equilibrium returns. This longitudinal relaxation process occurs exponentially and is governed by Equation 2.3.

$$M_z = M_0\left(1 - e^{\frac{-t}{T1}}\right) \qquad \text{Equation 2.3}$$

Where M_z is the component of magnetisation along the longitudinal axis, M_0 is the unperturbed net magnetisation vector, t is the time since recovery began and T1 is the relaxation constant that determines the rate of recovery. For this reason, longitudinal recovery is often termed T1 relaxation and T1 mapping is a valuable quantitative technique in MRI where this constant is measured for regions of tissue.

The mechanism by which the transverse component of magnetisation is lost following excitation is termed spin-spin relaxation and is due to the interaction between neighbouring nuclei. Transverse relaxation occurs much more rapidly than longitudinal recovery. The transverse component of magnetisation is dependent on adjacent nuclei precessing with a coherent phase. Immediately following an RF pulse the spins can be considered to be precessing in phase with each other. Due to the variation in the magnetic field strength at microscopic and nanoscopic scales these spins experience slightly different magnetic fields and so begin to precess at slightly different frequencies. Differences in precision frequency lead to magnetic interaction between neighbouring nuclei inducing further dephasing until the transverse component of magnetisation has a net value of zero. Transverse relaxation follows an exponential decay curve described by Equation 2.4.

$$M_{xy} = M_0 e^{\frac{-t}{T2}} \qquad \textit{Equation 2.4}$$

Where M_{xy} is the transverse component of the net magnetisation vector and $T2$ is the transverse relaxation decay constant. As was the case with T1 relaxation transverse relaxation through this spin-spin interaction is named for this relaxation constant and called T2 relaxation.

In any real experiment transverse relaxation occurs at a faster rate than would be predicted by inter-spin nuclear interactions. The cause of this faster decay is the inhomogeneities in the main magnetic field B_0. These inhomogeneities arise from many different imperfections in the system including hardware limitations, poor shimming, high magnetic susceptibility boundaries at tissue interfaces and magnetic particles. This accelerated T2 decay is called T2* decay and follows the same relaxation equation given in Equation 2.4. Importantly T2* relaxation can be recovered using a spin echo acquisition (see 2.3.5). This recovery is possible because the T2* relaxation is not random but dependent on position within the field and is therefore not a true relaxation process.

Following application of B_1 and perturbation of the magnetisation vector the coils switch to receive mode, where the precession of M_0 can be detected as an induced voltage within the receiving coil that may be the same one used to transmit the B_1 field. This voltage is induced by the interaction of a rotating magnetic field with a conductor. Typical MRI systems detect this voltage in quadrature. This means that two coils are used making the system sensitive to the voltage induced in two orthogonal directions. The detected signal from these orthogonal receivers can be represented as a vector in complex space where the signal from one channel is termed real and the other is termed imaginary and multiplied by the complex number i. This process is illustrated in Figure 2.5.

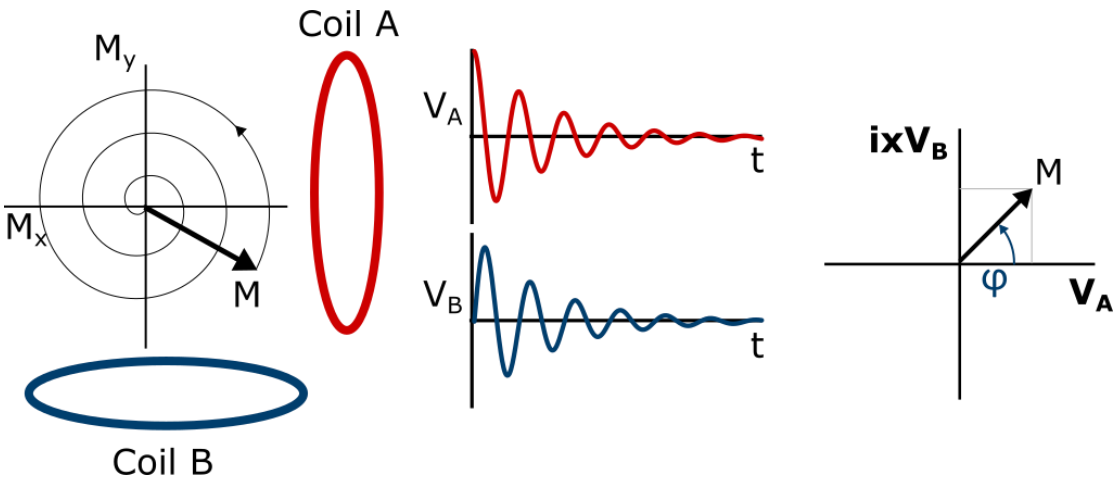

Figure 2.5 Quadrature detection of the NMR signal. Two coils sensitive to the magnetisation in orthogonal planes measure the same precessing magnetisation vector M meaning that it can be described with both a magnitude (M) and a phase (φ).

The voltages induced in each coil are able to describe the same precessing magnetisation (M) but with a π phase shift between them. This means the system can describe the magnetisation vector with both a magnitude and direction. The designation of which coil is imaginary or real is arbitrary since both coils measure the same real signal. The introduction of the imaginary

component is purely to allow for the description of the vector in complex space. The magnitude and direction of the quadrature detection are used to create images based on the MRI signal size in a 'magnitude' reconstruction or the angle of rotation in a 'phase' image. The values of magnitude and phase are calculated by Equation 2.5 and Equation 2.6 respectively. where V_A and V_B are the signals measured by each quadrature coil.

$$\mathrm{M} = \sqrt{{\mathrm{V_A}}^2 + {\mathrm{V_B}}^2} \qquad \text{Equation 2.5}$$

$$\varphi = \tan^{-1}\left({\mathrm{V_B}}/{\mathrm{V_A}}\right). \qquad \text{Equation 2.6}$$

These voltages are received by the MRI console where it is digitised before undergoing Fourier reconstruction. The processes by which these quadrature voltages induced by a precessing spin is translated to an image through spatial encoding is described in the next section.

2.3.4 Image formation and reconstruction

Using NMR for imaging can be traced back to the original experiments of Lauterbur and Mansfield (1973), who demonstrated that the application of spatially varying magnetic fields or gradient produced a spatially dependent precession frequency that could be used to create tomographic imaging planes.[113,114]

The 3 gradient sets described above in the introduction to MRI hardware are essential in creating this spatial selectivity in NMR that allows us to form images. The three gradients combine in a linear fashion with each other and the main magnetic field B_0 to produce magnetic gradients that can be orientated in any direction. The three orthogonal directions created by these gradients are termed the slice select, phase encode and frequency encode gradients. Each of these gradients is used to spatially localise the NMR signal within 3D space by altering the Larmor frequency with modulation of the magnetic field experienced by spins as a function of distance along that gradient. The full spatial encoding process will be described in 3 steps relating to the order in which the steps are played out during a typical MRI acquisition. The first step is slice selection, the second is phase encoding and finally frequency encoding. These three steps and how they encode position in 3D space is illustrated in Figure 2.6.

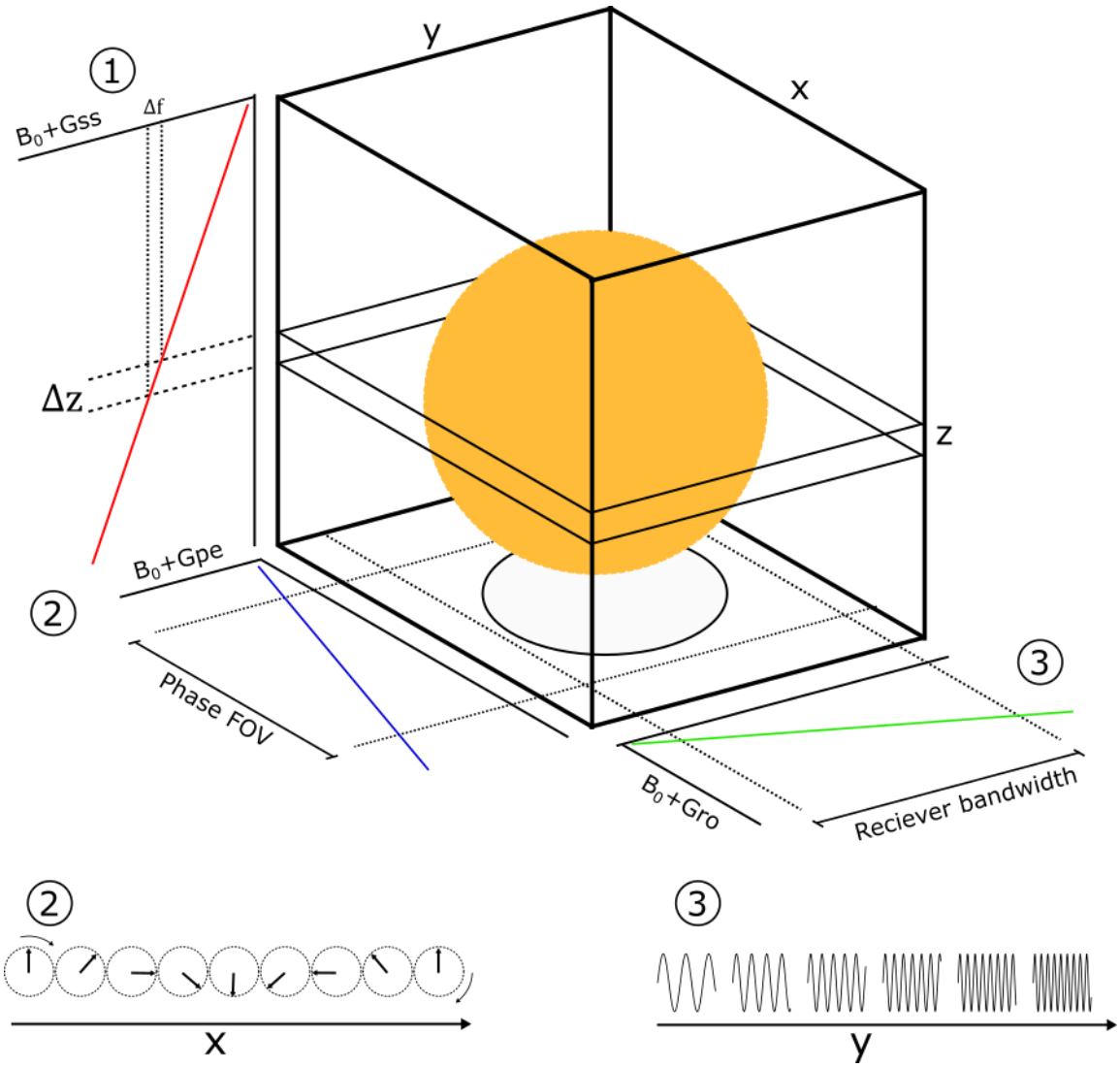

Figure 2.6 Full spatial encoding in 3D space requires the application of 3 orthogonal magnetic gradients defined as the slice select (1-Gss), phase encode (2-Gpe) and frequency encode (3-Gro) gradients. These are used to induce changes in the precession frequency or phase of spins with spatial dependence. The three orthogonal gradients can be reoriented to any direction to image different slice orientations. The acquired signal from this encoding is a superposition of all frequencies along one line of phase encoding and so requires separation by Fourier transform.

The first gradient to be applied is the slice select gradient (Gss), this is switched on during the application of the RF pulse and localises the excitation to a 2D plane with thickness Δz. The frequency of the coincident RF pulse will have a bandwidth Δf and this range of frequencies will centre on the Larmor frequency in a slice of tissue with thickness Δz. Where Δz depends on excitation bandwidth and the steepness of the slice select gradient.

The second applied gradient is the phase encoding gradient which while applied causes spins that have been excited by the RF + slice select gradient (i.e. in the imaging plane) to precess at different frequencies along that direction. Where the phase encode gradient is lower than the B_0 field the spins will precess slower and where it is higher they will precess faster. Once the

phase encode gradient is switched off, the spins return to precessing at the same frequency but have acquired a phase shift related to their position along the phase encode gradient.

The final spatial encoding gradient to be applied is the frequency encoding gradient which is applied for longer than the other two and coincides with the readout of the RF coil, hence this gradient is often called the readout gradient (Gro). The application of the readout gradient has a similar effect on the spins as the phase encode gradient, making the spins precess faster at high gradient and slower and low gradient strengths. The RF coils detect the precession frequencies of spins during the application of this gradient resulting in the detection of a composite signal containing many different frequencies corresponding to all points along the readout gradient direction. The process is repeated for a series of different phase encoding gradients that allow the readout gradient to read out one line of phase encoded data per repetition. This is repeated until the whole FOV has been sampled.

Since the data acquired is in the frequency domain, the data is filled into a mathematic k-space matrix. Simply put, k-space is to frequency information what an image is to spatial information and a Fourier transform is the mathematical process that can transform one to the other. Where in image space we observe x and y, in k-space we sample the spatial frequencies kx and ky. Each point in k-space represents how much of a specific spatial frequency is contained within the acquired image. In general, high spatial frequencies contain image resolution and edges, while low spatial frequencies contain the image contrast. The data acquired by digitising the detected signal during the readout/ frequency encoding gradient fills one line of k-space since it is a superposition of all the frequencies across the receiver bandwidth. In a standard Cartesian acquisition, the phase encoding gradient is stepped linearly across k-space so that one line of k-space is filled per repetition (also called a phase encoding step) resulting in a full k-space matrix that contains all the spatial frequencies required to reconstruct the tomographic slice being imaged.

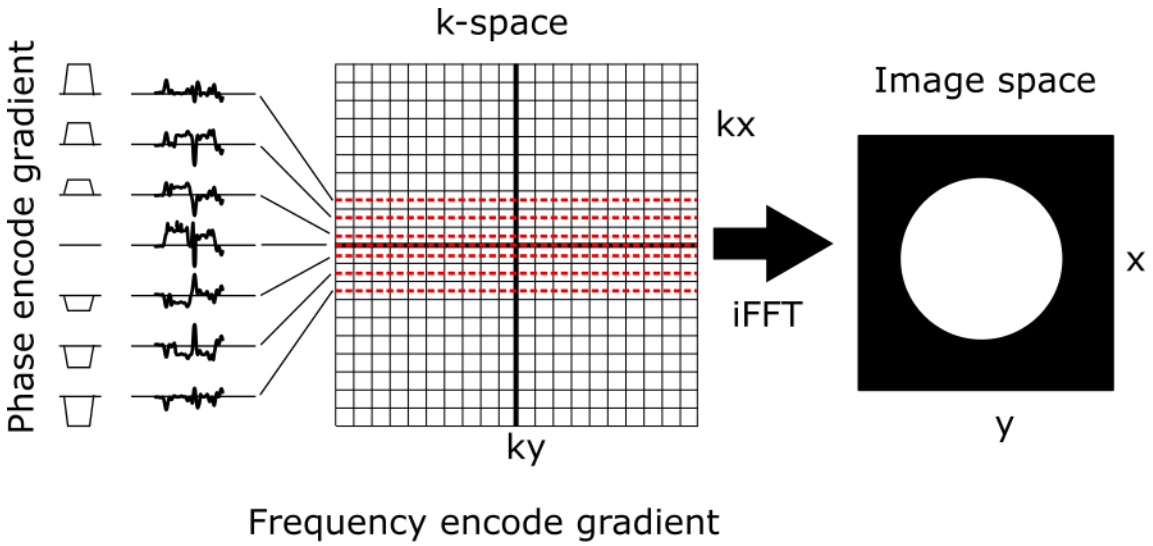

Figure 2.7 In a Cartesian acquisition k-space is filled in line by line requiring a separate phase encoding gradient for each line of k-space. Here only the central phase encoding steps are shown for clarity. Once k-space is filled an inverse fast Fourier transform can be applied to complex data to produce a complex image that can then be transformed to magnitude or phase contrast.

Each pixel in the acquired k-space matrix is of the complex form $V_A + iV_B$. Performing a 2D fast Fourier transform on this data produces another complex image in image space from which magnitude and phase images can be calculated as described in Equation 2.5 and Equation 2.6.

2.3.5 Gradient echo and spin echo

Specific compositions of RF pulses and gradients are called pulse sequences. The most common types of pulse sequence are the gradient echo and the spin echo which are the basic imaging modules often combined with other RF pulses and gradients to produce more specific contrast or encoding properties. It is therefore helpful to have an understanding of how the gradient echo and spin echo form images. A pulse sequence diagram represents each gradient and coil as a line with time in the horizontal axis. The basic pulse sequence diagrams for each sequence are shown in Figure 2.8 and Figure 2.9. The choice of gradient echo or spin echo readout depends on the application of the pulse sequence. Gradient echo pulse sequences tend to be much faster at acquiring data but spin echoes tend to have better SNR due to the refocussing pulse removing the T2* relaxation effect.

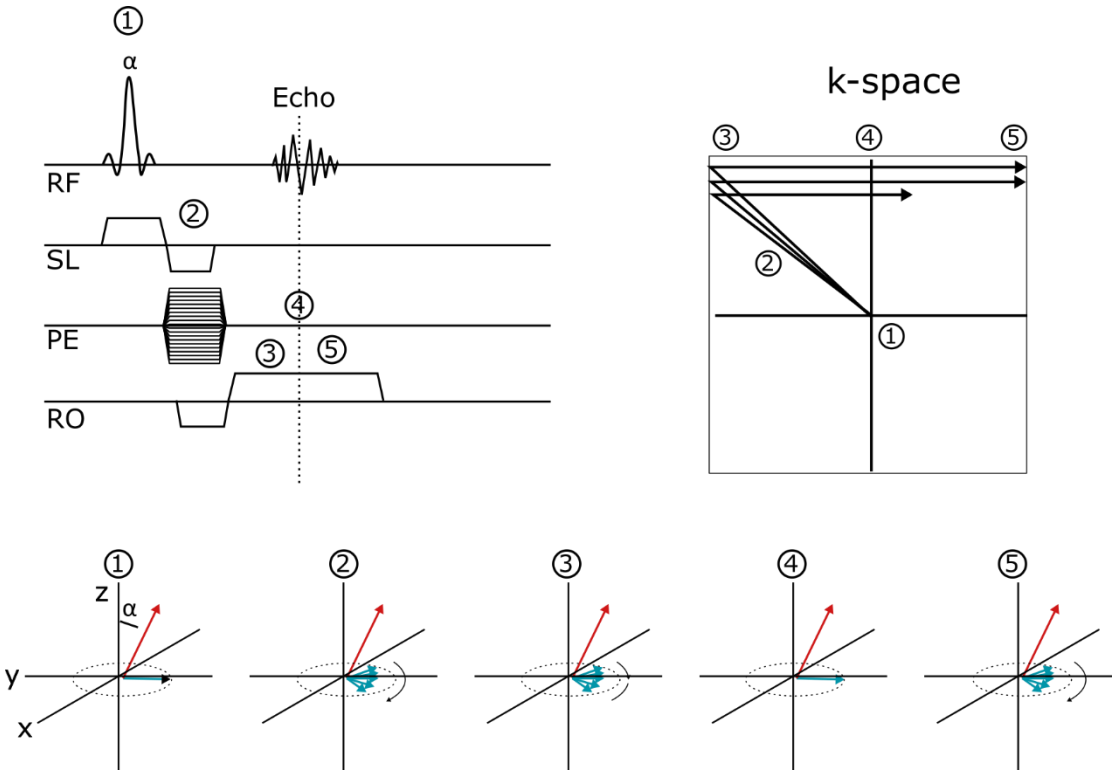

Figure 2.8 Gradient echo MRI acquisition pulse sequence. In this diagram the net magnetisation is displayed a red vector while the individual spins are represented in blue. (1) An RF pulse of flip angle α tips the magnetisation into the transverse plane where the spins are dephased by the gradients occurring at (2) reducing the magnitude of the net magnetisation. The spins are then brought back into coherence by the readout gradient at (3) before reaching complete coherence at (4) and then dephasing in the other direction at (5).

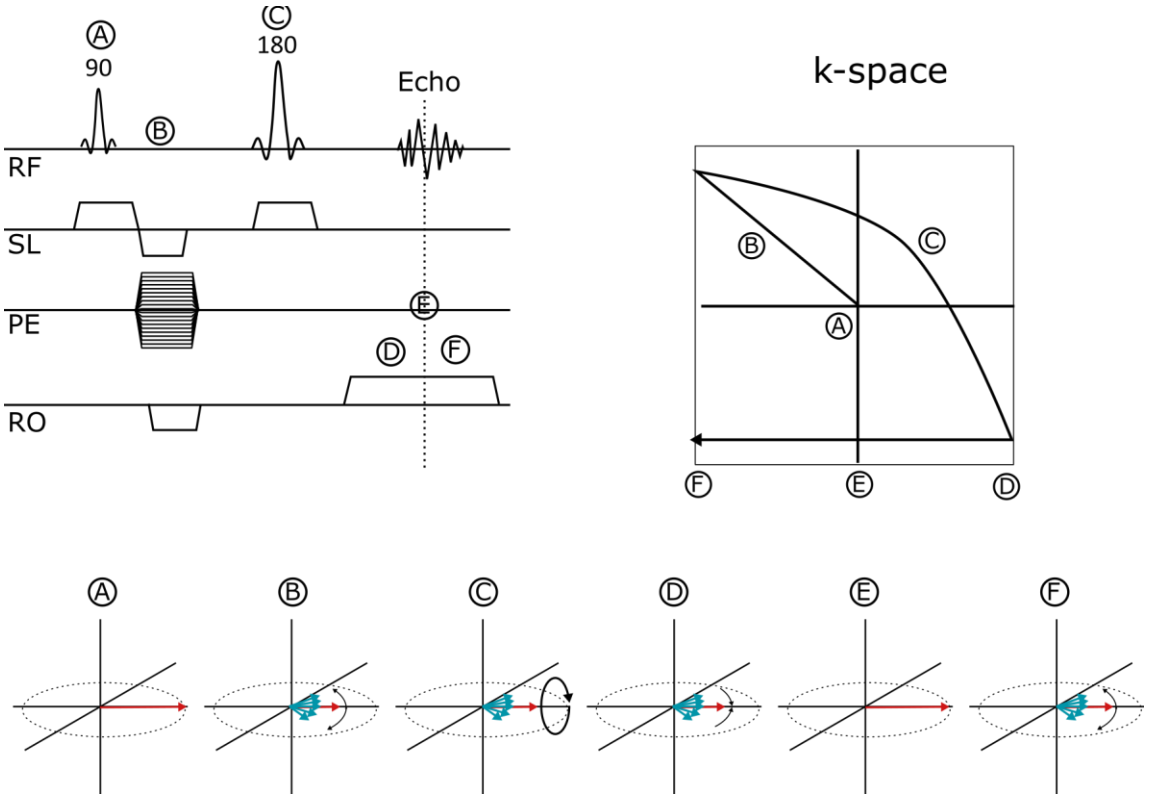

Figure 2.9 Spin echo MRI acquisition pulse sequence. In this diagram the net magnetisation is displayed a red vector while the individual spins are represented in blue. The magnetisation is tipped into the transverse plane by a large 90° RF pulse (A) before the spins are dephased by the phase encoding gradients at (B). Another RF pulse of 180° called a refocussing pulse flips the magnetisation around (C) so the spins are now rephrasing (D). An echo forms when the spins are totally rephased at (E) before losing coherence again after (F).

These basic pulse sequences are able to produce non-invasive in vivo images of the body. In most organs these sequences are suitable but for cardiac imaging a number of additional complications unique to the heart must be taken into consideration. The following sections will discuss MRI specifically in the context of practical cardiac imaging.

2.3.6 Local hardware

The MRI system used throughout this work was a 9.4T main field imaging system (Agilent technologies, Santa Clara, CA, USA). The system was equipped with 400mT/m gradients with a gradient bore diameter of 120mm, a geometrically smaller gradient set insert was available with a maximum ramp of 1000mT/m and a diameter of 60mm. These gradient configurations were used for rat and mouse imaging respectively. The basic components of the magnet setup are described in Figure 2.10.

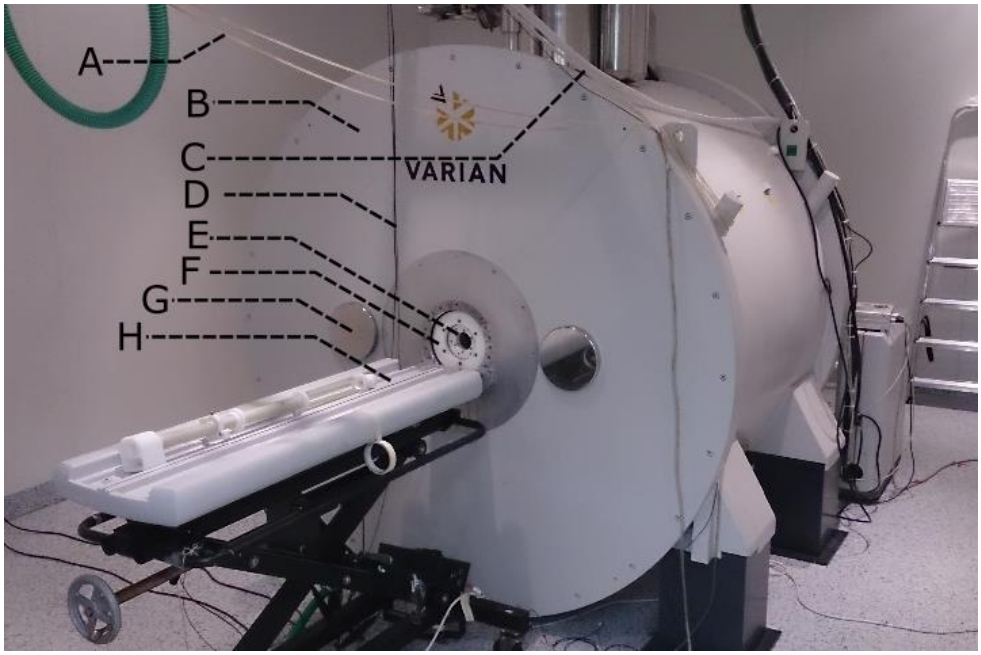

Figure 2.10 Varian system used for all MRI experiments. A- heated water lines; B- main magnet and cryogen storage; C- anaesthetic delivery and scavenger; D- fibre optic cables for physiological monitoring; E- small gradient inserts; F- larger gradients; G- shim coils; H- scanner bed.

RF transmission and detection was performed with a variety of MRI specific RF coils (RAPID Biomedical, Rimpar, Germany). All in vivo mouse imaging and ex vivo MRI used volume resonator quadrature RF coils with diameters between 26 – 39mm depending on the size of the imaging subject. Rat imaging was performed with a 72mm volume transmission coil with a 4-channel phased array surface coil for detection. Electrical resonance of the RF coil was tuned and matched for optimal signal detection at the NMR frequency of water using an external Probe Tuning Device 505NV+ (Morris Instruments Inc, Ottawa, Canada). The imaging system was controlled using the Varian VNMRJ software v 3.1 (Agilent, Santa Clara, CA, USA). This program performed imaging, shimming and calibration protocols as well as basic reconstruction. All custom sequences were written and optimised for implementation in the VNMRJ 3.1 environment.

Animals were anaesthetised in an infusion chamber under a mixture of isoflurane and oxygen before being transferred to one of the beds shown in Figure 2.11. The size of each is tailored to be suited to mouse or rat imaging but both incorporate rectal temperature probes and heated water lines to maintain thermostatis, a respiration balloon to record respirations, a gadolinium infusion line, 3 subcutaneous electrodes for recording the ECG signal and a nose cone to deliver anaesthetic while the animal is in the scanner.

Mice were positioned supine in the mouse bed with the ECG electrodes implanted in the Einthoven's Triangle configuration- positive and negative terminals placed on the anterior shoulders and a ground lead in the flank. The respiration balloon was taped across the abdomen and was decompressed during respiration as the chest moves upwards. For rat imaging the rat was placed prone on top of the RF surface array with ECG leads placed across the posterior shoulders and the respiration balloon taped across the flank.

The ECG, respiration and temperature probes were connected to a physiological monitoring system (SA Instruments, Stony Brook, NY). This monitoring system was integrated with the MRI console to allow for precise respiration and ECG image acquisition gating.

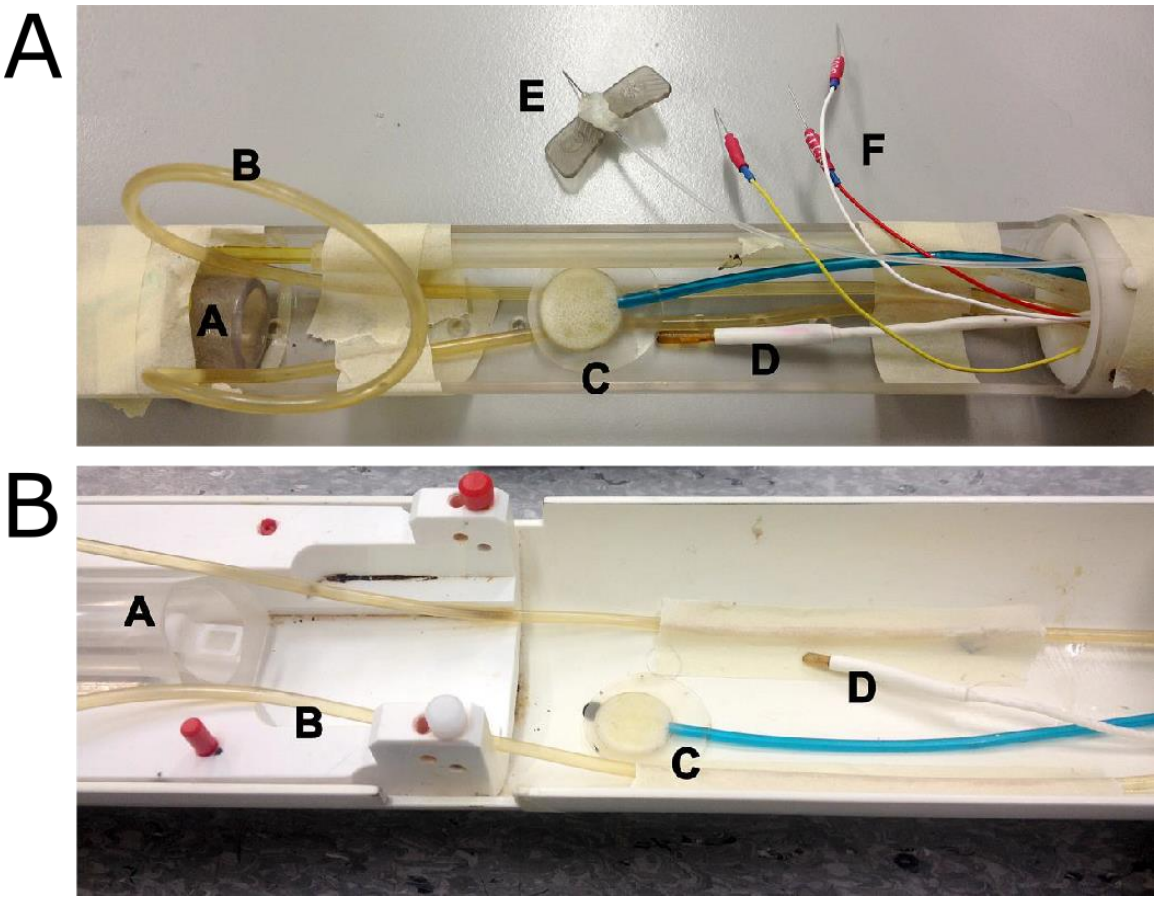

Figure 2.11 Cardiac MRI mouse (A) and rat (B) imaging configurations. A- anaesthetic nose cone; B- heated water lines; C- respiration balloon; D- rectal temperature probe; E- gadolinium infusion line; F- 3 lead ECG electrodes. Note that ECG leads and infusions lines are also present in the rat configuration but not shown.

2.3.7 Image acquisition gating

The heart is effected by two sources of motion effecting cardiac imaging. The first source is cardiac motion in the contraction and relaxation of the atria and ventricles as well as blood flow.

The second is respiratory motion that applies large displacements to the heart during inspiration and expiration. Images can be severely affected by artefacts if these sources of motion are not accounted for and corrected. For this reason the physiological monitoring equipment described in section 2.3.6 is used to synchronise the MRI acquisition to physiological motion in a process called gating.

In preclinical MRI where animals are typically anaesthetised during imaging the respiration and cardiac motion becomes periodic and predictable and so can be corrected using prospective gating techniques. The ECG trace recorded using the physiological monitoring equipment is evaluated where the start of each cardiac cycle is identified using a dynamic differential of the ECG signal identifying the sharp high amplitude characteristic peak of the R-wave. This event is converted to a transistor-transistor logic (TTL) pulse that can be interpreted by the MRI acquisition console as an ECG trigger. The same feature tracking system is used for identifying the start of inspiration and the end of expiration for respiratory gating.

For cardiac imaging it is necessary to freeze the motion of the heart during acquisition to prevent artefacts. This is typically done by segmenting the k-space acquisition with respect to the detected ECG triggers. This technique is described in detail as part of the description of cine MRI acquisition described below. Respiratory motion is accounted for by recording the respiration events through the balloon probe (see Figure 2.11A.C). This signal is converted to TTL pulses at the start and end of each respiration signalling the phases of respiration in which the heart is stationary. This gating process is illustrated in Figure 2.12. The analogue respiration signal and digitised signal are illustrated in blue and the ECG and digitised signal are shown in red. The respiratory motion is stationary when the RESP-GATE signal is 1. The heart is stationary at any identical point in the RR interval, and the digitised signal is used as a temporal reference to synchronise the scanner to keep acquisitions timed to the contraction cycle. Stationary phases of the heart are illustrated by the coloured blocks where blocks of the same colour illustrate coherent stationary phases between heartbeats.

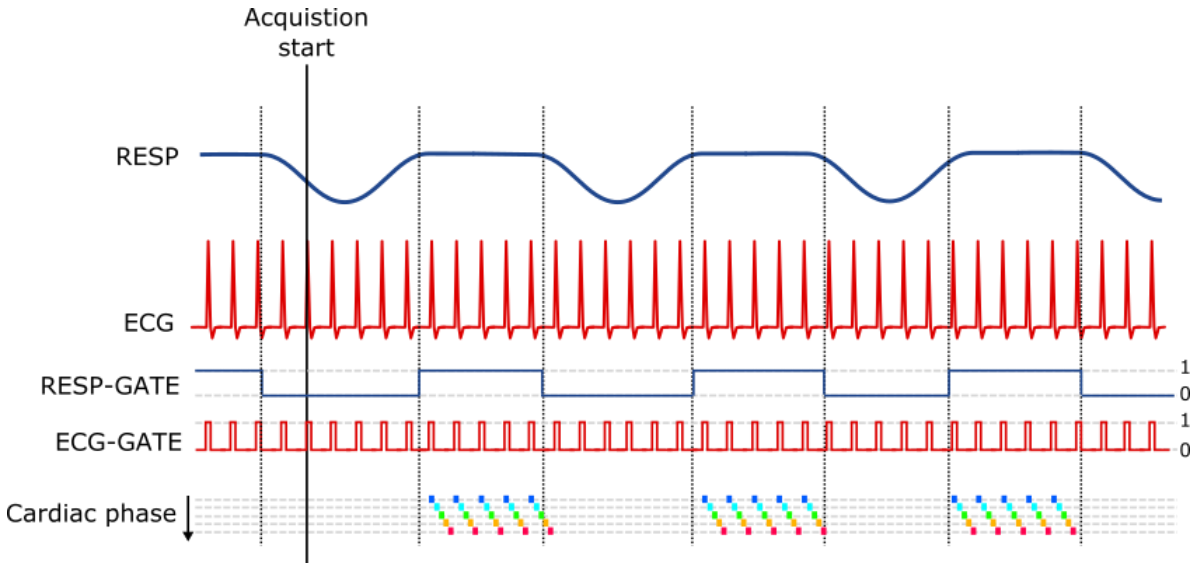

Figure 2.12 Description of image acquisition gating for cardiac MRI. The respiration trace and the ECG trace are converted to digital 0/1 signals. The heart is stationary and at end diastole when both gates are equal to 1 (blue blocks) equivalent to a logical AND operation. Applying a constant offset from the ECG trigger the heart can be viewed as stationary at different cardiac phases cyan, green, orange and red blocks show alternative stationary heart phases.

2.3.1 Cardiac imaging planes

The structure of the heart is not suited to imaging in the standard body axis image planes (axial, sagittal and coronal) due to its double oblique orientation. Tomographic images are therefore conventionally reoriented and acquired in the cardiac imaging planes, these are shown overlaid on an illustrated human heart in Figure 2.13. Typically three orthogonal planes (e.g. Figure 2.13.1-3-5) are used for orientation within the image space, once these planes are defined then imaging can begin. This reorientation process requires careful slice planning and several pilot scans at the start of any cardiac imaging procedure making imaging the heart more complex than many other organs. Images acquired in the cardiac axes however provide the best view of contractile motion and the simplest delineation of internal structures.

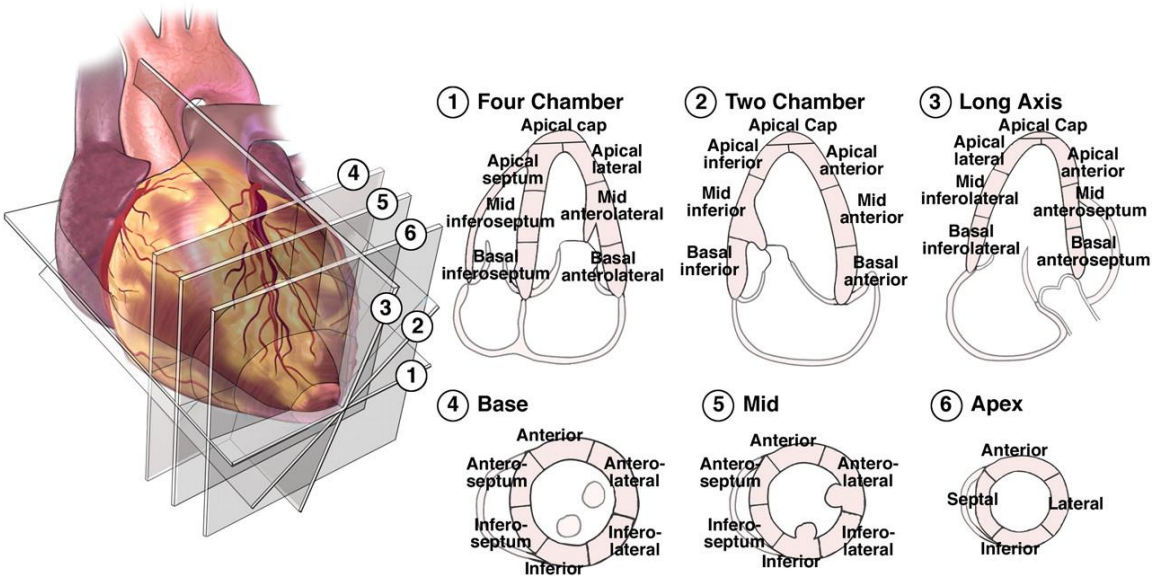

Figure 2.13 Illustration describing the cardiac imaging planes. Long axis images (1,2,3) are typically used for orientation of the short axis planes (4,5,6) although are also useful in providing the most complete single slice views of the heart. Cardiac MRI for structural and functional assessment typically uses a stack of cardiac short axis images covering the whole LV. Figure from Lang et al. (2006)[115]

Representative images of the wild type mouse heart in these planes are shown in Figure 2.14A at end systole and diastole to illustrate their appearance in MRI. The most commonly used axis for describing the heart is the short axis view and this will be used as convention for presenting results in this thesis. The 4 chamber long axis view provides a view of a large number of cardiac structures as illustrated in Figure 2.14B. The short axis is preferred since the LA view is severely affected by partial volume effects (see Figure 2.14A- 2ch LA at end-systole) when the contracting myocardium passes through the image plane making functional quantification difficult.

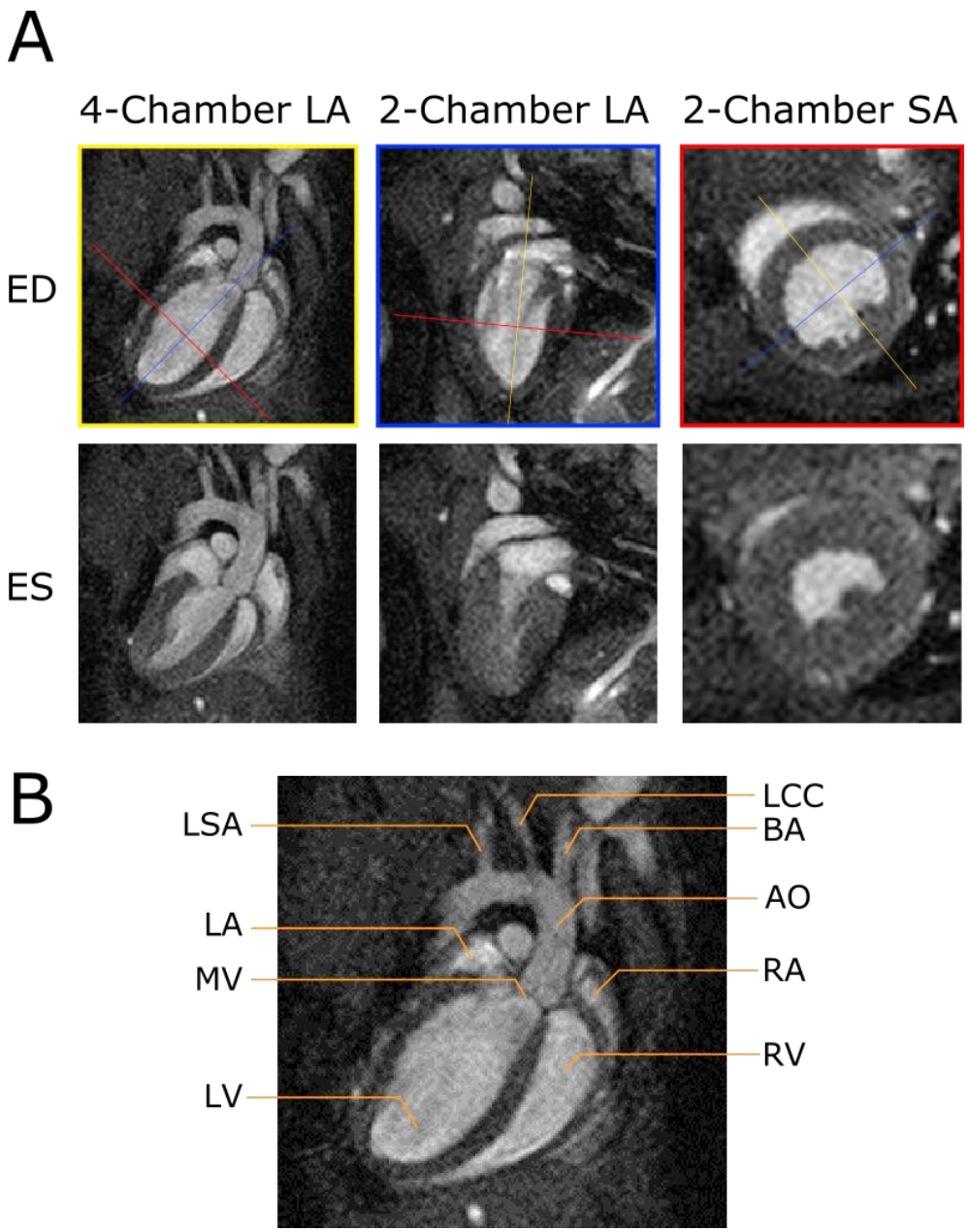

Figure 2.14 (A) Representative images showing the appearance of the cardiac axes in bright-blood MR images. LA- long axis; SA- short axis; ED- end diastole; ES- end systole. (B) detailed view of the 4 chamber long axis view of the heart at end diastole. LSA- left subclavian artery; LA- left atrium; MV- mitral valve; LV- left ventricle; LCC- left common carotid artery; BA- brachiocephalic artery; AO- aorta; RA- right atrium; RV- right ventricle.

2.3.2 Cine MRI

Cardiac cine imaging is the workhorse of cardiac MRI and is used to provide quantification of global cardiac function and visual assessment of cardiac motion. Cine imaging acquires a time series of static images of the heart that when displayed sequentially visualises the beating heart. Cine imaging relies on accurate gating for physiological motion as described above (2.3.6). Due

to the rapid heart rate of small animals used in preclinical imaging each segment of k-space must be acquired in <10ms requiring a fast gradient echo (GRE) acquisition sequence. Note that Figure 2.12 shows 5 stationary phases of the heart but the RR interval can be split arbitrarily into any number of stationary phases. Hardware limitations determine the maximum number of frames in a cine sequence. A typical mouse heart rate of around 550ms will allow for 20-25 frames with a TR=5ms. The basic principles of the cine acquisition scheme and the GRE pulse sequence are described in Figure 2.15.

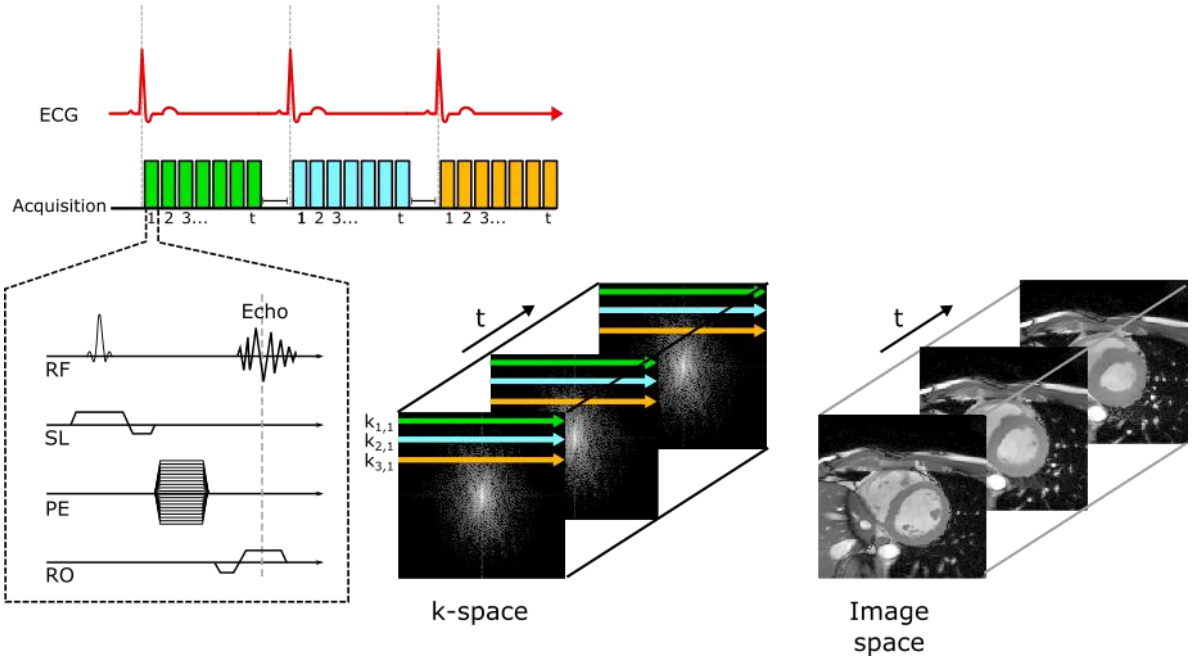

Figure 2.15 Cine MRI acquisition sequence. A GRE readout acquires one line of k-space per time frame sequentially for each ECG trigger. This repeats until each 2D k-space matrix is filled. A FFT applied to the data translates the frequency and phase information in k-space to image space.

The raw data the cine sequence acquires fills a stack of 2D k-space arrays where each 2D array is a stationary phase in the cardiac cycle. To describe the cine acquisition each line of k-space will be assigned $k_{n,t}$ describing the nth line of k-space in the image in the cardiac cycle t. Note that n and t are defined by the user as the image acquisition parameters for acquisition matrix size and number of cine frames respectively, A cine data stack will have dimensions $n \times n \times t$. The sequence starts after the detection of an ECG trigger initiating the acquisition of the first line of k-space for every frame in the cardiac cycle $k_{1,2}, k_{1,3}, k_{1,4}$ … $k_{1,t}$. At the detection of the next ECG trigger the acquisition repeats for the second line of k-space $k_{2,1}, k_{2,2}, k_{2,3}$ … $k_{2,t}$. This process repeats until $k_{n,1}, k_{n,2}, k_{n,3}$ … $k_{n,t}$ and each 2D k-space array is fully acquired for each point in time. During this acquisition respiratory motion continues, when the respiration gate switches to 0 the scanner continues to transmit the pulse sequence as normal but does not

acquire data. This means data is acquired only in the stationary phases of respiration but the magnetisation history is not perturbed helping maintain the steady state.

Cine sequences are typically acquired with low flip angles <30° which produces bright blood contrast aiding in the segmentation of the blood pool from the myocardium. In cases where it is necessary to identify the epicardial boundaries (e.g. wall thickening Chapter 4 a lower flip angle is used, at 9.4T good epicardial contrast is seen with a flip angle of around 5-10°. Typical cine acquisitions for assessing global cardiac function for the work undertaken for this thesis had resolution = 0.2×0.2×1mm; TR = 5ms; TE = 1.1ms; flip angle = 15°.

Visually cine images can provide qualitative assessment of myocardial mechanics and morphology but for research purposes it is necessary to quantify these images. This quantification requires segmenting cine images to identify the myocardial boundaries. An example of a processed cine image is shown in Figure 2.16. Cine images were processed by segmenting the endocardial boundaries at systole and diastole for each 2D image in the cine stack. Segmentation was performed using a semi-automatic method implemented in the freely available software Segment v2.0 R5294 (http://segment.heiberg.se/).

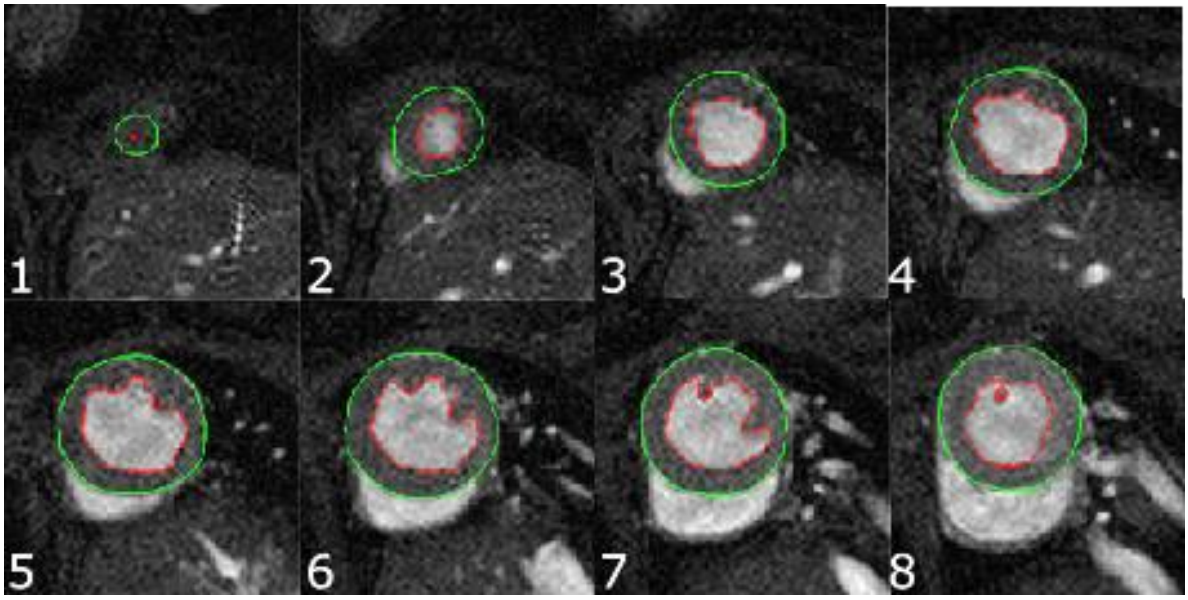

Figure 2.16 Cine image analysis in Segment, numbers indicate slice order from 1 (apex) to 8 (base). By identifying the epicardial (green) and endocardial (red) boundaries at systole and diastole information about the blood volume and myocardial shape can be calculated.

Once the endocardial and epicardial boundaries are segmented then a number of useful and quantitative cardiac metrics can be calculated, these are summarised in Table 2.1. The most commonly used value is left ventricular ejection fraction- the fraction of blood ejected from the LV during each cardiac contraction. This is a widely accepted value for global heart function and

is lowered is disease as the heart pumps less efficiently. End diastolic volume is another useful measure that gives information about the dilation of the LV following adverse post-infarct remodelling.

Table 2.1 Summary of quantitative values calculated from epicardial/endocardial segmentation. Where V is the volume of one voxel calculated from image acquisition matrix size and FOV, and N_{region}^{phase} is the number of pixels in a segmented region at a specific phase of the cardiac cycle and bpm is the heart rate.

Value	Principle	Equation
End systolic volume (ESV)	Volume of the heart at end systole [µl]	$ESV = V \times N_{blood\ pool}^{systole}$
End diastole volume (EDV)	Volume of the heart at end diastole [µl]	$ESV = V \times N_{blood\ pool}^{diastole}$
Stroke volume (SV)	Volume of blood ejected with each contraction [µl]	$SV = EDV - ESV$
Ejection fraction (EF)	Fraction of blood ejected with each contraction [%]	$EF = \frac{SV}{EDV} \times 100$
Cardiac output (CO)	Volume of blood pumped per unit time [µl /min]	$CO = SV \times bpm$
Left ventricular mass (LVM)	Mass of left ventricle [µg]	$LVM = V \times N_{myocardium} \times 1.05$

2.3.3 Cardiac T1 mapping

T1 mapping is used for quantitative assessment of T1 relaxation and is performed by fitting the T1 decay constant to every pixel time course in an image sampling the magnitude of the T1 signal. Inversion recovery is the most common imaging technique for measuring T1 relaxation. The standard cardiac inversion recovery sequence is shown below in Figure 2.17. Inversion recovery refers to the process of applying a complete global 180° inversion RF pulse that flips every spin within the imaging volume by 180°. Following inversion, the longitudinal T1 magnetisation begins to recover to the equilibrium following a T1 relaxation curve as described in Magnetic Resonance Imaging. Sampling at positions along this relaxation curve then allow for fitting of the T1 constant.

Following the first instance of respiration and ECG gate equal to 1, the 180° RF pulse flips all spins. The recovery of the T1 relaxation is then imaged at each RR interval. In the figure we show up to 3 ECG triggers acquiring at 3 different inversion times (TI – the time since the inversion pulse). In cardiac MRI the TI must always be integer multiple of the RR interval. The sequence shown is repeated for every phase encoding line to produce an image sequence showing the recovery of the T1 signal. Since the MRI scanner measures all signals as positive the recovery curve is constrained to lie above the x-axis resulting in an image sequence that starts bright, goes dark and then recovers to bright again. Following each sequence of samples an inversion recovery delay time is given to allow full magnetisation recovery before the next inversion.

This type of acquisition where the T1 relaxation curve is repeatedly sampled over the course of a single inversion-recovery cycle was developed by Look and Locker and carries their name (Look-Locker sequence). Each sample on the T1 relaxation curve requires an excitation and gradient readout that removes energy from the system and perturbs the relaxation. The result of this is that the magnetisation will recover to a saturated state. The Look-Locker sequence therefore typically uses a sequence of low flip angle gradient echo readouts to minimise perturbation to the T1 recovery curve. The more frequently the recovery curve is sampled the greater the saturation of the recovery and $M_z \rightarrow M_z cos(\alpha)$ as more samples are acquired. This saturated recovery can be accounted for when fitting the T1 recovery curve by applying the look locker correction factor as derived by Deichmann et al. (1992).[116] In brief the saturated Look Locker recovery can be fitted with the three parameter partial solution given by Equation 2.7. The fitted values of M_0, β and $T1^*$ can then be used to recover the true decay signal assuming linear spacing between echoes (i.e. consistent heart rate) using Equation 2.8.

$$M_z(t) = M_0\left(1 - \beta e^{-\frac{t}{T1*}}\right) \qquad \text{Equation 2.7}$$

$$T1 = T1^*(\beta - 1) \qquad \text{Equation 2.8}$$

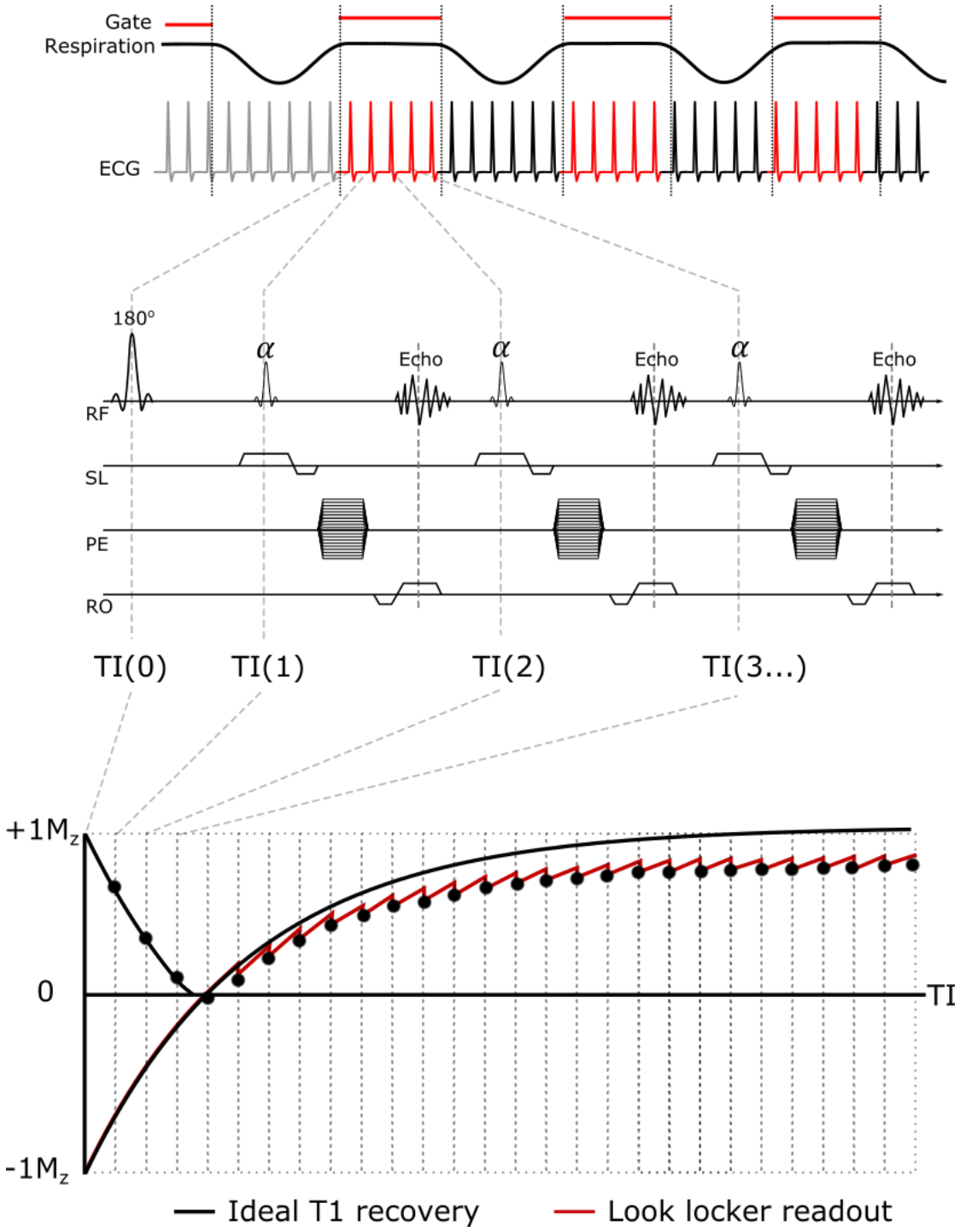

Figure 2.17 Basic cardiac inversion recovery imaging sequence. Following the detection of an ECG trigger the sequence applies a 180° inversion pulse and then samples the T1 recovery curve using a small flip angle (α) GRE readout at each subsequent ECG trigger to the specified number of inversion times. The sequence repeats for each phase encoding step. The saturation effect of the look-locker readout on the T1 recovery curve is shown in red.

The Look Locker acquisition scheme described above acquires a single line of k-space per RR interval. To fill a typical acquisition matrix for mouse imaging of 128 lines this requires 128×(IRD+NTI×RR) seconds, where NTI is the number of inversion times sampled, IRD is the

inversion recovery delay time and RR is the RR interval. Typical values for these parameters result in an acquisition time around 20 minutes depending on heart rate. This long acquisition time can make T1 impractical for inclusion in preclinical studies that perform a wide range of other imaging techniques, especially in the case of ECVF mapping (section 7.3) where two T1 maps are required. To reduce the scan time of T1 mapping a segmented k-space acquisition protocol was implemented for some work in this thesis. The segmented k-space approach was developed by Dr Adrienne Campbell-Washburn and has been extensively validated against the standard Look-Locker acquisition.[117] This approach acquires 4 lines of k-space per RR interval, thereby sampling the whole of k-space within a quarter of the time. Each of these 4 samples have individual excitation pulses and encoding gradients and so must be performed in quick succession to avoid motion artefacts. The T1 mapping performed for the preclinical thalassemia imaging project (Chapter 3) used the single line per RR interval scheme while every other chapter used the accelerated segmented k-space approach.

Both of the standard and segmented k-space Look-Locker techniques for investigating T1 relaxation are incompatible with respiration gating. This results in acquisitions over respirations resulting in corrupted images (Figure 2.18). The effect of this motion on T1 decay model fitting is dependent on the respiration frequency and heart rate. When the respiration rate is low (40 -50 /minute) the model fitting is robust to outliers as seen in Figure 2.18A. High respiration rates (50+ /minute) where a large fraction of images are corrupted can lead to inaccurate fitting shown by the different T1 relaxation curves in Figure 2.18B. To compensate for this a respiration image removal algorithm was implemented for all T1 data sets. Corrupted frames were automatically removed retrospectively using the phase encoded noise-based image rejection (PENIR) scheme.[118] PENIR exploits the presence of extra-corporeal ghosting artefacts in the phase encode direction induced by respiratory motion to identify acquisitions occurring during respiration without requiring a log of acquisition and respiration. When the mean noise signal in the extra-corporeal space exceeds a dynamic threshold determined by the noise mean + standard deviation then an image is said to be corrupted. The threshold was updated every 10 inversion times (TI's) to account for T1 signal recovery.

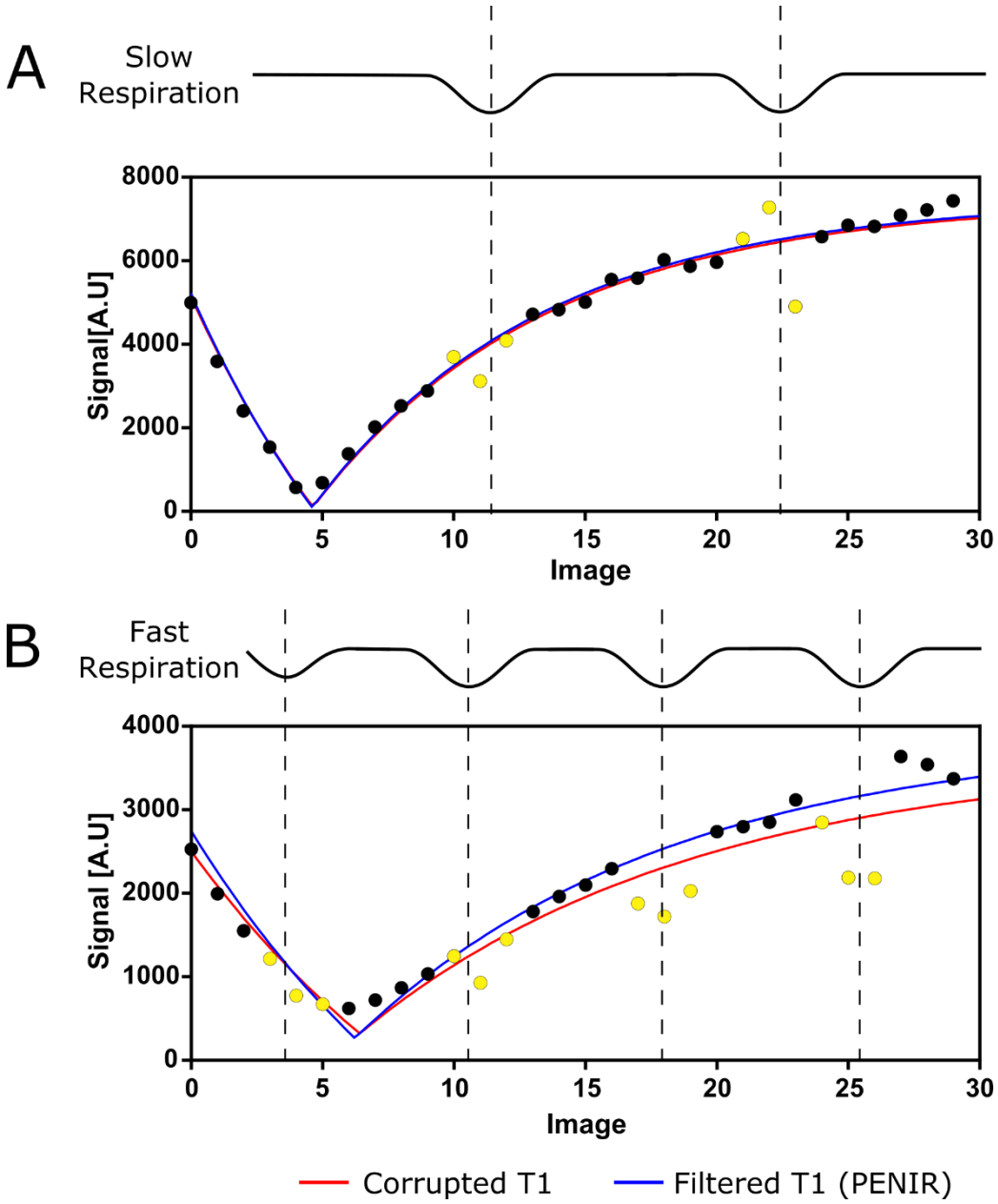

Figure 2.18 These images show the effect of motion corrupted frames (yellow) on T1 relaxation fits. Red lines show the fitted T1 including corrupted frames and blue lines are fitted with these frames excluded. Low respiration rates (A) have little effect on T1 fitting but at high respiration rates (B) the effect can become significant.

2.3.4 Contrast agents

Endogenous MRI contrast depends on three properties of tissue- T1, T2 and spin density. Differences in these properties alter the response of tissue to a pulse sequence resulting in varying signal magnitude with contrast depending on the pulse sequence applied. Contrast agents are exogenous molecules that alter the T1 and/or T2 of the tissue around them, providing sensitive and specific markers for their distribution. The spatial localisation of contrast agents

makes them valuable tools for tracking material such as regeneration cells or biomaterials as well as useful diagnostic agents for assessing pathology in which their distribution is altered.

Paramagnetic MRI contrast agents such as gadolinium shorten T1 relaxation in the surrounding tissue causing comparatively faster relaxation to equilibrium and therefore a brighter signal. When the contrast enhanced region is brighter than surrounding tissue this is known as positive contrast. Alternatively, superparamagnetic iron contrast agents have a T2/T2* shortening effect that creates regions of hypointensity in T2 weighted imaging. These regions of lower signal have negative contrast. A wide variety of MRI contrast agents based on gadolinium and iron oxide have been approved for use by the FDA and European Union.[119] The work undertaken in this thesis does not make us of exogenous iron contrast agents, although the T2/T2* shortening effect of iron is described in more detail in the context of pathological iron overload in Chapter 3.

Gadolinium based contrast agents universally contain the paramagnetic ion of the lanthanide metal gadolinium (Gd^{3+}). This ion has almost identical ionic radius to calcium meaning that it competes with calcium in all biological processes in which calcium is active.[120] The trivalent ion binds with higher affinity than biological Ca^{2+} and the replacement of calcium within these processes alters the kinetics of that biological process. This property makes Gd^{3+} as a free ion extremely toxic. For this reason, Gd administered as a contrast agent is always chelated with organic ligands such as diethylenetriaminepentaacetic acid (Gd-DTPA).

The T1 shortening effect of Gd based contrast agents such as Gd-DTPA arises from the seven electrons in the valence shell of gadolinium bestowing these molecules with a high magnetic moment. This high magnetic moment shortens T1 in the surrounding tissue by increasing the dipole-dipole relaxation interaction (2.3.3). This leads to an efficient exchange of energy between bound protons in tissue and nearby Gd ions shortening both the T1 and T2 relaxation constants. This prominently effects T1 at clinically approved concentrations of Gd-DTPA (between 0.1-0.3mmol/kg body weight) making Gd-DTPA primarily a T1 contrast agent.[121] Gd based contrast molecules are nonspecific agents that are too large to enter the intracellular space giving them a biodistribution occupying the vascular and extracellular space and cannot cross the blood-brain barrier in normal physiology.

Gadolinium based contrast agents are used throughout this work as an aid to enhancing the LV blood pool, for mapping ECV and identifying viable tissue through late gadolinium enhancement.

2.3.5 Late Gadolinium Enhancement

Late gadolinium enhancement (LGE) is a common cardiac MRI protocol that is used for assessing the extent of myocardial scarring following myocardial infarction. LGE is based on the inversion recovery MRI sequence as described for T1 mapping in 2.3.3. The shape of the Inversion recovery curve allows the signal from a tissue of a specific T1 to be nulled if imaged at the TI where the relaxation curve crosses zero. Selective nulling of tissues can allow easy delineation of nearby regions with different T1 by making them appear comparatively brighter.

Following injection of a Gd contrast agent the contrast distributes throughout the extracellular space. In healthy tissue this distribution is even throughout tissues. In infarcted tissue the increased extracellular volume fraction due to necrosis and fibrosis causes these regions to accumulate a higher fraction of Gd compared to surrounding healthy tissue. This increased concentration gives the non-viable infarcted tissue a shorter T1 relative to viable tissue. LGE uses this selective distribution of gadolinium contrast within the extracellular space to quantify infarcted tissue and identify salvageable myocardium by the relative enhancement versus healthy tissue.

For a typical preclinical LGE imaging protocol an intraperitoneal bolus of Gd-DTPA is injected and 15-20 minutes given for circulation. During this time, it is sometimes useful to perform a cine imaging protocol to take advantage of the brighter blood pool resulting from the circulating Gd-DTPA. Following this initial waiting period, a T1 scout will be acquired. The T1 scout is a shortened version of the Look-Locker sequence described in 2.3.3 that acquires a low resolution (96×96) sequence of images only over 6-8 heartbeats in a single mid-papillary level slice. The goal of this acquisition illustrated in Figure 2.19 is to identify the number of RR intervals at which the healthy myocardium signal is most effectively nulled providing the best contrast with the hyperenhanced infarcted tissue.

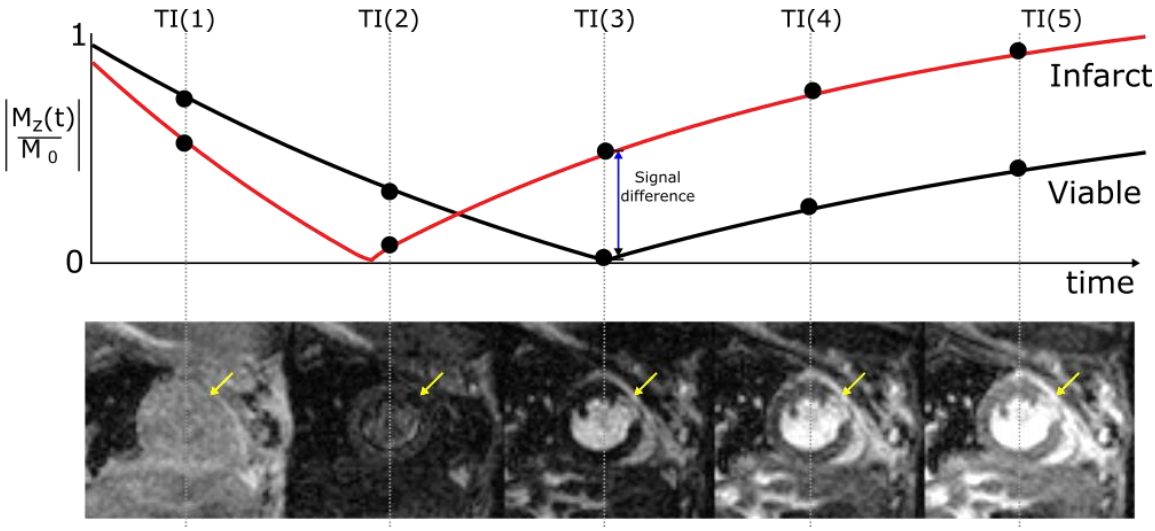

Figure 2.19 TI scout for LGE. The purpose of this acquisition is as a primer for the full LGE image acquisition. The aim is to identify the TI at which the differing T1 of viable and infarcted myocardium provide the greatest contrast. Typically, this is when the viable myocardium is nulled. In this example the myocardial null point is closest to TI (3) or 3 RR intervals after the inversion pulse. Yellow arrow indicates infarction.

The TI scout acquisition is required due to the variability between animals and acquisitions. Small differences in heart rate, weight and dosage mean that the null point of the myocardium will occur at a different time after inversion and identifying the closest RR interval to the null point must always be determined empirically. Following the low resolution scout a multislice, high resolution (192×192) image is acquired at the appropriate inversion time. An example full resolution image stack in an infarcted mosue is shown in Figure 2.20.

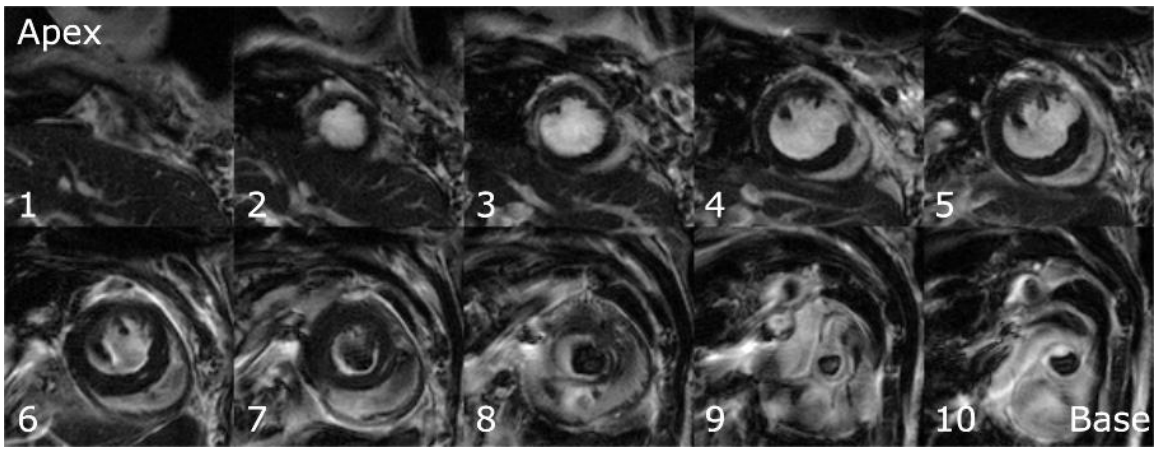

Figure 2.20 Example full acquisition for LGE. The high resolution and multislice acquisition allows for accurate quantification of the infarcted tissue as a fraction of the whole LV myocardium. In this example the infarct can be seen in the anterior wall in slices 3,4, 5 and 6.

Quantifying the volume of scarred myocardium was performed by the semi-automated Expectation maximisation, Weighted, A priori information (EWA) method proposed by Engblom

et al. (2016) and implemented in Segment v2.0 R5270.[122] In this method the user defines the endocardial and epicardial boundaries and the midventricular septum. This information is used to restrict the identified infarction to areas of hyperintensity within the myocardium and to utilise a priori information about vessel anatomy. The algorithm is given a culprit artery as a priori information allowing for exclusion of artifactual hyperintensity. Step 6 weights the size of each pixel based on its intensity. This allows for compensation of partial volume effects where the weight of each pixel is a representation of the fraction of dead cells contained within a voxel. A processed example is shown in Figure 2.21 for the full acquisition data shown in Figure 2.20 with the LAD defined as the culprit artery. Knowledge of the culprit artery helps constrain infarction identification to physiologically accurate regions.

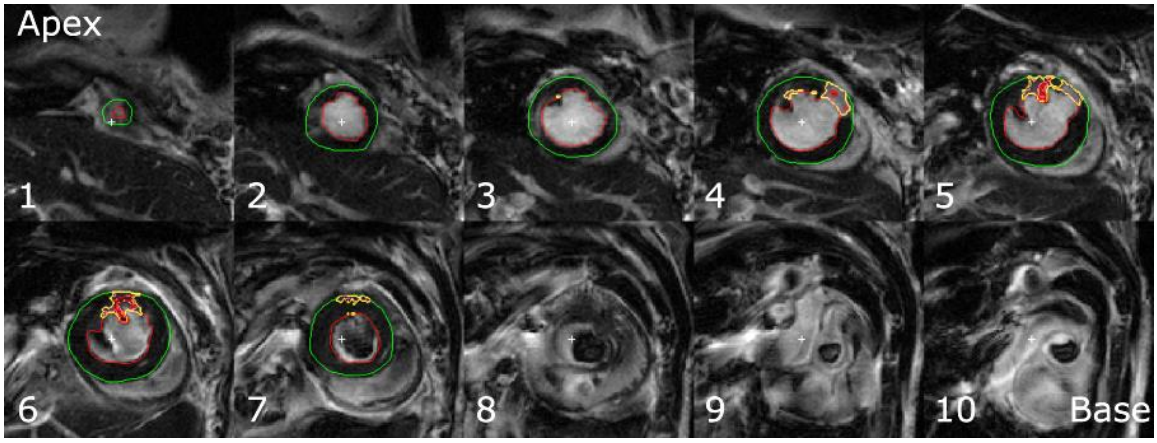

Figure 2.21 LGE image with infarct quantification performed by the EWA method. Yellow boundaries show infarcted pixels. The algorithm has successfully picked up regions of hyperenhancement as seen in Figure 2.20 and has used a priori information to restrict artifactual identification of infarct.

2.4 Optical Projection Tomography

Optical projection tomography (OPT) is a fluorescent tomographic imaging technique that is used in Chapter 7 to locate the distribution of a transplanted cell sheet. OPT is introduced here in the imaging theory section so that its imaging mechanism and uses can be described more fully. The advantage of imaging fluorescent samples with OPT over more traditional methods such as fluorescence microscopy is that it offers a wider large field of view that can image whole organs with the 3D distribution of fluorescence. OPT is a non-destructive technique making it applicable to imaging the in situ distribution of fluorescent molecules such as those bound to cells. This wide field of view does however come at a cost of spatial resolution. OPT is not able to resolve single cells but is a valuable tool for imaging the distribution of transplanted cells over a wide area.

2.4.1 Origin of OPT signal

Optical projection tomography is a 3D ex vivo optical imaging technique using light emissions or transmission for transparent samples of approximately 1-20mm. In transmission mode, the system works in a fashion analogous to x-ray computed CT, where the attenuation of x rays as they pass through a sample generate image contrast. In this case, light in the optical band is attenuated through the sample and the variable attenuation coefficient of the tissue for that wavelength provides tissue contrast. In transmission mode then the contrast originates only from tissue features and can provide high resolution structural information with resolutions of approximately 100um. An alternative contrast mechanism for OPT is from optical fluorescence. In fluorescence mode an excitation and or emission filter is introduced to isolate specific spectral contents of the optical signal. This allows OPT to produce contrast from light emissions from fluorescent molecules. In fluorescence mode the OPT system behaves less like X-ray CT and more like a single photon emission computed tomography (SPECT) system where a distribution of fluorescent particles provide contrast within a volume. The origin of these molecules can be endogenous or exogenous. Fluorescence from endogenous tissues result in a wide range of wavelengths from the natural fluorescence of tissue in a process called autofluorescence. Alternatively, a targeted exogenous molecular probe can be introduced to the tissue before or after excision to produce more specific emissions. These molecular probes can be manufactured to bind to specific proteins to produce a fluorescent signal originating only at the site of a specific tissue or molecule of interest. Multiple probes can be used in fluorescence imaging with appropriate excitation/emission filters. Introducing these molecular probes makes OPT unique in being a sensitive and specific modality for imaging gene expression or cellular distributions over the scale of a whole organ.

Optical light is strongly absorbed and scattered in biological tissue limiting visible light penetration to approximately 100µm.[123] Due to the relatively large samples imaged using OPT this necessitates the addition of a chemical clearing process to allow transmission of excitation light into tissue as well as emission light out of tissue. Clearing refers to the process of making a sample transparent to optical light. The goal of this optical clearing process is to alter the refractive index of tissue to match its surroundings. The process of optical clearing was pioneered by Tuchin et al. who proposed diffusing a clearing agent with a high refractive index into tissue to reduce the degree of internal scattering.[124,125] Biological tissue is composed of a mixture of components with high e.g. collagen, cell membranes and low e.g. interstitial fluid,

cytoplasm refractive index. This combination of refractive indices causes penetrating light to frequently change path, scatter and lose coherence. By diffusing the high refractive index clearing agent into the extracellular space the refractive indices become matched and are more permissive to optical transmission.

2.4.2 Image acquisition and reconstruction

A schematic of the basic imaging components for an OPT system is shown in Figure 2.22. As opposed to CT or SPECT systems the imaging components remain fixed and the sample is rotated to provide angular projections. The system operates in a 'step and shoot' mode where the sample rotates by a fixed angular increment, stops then undergoes illumination and imaging before rotating again. A series of lenses focus the emission and excitation light to create a focal plane within the sample. Filters within the OPT system can be switched to tailor each acquisition to the molecular probes under investigation. An appropriate narrow bandwidth excitation filter with peak transmission in the absorption wavelength of the probe produces the maximal excitation while minimising the autofluorescent background signal. The excitation filter can further isolate the signal from the probe by removing remaining autofluorescent signal. Following excitation/emission focussing /filtering the image is formed on a CCD camera resulting in a sequence of images showing the angular projections of the sample. An example OPT acquisition using transmission and fluorescence mode is shown in Figure 2.23.

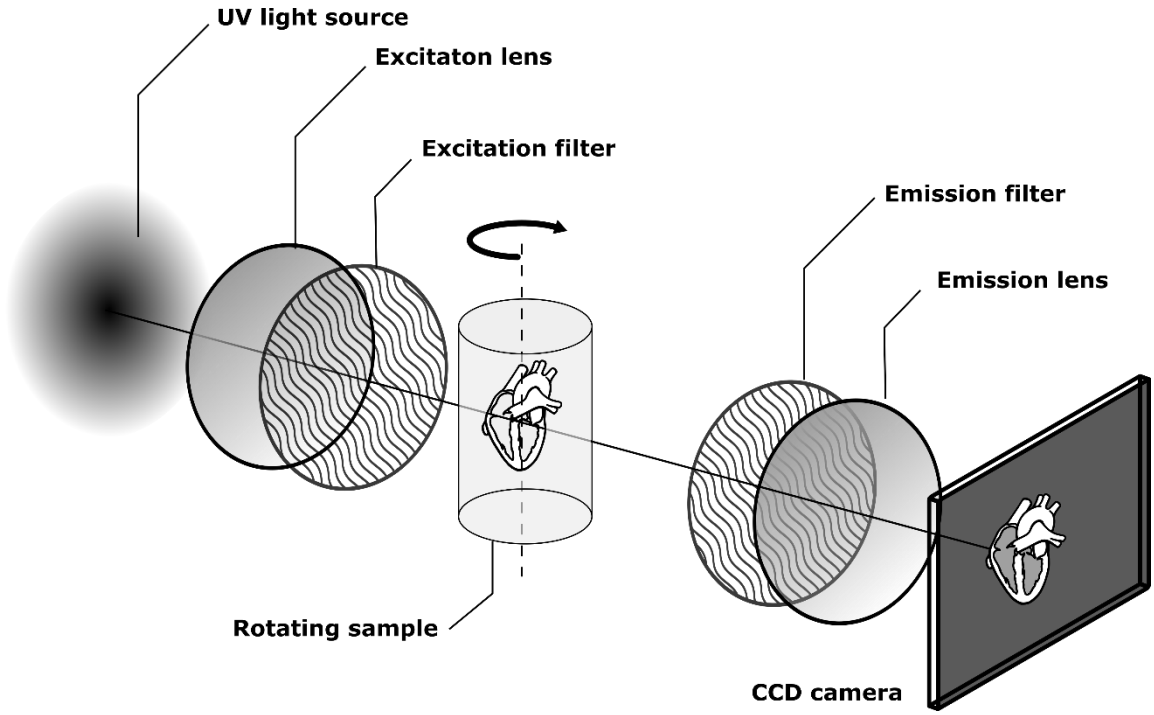

Figure 2.22 OPT imaging system schematic. An ultraviolet light source illuminates a sample after focussing and filtering the light to specify the optical excitation bandwidth. The light then passes through the rotating sample before the signal is filtered to isolate the optical emission bandwidth and focussed onto a CCD camera.

To create a tomographic volume from the imaged projections the data is restructured to form a sinogram. A sinogram is created by extracting each line of 1D image data orthogonal to the axis of rotation and create an array where one axis is the 1D image data and the second axis is rotation angle. A sinogram can be transformed into tomographic image space using the radon transform with filtered back projection to create a 2D tomographic slice for each line of image data.[126]

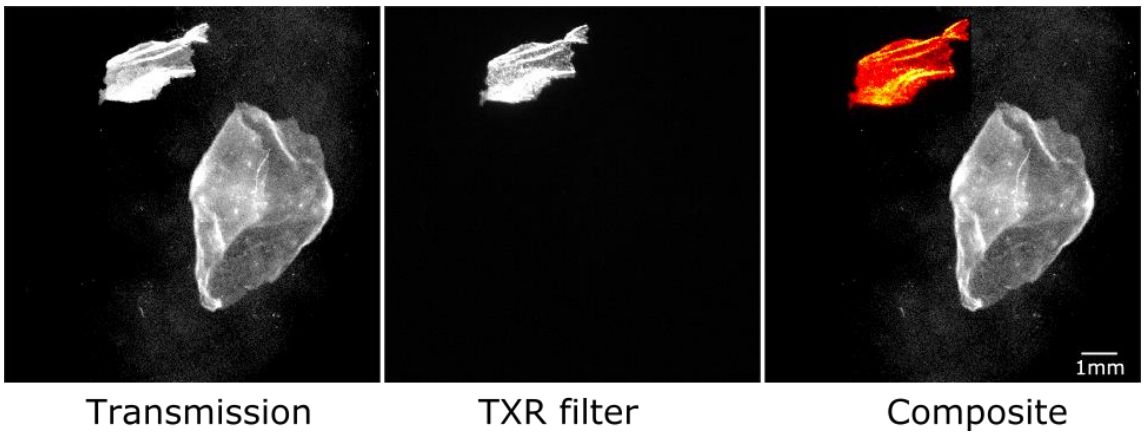

Figure 2.23 Example of OPT projections. Here two scaffoldless single cell thick fibroblast sheets (discussed further in 7.2) are imaged suspended in agarose. The sheet at the top is composed of cells labelled with the membrane stain DiL that has a fluorescent peak at 565nm. In the

transmission image both sheets show light attenuation. In fluorescence mode with a Texas red filter (peak transmission 560nm) only the labelled cells are visible. A composite image is then shown with the fluorescence in the red channel. This figure is extracted from section 7.2

2.4.3 Local hardware

Prior to OPT imaging samples required optical clearing to allow optical transmission for illumination and detection. The optical clearing process began by excising hearts by perfusion fixation. The hearts were then immersed in 70% ethanol in PBS for 2 days before switching to 100% ethanol and allowed to diffuse over 7 days, changing the ethanol every 2 days. This removed all water from the tissue, this step is necessary since the clearing solution is hydrophobic, dehydration is required to allow the solution to penetrate the tissue. Following dehydration, the sample is moved to a solution of benzyl alcohol and benzyl benzoate in a 1:2 ratio referred to as BABB or Murray's clear. The sample is left immersed in the clearing solution for 10 days, changing the solution every 2 days. Following clearing ,samples were imaged using the Bioptonics 3001 OPT system shown in Figure 2.24 (Bioptonics, Edinburgh, UK). The sample is attached to the rotating imaging stage using superglue adhesive in a region of tissue that was not to be imaged. The sample is then lowered into the imaging chamber and the optical system focused to achieve the best resolution in the structures of interest. The sample is then raised and a background light field acquisition performed and corrected for. The sample is then lowered back into the chamber and the exposure time set for each fluorescence filter. The sample is rotated by 0.45° over a full 360° resulting in the acquisition of 800 angular images.

Figure 2.24 Bioptonics 3001 optical projection tomography imaging system. A- control system; B- light-sealing door; C- rotating imaging stage; D- Light source and diffuser; E- sample chamber; F- optical focusing and filtering chamber.

2.4.4 Applications

The wealth of existing fluorescent optical imaging probes manufactured for use in standard microscopy techniques are applicable to OPT imaging with the correct filtering and detection systems. This makes OPT uniquely valuable in imaging the whole organ distribution of these established probes in 3D. Although the resolution of the system is inferior to standard 2D fluorescent microscopy techniques, the capability to image larger samples without sectioning makes it useful in imaging larger 3D structures such as in situ engineered tissue. One field in which the availability of fluorescent probes has made OPT a useful tool is gene expression. Molecular probes that exhibit fluorescence as a marker for the spatial distribution of gene expression can be imaged with OPT. An advantage OPT has over standard microscopy techniques here is the ability to rapidly image whole samples making high throughput studies using multiple markers of gene expression viable. For example Sharpe et al. used multiple probes to investigate the 3D developing shape of embryonic mouse organs.[127] The authors imaged mouse embryos at multiple time points following labelling with two antibodies targeted to the HNF3β protein and neurofilaments with individual fluorochromes assigned to each. The resulting 3D volume allowed high resolution tracking of the development of nerve tracts and HNF3β expressing tissues such as the oesophagus, stomach and lungs. OPT has also found use in cardiac imaging. For example, recent work by Zhao et al. (2015) has shown that following myocardial infarction and consequential myocardial remodelling the autofluorescence in

infarcted tissue measured by OPT is brighter than remote regions.[128] The regions of OPT hyperintensity correlated with non-viable tissue identified by LGE MRI in vivo. Making it a useful alternative to measuring infarct volume in studies of myocardial infarction where expensive MRI systems are not available. Finally, and most relevant to studies of tissue engineering and cardiac regeneration therapy OPT is able to image high resolution distributions of fluorescently labelled cells or structures. Transplantation of labelled therapeutic cells can then be checked for retention in the organ as well as the redistribution of cells at the transplant site following transplantation. In a related example, Wilkie et al. (2003) used OPT imaging to track progenitor cells migrating across the mouse embryo. Knowledge of the intrasample migration of cells will be a useful feature of improving cell retention in cardiac regeneration therapy.

2.5 Ultrasound

In the work presented in this thesis, ultrasound is used to deliver regenerative therapies to the heart in two of the studies presented in Chapter 7. US is well suited to deliver intracardiac injections due its unique ability to image the beating heart in real time with sufficient resolution to locate the myocardial boundaries. It is worth noting that US is commonly used for assessment of cardiac function and is well suited to this purpose. However, preclinical cardiac MRI is able to provide superior images describing heart function in 3D as opposed to the 2D interpolated methods found in preclinical US systems.[129] For this reason in this work, MRI was always used for quantifying heart function and US was used for image guided procedures.

2.5.1 Origin of US signal

Ultrasound (US) refers to acoustic pressure waves above the audible range of humans (>20Mhz). The use of ultrasound as a medical device began with Karl Theo Dussik in 1941 who measured the ventricles of the human brain using transmission of US. He was followed closely by Wolfe Dieter Keidel in the late 1940s who attempted to measure the volume variations of the heart also using transmission of US. Neither technique was considered effective or quantitative due to limitations of transmission US.[130] The first to observe US reflections from the myocardium was Inge Edler and Carl Hertz in 1953 who borrowed an ultrasonic Reflectoscope normally used to investigate ships hulls for cracks.[131] From this first observation Edler and Hertz developed the field of echocardiography.[132] Today clinical US is typically generated in the 1-20MHz range depending on the depth of the tissue being examined. Lower frequencies are able to penetrate the body further but suffer reduced spatial resolution compared to weakly penetrating high

frequencies. Ultrasound is generated by a piezoelectric crystal transducer placed at the surface of the body under investigation, this emits and detects ultrasonic pressure waves that pass into and out of the body. The passage of US through the body is scattered and reflected by internal acoustic boundaries that occur at interfaces between tissues or tissue structures. This scattering property known as acoustic impedance is analogous to refractive index and causes reflections and deflections of acoustic waves as is the case of refractive index with optics. An ultrasound image is formed from information on echo amplitude, echo time and frequency.

2.5.2 Image acquisition and reconstruction

Modern US commonly operates in 2 modes. M-mode US uses a series of 1D US pulses to rapidly measure the relative separation of tissue interfaces. M-mode has been found to be useful in measuring myocardial contraction and can be used to assess myocardial function along the axis of the US beam with very high temporal resolution. Alternatively, B-mode ultrasound forms an image by sampling multiple m-mode lines in a cross section of the body. These multiple samples are produced either using a linear array of transducers and/or sweeping the US beam back and forth using a phased array of transducers. Knowledge of the time of emission and detection allow the depth of tissue interface to be determined while the echo magnitude determines the brightness of the displayed echo to provide contrast at tissue boundaries with a mismatch in acoustic impedance. Figure 2.25 illustrates this process, where the red line depicts a single 1D m-mode acquisition line. An echo is reflected every time the 1D beam passes through an acoustic boundary. The echoes shown in Figure 2.25 are formed as the beam is reflected at the front and back boundaries of object 1 and object 2. The amplitude of the echo is determined by the proportion of reflected energy depending on acoustic impedance Z where a higher difference in Z resulting a larger echo in the figure $Z_2 > Z_1 > Z_{body}$. To extend this illustration to b-mode imaging consider multiple lines emitting from the transducer following the black outlines of the focussed beam. The circumference of object 1 and 2 would become visible by the change in echo time and echo separation 2D.

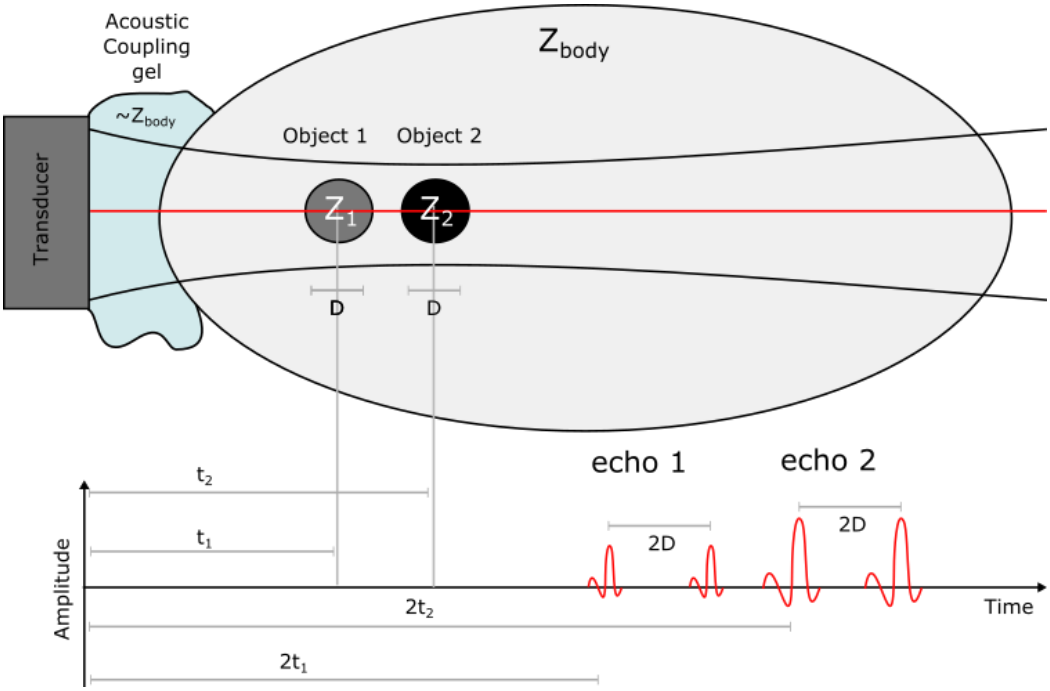

Figure 2.25 Principles of US imaging. The ultrasound transducer produces a beam that passes through the body and is reflected at every acoustic impedance (Z) boundary it passes through. These echoes are detected at the transducer and the amplitude and detection time can be used to infer the location and acoustic properties of the structure that caused the reflection.

Example echocardiography data from a mouse is shown in Figure 2.26. The LV endocardium is identified by blue circles. By identifying the endocardial boundaries global LV function parameters such as ejection fraction, stroke volume and systolic and diastolic volumes can be calculated - often incorporating geometric models of the LV. Also visible in this example data is the characteristic speckle texture present in ultrasound images. Tracking this acoustic speckle can allow quantification of regional myocardial function, this is discussed in further detail in Chapters 4, 5 and 6.

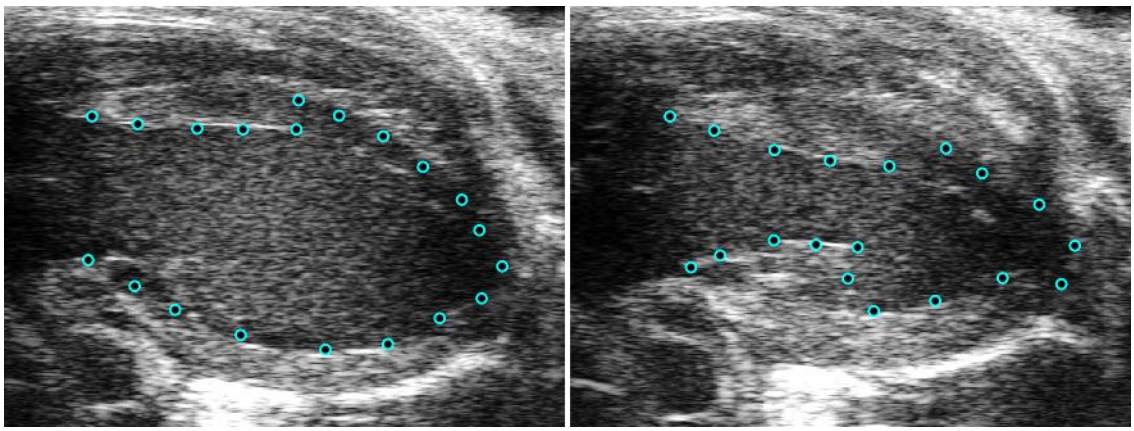

Figure 2.26 Example US acquisition. This image shows the long axis view of the heart at end-diastole (left) and end-systole (right). The LV endocardial boundary is indicated by the green

circles. By identifying the endocardial boundaries global LV function parameters such as ejection fraction can be extracted often incorporating geometric models of the LV.

2.5.3 Local hardware

The ultrasound system used for imaging and guided procedures was a Visualsonics Vevo 2100 system (Visualsonics, Toronto, CAN). The system was adapted for the mouse and rat experiments by equipping a 55MHz transducer for mouse and 24MHz for rat imaging. The setup for US imaging is shown in Figure 2.27. Animals were anaesthetised using a mixture of isoflurane and oxygen. Hair is a major scatterer of ultrasound on transmission and detection so the bulk of fur covering the imaging window was removed using a shaver and finer hairs removed using hair removal cream (Veet, Reckitt Benckiser, Slough, UK). The animal was then transferred to the imaging stage and acoustic coupling gel was applied to the shaved region. Surface electrodes at all 4 paws were used to monitor the ECG trace and a rectal thermometer and heat lamp used to maintain temperature.

Figure 2.27 Visualsonics Vevo 2100 ultrasound preclinical imaging system. A- display and control system; B- Anaesthetic vaporiser and delivery; C- transducer; D- imaging stage; E-heating lamp; F- guided injection stage.

2.5.4 Applications

Ultrasound has found a wide range of diagnostic and therapeutic uses. Perhaps the most well-known application of medical US is in obstetrics for assessing foetal health. This has become widely used a tool to evaluate growth, malformations and identify multiple gestations.[133] Echocardiography is another common use of medical ultrasound and has become one of the most valuable tools for the diagnosis and assessment of clinical heart disease. Thanks to its low material costs, high temporal resolution and wide availability echocardiography is frequently preferred to cardiac MRI despite its lower spatial resolution, contrast and the more limited range of diagnostic information it is able to provide. Cardiac US can provide information about the geometry of the heart, functional pumping information and identify damaged regions of tissue through measures such as wall thinning. Common measurements made in clinical cardiac US are measures of ejection fraction, diastolic function and cardiac output measurements. The acoustic scattering properties of red blood cells make it possible to image the frequency shift associated with scattering from flowing blood (Doppler effect). Doppler ultrasound has revolutionised the diagnosis of valvular heart disease. Abnormal flow defects such as valvular regurgitation and turbulent/jet flow in stenosis can be quantified using Doppler ultrasound. US has also been used for interventional procedures, such as using the cavitation effect of high amplitude US to break apart kidney stones.[134] The high temporal resolution and real time reconstruction of US imaging makes it ideally suited to image guided procedures. For example, ultrasound guided injections use the high acoustic impedance mismatch between the needle and surround tissue make the needle easily differentiable from surrounding tissue. This makes it possible to inject or aspirate fluids with a high degree of accuracy from within the body.[135]

Adapting clinical ultrasound systems for preclinical use has been hindered by the rapid murine heart rate that requires a very high frame rate for accurate US quantification and the small size of mice with the associated imaging requirements- less penetration, higher resolution- higher frequencies meaning that hardware could not be directly translated from human systems. However, over the last 10 years dedicated preclinical US systems have become available opening up preclinical research to the benefits of high throughput accurate in vivo imaging.[136,137]

2.6 Bioluminescence Imaging

Cell tracking is an important aspect of cell based therapies as it allows a change in organ function to be attributed clearly to the presence of therapeutic cells in that organ. Although cell tracking is possible using MRI by transfection of iron oxide nanoparticles this technique is non

quantitative and provides no information about cell viability. Direct labelling of cell with radionuclide tracers allow nuclear imaging techniques SPECT/PET to provide high resolution and quantitative cell tracking but also offer no information on cell viability. Cell tracking was therefore performed using bioluminescence imaging since this offers a semi-quantitative information on cell population and crucially is able to track cell viability. Bioluminescence is used in the cell retention studies presented in Chapter 7.

2.6.1 Origin of BLI signal

Bioluminescence is the emission of light from a living organism. This phenomenon occurs in a wide variety of marine species and a smaller number of land dwelling plants, fungi and insects. The chemical reaction that results in the bioluminescence emission occurs between a Luciferin molecule and a luciferase enzyme. The reaction is markedly similar in most species. In every case a luciferin and luciferase reaction is observed although in some species this reaction is assisted by other reactive cofactors such as metal ions or adenosine triphosphate (ATP).[138] Luciferin and Luciferase are generic terms for a wide range of biologically occurring light emitting compounds where different bioluminescent species have different forms of Luciferin and Luciferase. The most commonly used variants for biomedical imaging originates from the North American firefly, p*hotinus pyralis.* The peak emission of firefly luciferase is around 560nm; this relatively long wavelength is better at penetrating tissue making it suitable for in vivo imaging. For BLI to be a practical imaging modality the bioluminescent property must be translated into traditional research species such as mice. This is done by creating transgenic mice or cell lines with the firefly DNA fragment encoding the production of luciferase typically through the use of a viral vector. The luciferin enzyme required to provide the bioluminescent emission (D-luciferin) must be injected prior to imaging since there is currently no technique to produce this in situ. Since the bioluminescence reaction requires ATP to produce an emission, BLI has found use as an in vivo tool for tracking the distribution of viable cells.

2.6.2 Image acquisition and reconstruction

Following the injection of the firefly luminescence substrate D-Luciferin the mouse is anaesthetised and placed within the BLI system. The system is contained within a light tight container with an ultrasensitive CCD imaging system above the mouse (Figure 2.28). The CCD

system operates as a photon counter and can determine properties such as light flux, radiance and emission count.

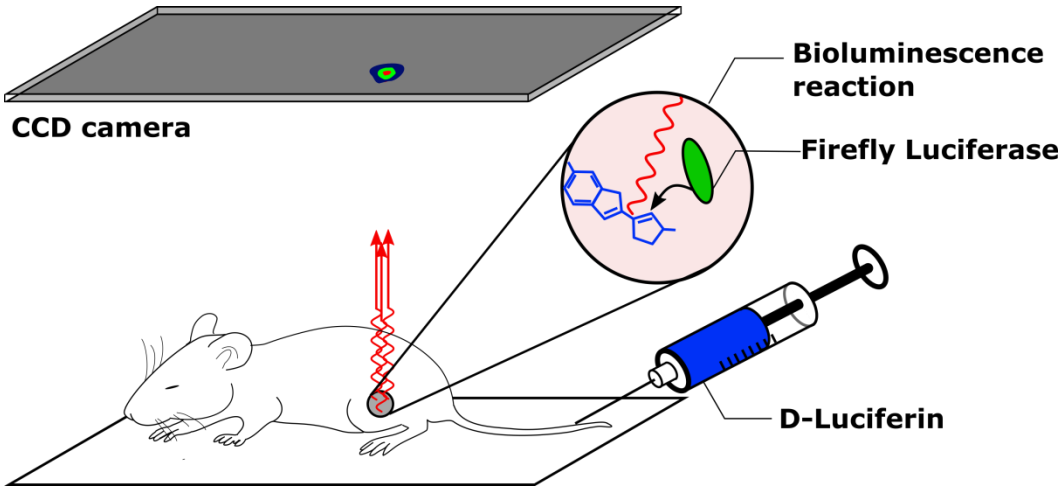

Figure 2.28 BLI acquisition schematic. The reaction of the firefly luciferase substrate contained within cells of interest with the D-luciferin bolus results in the emission of a photon that can be focused and detected by a sensitive cooled CCD array. Since the bioluminescence reaction requires ATP only metabolising cells are detected.

As was the case with OPT biological tissue presents a challenging optical environment with high degrees of scattering and absorption. Unlike fluorescent imaging, for BLI there is no need to get light into the sample as the photoreaction occurs internally. The emitted photon is scattered at structures such as cell membranes and is absorbed by pigmented macromolecules depending on the wavelength of emission.[139] The depth of emission is importnat and superficial tissues provide higher signal than internal organs. The high degree of scattering from internal structures means that light may be scattered many times before passing out of the body. This results in a highly diffuse light emission that is the primary contributor to the poor resolution of BLI systems. Example BLI acquisition data from intracardiac injections of bioluminescent macrophages are shown in Figure 2.29.

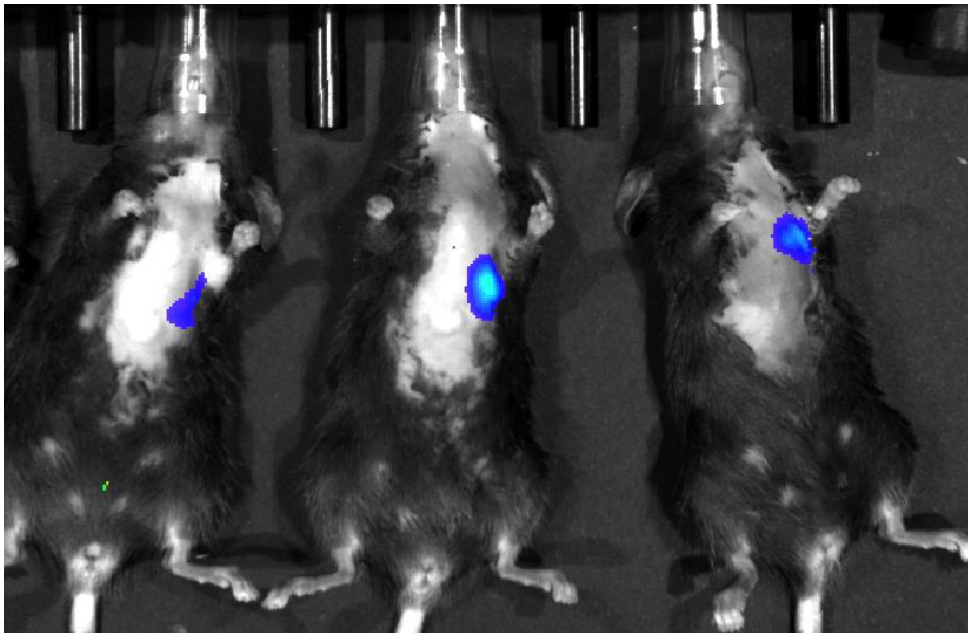

Figure 2.29 Example BLI image data. Here 3 mice underwent Intracardiac injection of bioluminescent luciferase transduced macrophage cells. The BLI overlay shows that the majority of cells remain localised to the heart. Units are radiance [photons/s/cm^2/sr].

2.6.3 Local hardware

Imaging was performed with a Biospace PhotonImager (Biospace lab, Nesles-la-Vallée, Fr), this system is depicted and labelled in Figure 2.30. Animals were injected with an intraperitoneal infusion of D-luciferin potassium salt solution at a dose of 150mg/kg.[140] The animals were then placed on the heated bed and the system would acquire an illuminated reference image. The illumination would then turn off and the bioluminescence signal acquired for some time. The number of photons emitted from an area could be converted to units of photon radiance- count per square metre per steradian per second [m^{-2} sr^{-1} s^{-1}]. This unit of measure removed dependence on exposure time. The system was capable of fluorescence imaging and was equipped with illumination devices for this purpose although this was not used for this project due to the low penetration of this light for in vivo studies.

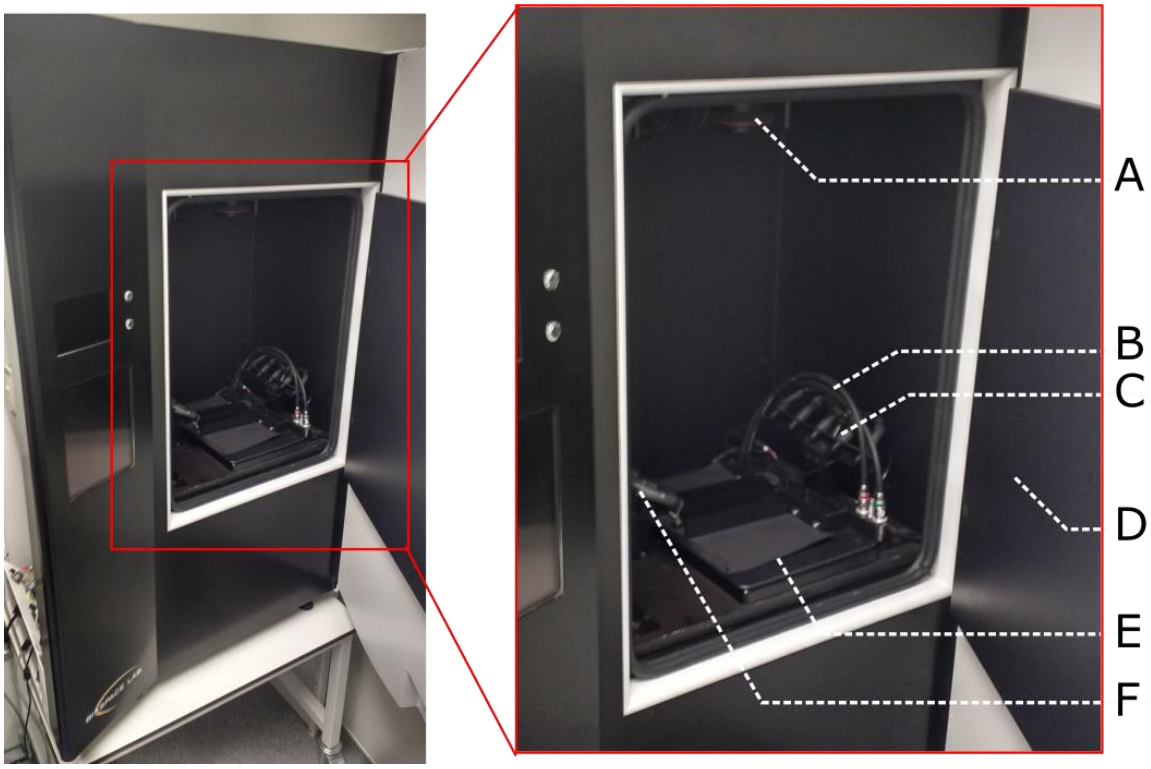

Figure 2.30 Biospace PhotonImager BLI imaging system. The basic system consists of a light proof box with an ultra-sensitive cooled CCD positioned above the imaging stage for detecting bioluminescent emissions. A- cooled CCD; B- anaesthetic delivery; C- fluorescence illumination; D- light-sealing door; E- heated imaging stage; F- secondary illumination.

2.6.4 Applications

The requirements for the bioluminescence reaction, Luciferin, luciferase, ATP and oxygen make it highly applicable to investigation of viable cells or cell environments conductive to proliferation. BLI is also applicable to in vitro applications for validating processes such as cell proliferation in real time.[141]

Xiong et al. (2005) used BLI imaging to provide real time quantification of the efficacy of novel antibiotics in a rat model of endocarditis; a bacterial infection of the endocardium. The authors transduced the *Staphylococcus aureus* bacteria that causes the infection to produce firefly luciferase. The proliferation of the infection and the antibiotic efficacy of their agents could then be monitored serially in vivo. The decline in BLI signal following the antibiotic treatment could be quantified along with the infection relapse upon removal of treatment. BLI has also been used for tracking precursor cells with a view to regenerating the damaged liver by Di Rocco et al. (2012).[142] The authors produced hepatic precursor cells transuded with lentiviral vectors expressing firefly luciferase. This allowed them to transplant cells and track their viability and

retention over time. Zhao et al (2008) used BLI to investigate the kinetics and efficacy of a vascular disrupting agent (VDA) for chemotherapy.[143] The authors imaged luciferase expressing cancer cells before and after the application of a VDA. Prior to the therapy the cancerous cells produced a reproducible and bright BLI signal in the tumour region. Following the application of the VDA therapy the tumours showed a 50-90% decrease in radiance. This is caused in part by the reduced perfusion of the d-luciferase substrate and partly by the ischemia cutting off the tumours blood supply. BLI in cardiac regeneration therapy and tissue engineering is a valuable tool for tracking transplanted cells to ensure retention and survival within the target region or the engrafted biomaterial.

2.7 Summary

This chapter has introduced the imaging techniques that will be used throughout this thesis. The bulk of this thesis is focused on developing MRI imaging techniques for quantifying cardiac function and structure. Other relevant techniques were also described, introducing the added value of multi modal imaging studies and the combination of unique information from different imaging systems. In the next chapter a multi-parametric MR imaging platform is established that is widely applicable to the assessment of cardiac disease. This next section will draw on the physical principles outlined in this chapter. Later chapters 5 and 6 in which advanced imaging techniques are developed for assessing regional cardiac function also draws from the imaging theory introduced here. The OPT, US and BLI imaging are used only in the final results chapter (chapter 7) where they are used in several studies for cell/material tracking and guided injection.

Chapter 3 MRI biomarkers for the early assessment of iron overload in a humanized mouse model of β-thalassemia

3.1 Introduction

MRI is frequently used clinically to diagnose and monitor disease and as a research tool to investigate experimental animal models. In order to develop and validate advanced in-vivo MRI imaging techniques for tissue engineering I undertook a quantitative study to investigate MRI detectable changes in cardiac function and tissue composition in a clinically relevant mouse model of cardiac disease. The multiparametric imaging tools developed in this chapter are applicable to the wider field of cardiac imaging and are able to provide quantitative information on cardiac health. This study was performed in collaboration with Professor John Porter (University College London) and Professor Anna David (University College London). We were asked to develop imaging tools that would be able to quantify the presence of cardiac dysfunction and tissue iron deposition in a novel animal model of beta thalassemia, a disease with cardiac implications that frequently leads to heart failure.

The role of this chapter in the thesis as a whole is to present the established cardiac MRI imaging techniques used to evaluate cardiovascular disease. The techniques presented are applied here to a mouse model of thalassemia but the methods are broadly applicable to any study requiring evaluation of the cardiovascular structure or function. This chapter then serves as an introduction to existing techniques to provide context before the technological developments presented in Chapters 5 and 6, these technologies, along with the established techniques presented in this chapter are then used in combination in studies of cardiac regeneration in Chapter 7.

Parts of this chapter are contained in the paper: MRI biomarkers for the early assessment of iron overload in a humanized mouse model of β-thalassemia. (2016) Laurence H. Jackson, Evangelia Vlachodimitropoulou, Panicos Shangaris, Thomas A. Roberts, Thomas M. Ryan, Adrienne E. Campbell-Washburn, Anna L. David, John Porter, Mark F. Lythgoe and Daniel J. Stuckey. (under review)

Work contained in this chapter was presented at the British Chapter ISMRM annual meeting 2015 where it won runner up for the British chapter prize for in-vivo imaging with potential utility in medicine.

β-thalassemia (βT) is a genetic blood disorder that can result in profound and life threatening anaemia. Current clinical management of βT is a lifelong dependence on regular blood transfusions, a consequence of which is systemic iron overload that leads to acute heart failure. Recent developments in gene and chelation therapy give hope of better prognosis for patients, but successful translation to clinical practice is hindered by the lack of thorough preclinical

testing using representative animal models and clinically relevant quantitative biomarkers. Stem cell transplantation has also been demonstrated as a therapy for beta thalassemia, demonstrating the versatile applications of regenerative cell transplant in disorders outside of ischemic heart disease.[144,145] The aim of this work was to produce a quantitative, non-invasive and in vivo preclinical MRI platform for the assessment of βT in a clinically relevant humanized mouse model to accelerate the development of these therapies.

3.1.1 β-thalassemia and iron overload

β-thalassemia is a genetic disorder resulting in the production of ineffective red blood cells (RBC) that are unable to sufficiently transport metabolic oxygen resulting in life threatening anaemia.[146] βT affects the production of haemoglobin (Hb) in the body. Hb is the main molecular component of RBCs making up 96% of the cell's dry weight and are the main transporters for oxygen in the body.[147] Hb is composed of 4 subunits, each subunit consisting of a globular amino acid bound to a haem group. The haem group is an iron containing protein that can bind to a single oxygen molecule, the 4 subunits of Hb then allow for each Hb molecule to transport 4 oxygen molecules. The use of Hb results in a seventy-fold increase in the ability of blood to transport oxygen compared to if the circulation relied on dissolved oxygen in other blood liquids, making it essential for functioning human metabolism.[148] The variants of the protein chain components of Hb and their relative proportions with age are outlined in Figure 3.1.

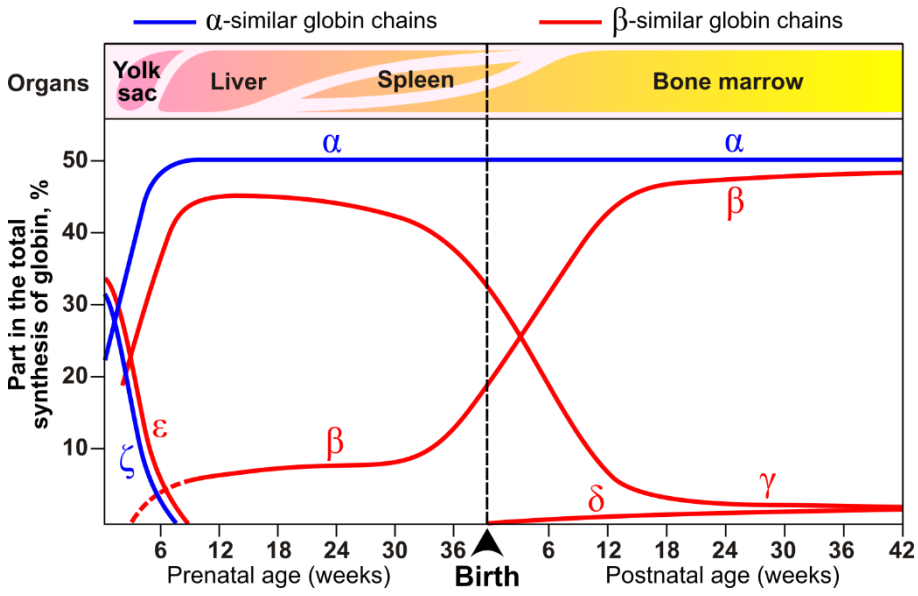

Figure 3.1 The relative proportions of the globin chain components of Hb over time. Following birth there is a transition at 6 weeks from HbF ($\alpha_2\gamma_2$) to HbA ($\alpha_2\beta_2$). Note also the change in production

organ, from the liver and spleen during foetal development to the bone marrow in adults. Figure adapted from [149]

In human physiology Hb undergoes a characteristic structural change during the transition from foetal to adult development. In the foetal stage of development, the body survives on foetal haemoglobin (HbF) composed of 2 α chains and 2 γ globin chains. After birth there is a transition at approximately 6 weeks of age to adult haemoglobin (HbA) consisting of 2 α chains and 2 β chains. In adults there is also residual production of HbF and HbA2 (2 α chains and 2 δ chains), together making up approximately 3% of the total Hb fraction.[150]

βT causes severely reduced or absent synthesis of the beta globin chain of HbA. The resulting α/β-globin chain imbalance leads to the production of ineffective RBCs. At birth βT patients survive on HbF and do not present symptoms until completing the transition to adult haemoglobin HbA at around 6 weeks of age. Survival into adulthood is then dependent on regular blood transfusions.[151,152] A consequence of these repeated blood transfusions is the accumulation of iron due to the systematic infusion of RBCs.[146]

Iron overload is the pathophysiological accumulation of iron in body tissue and can have deleterious effects on the heart and other organs. The mechanism by which transfusional iron overload occurs is outlined in Figure 3.2. RBCs from native and transfused blood load the macrophage system with non-transferrin bound iron (NTBI). In normal physiology most of this NTBI is bound to the iron stabilising protein transferrin that transports the iron for metabolism or to the liver for storage. The liver has a high tolerance to iron and is able to remove NTBI and transferrin from the circulation and store the deposits safely. In thalassemia the unbound transferrin in circulation is greatly reduced resulting in a high proportion of circulating NTBI. This iron is then free to accumulate in extra-hepatic tissues where it can produce toxic hydroxyl radicals via the Fenton reaction as well as inhibit cardiomyocyte coupling.[153]

Iron overload occurs initially in the macrophage system of the spleen, liver and bone marrow but subsequently spreads to hepatocytes and ultimately to the heart and endocrine systems. Iron overload in βT is compounded by increased iron absorption due to hepcidin suppression associated with ineffective erythropoiesis.[154] If left untreated, iron accumulation leads to tissue iron overload and heart failure as a result of cardiac siderosis. This remains the leading cause of death in transfusion dependent patients.[155,156]

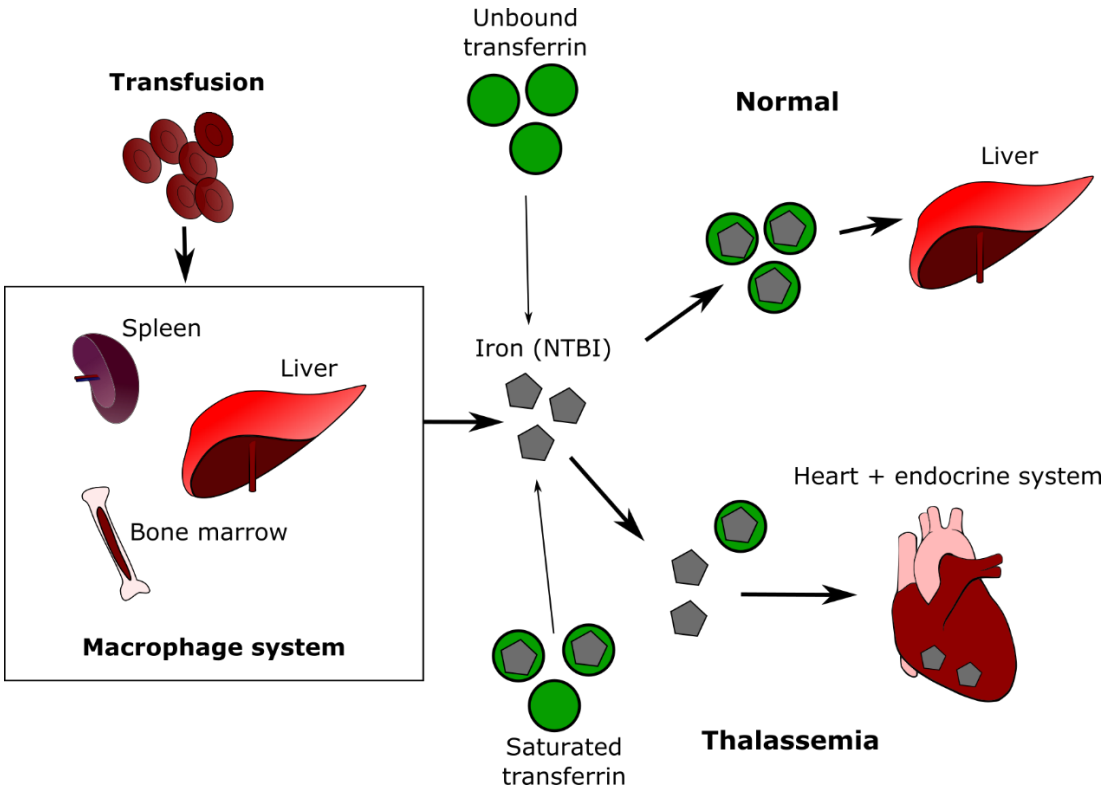

Figure 3.2 Mechanisms of iron overload. In normal physiology transferrin is used to transport NTBI for metabolism to the liver for storage. In thalassemia due to high NTBI levels from broken down native and transfused RBCs the transferrin system becomes saturated leaving a high proportion of NTBI in circulation.

An additional consequence of βT is splenomegaly (enlargement of the spleen). The role of the spleen is to filter blood by breaking down senescent and defective RBCs. Haemoglobin is broken down into its constituent globular amino acids and haem groups. In normal physiology these constituent parts are then reused in the formation of new RBCs. In βT the typically small misshapen RBCs can become stuck in the spleen without breaking down completely resulting in the haem portion of Hb not being removed leading to splenic iron overload and organ enlargement.[157,158] Another mechanism of splenomegaly in βT is extramedullary erythropoiesis; this happens when organs other than the bone marrow begin to produce RBCs in response to low Hb levels. Splenomegaly leads to the spleen becoming overactive (hypersplenism), an irreversible change that requires partial or complete splenectomy.

Thalassemia affects approximately 1 in every 2200 births, the disease has a regional variation with those in southeast Asia particularly affected. Since the widespread introduction of iron chelation therapy in the 1970s survival rates have improved dramatically, patients can now be expected to live into their 40-50's. However myocardial iron removal is slow with existing chelation regimens and the development of more effective therapies and curative approaches to

βT has been limited by the paucity of relevant animal models in which testing of new treatments can be investigated.[159-161]

3.1.2 Experimental models of thalassemia

Mouse models of thalassemia have great potential for therapeutic research and there have been many efforts to create a clinically representative model of disease. The first method to be used to create a mouse model of βT was through deletion of the mouse β-globin gene. Yang et al. (1995) used a "plug and socket" targeting technique to delete the β-globin locus from the mouse DNA.[162] Mice homozygous for this deletion lack the ability to produce Hb and die in-utero due to switching from embryonic to adult haemoglobin at around 7-8 days prior to birth. Although this makes these mice unsuited to studying serially they have found use in studies using in-utero gene therapy.[163] Mice heterozygous for the β-globin deletion survive into adulthood but present characteristic traits of thalassemia such as splenomegaly, iron overload, and abnormal RBC indices making them useful for studying the pathophysiology of thalassemia. In a separate study in the same year Ciavatta et al. (1995) also produced a β-globin deletion model that expressed similar traits. In this case the authors bred the deletion mice with a transgenic model that expressed high levels of Hb and found that anaemia was alleviated in the offspring.[164] This study was one of the first to take a genetic approach to therapy in thalassemia. These mice however are not clinically accurate since they are created through deletion of the β-globin gene rather than possessing the mutated gene seen in human thalassemia. The differences in phenotype between deleted and mutated genes in transgenic models is complex and has implications for creating accurate models of human disease. For example, disruption of the β-globin gene in a mouse model created by Shehee et al. (1992) resulted in perinatal death but deletion of the same gene resulted in a 60% survival into adulthood with only mild anaemia.[165]

More recent models of β-thalassemia have spliced the human β-globin locus expressing the thalassemia mutation into the mouse genome.[166,167] These 'humanised' mouse models with knock-in genes have become feasible models of disease since the availability of intact functional human genes from the Human Genome Project as well as efficient methods of gene transplantation.[166] However, models such as those discussed above do not express the characteristic transition from HbF to HbA seen in humans since mice have no equivalent of human HbF. Recent work by Huo et al. has developed a more clinically accurate mouse model of βT that closely mimics the temporal onset of anaemia seen in humans with βT as well as the pathophysiological RBC indices and splenomegaly.[168] This model was created by replacing the

mouse β-globin gene with a human HbF to HbA switching cassette ($\gamma^{HPFH}\delta\beta^{0}$), the mouse survives by synthesising human HbF at birth but shows typical symptoms of βT following the HbF to HbA transition including splenomegaly and anaemia. Heterozygous knockin mice ($\gamma^{HPFH}\delta\beta^{0}/\gamma\beta^{A}$) persistently express HbF from the HPFH (hereditary persistence of foetal haemoglobin) allele and so exhibit mild anaemia despite significant changes in red blood cell (RBC) indices. Homozygous knockin mice ($\gamma^{HPFH}\delta\beta^{0}/\gamma^{HPFH}\delta\beta^{0}$) suffer from severe anaemia and are transfusion dependent following haemoglobin switching and mimic the subsequent onset of iron overload in human βT.

3.1.3 MRI in thalassemia

MRI for quantification of iron content in tissue was first conceptualised in the 1980s by Stark et al. (1983) who observed hypointensity of the MRI signal in the livers of patients with thalassemia.[169] Liver biopsy was the gold-standard method for somatic iron stores and the development of MRI was fuelled by the need for a non-invasive alternative. MRI has two primary advantages over other imaging or invasive diagnostic techniques; accurate quantification of cardiac structure and function and importantly, direct sensitivity to the concentration of iron stores within tissues. However, it was not until the early 2000s that MRI developed to the point where it could become clinical practice initially as a measure of chelation response but eventually for diagnosis of iron overload in asymptomatic transfusional patients.[170,171] Anderson et al. (2001) produced the seminal paper establishing MRI in thalassemia, describing how myocardial T2* could be related to left ventricular ejection fraction (LVEF). In a study of 104 thalassemia patients it was found that those with a myocardial T2* of >20ms presented normal cardiac function while those <20ms saw a decrease in LVEF proportional to T2*. Additionally it was observed that some patients exhibiting short T2* relaxation and detectable iron content had normal LVEF suggesting that MRI could be used to detect cardiac iron overload before the onset of symptoms.[172] In the 15 years since Anderson's paper the use of magnetic resonance imaging (MRI) to assess the extent of iron loading in organs has revolutionized the diagnosis, management and treatment of βT patients.[173-176]

The sensitivity of MRI to iron arises from perturbations to the local magnetic field in the presence of iron and results in faster transverse relaxation in direct proportion to iron concentration.[177,178] However, not all forms of iron are MR visible. The most disruptive and toxic form of iron is cellular labile iron which is not visible by MRI in physiological concentrations. The primary source of iron based MRI contrast is the storage protein ferritin and its breakdown

product haemosiderin. Ferritin and haemosiderin are relatively safe forms of iron but they exist in a dynamic equilibrium with the toxic labile iron making the detection of one a clinically useful marker for the indirect quantification of the other.[179] The primary clinical method for quantification of tissue iron is gradient echo T2* mapping and a T2* of <10ms is seen as sign to begin aggressive chelation therapy. In addition to tissue iron sensitivity, MRI is able to perform structural and functional measurements during the same imaging protocol. In βT patients relevant additional imaging is cine-MRI to quantify cardiac function and structural imaging to quantify spleen size.[157,158]

There was initially some controversy surrounding the relationship between cardiac T2* and liver iron as well as variability in LVEF with decreasing cardiac T2* in patients with β-thalassemia. The first point of contention arose following another study by Anderson et al. (2004) in which it was shown that there is a significant difference between the rates of iron clearance in the liver, serum ferritin and the heart.[180] The authors found that under chelation therapy patient's liver iron and serum ferritin reached clinical end points where therapy could be stopped before the cardiac iron loading had returned to acceptable levels. This finding contradicted established treatment protocols for patients with iron overload where liver iron or serum ferritin were seen as indirect markers for total body iron. The reason for this difference is the different iron uptake/clearance mechanisms in the heart and liver, as described in 3.1.1 the liver acts as the body's primary iron storage and readily acquires excess transferrin and NTBI whereas the heart is much more vulnerable to rapid uptake of NTBI as the transferrin system become saturated. The clearance of cardiac iron is a two-step process, initially chelators are able to remove the toxic labile iron but removal of the stored ferritin and haemosiderin is dependent on the natural degradation of these molecules. This relates to the second point of controversy in that it is these storage proteins that create the detectable iron signal, so patients with severe cardiac iron loading detected by T2* MRI may be totally asymptomatic due to low labile iron but elevated haemosiderin stores. The gradual breakdown of these iron stores does however lead to eventual labile iron free to cause oxidative damage to heart tissue, high iron in the heart is therefore seen as a high risk precursor to iron related cardiomyopathy. Although MRI has gradually become the standard for clinical care and major clinical trials relating to iron chelation it has seen little use as a tool for preclinical animal research.[181] Preclinical MRI in models of thalassemia will be valuable in the assessment of therapy and may offer insight into the controversial relationship between cardiac T2* and liver iron in thalassemia.

This study applied clinically established MRI assessment methods to the novel $\gamma^{HPFH}\delta\beta^{0}$ knockin mouse model of βT in disease and in the presence of iron overload for the first time. Tissue

magnetic resonance relaxation rates (T1/T2/T2*), spleen volumetrics and cardiac function were quantified and provide a proof of principle for the use of preclinical MRI assessment in small animal models of thalassemia as an enabler to in-vivo and non-invasive serial investigation for the development of new therapies.

3.2 Methods

3.2.1 Animal model

All animal studies were approved by the University College London Biological Services Ethical Review Committee and licensed under the UK Home Office regulations and the Guidance for the Operation of Animals (Scientific Procedures) Act 1986 (Home Office, London, United Kingdom).

The transgenic mouse models of βT were prepared by Evangelia Vlachodimitropoulou (University College London). Three groups of animals were studied, a humanised control group, a thalassemia control group and a thalassemia iron loaded group. The process by which these animal groups were created and prepared is outlined in Figure 3.3.

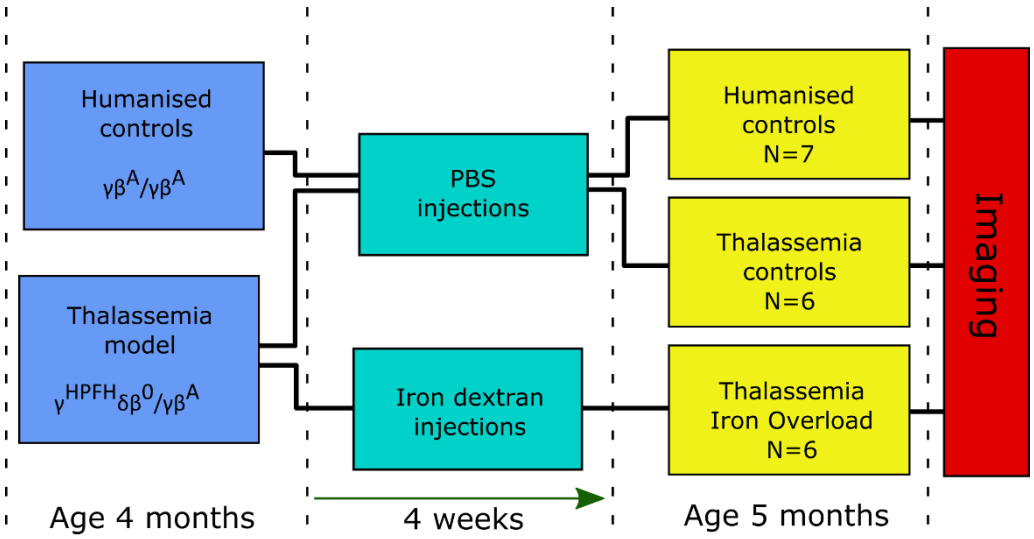

Figure 3.3 Outline for preparation of animal groups. Injections began at 4 months of ages and mice received daily injections of either PBS or 100mg iron dextran for a period of 4 weeks. Imaging was then performed at 5 months of age.

Heterozygous knockin $\gamma^{HPFH}\delta\beta^{0}/\gamma\beta^{A}$ thalassemia mice (n=6) received intraperitoneal injections of iron dextran solution (10mg in 100µL 5 days/week for 4 weeks) to simulate iron loading resulting from repeated blood transfusions. Control and thalassemia mice received injections of PBS with the same regimen. All injections began at 4 Months of age.

3.2.2 In vivo MRI

Imaging was performed at 5 months of age using a 9.4T MRI system (Agilent Technologies, Santa Clara, USA) equipped with 1000mT/m gradient inserts and a 39mm volume resonator RF coil (RAPID Biomedical, Rimpar, Germany). A small animal physiological monitoring system (SA Instruments, Stony Brook, NY) was using to record the ECG trace, respiration rate and internal temperature. Animals were anesthetised under a mixture of isoflurane and oxygen with physiological measurements used to maintain depth of anaesthesia.

3.2.3 Spleen volume

Spleen volume data were acquired in control and non-loaded thalassemia mice using a respiration gated multislice gradient echo axial sequence (GRE) with resolution = 156×156×500um, flip angle = 20°, TE = 3.2ms. In iron loaded mice due to ultra-short T2/T2* decay in the spleen a GEMS protocol was impractical (see Figure 3.4), in this case a respiration gated T1-weighted spin-echo multislice sequence was used (SEMS) with in-plane resolution = 234µm, slice thickness = 1mm, TE = 2.5ms, TR = 600ms. In both cases the number of slices was adapted to cover the whole spleen volume. Image data was reconstructed offline and spleen tissue was identified by drawing contours on individual 2D slices and propagating through plane to measure organ volume. The ratio of spleen volume to total animal mass was used as a quantitative and animal-independent value for spleen size.

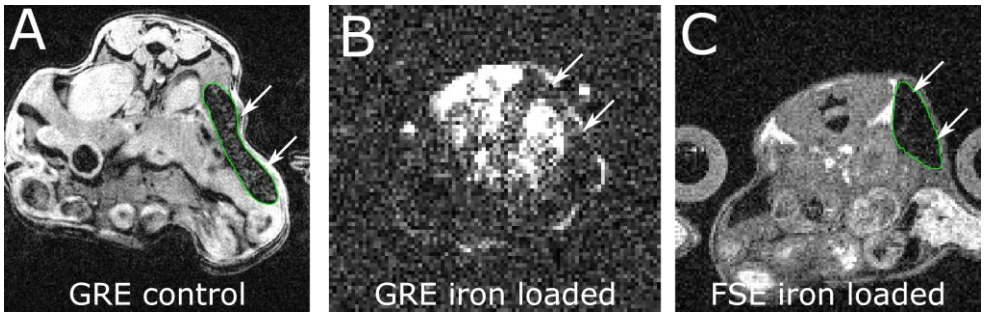

Figure 3.4 Example of the issues encountered when imaging in iron loaded mice. In the control group (A) the spleen is clearly visible (green contour), due to the high iron content in iron loaded mice (B) gradient echo (GRE) sequences are unsuitable, for this reason in iron loaded mice a T1 weighted fast spin echo (FSE) sequence was used to quantify spleen volume (C).

3.2.4 Relaxometry imaging

To fully characterise the magnetic properties of tissue, imaging sequences were designed to measure T1, T2 and T2*. When acquiring data for relaxometry in the heart consideration must be made to acquire images at the same cardiac phase at each echo time. This results in some limitations as to echo spacing and acquisition protocols. The following section describes how T1, T2 and T2* data sets were acquired in the heart.

3.2.4.1 T2 relaxation imaging

For measuring T2 this study used a double gated multi-slice spin echo T2-mapping acquisition scheme designed by Dr. Adrienne Campbell-Washburn (University College London). This acquisition scheme is based on a spin echo imaging sequence and is detailed in Figure 3.5. Image acquisition starts when the respiration gate switches to open (i.e. not during inspiration or exhalation) and an ECG pulse is received. The first ECG pulse triggers the acquisition of a single line of k-space and each subsequent ECG pulse in the same respiration cycle acquires the same line in adjacent slices. Any ECG pulses received when the respiration gate closes are ignored. This cycle repeats and each successive respiration acquires the next phase encoding line. Therefore, the respiration rate determines the number of slices that can be acquired and the total acquisition time. Typical murine respiration and heart rates allowed for 5-8 slices. To sample the T2 decay curve separate image volumes were acquired with different TE's. An excitation delay was included following each ECG trigger equal to 30ms minus the current TE. This was included to ensure that the acquisition echo always occurred at the same point in the cardiac cycle (QRS + 30ms).

In this study T2 data was acquired at 8 echo times ranging from 2.7 – 20ms these values were chosen to sufficiently sample the T2 decay curve for accurate fitting. TR was the respiration interval, image resolution was 0.3×0.3×1.5mm, 7 slices were acquired in total with 1mm thickness, where 6 slices passed through the heart and liver and one offset slice through the spleen.

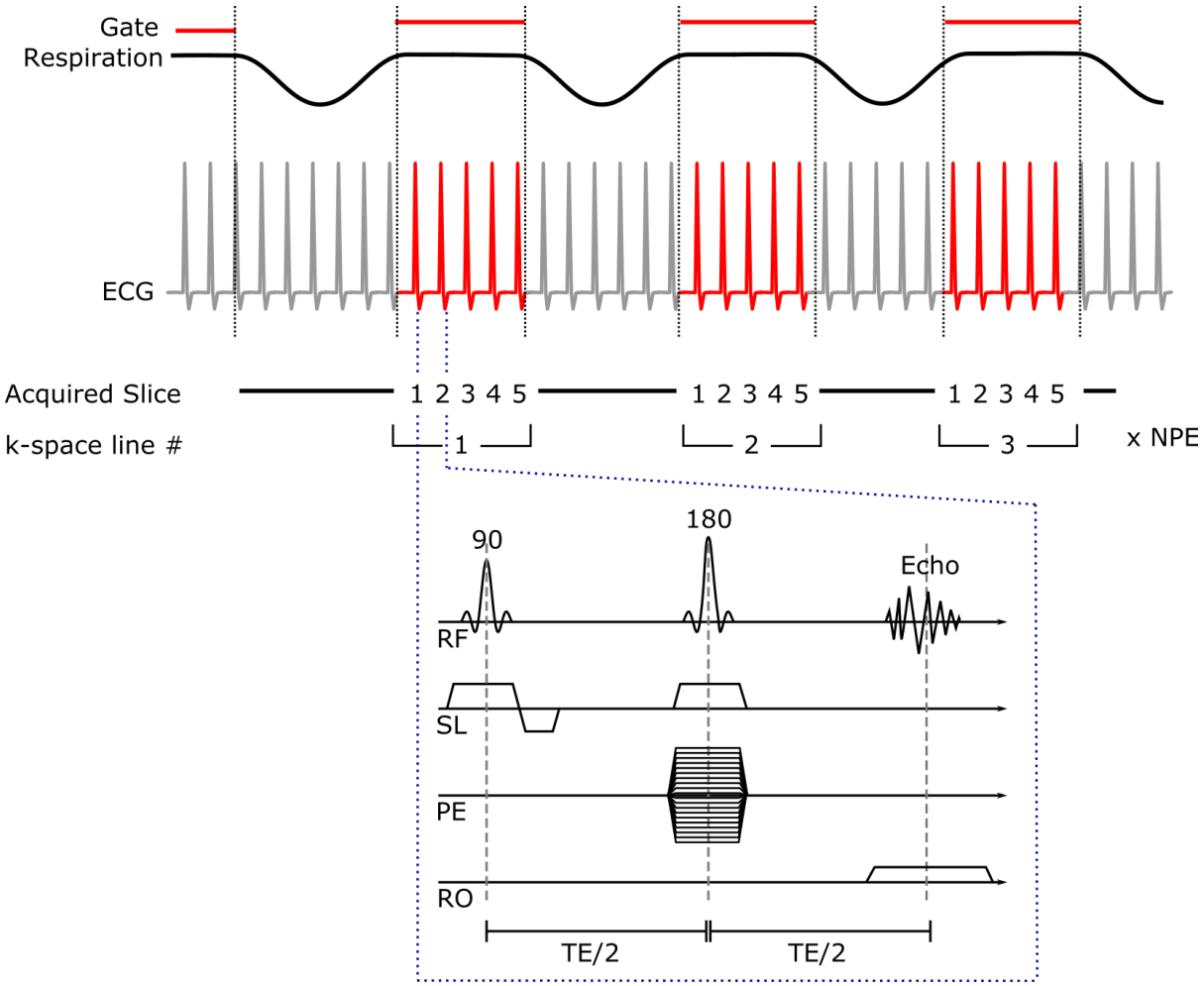

Figure 3.5 MRI sequence used for acquiring multislice T2 mapping data. In this example 5 slices are acquired for each respiration cycle. Each respiration triggers the acquisition of 5 lines of k-space, 1 for each ECG pulse in successive slices (red ECG) at a fixed TE interval. The imaging protocol used a standard 90-180 spin echo acquisition.

3.2.4.2 T2* relaxation imaging

T2* decay was imaged using a double gated multi-echo gradient echo sequence. Each ECG pulse detected outside of a respiration triggered the acquisition of one phase encoding line in each of 15 sequential images with a temporal resolution of 0.92ms.

T2* relaxation was measured using 15 echo times in the range of 0.9 – 14.9ms, image resolution was 0.23×0.23×1.5mm. Two single slice acquisitions were performed with one slice placed in the same orientation as the T1 look locker and second acquisition orientated to pass through the largest part of the spleen based on the earlier volumetric scan.

3.2.4.3 T1 Inversion recovery

T1 image data were acquired using an extended version of the inversion recovery (IR) scout described in section 2.3.5. The IR scout sequence was extended to sample the T1 decay at each ECG trigger and continue over respirations. Resulting in respiration corruption as described in 2.3.3. Initially acquisitions were inspected by eye and the respiration corruption in some cases deemed to be effecting the accuracy of T1 fitting. The PENIR respiration corruption removal scheme was therefore implemented to minimise this effect. To measure T1 relaxation a cardiac gated look locker sequence was used with a minimum TE of 2.8ms followed by 30 echo times separated by the RR interval.[182] The slice was orientated so as to cover the mid-papillary level short axis of the heart and a portion of liver allowing for both tissues to be quantified during a single scan with an in-plane resolution of 0.3×0.3×1mm and a slice thickness of 1.5mm.

3.2.5 Relaxation model fitting

Regions of interest (ROIs) were drawn manually using ITK-SNAP[183] in each image slice to segment organs and remove contributions from surrounding tissue or blood vessels, representative ROIs are shown in Figure 3.6. The relaxation of the mean pixel value in each ROI was used to fit a curve so a single value could be assigned to each organ. The heart was split into 4 regions that could be used individually or combined to get a single value for the whole heart.

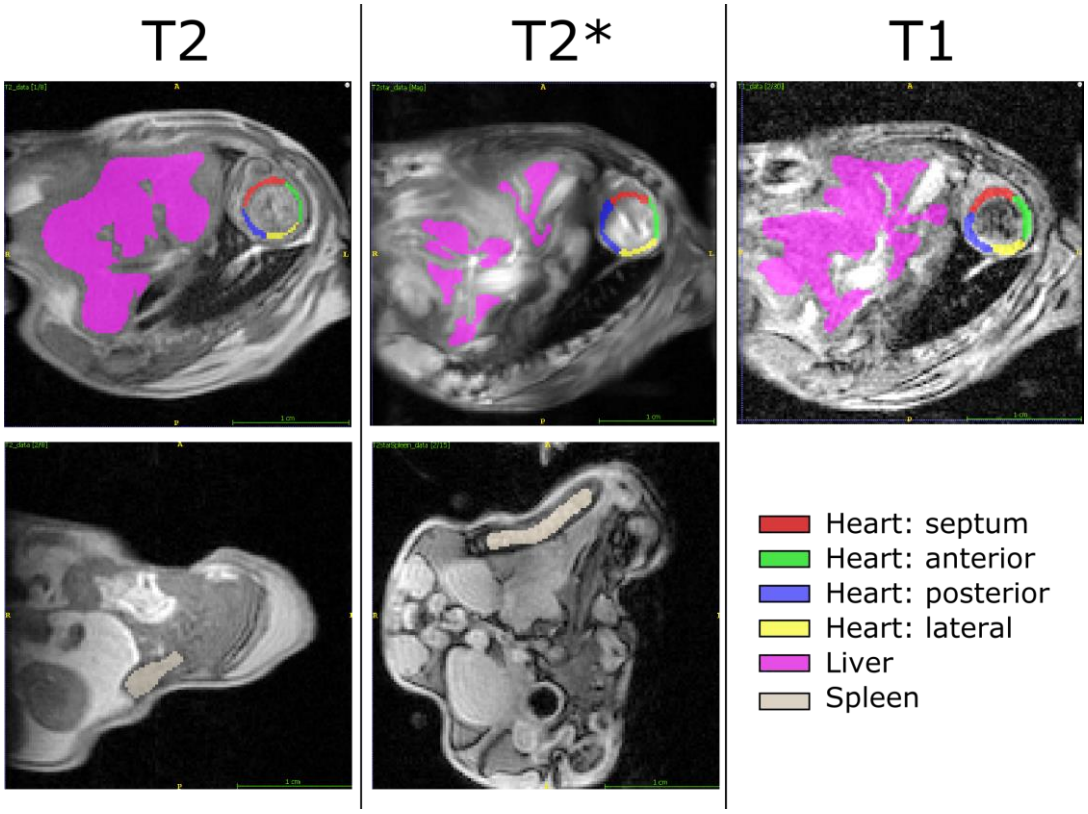

Figure 3.6 Representative ROIs drawn to fit relaxation. The heart was split into 4 regions which could be combined for an overall measure for heart tissue. Liver regions were drawn to minimise the contribution from major hepatic blood vessels.

T2 signal decay was modelled from the image series using Eq. 3.1, where TE is echo time. T2* decay was also modelled using Eq. 3.1 with T2* substituted for T2.

$$S(TE) = S_0 e^{-TE/T2} + C \qquad \textit{Eq. 3.1}$$

The T1 acquisition described in section 3.2.4.3 resulted in an image sequence where T1 image intensity could be modelled by Eq. 3.2.

$$S(TI) = S_0 \left(1 - Be^{-TI/T1^*}\right) + C \qquad \textit{Eq. 3.2}$$

Where S_0 initial signal intensity, TI is the time following the look locker inversion pulse, B is a fitted parameter to account for imperfect inversion, C is a fitted offset to account for image noise and $T1^*$ is the apparent T1 under the influence of look locker saturation, this is corrected by the look locker correction factor (Eq. 3.3).

$$T1 = (B - 1)\, T1^* \qquad \textit{Eq. 3.3}$$

Pixel values from the segmented tissue regions were taken and models fitted to mean ROI values at each echo time. Model fitting was performed in Matlab (2014b, The Mathworks, Inc., Natick, USA) using a minimisation function based on the Nelder-Mead Simplex method.[184] Results are presented as mean value ± standard error and significance values were calculated by one way analysis of variance corrected for multiple comparisons (Holm-Sidak).

3.2.6 Cardiac function

Cardiac function was assessed with a spoiled gradient echo cine MRI sequence with a temporal resolution of 5.2ms, an in plane spatial resolution of 0.17×0.17×1mm. The left ventricular blood pool was segmented at systole and diastole using Segment v1.8 R0462[185] and the corresponding volumes used to calculate left ventricular ejection fraction (EF), stroke volume (SV) and end systolic/diastolic volumes (ESV/EDV).[186]

3.2.7 Iron quantification and histology

Ex-vivo iron assay and staining were performed by Evangelia Vlachodimitropoulou and Panicos Shangaris (University College London). Animals were sacrificed after imaging and samples of heart, spleen and liver fixed in 4% PFA for analysis. Non-haem tissue iron concentration was measured using the iron assay described by Bothwell et al. and iron deposits were observed histologically by Perls' stain.[187].

3.2.8 Statistical tests

All results are presented as mean value ± standard error. All data were tested for normality using the Kolmogorov-Smirnov test and significance values were calculated by one-way analysis of variance corrected for multiple comparisons using the Holm-Šídák method. In all cases a p-value of less than 0.05 was considered significant.

3.3 Results

3.3.1 T2/T2* relaxation

Example data sets and fitted relaxation curves are shown in Figure 3.7. Both acquisitions provided data suitable for fitting the relaxation curves although additional samples at late times (>25ms) may have improved T2 curve fitting in controls due to incomplete relaxation in the current sampling scheme. Note also the difficulty in measuring T2* in the heart (Figure 3.7B). Due to inhomogeneity caused by the lungs and blood flow there is a major discrepancy between T2* on the anterior and posterior sides of the heart best seen by the visibly brighter anterior wall. Of the 4 ROIs drawn in the heart the septum is the least effected by inhomogeneities and so this region was used for heart T2*, this is the solution used in clinical measurements of T2*.

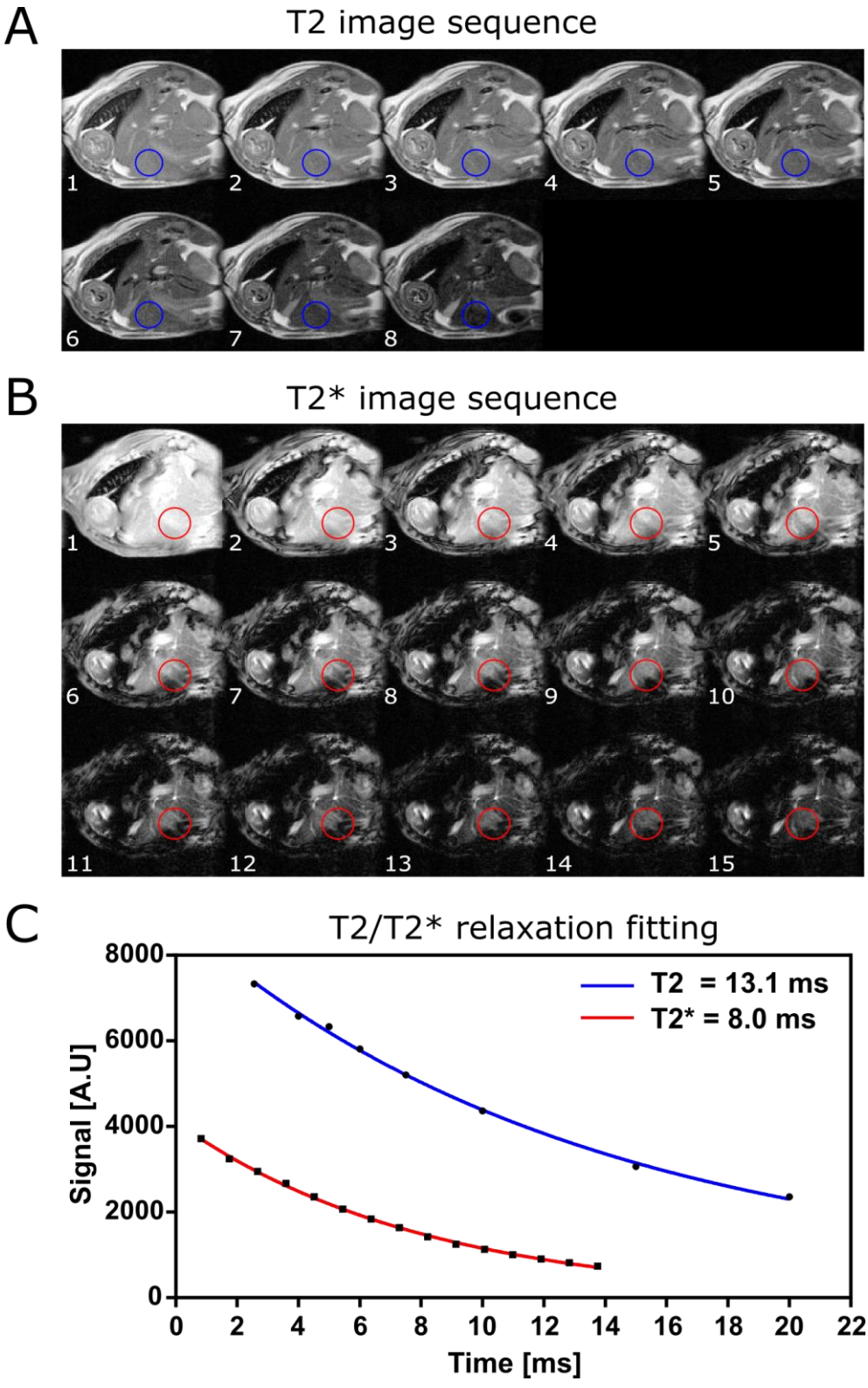

Figure 3.7 Representative T2 (A) and T2 (B) data from control group. To demonstrate the relaxation signal from which T2 and T2* are calculated this example takes a circular region of interest in the liver and plots the signal decay (C) with fitted T2 and T2* curves.*

Measurements of cardiac, hepatic and splenic T2 and T2* are shown in Figure 3.8A and Figure 3.8B respectively, along with representative images from each group at identical echo times.

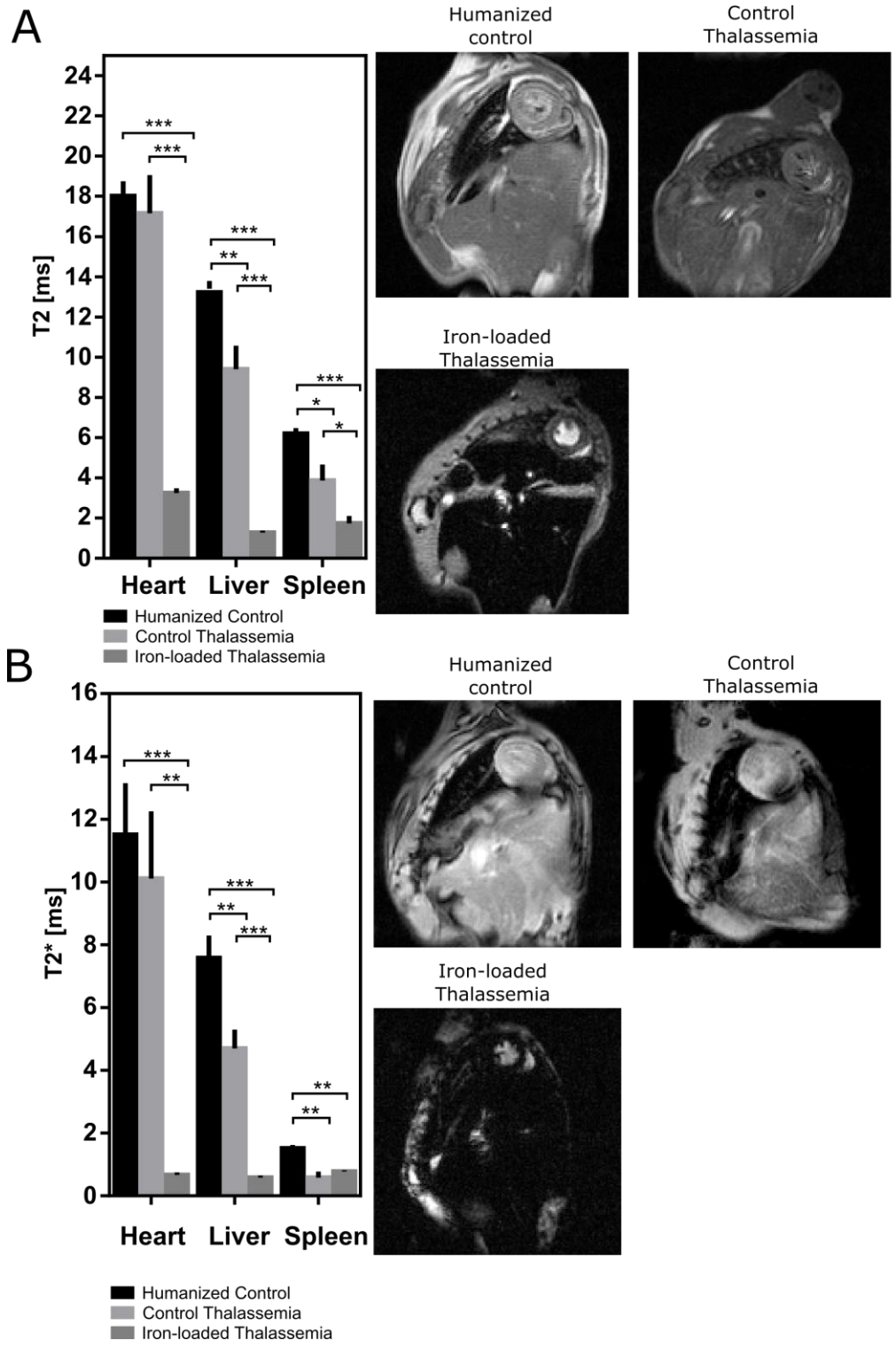

Figure 3.8 Results of T2 (A) and T2 (B) measurements. RepresentativeT2* images at TE=1.8ms. (*p<0.05, **p<0.01, ***p<0.001)*

Myocardial T2 was shortened in iron-loaded thalassemia mice (3.3±0.3ms) versus humanized controls (18.0±0.8ms) and thalassemia controls (17.2±2.1ms). Similarly, myocardial T2* in iron

overload (0.7±0.2ms) was shortened relative to humanized controls (11.5±4.3ms) and thalassemia controls (10.1±5.2ms). These data show that T2 and T2* measures are sensitive to iron loading in this animal model. It can be inferred from this that the additional gastrointestinal iron uptake in the $\gamma^{HPFH}\delta\beta^{0}$ knockin is not severe enough in itself to produce a detectable change in cardiac T2 or T2* at 5 months of age.

Hepatic T2 was shortened in both the control thalassemia (9.4±2.9ms) and iron-loaded thalassemia mice (1.3±0.3ms) relative to humanized controls (13.2±01.0ms). Similarly, hepatic T2* was shortened in the control thalassemia (4.7±1.5ms) and iron-loaded thalassemia mice (0.6±0.2ms) models relative to humanized controls (7.6±1.9ms). This shortening of T2 and T2* in both the thalassemia groups can be related to the role of the liver as the primary reserve for body iron stored as ferritin. In the thalassemia control group increased dietary iron uptake could explain this shortening while in the iron-loaded thalassemia group we see this effect exaggerated by the additional iron intake.

The role of the spleen in breaking down senescent erythrocytes makes it hyperactive in thalassemia where a large population of erythrocytes are defective. Iron deposition is a by-product of the metabolism of the haemoglobin in the spleen. The shortened T2 and T2* in both thalassemia groups reflects this process. Splenic T2 was shortened in control thalassemia mice (3.9±0.8ms) and iron-loaded thalassemia (1.7±0.9ms) compared with humanized controls (6.2±0.8ms). Splenic T2* was shortened in iron overload mice (0.8±0.1ms) and control thalassemia (0.6±0.5ms) relative to humanized controls (1.5±0.3ms).

It is known that iron accumulation occurs initially in the macrophage system of the spleen, liver and bone marrow but subsequently in hepatocytes and ultimately in the heart and endocrine systems. These MRI measurements show that at 5 months of age the liver and spleen in the knockin mice are showing signs of iron loading but the process has not yet begun to accumulate iron in the heart suggesting that is a relatively early stage of disease

3.3.2 T1 relaxation

T1 values were significantly shorter in the presence of iron loading (Figure 3.9).Cardiac T1 was shorter in iron-loaded mice (620±125ms) relative to control thalassemia mice (1041±261ms) and humanized control animals (928±115ms). This was also the case for hepatic T1, with iron loaded thalassemia animals having shorter T1 (456±85ms) than control thalassemia (1014±255ms) and humanized control animals (929±117ms). These data show that T1 is sensitive to the presence of

iron loading however, T1 changes in the presence of iron require direct interaction with ferric molecules, the sensitivity is therefore lower than T2/T2*. T1 measurements could be most useful at particularly high iron concentrations where T2/T2* can be too short to accurately quantify.

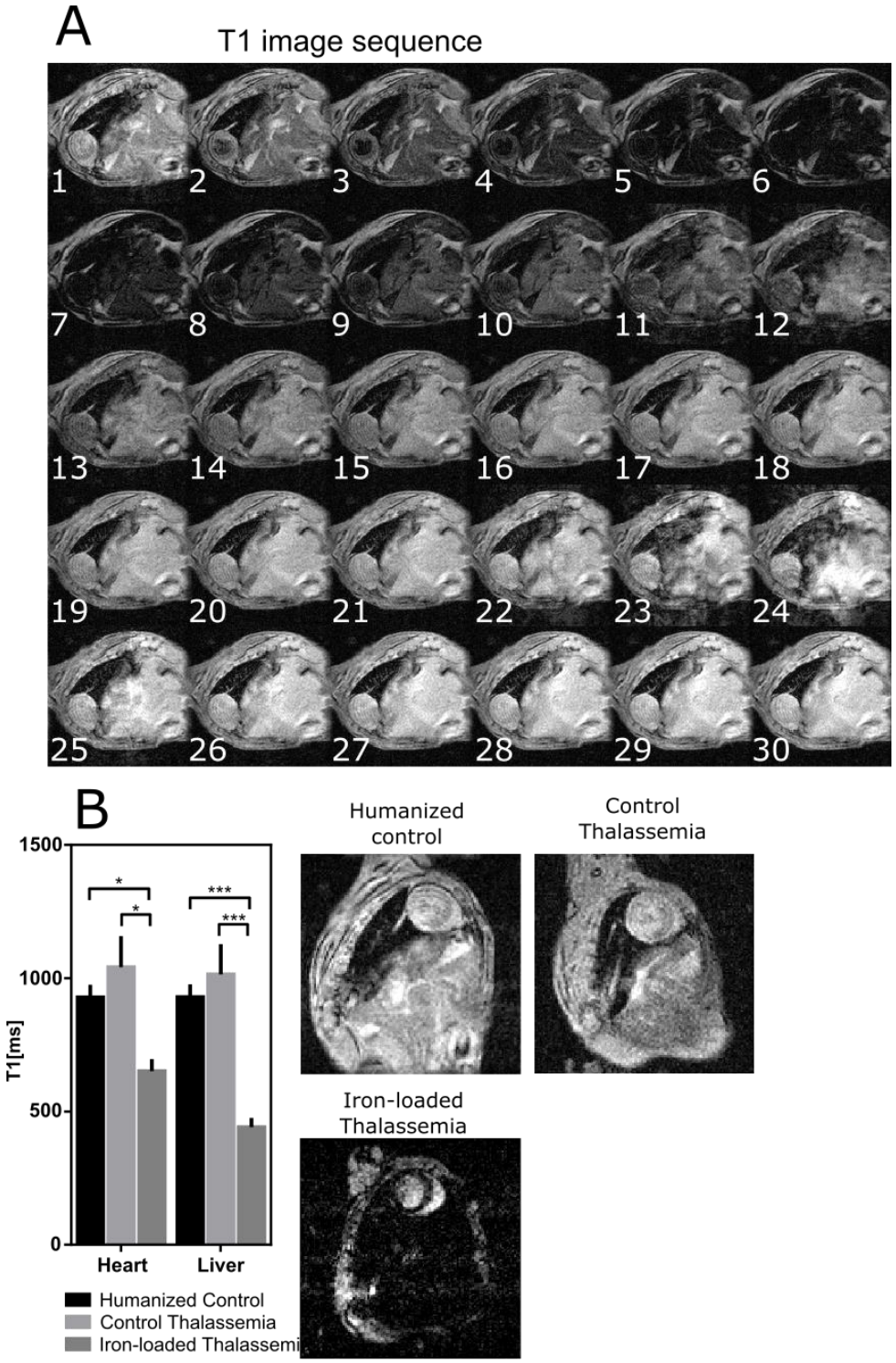

Figure 3.9 (A) Example of control group inversion recovery T1 look locker image sequence. Although far less sensitive to the presence of iron than transverse relaxation, T1 in heart and liver

*was significantly shortened in iron-loaded thalassemia mice (B). Representative images for groups at TI=200ms (*p<0.05, ***p<0.001)*

3.3.3 Spleen volume

A severe increase in spleen size was observed in the presence of the $\gamma^{HPFH}\delta\beta^0$ gene. Figure 3.10 shows a comparison of the axial spleen images and highlights the enlarged spleens in iron loaded and control thalassemia mice. Spleen volume normalized to body mass was significantly increased in control thalassemia (9.5±1.2mm^3/g) and iron loaded thalassemia mice (9.1±1.3mm^3/g) relative to humanized control mice (4.0±0.4mm^3/g), however there was no significant change in volume between iron loaded and control thalassemia mice suggesting that hypersplenism in this animal model is a consequence of $\gamma^{HPFH}\delta\beta^0$ knockin and is not directly altered by the degree of iron deposition.

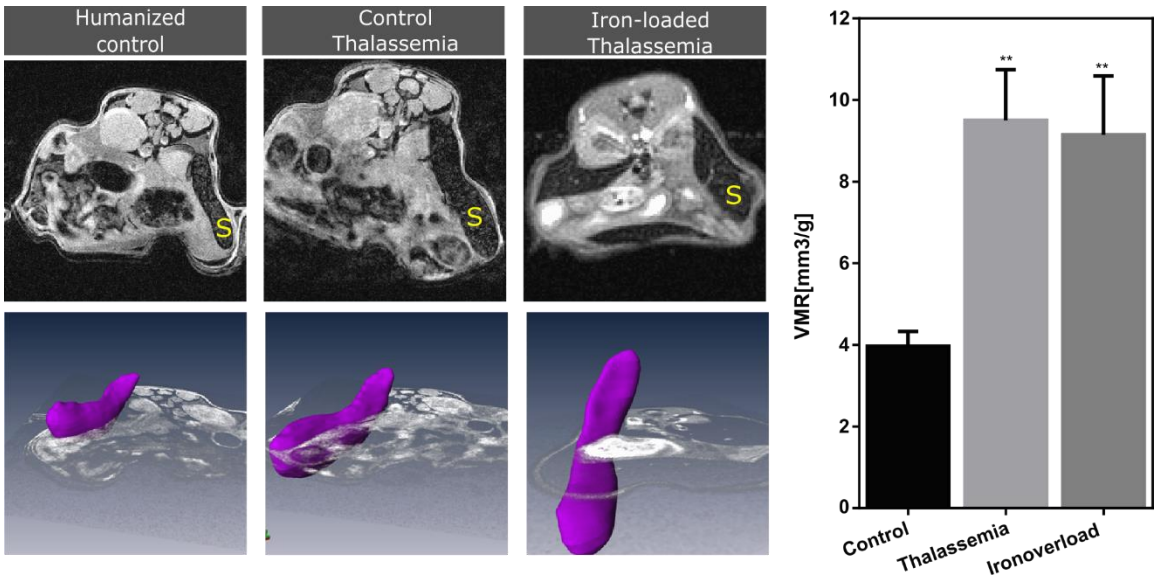

Figure 3.10 Spleen volume was dramatically increased in the thalassemia groups. The top row of images shows axial MRI images of the spleen (S), below are the corresponding volume renders of the segmentation used to quantify volume. The figure plots the organ volume to animal mass ratio for each group. VMR = volume spleen/ animal mass ratio.

3.3.4 Cardiac function

Quantitative values describing left ventricular function are shown in Figure 3.11. Left ventricular end diastolic, end systolic and stroke volumes (SV) were preserved between groups. Cardiac output (CO), measured as the product of stroke volume and heart rate was not significantly altered in control thalassemia mice (14.1±2.1ml/min) relative to humanized controls

(15.6±1.1ml/min) and iron-loaded mice (12.4±1.5ml/min) indicating that at 5 months of age that the two heterozygous knockin groups have not developed the pathological high output state characteristic of anaemia. Left ventricular EF was also unchanged in iron-loaded mice (70±2%) relative to control thalassemia mice (57±4%) and humanized control animals (65±2%).

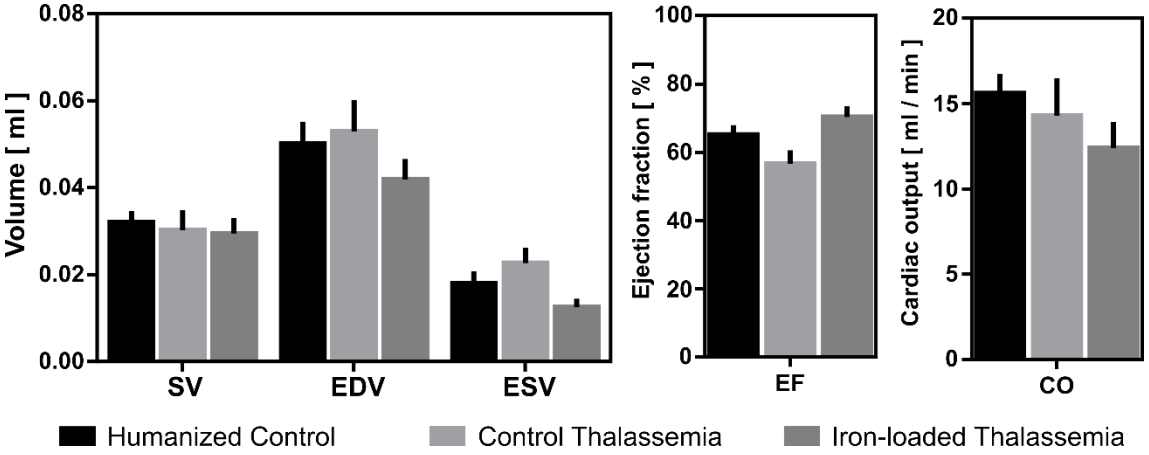

Figure 3.11 Heart function measured by cine MRI was not significantly changed in all groups. It can be concluded that relaxometry changes precede the onset of cardiac dysfunction and can offer an early biomarker for iron induced heart failure.

3.3.5 Histology

Histological sections of spleen, heart and liver are shown in Figure 3.12A. Iron deposits are visible as blue regions in the liver and spleen thalassemia control group and there is no accumulation of iron in cardiomyocytes. This iron distribution is consistent with early stage iron overload where the iron has not spread beyond the macrophage system of the liver and spleen. In the iron loaded thalassemia group there are large iron deposits in the liver and spleen but most importantly iron is also visible in the myocardium. Iron concentration determined by the Bothwell non-heme assay for each organ and group is shown in Figure 3.12B. Control thalassemia hearts did not show significantly higher iron content than humanized controls but iron loaded thalassemia animals showed large myocardial iron depositions. Hepatic iron content was higher than humanized controls in control thalassemia and iron-loaded animals while splenic iron showed an increasing trend but the results did not reach statistical significance. These results match the T2/T2* relaxometry measurements.

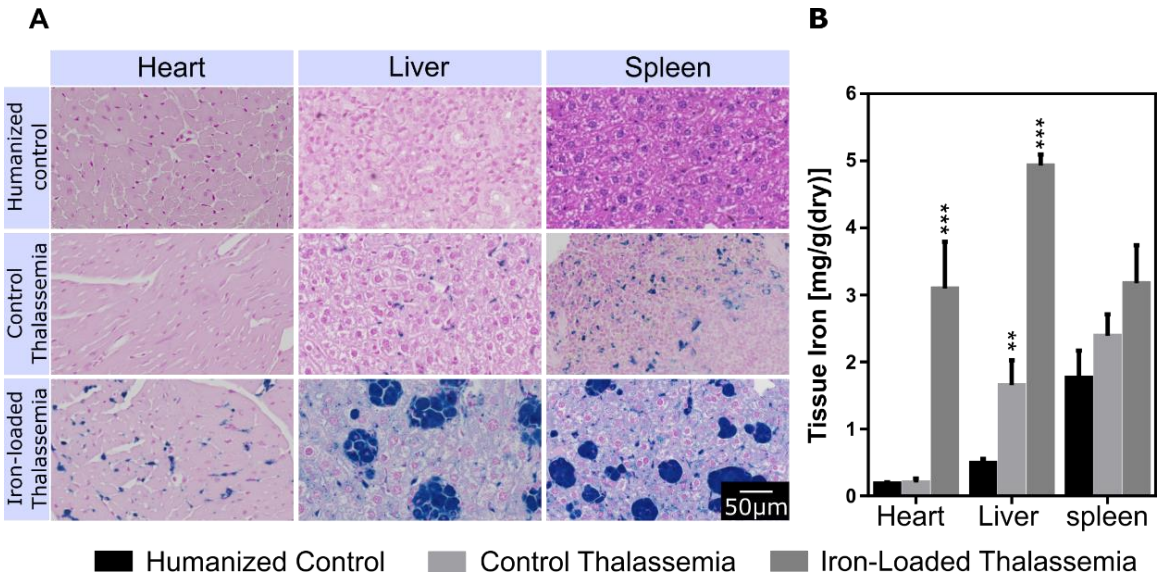

Figure 3.12 Perls stain for iron (A) show iron deposits in the spleen, liver and heart. However, only after iron-loading do the thalassemia mice exhibit iron accumulation within cardiomyocytes. Results of the Bothwell iron assay (B) show that T2 and T2 measurements are good markers for iron content, significance relative to humanized controls (*p<0.05, ***p<0.001).*

3.3.6 Iron calibration

The cardiac T2* and iron dry weight measurements can be used to create a calibration curve to estimate iron content of dry tissue. This relationship can be modelled as Eq. 3.4.[188]

$$[Fe]_{dry} = (1/T2^* - 1/T2_0{}^*)/K_{dry} \qquad \textit{Eq. 3.4}$$

Where T2* is the measured T2* value, $T2_0$* is the T2* of the heart in the absence of iron loading and K_{dry} is a proportionality constant for dry tissue. Here the average T2* of humanized controls is taken as $T2_0$* and fitted K_{dry} to the measured T2* and dry iron concentrations. The resulting calibration curve fits measured values moderately well (Figure 3.13) and shows a sharp increase in estimated tissue iron at T2* < 2ms. The process can be repeated for T2 measurements by substituting T2 for T2*. In this case we find that iron concentration increases sharply at T2 < 5ms.

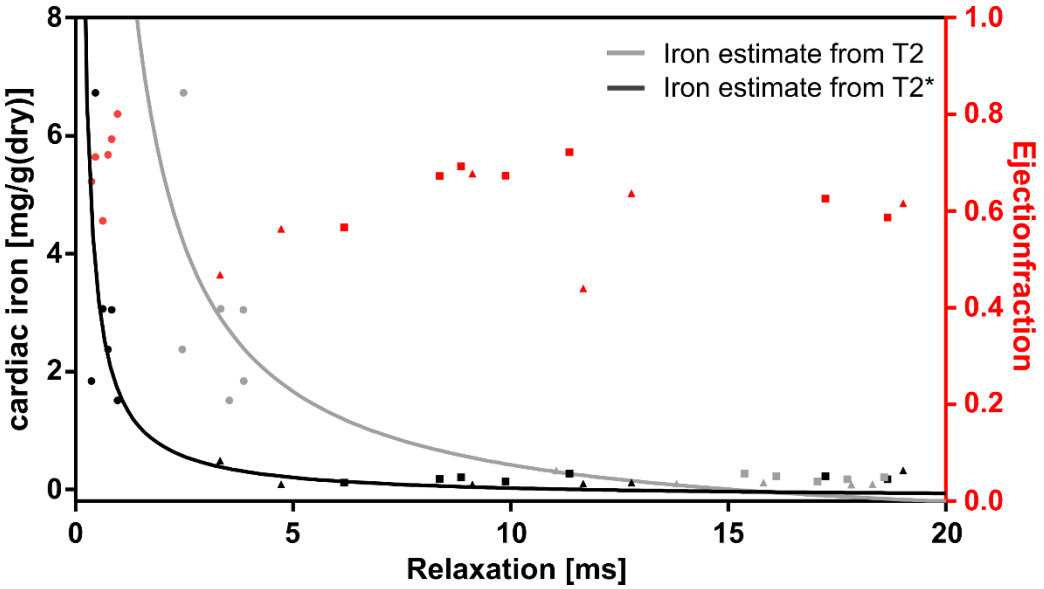

Figure 3.13 Iron calibration curves overlaid with ejection fraction (red – right y-axis). The lack of any relationship between heart iron content and ejection fraction may be explained by the early imaging time point.

If the ejection fraction is overlaid on the right axis (Figure 3.13 Red) we could expect to see a decrease in ejection fraction as cardiac T2* get shorter as shown by wood et al.(2005).[188] In this data we do not see this trend. The most likely reason for this is that the imaging time point is too early to observe the onset of reduced ejection fraction. This is consistent with the pattern of iron accumulation in non-loaded thalassemia mice, where iron accumulates in the liver and spleen before affecting the heart. The Bothwell iron assay used to measure iron content does not differentiate between the forms of physiological iron. The cardiac iron in the iron loaded mice may therefore be stored in a safe form that does not immediately affect cardiac function such as ferritin.

3.4 Discussion

In humans T2* measurement by MRI is the primary technique for identifying pathological iron overload in βT and has revolutionized the early diagnosis of disease prompting a leap in life expectancy as MRI becomes more readily available.[146] A myocardial T2* of <10ms is the recognized primary predictor of heart failure in humans. In this study, we find a similar rapid increase in estimated cardiac iron content at <2ms. The T2 and T2* calibration curves fitted in Figure 3.13 are representative of calibration curves seen in humans. This is a promising sign that the animal model is clinically representative and that serial measurements of tissue iron by MRI can establish trends in tissue iron loading during the onset and following the treatment of βT, enabling more clinically useful interpretation of efficacy of such treatments.

The small organ size of rodents necessitates the use of high field MR imaging systems to obtain adequate temporal and spatial resolution, but this brings its own challenges, with relaxation times shortened and field inhomogeneity accentuated. T2* is currently the clinical standard for assessment of iron overload and has been universally adopted, however T2* is influenced by a number of factors independent of tissue iron concentration. The dense capillary networks within the myocardium have a significant impact on cardiac T2* relaxation due to their geometry and susceptibility which can be altered in disease, additionally in βT blood of varying degrees of oxygenation depending on severity of disease can drastically alter T2* relaxation rates. Variation in B0 shimming and long range susceptibility effects from the lungs can also influence measurements. As an alternative, T2 relaxation is less affected by these variations but has a lower sensitivity to iron. Here we found that T2 and T2*provide the same information with regards to iron concentration in the heart, liver and spleen. It is therefore feasible to use T2 as a more accurate quantitative measure of tissue iron when high sensitivity to iron is not required. T2 has also been shown to be a useful and reproducible measure of tissue iron in humans, however T2* remains the gold standard due to the substantial number of validation studies performed to establish this technique.[189,190]

The true relationship between myocardial iron and T2/T2* relaxation has previously proven difficult to determine; although the shortening effect of iron is recognized it must be determined that iron is the dominant factor in faster transverse relaxation in βT as opposed to the abnormal haemodynamics. Iron concentration in this study was found to match T2 and T2* values for each organ. The control thalassemia and iron-loaded thalassemia groups have the same $\gamma^{HPFH}\delta\beta^{0}/\gamma\beta^{A}$ knockin gene and present the same variable blood oxygenation and myocardial capillary networks of βT. The iron-loaded animals demonstrated a shortening of T2 and T2* regardless of this similarity providing evidence that the dominant T2/T2* shortening factor in βT is iron accumulation.

Pronounced splenomegaly was observed in the $\gamma^{HPFH}\delta\beta^{0}$ knockin mice irrespective of the presence of iron overload in the organ. Hypersplenism shortens the lifetime of transfused RBCs creating a requirement for more frequent transfusions and compounding the consequential iron overload, therefore successful treatment of βT will require slowing or reversing the effects of hypersplenism. These results show that MRI can quantify the change in spleen volume caused by the knockin thalassemia gene making it a useful tool for assessing therapy.

In anaemic states the heart compensates for a lack of blood oxygen capacity by increasing cardiac output to maintain tissue oxygenation, typically through increasing end diastolic volume.[191] Results here however do not show a significant increase of these cardiac metrics in

$\gamma^{HPFH}\delta\beta^{0}$ knockin mice relative to humanized $\gamma\beta^{A}/\gamma\beta^{A}$ controls. One likely explanation for this is the mild anaemia and persistent HbF known to be expressed in the heterozygous $\gamma^{HPFH}\delta\beta^{0}$ knockin mice, this would preserve the ability of the blood to transport oxygen, meaning that compensatory increases in cardiac output are not required. Although cardiac dysfunction is not observed, an increase in iron content through assay and relaxometry measurements is seen in iron loaded and thalassemia mice and is known to predispose a patient to cardiac dysfunction in the future.[192] The onset of cardiac dysfunction in the presence of iron overload is well established and the data presented here suggests that relaxometry measurements and increased spleen volume precede the onset of cardiac dysfunction and can be used as early markers for the progression of disease and is the same in the clinical setting.[146]

Current research into therapies for βT typically focuses on either gene therapy, iron chelation agents or inducing post-natal production of HbF. Gene therapy approaches aim to modify harvested autologous haemopoietic stem cells in-vitro, repairing the dysfunctional β-globin genes before transplanting them back to the patient.[193] Gene therapy has been shown to be effective in mice for various forms of β-thalassemia.[194-196] These studies required animals to be culled at each time point to assess severity of disease, the in-vivo nature of MRI imaging means it would be a valuable addition to these studies providing a means to characterizing the time course of treatment.

Iron chelation therapy is a necessary accompaniment to regular blood transfusions in clinical treatment. Currently there are three FDA approved iron chelators: Deferoxamine, Deferiprone and Deferasirox. Each drug has its relative adverse effects and challenges making the development of new chelating agents is an active field of research.[197] There are promising agents such as FBS0701 that has many advantageous properties relative to current chelators and is currently undergoing phase II clinical trials in which MRI assessment of iron concentration and cardiac function are primary endpoints.[198] FBS0701 has undergone preclinical assessment of toxicity and safety but these studies did not utilize MRI techniques which would have provided translatable information for clinical trials.[199,200] Future preclinical studies into the safety of new agents will greatly benefit from integrating the MRI assessments that we present here, allowing parallel investigation of toxicity and iron chelation efficacy serially in vivo.

This study has been limited by the single measurement at 5 months. Cardiac factors in βT such as dysfunction and iron accumulation without iron loading may have provided interesting results if the study had imaged at multiple later time points. The next stage in continuation of this project would be to incorporate a therapeutic element to the study. This could be any of the approaches discussed above. This work has shown that MRI analysis of these animals is able to quantify

changes in severity of disease in terms of spleen volume or iron accumulation in tissue. Assessment of chelation agents in particular would benefit from the ability of MRI to image at multiple time points to track the accumulation and removal of iron along with the consequential cardiac dysfunction.

3.5 Conclusion

The data presented here demonstrates that MRI can be used to characterize the $\gamma^{HPFH}\delta\beta^{0}$ knockin mouse model of βT. Both spleen volumetrics and relaxometry distinguished between humanized controls, control thalassemia knockin mice and iron-loaded thalassemia mice with a marked increase in spleen volume and shortening of relaxation times in βT mice. The increasing iron content in the thalassemia animals quantified by chemical iron assay and visualized by Perls' stain (Figure 3.12) confirms the inverse relationship between increasing iron load and decreased T2 and T2*relaxation time in tissue.

In conclusion we have presented the first study to use quantitative MRI to assess tissue iron, spleen volume and cardiac function in the $\gamma^{HPFH}\delta\beta^{0}$ knockin mouse model of βT. Measurements of T2/T2* show great potential as a sensitive biomarker for preclinical monitoring of iron accumulation, while measurements of spleen volume and heart function are able to provide additional biomarkers to assess disease progression. Using MRI to quantify βT in experimental animal models will have application in the development of new therapies and is directly translatable to clinical practice.

The multiparametric imaging platform developed here in the context of preclinical beta thalassemia has applications in the quantification of cardiac disease and regeneration therapy. Relaxometry changes are often the hallmarks of underlying pathology, in this case a reduced T2* represents increased iron content, similar links exist between T2 and oedema or T1 and contrast agent concentration. Measurements such as these offer valuable quantitative measurements of underlying physiology.

Chapter 4 Introduction to regional function and regional structure from cine images

4.1 Part 1 - Introduction to regional function

Many cardiac diseases, myocardial infarction (MI) included, are regional in nature. Localised damage and regional dysfunction are characteristic symptoms of MI. It is necessary therefore to quantify cardiac disease using regional function measurements. Only with this information can cardiac mechanics be accurately described. This chapter provides an introduction to regional function measurements using MRI. The development of techniques for assessing regional function in the heart using MRI is the main component of the imaging platform being developed within this thesis. Chapter 5 and chapter 6 will describe my work in developing advanced preclinical tissue tracking methods and the present chapter serves as an intro to these chapters.

This chapter is presented in two parts. The first provides an overview of regional function and ways it can be measured. In this section the limitations of quantifying heart function using only global functional measures are described, the quantitative values used to describe regional function are defined and an overview given of the various imaging modalities that are able to quantify regional heart mechanics.

The second part of this chapter describes my work in implementing regional function assessment in cine MRI images to demonstrate and quantify the regional nature of myocardial infarction. This is performed through morphology based measurements of wall thickening and fractional shortening with radial sampling of the LV endocardial and epicardial borders.

4.1.1 Limitations of global function

The cardiac system is immensely complex and when healthy, operates in a finely tuned state of optimal efficiency. The normal function of the heart depends not only on the mechanical contraction of the myocardium but on the entirety of the cardiac system through feedback mechanisms that regulate cardiac performance.

A large interconnected network of variables is required to describe cardiac function. Abnormalities in heart rate, blood pressure, renal function, myocardial function and vascular compliance can all impact a healthy and properly functioning heart. Despite this, the vast majority of research and clinical investigations rely on a single measure, namely left ventricular ejection fraction (LVEF) for an overall measure of cardiac health.[201] LVEF is the fraction of blood ejected between end diastole and end systole. This value is given as a percentage and typically ranges from 51-80% in healthy humans when measured using MRI.[202] In mice this range is 60-70%.[203,204] Using only a single value to measure global cardiac function has limitations, LVEF is

used as a pseudo-average, combining all mechanisms contributing to heart physiology that can mask irregularities in contraction that do not directly alter LVEF. This has led to two categories of heart failure (HF) known as heart failure with preserved ejection fraction also known as diastolic heart failure (DHF) and heart failure with reduced ejection fraction also known as systolic heart failure (SHF).[9] In DHF the myocardium contracts and maintains an ejection fraction within the normal range but does not relax normally resulting in impaired ventricular filling. In SHF the opposite is true and the myocardium does not contract causing a reduction in ejection fraction. SHF is a common outcome in MII with 40% of MI patients developing systolic dysfunction detectable by reduced LVEF.[205] LVEF has proven to be limited in its ability to predict HF, in a study by Curtis et al. (2003) LVEF was found to be a good predictor of HF in patients with LVEF <45% but an LVEF >45% although still below the typical range was not related to the occurrence of HF.[206] This suggests that LVEF lacks the specificity to identify those at risk from HF in borderline cases. Gottdiener et al. (2002) showed that mortality was greater in elderly patients with preserved LVEF than those with reduced LVEF.[207] This result is significant in that it shows LVEF cannot be used exclusively as a predictor of cardiac health and cannot independently determine prognosis.

MI is a regional pathology where the infarcted region develops contractile dysfunction due to adverse remodelling, as described in 1.2.3.2. However, regional changes in contraction are not limited to the infarct area. Remote tissue can be affected by the propagation of systolic wall stress and loading from the non-contractile infarct tissue.[208] This remote dysfunction has been shown to significantly contribute to the reduction of global LVEF.[209] The homogeneous appearance of the myocardium in MRI however makes standard imaging tools unsuited to regional investigation. The complex motion of the heart includes through plane and rotational motion meaning that any imaging technique based solely on epicardial and endocardial boundaries will exclude this intramural motion. Imaging tools sensitive to regional motion are therefore desirable for their ability to provide additional information in combination with LVEF to comprehensively describe myocardial mechanics in myocardial infarction.

4.1.2 Quantifying myocardial mechanics

There are a number of ways of quantifying the movement of the heart in a way that provides information about the health or function of that region of tissue. This can be based on tissue morphology, velocity or displacement.

Tissue morphology provides the most basic measurements of myocardial mechanics. These measurements are based on the physical dimensions of the myocardium and include values such as fractional shortening or wall thickening that are based on delineation of the epicardial and endocardial boundaries. Tissue velocity measurements can be performed using ultrasound or phase contrast MRI but tissue velocity is a poor measure of function since it describes only moving tissue not mechanical deformations and so can be corrupted by the tethering effect. The tethering effect is observed when non-contractile tissue such as infarct scar is dragged by surrounding viable tissue. Velocity measurements are unable to differentiate between motion caused by viable tissue contraction or this tethering effect making its use in ischemic disease limited.

The most complete metric for myocardial motion is mechanical displacement that can be used to quantify myocardial strain through the strain tensor $\boldsymbol{E}$ (Equation 4.1). The strain tensor is an $N \times N$ matrix that contains information about an N dimensional deformation for a finite element of tissue.

$$\boldsymbol{E} = \frac{1}{2}(\boldsymbol{F}^T\boldsymbol{F} - \boldsymbol{I}) \qquad \text{Equation 4.1}$$

Where T represents the transpose operator, $\boldsymbol{F}$ is the deformation gradient tensor and $\boldsymbol{I}$ represents the identity matrix. Figure 4.1 depicts the deformation of a square element and how this deformation can be used to define the deformation gradient tensor $\boldsymbol{F}$. The deformation is described by 3 material points (a, b, d) and their positions following deformation (a', b', d'). It is therefore possible to define the strain tensor in 4 different ways for a material point surrounded on all sides corresponding to the displacement vectors above, below, left and right of the point a. It is common to average the strain tensor for all available configurations of $\boldsymbol{F}$ and use this mean tensor to calculate $\boldsymbol{E}$ for that point.

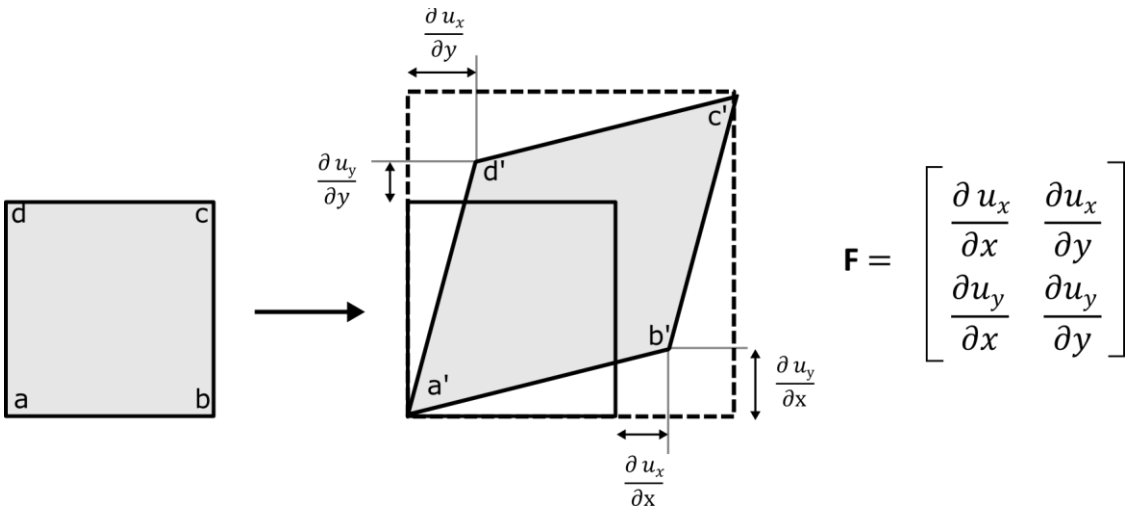

*Figure 4.1 Definition of the 2D deformation gradient tensor **F**, for a square element of uniform material that is used to calculate the strain tensor as described by Equation 4.1.*

The strain tensor contains all the information about how an element of tissue has deformed. Decomposing the tensor into its eigenvalues and eigenvectors provides the principal strains for that element. For the 2D case this corresponds to two components, the first principle component describes the largest deformation by magnitude and gives its direction while the second describes the second principle strain. These can be visualised as the major and minor axes of an ellipse. When investigating cardiac mechanics, images are typically acquired in the short axis where the strain tensor is given reference to the LV centre and projected on the circumferential and radial directions, these strains are illustrated in Figure 4.2. This gives a quantification of circumferential strain (E_{RR}) and radial strain (E_{CC}), and in the case of a 3D tensor this definition can be expanded to provide through plane or longitudinal strain(E_{LL}). These strain components are more physiologically relevant to the heart since the contraction of the heart in the short axis can broadly be considered as circularly symmetric in healthy function.

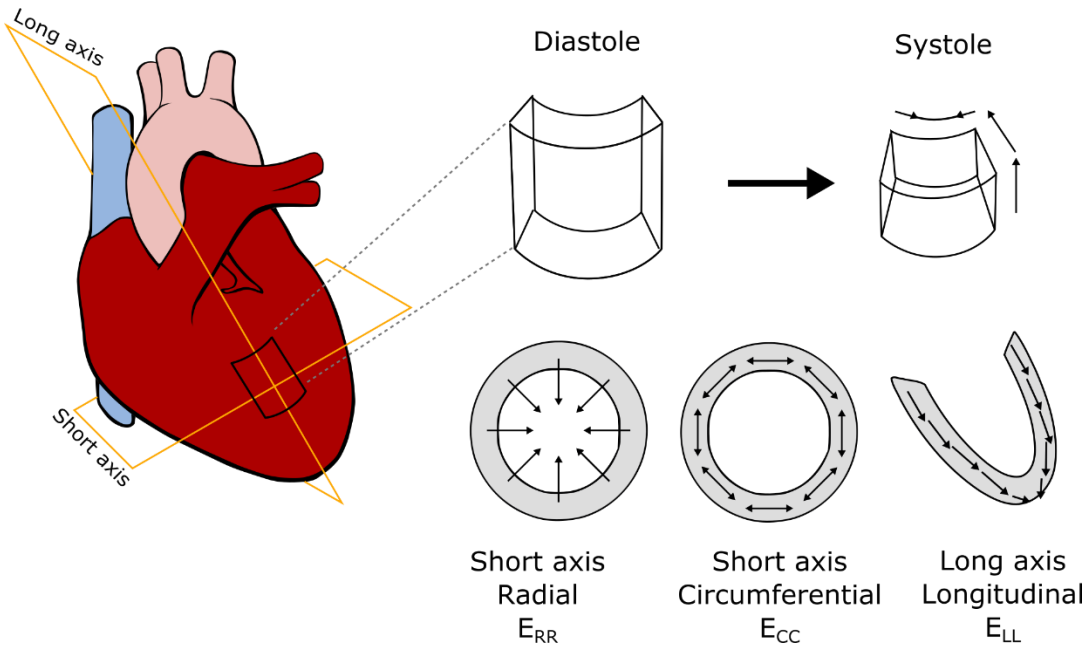

Figure 4.2 Myocardial wall motion can be described through mechanical strain. The 3 components of the strain tensor can be projected onto the cylindrical axis of the LV to give 3 principle strains; radial, circumferential and longitudinal to describe the deformation of the myocardium.

4.1.3 Techniques for measuring regional function

The first measurements of regional heart function were performed using ultrasound or planar X-ray imaging following the implantation of an invasive marker to provide contrast.[210,211] The uniform x-ray attenuation of myocardium in x-ray imaging means that measuring regional displacement once required the implantation of trackable radiopaque markers. One of the first such studies by Rankin et al. (1976) surgically attached multiple ultrasound transducers to the epicardium to investigate changes in geometry during contraction.[212] Brower at al. (1978) implanted a string of platinum shapes onto the epicardium and tracked their displacement with planar x-ray imaging.[210] A later study by Villarreal et al. (1988) developed this technique to measure 2-dimensional strain (see 4.1.2) in the myocardium based on the relative deformation of a triangular array of surgically implanted ultrasound crystals.[211] These techniques were crude and presented a number of issues regarding safety and accuracy. Invasive methods raise concerns about the damage caused by implantation of markers into the myocardium, the effect of markers on myocardial contraction, the risk of performing repeated measurements and the limited number of tracking points available. Modern methods are able to measure regional heart function non-invasively using advanced ultrasound or MRI.

Regional assessment by ultrasound can be performed either through tissue Doppler imaging or speckle tracking. Tissue Doppler imaging (TDI) measures the frequency shift of the ultrasound signal due to moving tissue to calculate the velocity of the tissue relative to the transducer. TDI, although fast and simple to perform, is limited in that it can only measure the velocity vector in parallel to the ultrasound beam, this limitation is particularly problematic in the heart due to complex torsion mechanics.[213] Additionally TDI is limited by the 'tethering effect' limiting its use in assessment of myocardial infarction. The alternative ultrasound technique is speckle tracking echocardiography (STE). STE is a software based method that tracks the acoustic speckle texture present in the myocardium in b-mode imaging. The speckle pattern in the myocardium is randomly created by reflections, refractions and scattering of the ultrasound beam. Any region of heart tissue will have a unique speckle pattern that is mostly maintained throughout the contraction cycle. The regional pattern produced by a cluster of speckles in tissue is called a kernel, this kernel is tracked between successive b-mode frames by a feature recognition algorithm. This information can be used to measure myocardial strain, strain rate or tissue velocity. STE is not susceptible to the tethering effect since it directly measures myocardial displacements of tissues rather than their velocities, this allows accurate strain calculations based on deformation of tissue. Another advantage of STE is its ability to measure deformations in non-parallel directions, however the resolution of ultrasound tends to be much higher in the axial direction due limitation in beam width resulting in more accurate strain information in the direction parallel to the beam.

MRI methods have superior signal-to-noise ratio (SNR) and contrast relative to ultrasound as well as comparable spatial resolution. There are a large number of approaches used to measure regional function with MRI (see Ibrahim et al. (2011) for a comprehensive review [214]). There are three main approaches, the simplest method is to use standard cine-MRI data and analyse regional wall thickening or feature movement during contraction, secondly the position or displacement of the myocardium can be encoded within the MRI signal in a process known as 'tagging' or tissue velocity can be measured using phase contrast techniques. Assessing regional function based on velocity measurements in MRI suffers from the same tethering effect discussed above in the case of TDI, for this reason only cine based and MRI tissue tagging methods will be discussed here.

Tissue tagging for assessing regional function began in the late 1980's with the development of magnetisation saturation methods by Zerhouni et al. (1988).[215] The authors used selective radiofrequency saturation of the MRI signal to create planes of hypointensity that were a magnetisation property of the tissue. These tagged planes appear as lines in the orthogonal

imaging plane and could be seen to deform during systole providing the first non-invasive means of directly measuring myocardial contraction. The lifetime of these saturated 'tagged' planes depends on the degree of saturation and the T1 relaxation of the tissue, resulting in tag fading over the cardiac cycle. In the time since this first study there have been two periods of development for tagging techniques. The first period developed basic tagging methods based on magnetisation saturation and provided a deforming pattern of linear, gridded or radial tag lines in MRI magnitude images that were conductive to visual assessment of function but proved difficult to quantify. This included tagging sequences such as spatial modulation of magnetisation (SPAMM) (discussed in detail in chapter 5), complementary SPAMM (CSPAMM) and delay alternating with nutations for tailored excitation (DANTE). The second period of tagging development came about with advanced tagging methods based on image phase and manipulation of image k-space. These advanced tagging methods allowed for faster and more accurate quantification of cardiac motion relative to the basic pattern tracking techniques. These second period techniques are the most commonly used methods today and include harmonic phase (HARP), displacement encoding using stimulated echoes (DENSE) and strain encoding (SENC) MRI. My developments of SPAMM/HARP and DENSE will be discussed in detail as part of this chapter in chapter 5 and 6 respectively.

4.1.4 Regional function with MRI in disease

The first instance of someone using assessment of regional function by MRI to show heterogeneity between contracting myocardial region was performed by Clark et al. (1991).[216] The authors used gridded SPAMM tagging to calculate regional circumferential shortening (FS) from the end systolic tag line separation. This study found that apical segments of the LV have a higher FS than basal segments suggesting more forceful contraction towards the apex. The study also investigated intra-slice contraction and showed that the FS was highest in the endocardium. This describes an upwards twisting motion from apex to base with a large endocardial contraction component pumping the blood. Fractional shortening is a tool for extracting regional function from standard cine images. This study showed the utility of tagged MRI for quantifying myocardial mechanics and demonstrated that SPAMM was sensitive to regional heterogeneity. The results were confirmed in a later study by Azhari et al (1993), who introduced 3D strain analysis to tagged images (section 4.1.2) to show that the principle component of strain was aligned with the myofiber angle at the epicardium but was misaligned at the endocardium suggesting a reorientation of endocardial fibres during systole.[217] More recently Bogaert et al.

(2001) confirmed these results using higher resolution images aiding in transmural observations.[218] These studies among others[219-223] form a wide body of work aiming to fully characterise the regional function profile of the human heart in normal physiology. The result is a better understanding of the complex 3D contraction of the heart and an acceptance that the heart cannot be treated as a symmetrically contracting cylinder. These works have helped establish what can be considered normal heterogeneity between different regions aiding the diagnosis of regional dysfunction.

A wide variety of cardiomyopathies have been investigated using regional function assessment by MRI. Including, but not limited to dilated/hypertrophic cardiomyopathy, valvular and congenital heart disease and ischemic heart disease. The following section will present a brief review of some key papers and notable results for these categories of cardiac disease.

The first regional assessment of hypertrophic cardiomyopathy (HCM) was performed by Maier et al. (1992).[224] Maier observed moderately reduced myocardial torsion in patients with HCM that occurred in all segments. A later study by Mishiro et al. (1999) showed that HCM patients have intraventricular dyssynchrony. Using SPAMM tagging the authors showed that the strain rate of regions was not coherent. This is likely due to the underlying pathology of HCM, where cardiomyocyte disarray and fibrosis in hypertrophied regions causing reduced contraction or delayed electrical propagation. Dilated cardiomyopathy (DCM) is a common result of adverse cardiac remodelling following infarction and is therefore a valid target for therapy in cardiac regenerative medicine. The first study to examine the effect of DCM with a regional approach using MRI was performed by MacGowan et al. (1997). The authors showed that in normal physiology the epicardial principle strain component aligned with the cardiomyofibres but in the endocardium it was perpendicular suggesting wall thickening is the dominant contraction mechanism in the endocardium. The authors also showed that this transmural contraction pattern is unaltered in DCM despite significantly reduced fibre shortening. This suggests that in ischemic DCM the fibre structure is partially preserved and may present a viable regenerative target.

In an interesting study of the effect of valve disease on regional function Sandstede et al. (2002) used MRI SPAMM tagging to assess the effect of chronic pressure overload due to aortic stenosis and the associated regional benefits following surgical valve replacement.[225] The results showed that prior to surgery patients exhibited an LV wringing motion where basal and apical regions twist in opposite directions during systole. Following surgical valve replacement there was a recovery of LV torsion to normal physiology 1 year after surgery. This study showed the benefits of a regional assessment in following up surgical intervention and also provides evidence of the

myocardium producing a reversible adaptation to its contraction mechanism to pressure loads. This is a promising example for myocardial recovery showing that the heart may have the ability to reverse certain remodelling processes.

MRI tagging was used in a study by Donofrio et al. (1999) to establish the abnormal ventricular systolic function following full cardiac transplantation in paediatric patients.[226] The authors showed that compared to healthy controls transplanted hearts showed normal regional strain but abnormal twist. Including regions of akinetic tissue and abnormalities in regional contraction even in cases where the transplant was not rejected by the patient. This study will have relevance to ensuring the successful transplantation of engineered heart tissue. The introduction of abnormal function following transplant in the absence of rejection suggests that if tissue engineering will become clinical practice it will require longitudinal studies into the effect of the graft on regional function. MRI is the ideal tool for this sort of longitudinal validation due to its non-invasive and use of non-ionising radiation making repeated investigations practical.

The regeneration of tissue following myocardial infarction is a major goal for cardiac regenerative medicine and studies involving MI represent a large fraction of this work. The assessment of the myocardial mechanics following MI has been an active area of research since the development of the first open chest video based regional assessment techniques.[227] Myocardial remodelling following MI produces a number of changes to the function of the heart in both the directly affected ischemic area and neighbouring and remote tissue as the whole heart adapts to the changes in contraction forces. A 1995 study by Lima et al. used SPAMM tagging to investigate the effect of MI on myocardial strain mechanics.[228] The authors were the first to use MRI tagging to show that strain is severely reduced in non-reperfused sheep hearts as early as 1 week after coronary ligation. The orientation of these principle strain components was also affected following MI with contraction showing an overall reduction in contraction. An important study the next year by Kramer et al. (1996) showed that dysfunction following MI was not restricted to the infarcted tissue.[209] SPAMM tagging was performed in patients with single vessel (LAD) disease who had undergone reperfusion therapy but maintained a low ejection fraction. Analysis showed that these patients showed 15% less contraction at the apex due to the infarcted tissue, but also 10% and 3% lower in the mid papillary and base levels respectively. The base level should be relatively unaffected by LAD occlusion. The authors suggest factors such as tethering or altered mechanical loads and coronary vasculature have significant effects not isolated to the infarcted tissue. A later MRI tagging study by Marcus et al. however showed that contraction strain in remote tissue was *increased* as a compensation mechanism for reduced apical contraction. The authors suggest this is a result of the Frank-Starling mechanism.

This mechanism states that when a larger volume of blood enters the LV the LV myocardium stretches, this in turn causes a more forceful contraction as the LV returns to its systolic shape. Early after MI the end diastolic volume increases to maintain cardiac output, this increased volume stretches non-infarcted myocardium and produces the hypercontraction seen in remote tissue. More recently, advanced tissue tagging techniques such as HARP and DENSE have been applied to investigate mechanics in MI.[229] A novel study by Ashikaga et al. (2005) correlated electrometrical properties of the infarcted myocardium. The authors performed electrophysiological mapping of the heart using epicardial electrodes immediately before and after MRI imaging using LGE, cine and high resolution 3D DENSE. The authors showed that the infarct region exhibited delayed conduction of the action potential. In the border zone of the infarct however, despite normal conduction properties the authors showed abnormal strain properties extending far beyond the infarct zone. This study shows that border zone dysfunction is not caused by abnormal electrical properties but by mechanical interaction with the infarct zone. This study is an example of how multiparametric MRI imaging is able to provide many layers of complementary data. The LGE imaging was used to isolate the infarct and border zones while regional function showed the differences in strain between them and cine imaging quantified global cardiac function. This multiparametric approach is a valuable tool for complete investigation of cardiac function and MRI as an imaging modality is well suited to this methodology.

4.1.5 Regional function with MRI in regenerative medicine

Measurements of region myocardial mechanics are particularly relevant in tissue engineering since successful integration of a therapeutic graft to a particular region will require close mechanical matching with healthy tissue and must be proven not to negatively influence contraction in border and remote regions.

Regional motion assessment has been part of a relatively small number of clinical and preclinical tissue regeneration studies. Rickers et al. (2004) established methods for real time MRI guided injections to graft cells, gadolinium contrast and blue dye into the myocardium.[230] The use of HARP assessment of regional function gave evidence of better contraction in cell treated groups at 4 months post-engraftment in large animals. In a subset of the Prospective Randomized Study of Mesenchymal Stem Cell Therapy in Patients Undergoing Cardiac Surgery (PROMETHEUS) trial (2014), chronic ischemic cardiomyopathy patients receiving injections of autologous MSCs were assessed using tagged MRI images. The study was able to demonstrate that in myocardial

segments that received cell transplants there was a significant increase in wall thickness and contractility relative to segments that did not receive cell transplants after 18 months.[231] Another study by MacArthur et al. (2014) showed using tagged MRI, that a larger region of infarct border tissue underwent functional recovery following MI in sheep after injections of stromal cell-derived factor 1α.[232] Tissue tagging for regional function was investigated in a subset of the autologous stem cell transplantation in acute myocardial infarction clinical trial (ASTAMI).[233] This study aimed to improve left ventricular (LV) function and reduce scar size by transplantation of mononuclear bone marrow cells (mBMC). However, regional myocardial strain was not significantly altered following the intracoronary injection of mBMCs. Tissue tagging applied to this study allowed more detailed analysis of myocardial contraction and verified the negative result.

4.2 Part 1 – Summary

Here I have highlighted articles of interest from a large body of work involving regional assessment. The role of regional function measurements has been largely limited to a research role due to the long scan times and/or complex processing techniques that are necessary for measuring regional function and has seen limited clinical implementation. The value of regional function as a research tool is clear in the detailed functional information it provides over measures such as ejection fraction. Accurate assessment of regional function is essential for investigating regenerative therapies that aim to repair specific regions of tissue. This is especially important when combined with MRI cell and biomaterial tracking so that changes in the regional function of myocardium can be directly related to the site of engraftment. A large component of this work (chapters 4,5 and 6) describes my work in developing MRI tools for assessing regional function in small animal models of myocardial regeneration therapy. An advantage of using MRI for this purpose is the inherent translational potential of MRI methods. All of these methods are compatible with human studies of myocardial regeneration and it is hoped that this work will contribute the use of regional function measurements in clinical cardiac MRI.

4.3 Part 2 - Regional function from cine MRI

For part 2 of this introduction to regional function in the heart I present tools I developed for assessing radial cardiac structure from previously acquired cine MRI data in myocardial infarction. This demonstrates the basic principles of regional function and how it is altered in cardiac disease.

One of the most basic methods of measuring regional heart function is to extract regional morphological information from the standard cine images on which volumes such as LVEF are calculated. The advantage of this approach in MRI is that regional analysis can be performed without requiring additional specialised acquisitions. Two basic methods for collecting regional information from images of the hearts are fractional shortening and wall thickening, these measurements are based on the LV centre and epicardial/endocardial borders depicted in Figure 4.3.

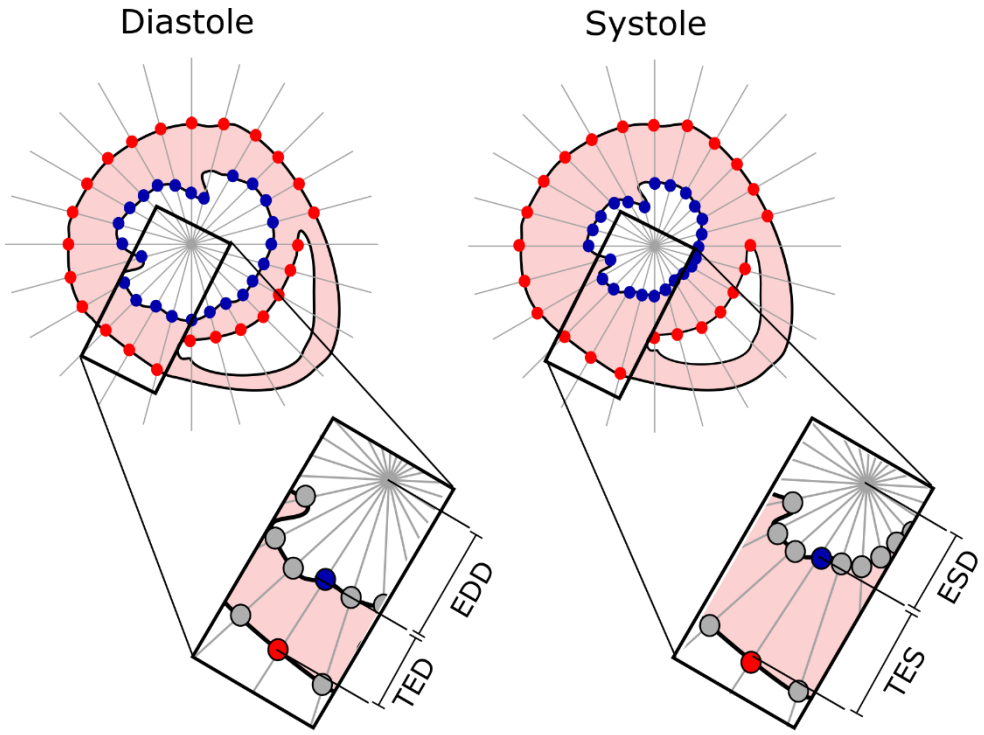

Figure 4.3 Schematic illustrating wall thickening and fractional shortening. Using the centre of the LV as a reference point for line projections are measured at the points they cross the epicardial (red) and endocardial (blue) borders this process is repeated for all radial projections.

Fractional shortening (FS) is an alternative measurement that is sometimes used in the quantification of m-mode ultrasound images. FS is based on the fractional change in ventricular diameter between diastole and systole computed from the radial distance between the centre of the LV to the endocardium Equation 4.2 describes how to calculate FS as a percentage from the LV end diastole diameter (EDD) and the LV end systolic diameter (ESD).

$$FS[\,\%\,] = \frac{EDD - ESD}{EDD} \times 100 \qquad \textit{Equation 4.2}$$

Myocardial wall thickening (WTHK) is a similar measure to FS and can also be measured using m-mode ultrasound but investigates the radial thickening of the myocardium based on the epicardial and endocardial boundaries with the centre of the LV as a reference point.[234] WTHK is calculated using Equation 4.3 where TES is wall thickness at end systole and TED is wall thickness and end diastole.

$$WTHK[\,\%\,] = \frac{TES - TED}{TED} \times 100 \qquad \textit{Equation 4.3}$$

Assessment of FS and WTHK measurements by m-mode ultrasound is a 1D measurement requiring a new beam path for every region of tissue. Additionally, there is uncertainty in the region of tissue being measured due to difficult positioning of the transducer as well as restrictions on which regions of tissue can be measured due to the requirements for an acoustic window. In MRI a complete 3D stack of images can be segmented to provide a regional map of fractional shortening or wall thickening without limitations on transducer placement.

4.4 Methods and development

4.4.1 Animal preparation and imaging

The FS and WTHK processing methods were developed on image data acquired by Dr Thomas Roberts (University College London) as part of an unrelated study investigating the utility of retrospectively gated cine MRI in myocardial infarction. In this study standard prospectively gated cine images were also acquired and it was this data that was used here.

Two groups of mice were studied, a wild type control group (N=8) and a myocardial infarction group (N=8). Myocardial infarction was induced surgically using the methods described in 1.2.3.4. Image acquisition included the standard cine-MRI sequence with the following parameters: TR = 5ms, TE = 1.21ms, FA = 15°, resolution = 0.2×0.2×1mm. In addition, LGE imaging was performed in the MI group to assess infarct severity with the following parameters: TR = 3.1ms, TE = 1.21ms, FA = 90°, TI =4× RR interval, resolution = 0.2×0.2×1mm.

4.4.2 Image processing

Following image acquisition the cine images were segmented in Segment v1.8 R0462.[185] The LV endocardial borders were identified using a semi-automatic method at end systole and end diastole with the corresponding volumes used to calculate left ventricular ejection fraction (EF). Due to the labour intensive process of segmenting the epicardium this was only performed in one mid-apical slice where infarction forms following LAD occlusion.

The myocardial boundaries extracted from Segment were then then used as an input to custom Matlab software to extract the FS and WTHK information. The major processing stages in this Matlab code are depicted in Figure 4.4.

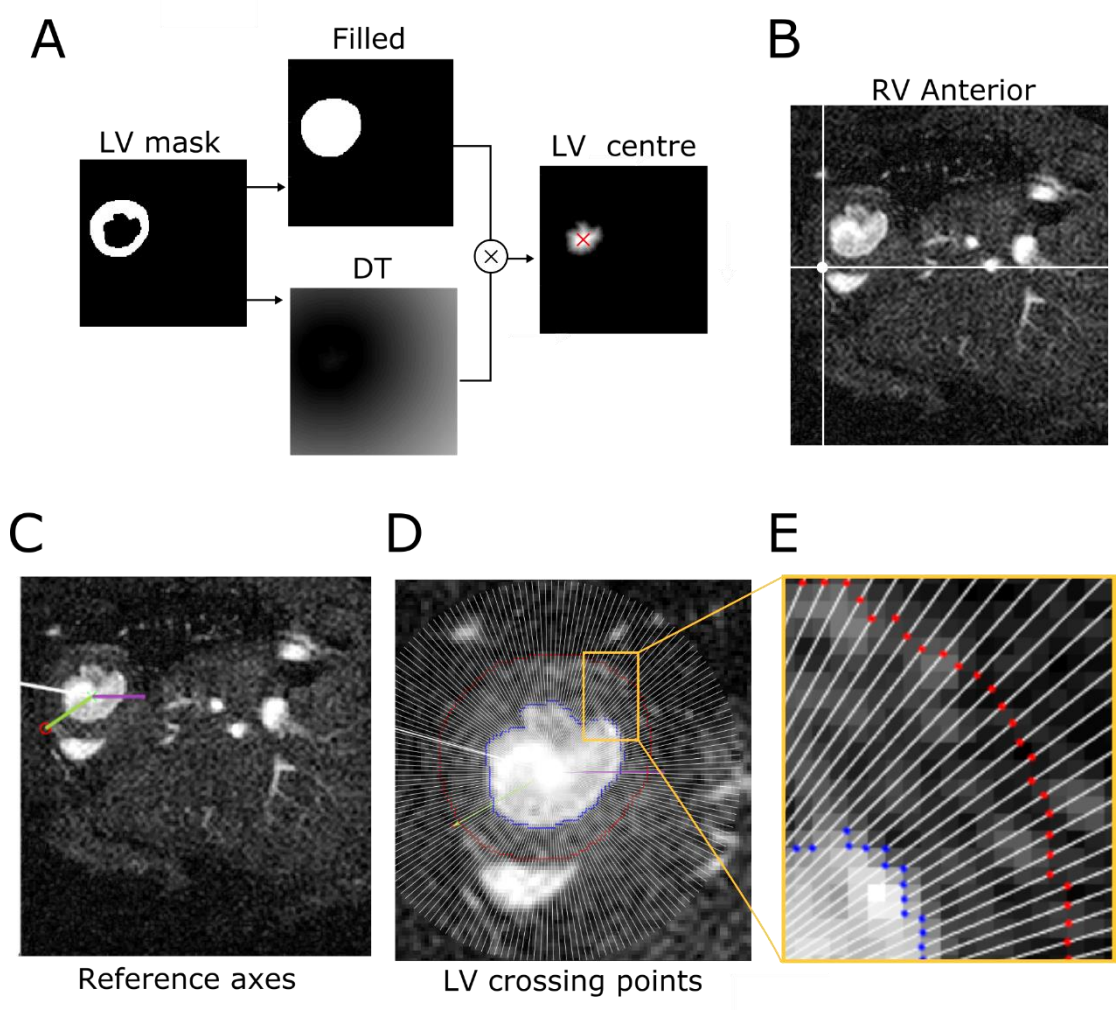

Figure 4.4 Cine regional function analysis pipeline. The centre of the LV was found in each slice automatically using a distance transform (A) and the RV anterior corner was chosen manually (B). This created a consistent reference system (C) for drawing and measuring LV 'spokes' from which the epicardial and endocardial boundaries and their radial separations could be established (D, E).

A consistent cardiac region reference system is needed to compare between animals, this is based on the centre of the LV and the anterior RV corner. Locating the centre of the LV in MI can be difficult due to the non-linear wall thicknesses due to tissue atrophy so a system was created to located the centre of the LV automatically to reduce operator bias. Figure 4.4A outlines this process. Two images were created from a 2D short axis LV mask, a filled image where the ventricular cavity was also masked and a distance transform (DT). A distance transform changes every pixel value to reflect the distance of that pixel from the nearest boundary to create a distance field. The product of the DT and filled images showed only the DT for the LV cavity, co-ordinates of the maximum value in this image then corresponds to the pixel furthest from the LV wall which was taken to be the LV centre. The anterior RV corner was identified manually using a crosshair tool. The radial distance from the LV centre to the epicardial and endocardial borders was measured in a clockwise direction using 180 line spokes where the intersection of each spoke with the myocardial borders was recorded and used to calculate FS and WTHK for that radial segment of heart tissue. The number of spokes is an arbitrary measure, 180 spokes was chosen as a good compromise between speed and accuracy, excessive spoke counts can become slow to process without significant improvement in information.

4.5 Results

Fractional shortening (Figure 4.5A,C,E) in naïve mice was largest in anterolateral, inferolateral and inferior segments. This corresponds to the free wall of the heart. The free wall defines the posterior and lateral region of LV myocardium that are not in contact with the interventricular septum or the apex. In infarcted mice there is a reduction in FS for free wall regions but when compared to naïve mice there was no significant change in anterior or septal regions. This is consistent with infarct by LAD occlusion. The regions myocardium supplied by the LAD include the tissue regions where we see a reduction in FS while remote tissue regions such as the septum and anterior wall are comparatively unaffected.

Wall thickening (Figure 4.5B,D,F) showed uniform contraction in all regions of myocardium in naïve mice at around 40-45%. Following MI all regions show a reduction in WTHK. This is opposed to FS where remote tissue retained normal function, in this case the anterior and septal regions also showed a reduction in WTHK, although the infarcted tissue showed the largest reduction in WTHK.

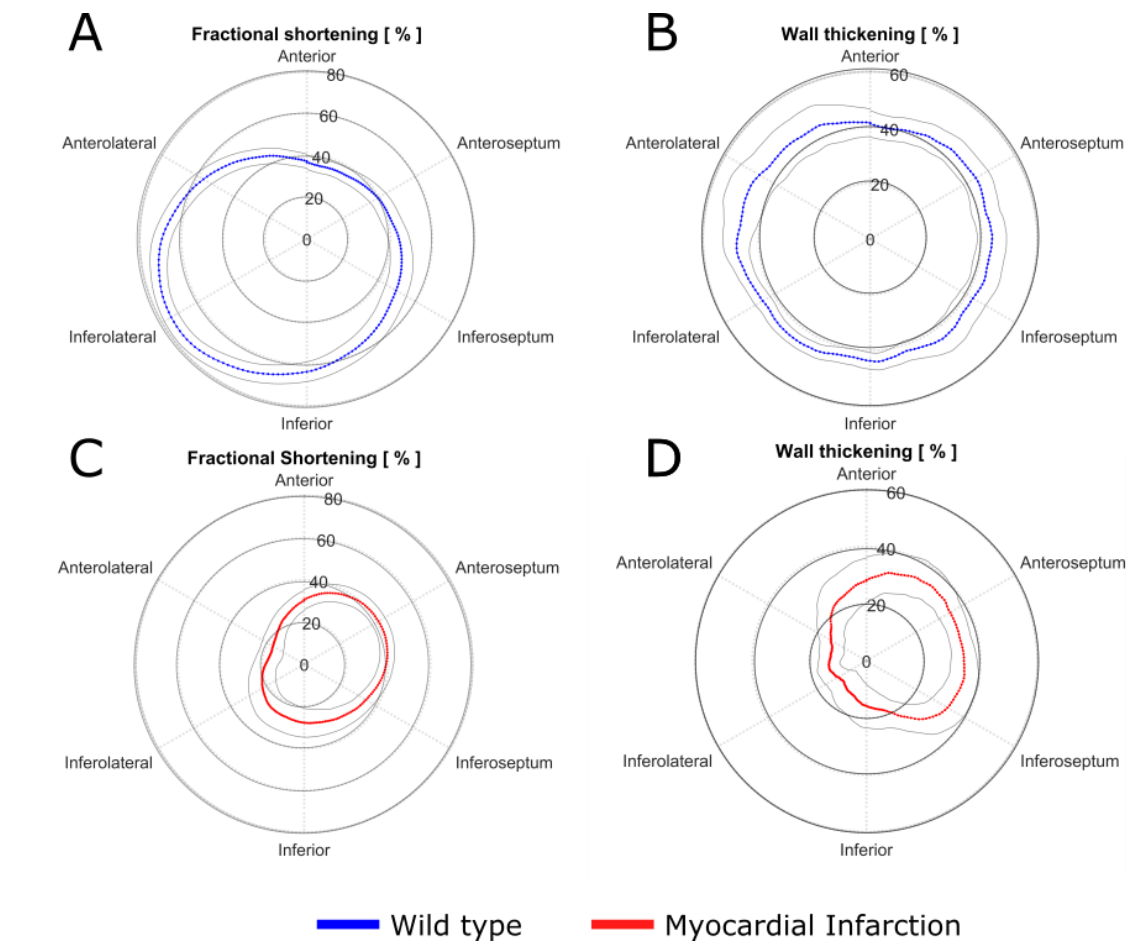

Figure 4.5 Changes in fractional shortening and wall thickening in myocardial infarction. Both FS and WTHK were significantly reduced relative to wild type animals (A and B) in all regions following myocardial infarction (C and D). This reduction is greatest in the anterolateral to inferior regions of myocardium which correspond to where an infarct is expected to form following LAD occlusion. Polar plots displayed as mean ±SEM.

To validate the regional impairment seen with FS and WTHK. The infarct location was confirmed by matching regions of reduced FS and WTHK with regions of hyperenhancement in the LGE images. A representative LGE image from an infarcted mouse is shown in Figure 4.6. The Hyperenhancement in the anterolateral – inferior slices are clearly visible in the inset slice. This provides evidence that FS and WTHK are able to detect regions of impaired function and that these regions correlate to regions of hyperenhancement in LGE images.

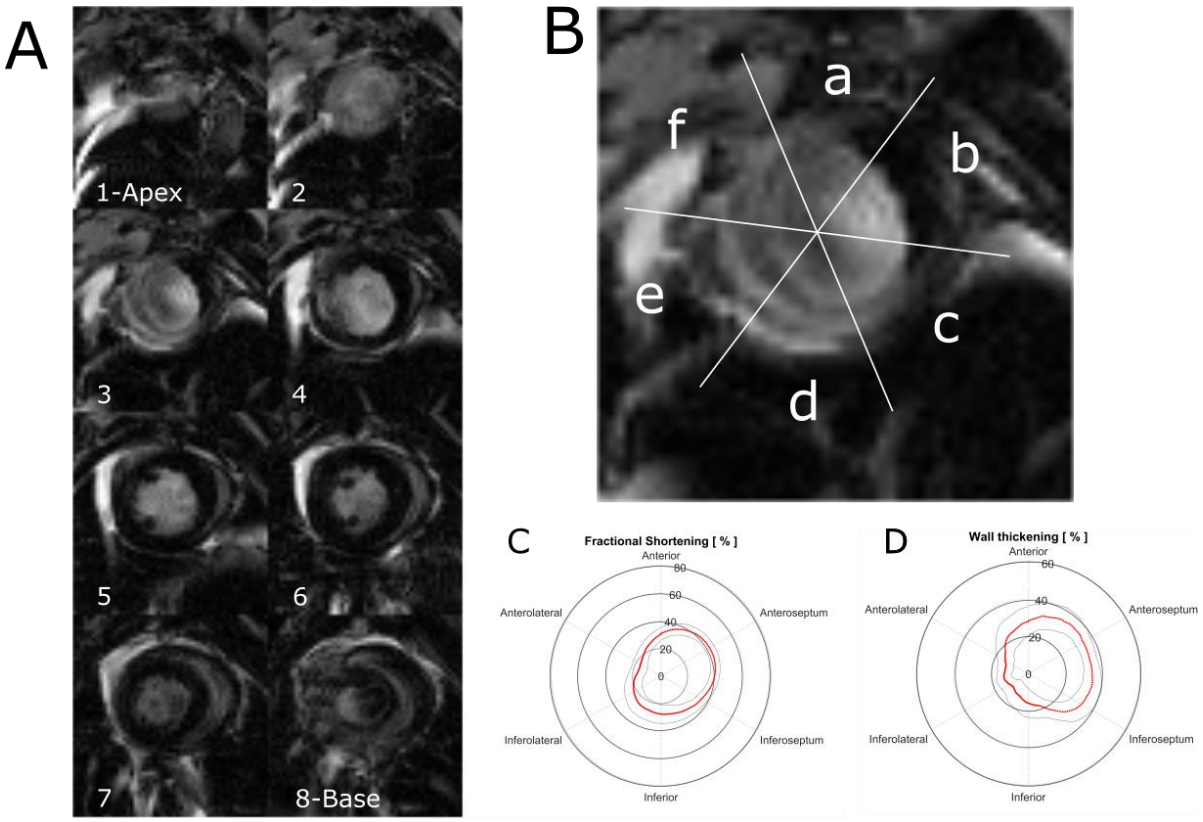

Figure 4.6 Representative LGE image from MI group. (A) Going from apical slices (1) to basal (8). Regions of the heart are defined in (B) (B.a) Anterior, (B.b) anteroseptal, (B.c) inferoseptal, (B.d) inferior, (B.e) inferolateral, (B.f) anterolateral. The infarct (hyperintensity) can be seen to develop on the mid apical inferolateral wall validating the FS and WTHK results in the infarct model (C and D).

4.6 Discussion

As a measure of regional function FS and WTHK are able to detect functional impairment in regions of tissue corresponding to increased ECV as measured by LGE imaging. This impairment manifests itself as reduced wall thickening and a reduced ventricular shortening in infarcted tissue.

The key advantage of using FS or WTHK measures of regional function is that they require no additional image acquisitions as is the case with more advanced techniques such as SPAMM and DENSE. The measurements obtained are morphological changes during contraction that can be easily interpreted as healthy or impaired. The measurements also have the advantage of being widely reported in cardiac ultrasound literature making them accessible to the wider cardiac field outside of advanced imaging techniques.

The values reported here are for the end-systolic frame only however it could be useful to analyse the WTHK and FS over the duration of contraction. This could provide temporal

information about systolic or diastolic impairment that may be beneficial. The process of accurately segmenting the epicardial borders over the contraction cycle is labour intensive and time constraints meant that this could not be performed in this instance. For the same reason the data presented uses just a single 2D slice passing through the infarct zone, segmenting additional slices could be useful in investigating how the remote tissue is effected to compensate for reduced function in the infarcted tissue.

The high dependence of these techniques on accurate delineation of the myocardial borders makes it susceptible to inter user variability in cases where these borders cannot be automatically segmented as is often the case with preclinical MRI. This will also be affected by the inclusion or exclusion of the papillary muscles in the borders. The effect of the papillary muscles should be beneficial due to their contribution to cardiac mechanics, but if they may introduce rapid artificial changes in FS and WTHK when they cross different radial spokes. Further investigation will be required to determine whether their inclusion is beneficial to analysis. Another disadvantage of these methods is the linear nature of the measurement. FS and WTHK are based on a total of three points all placed along a single radial line. The location of the points at the epi and endocardial borders takes no account of the through plane motion, torsion or twist of the myocardium during contraction. This results in a limited view of heart contraction excluding several degree of freedom for cardiac motion. Another consequence of these sparse radial measurements is a lack of sensitivity to transmural dysfunction. Using this method, a single measurement for WTHK or FS is assigned to each spoke, however the tissue the spoke passes through may exhibit different degrees of dysfunction dependent on disease and severity. Additionally, the magnitude of myocardial contraction has transmural dependence in healthy tissue where subendocardial tissue shows greater deformation than subepicardial tissue.

These disadvantages do however come from a processing technique that operates on standard acquisition data, essentially FS and WTHK are able to provide regional function information without additional acquisition time costs. The processing methods although relatively slow and labour intensive can be applied to studies where regional function was not initially planned giving them some utility in reinterpretation of old data if required. In tissue regeneration studies however accurate, transmural data of myocardial function is required. It is not clear whether FS and WTHK can by themselves provide enough information on the regional effect of transplanted cells or material in the heart. Additionally, work by Bogaert et al. (2001) has previously shown that simple regional function measures such as wall thickening and fractional shortening are not directly related to the local contribution to ejection fraction.[218] For these reasons, two advanced

regional analysis methods; SPAMM/HARP and DENSE based on dedicated acquisition schemes were developed and are discussed in chapters 5 and 6 respectively.

4.7 Conclusion

The first part of this chapter introduced the field of regional assessment for cardiac MRI has been introduced with key papers and concepts introduced. In the second part, post processing techniques were developed to apply some of these concepts to provide retrospective regional analysis to cine images. Fractional shortening was found to be greatly reduced in regions of myocardial infarction while remote tissue maintained similar values to naïve animals. Wall thickening was shown to be reduced in all regions of the heart including infarcted and remote tissue. Regional accuracy was confirmed by late gadolinium enhancement for scar identification. The radial and 1 dimensional measurements provided by WTHK and FS do not fully describe the complex contraction of the heart and offer no information about transmural function, mechanical twist or strain during systole. Fully quantitative and descriptive information about cardiac function require the development of specialised MRI acquisition strategies. The following chapters describe my work in developing two advanced preclinical imaging sequences for complete regional analysis.

Chapter 5 Development of Spatial Modulation of MAgnetisation (SPAMM) and HARmonic Phase (HARP) MRI

5.1 Introduction and theory

5.1.1 Study overview

This chapter describes my work in developing, implementing and validating a preclinical spatial modulation of magnetisation (SPAMM) tagging sequence with harmonic phase (HARP) processing. SPAMM and HARP are currently the clinical standard tools for assessment of regional myocardial function. The objectives of this chapter are outlined in the following points.

1. Implement a preclinical SPAMM sequence
2. Create advanced motion phantom for validating sequence
3. Optimise acquisition parameters for preclinical imaging
4. Validate optimised sequence using motion phantom

First an introduction is given describing the concepts underpinning the development of the motion phantom, SPAMM sequence and HARP algorithm. Next a series of experiments are performed to implement and optimise the sequence before finally it is validated using the designed motion phantom and demonstrated in vivo. The result is an optimised SPAMM sequence and HARP processing method for quantifying regional myocardial strain in the mouse or rat heart following engraftment of regenerative cells or material.

The workflow for the methods and development of this chapter is shown in Figure 5.1. The methods and results are divided into 3 parts relating to the field of work undertaken. The first part covers the motion phantom development (red components Figure 5.1), the second describes the sequence implementation and optimisation (blue components Figure 5.1) and the final section describes the HARP implementation and the validation of the sequence for measuring displacement (green components Figure 5.1).

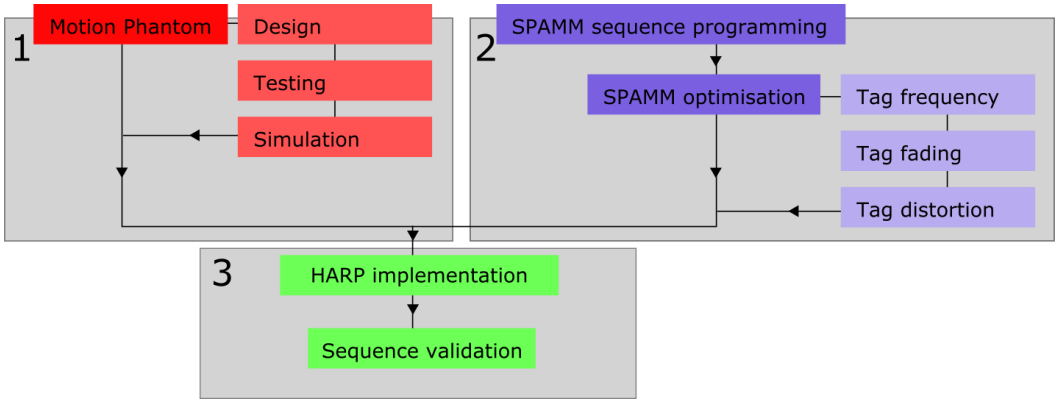

Figure 5.1 SPAMM sequence development and validation workflow. The aim of this study was to implement, optimise and validate a cine SPAMM sequence for assessing cardiac contraction.

5.1.2 Requirements for cardiac motion phantom

To assess the accuracy of MRI techniques for measuring regional displacement a ground truth is required for comparison. For this purpose, a controllable rotation phantom was designed and manufactured to provide a known displacement with which to compare measurements from MRI. The basic specifications I propose for the design of this phantom are listed in Table 5.1.

Table 5.1 Proposed basic requirements for an MRI compatible cardiac motion phantom

Requirement	Description
MRI compatible	No metal components or electronics near scanner
Periodic motion	Reproducible back and forth motion
Stable and easy to position	As similar to scanner set up for mouse as possible
Variable displacement	Provide a range of motion magnitudes

The primary concern when designing any phantom is MRI compatibility. Metal parts present hazards to the user and can cause damage to the scanner while electronic components have the potential to produce image artefacts through RF interference and spark conduction. Reproducible, periodic and controllable motion is necessary to simulate the movement of the heart. Cardiac phantoms have previously been produced based on continuous rotation, and although this motion is simpler to produce and more reproducible, they do not properly mimic heart motion.[235] It is important for the phantom to be stable when in motion to prevent uncontrolled displacements or vibrations, these can cause not only inaccuracies when validating displacement but also motion artefacts due to non-periodic oscillations. A range of displacements is useful to define the range over which the imaging technique is valid. Variable displacements are simple to achieve in a rotating phantom since displacement is a function of a points separation from the axis of rotation.

5.1.3 Spatial modulation of magnetisation (SPAMM)

A year after Zerhouni et al. (1989) developed the first MRI tagging sequence using spatially selective RF pulses, Axel and Dougherty (1989) introduced a more efficient tagging sequence that is still in use today.[236] Spatial modulation of magnetisation (SPAMM) is able to apply a regular tag pattern across the whole field of view fast enough to be unaffected by the start of systole. The next sections discuss the theory of SPAMM and the harmonic phase (HARP) tag analysis technique developed by Osman et al. (1999) that made regional analysis by SPAMM a practical clinical tool.[237] Since SPAMM's applications to cardiac disease have been discussed in

Chapter 4 this section will focus on the technical developments of the sequence, post processing and analysis.

SPAMM is an alternative to the magnetisation saturation technique presented by Zerhouni et al., which takes advantage of magnetisation wrapping to apply a regular 1D sinusoidal tagging pattern in the direction of an applied tagging gradient. The pulse sequence and acquisition scheme that produces this modulation is shown in Figure 5.2A. The SPAMM sequence can be separated into two modules; the tagging module and an imaging modules. Imaging is typically performed using a gradient echo or balanced steady state free precession cine sequence that samples the transverse magnetisation uniformly over the cardiac cycle.

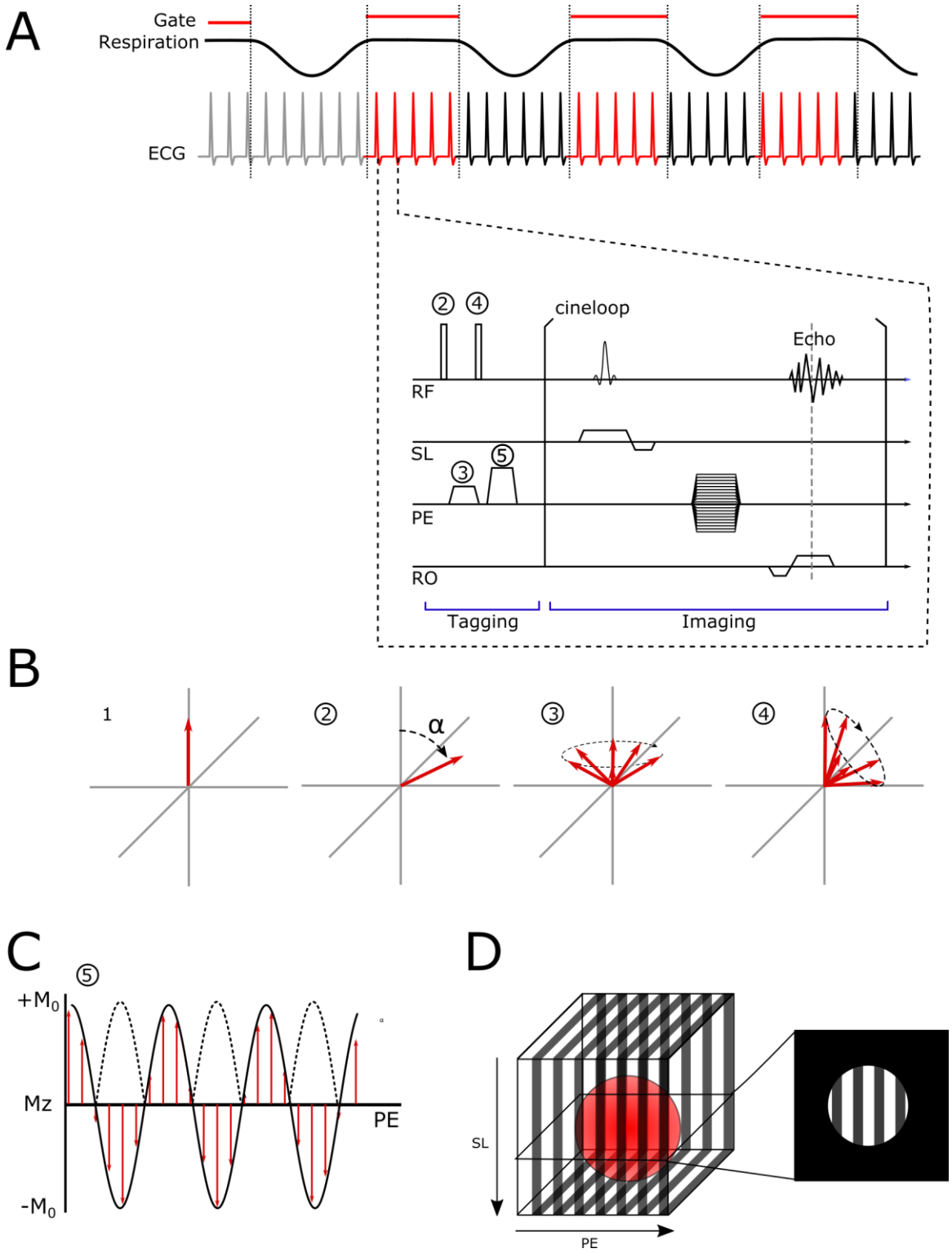

Figure 5.2. Principles of SPAMM tagging. On detection of an ECG trigger (A) a short tagging module encodes a cosine modulation to the magnetisation in a chosen direction before being imaged by a standard cine readout. The magnetisation is modulated in the wrapping gradient direction as described in the text (B). The magnetisation modulation (C) creates a series of parallel planes of saturated signal (D) that appear as tag lines in the orthogonal imaging plane.

Tagging begins with the detection of an R-wave signalling the start of systole. This triggers an RF pulse with flip angle α tipping the magnetisation into the transverse plane. This is followed by

the application of a gradient known as the modulation gradient that gives the spins along the direction of the gradient a phase shift as a function of the strength of the gradient experienced i.e. position along the tagging gradient direction. Since this phase shift can only take values in the range ±π there is a periodic magnetisation wrapping effect over the FOV. A second RF pulse then tips the magnetisation back into the longitudinal plane and a large crusher gradient removes residual transverse magnetisation. This preserves the modulation pattern by taking it from the transverse magnetisation plane where relaxation occurs rapidly and storing it in the longer T1 recovery. It can then be sampled by the imaging component over the duration of the cardiac cycle using an excitation RF pulse to partially tip it back into the transverse plane. Each stage of this process is depicted in Figure 5.2B-C. The non-selective RF pulses used to create the modulation means that this magnetisation pattern is applied throughout the entire imaging volume in a 1D pattern creating planes of magnetisation saturation. The tagging plane is orientated to be orthogonal to the imaging plane creating the tag lines. Figure 5.2D illustrates this concept, the red sphere representing the imaged object. A 1D in-vivo example of the SPAMM tagging pattern is shown in Figure 5.3. Often a 2D grid tagging pattern is used to visualise the tag deformation this can be achieved by combination of 2 separately acquired 1D tag patterns or alternatively two SPAMM tagging modules can be applied consecutively during acquisition, with the wrapping gradient in orthogonal directions.

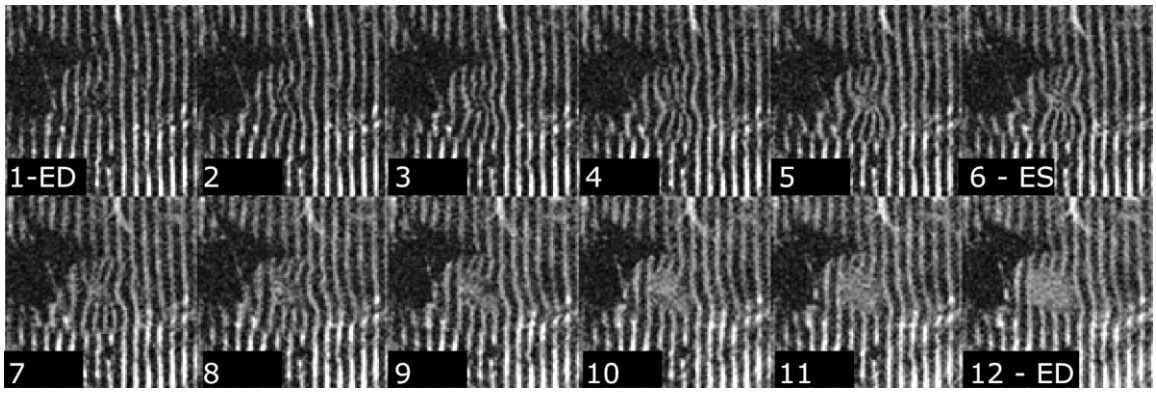

Figure 5.3 The appearance of the SPAMM tagging sequence is a periodic cosine pattern applied at end diastole that deforms as the heart contracts.ES end-systole; ED end-diastole.

The properties of the tagging pattern are controlled by altering the RF flip angle α and the tagging gradient area. The frequency of the tagging modulation is controlled by altering the tagging gradient strength and duration and follows the relationship described by Equation 5.1.

$$K_e = \gamma_H \int G_{enc}(t)\, dt \qquad \textit{Equation 5.1}$$

Where G_{enc} is the gradient strength, t is the duration of the gradient, γ_H is the gyromagnetic ratio for hydrogen and K_e is the tagging pattern encoding frequency. This tagging frequency can be used to describe the magnetisation across the image immediately following tagging and prior to any deformation according to Equation 5.2.

$$M_z(x) = M\cos(K_e\, x) \qquad \textit{Equation 5.2}$$

Where M_z is the longitudinal magnetisation, M is the magnetisation prior to RF excitation and x is the position in the tagging direction. The tagging modulation is stored in the T1 decay of tissue so it is retained throughout the contraction cycle, however unavoidable T1 relaxation results in a degree of tag fading towards the end of the cardiac cycle. This T1 relaxation factor can be incorporated into the function describing the image modulation (Equation 5.2) by including a T1 decay term.

$$M_z(x,t) = (M\cos(K_e\, x) - M_0)e^{-\frac{t}{T1}} + M_0 \qquad \textit{Equation 5.3}$$

Where t is the time over which T1 decay has occurred, $T1$ is the T1 constant of the tissue and M_0 is the equilibrium magnetisation of the tissue. The result of this is a sinusoidal tagging pattern that loses amplitude as T1 relaxation occurs creating a time dependent tagging contrast. This tag fading process described by Equation 5.3 can be simulated in Matlab to illustrate this process. Figure 5.4 shows the T1 relaxation induced tag fading of synthetic data where input parameters were chosen to be representative of the mouse myocardium.

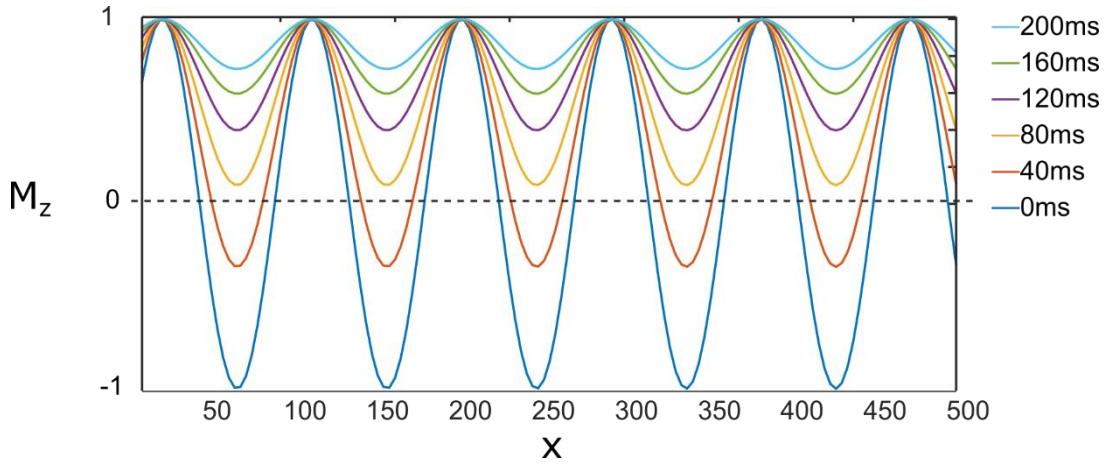

Figure 5.4 SPAMM tag fading of synthetic tag data. Function inputs were chosen to match mouse myocardium. Tag fading occurs at a rate equal to the T1 of tissue (simulated with T1 = 1200ms), although in in vivo data tag fading occurs more rapidly due to hardware limitations and tissue inhomogeneity.

In this simulated example the synthetic tags are persistent throughout the duration of the cardiac cycle (approximately 110ms). In vivo data however suffers from imperfect tag application, T1 variations, intravoxel dephasing and lost magnetisation through imaging readout. These imperfections accelerate tag fading and can making end diastolic function difficult to image accurately. Tag fading is an important consideration when quantifying tagged images since all displacement information is determined from the tag lines. As the tagging modulation fades the information about the displacement becomes noisier and is more prone to errors.

A second important tagging variable is the frequency of the modulation pattern. Optimal tag frequency is a compromise between image SNR and spatial tagging information. A high tag frequency may provide detailed spatial deformation information but comes at a cost of rapid tag fading and low signal due to intravoxel dephasing and saturated tissue respectively. Lower tag frequencies are less susceptible to intravoxel effects due to a slower rate of change of the signal modulation over adjacent voxels but sparse tags provide less information on local deformations.

5.1.4 Harmonic Phase (HARP) analysis

The conversion of tagged MRI data into a relevant quantifiable value describing myocardial mechanics, such as those introduced in 4.1.2 is a complex problem that has been approached from many angles since the development of SPAMM. Active contours, optical flow, sinusoid analysis and finite element modelling are some examples of tag analysis approaches that have been implemented.[214,223,238-241] These tag analysis methods almost universally operate on 2D grid tagged images. The fundamental requirement of these tag analysis algorithms is to find every tag intersection point consistently and accurately for all images covering the cardiac cycle. These can then be connected to form a deforming quadrilateral element that describes the deformation of that piece of myocardium. One major issue with this kind of analysis is that since all deformations are based on tag intersection the resolution of the deformation information is limited by tag spacing. Increasing tag frequency to improve strain resolution causes an SNR penalty as described above. There have been several attempts to work around this limitation using interpolation or biomechanical modelling systems. For example, Young and Axel (1992) fitted a 3D deformable model of LV geometry to the tag intersections.[242] Alternatively, Kumar and Goldof (1994) used a thin plate spline model with active contours in the imaging plane to interpolate the space between intersection points.[243] These methods are computationally intense and highly susceptible to inaccurate tag identification, often requiring manual intervention making them time consuming and unsuitable for clinical timeframes.

Harmonic phase (HARP) analysis for SPAMM images was proposed by Osman et al. (1999) as a way to improve accuracy in tag analysis and reduce processing time.[244] HARP analysis is based on filtering of the harmonic stimulated echoes produced by the SPAMM tagging pattern in k-space. These peaks occur at positive and negative integer multiples of K_e from the central peak (T1 echo) of k-space and are known as the displacement encoded stimulated echo in the positive gradient direction and the complex conjugate/anti echo in the negative direction. Each of these peaks contains information about the motion encoded in the tagging dimension due to them containing spatial frequencies associated with the periodic tag lines. The appearance of these k-space peaks in image space and k-space is shown in Figure 5.5 along with a profile showing the separation of these peaks.

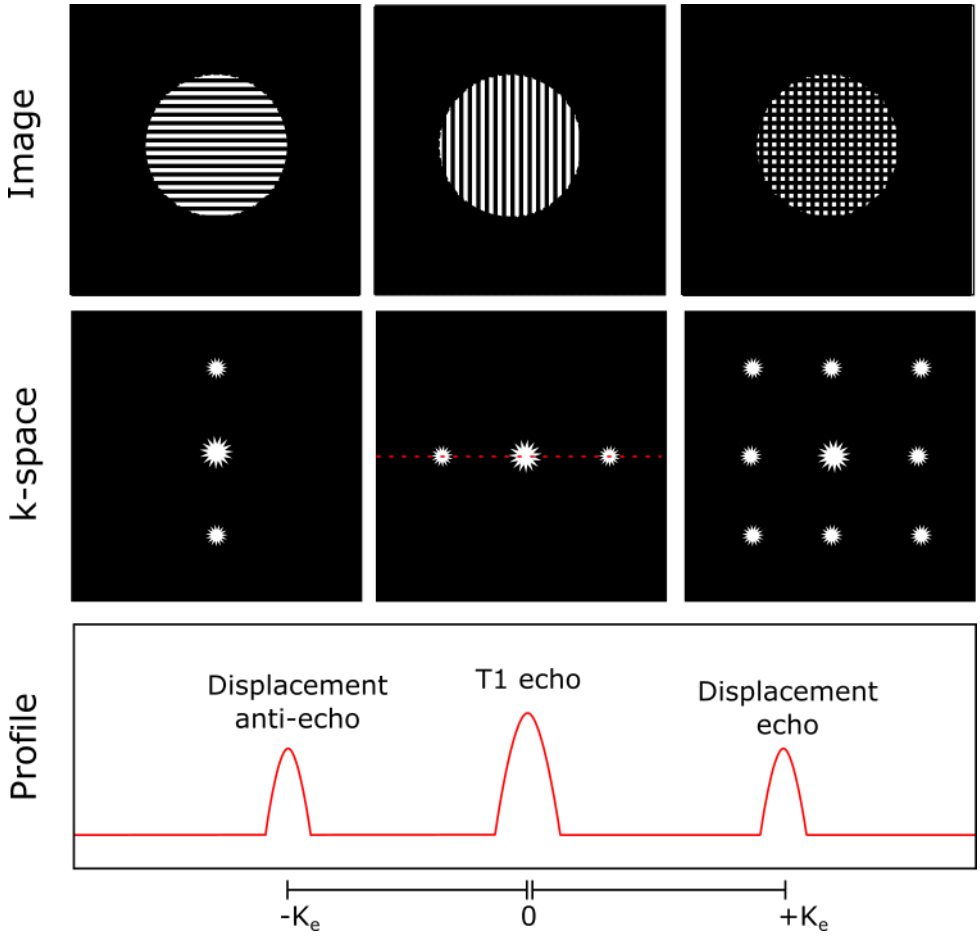

Figure 5.5 Appearance of SPAMM tagged MRI images in k-space. The displacement encoded echo and anti-echo arise from the periodic SPAMM tag lines and are offset from the T1 echo at the centre of k-space by integer multiples of the encoding frequency ±Ke.

These spectral peaks arise from the evolution of magnetisation described by Equation 5.3 following RF excitation. These displacement-encoded echoes, once isolated from the T1 echo and anti-echo, can be reconstructed using an iFFT to create a complex image where phase is linearly related to the position along the encoded dimension. The stimulated echo containing

the tagging frequencies must be filtered to isolate it from the T1 and anti-echo since these introduce additional signal contributions unrelated to displacement. HARP images are defined as the phase reconstruction images following isolation of the displacement encoded peak. Where the constraint on image phase to lie between ±π creates a densely wrapped phase image that describes pixel wise heart motion. Figure 5.6 illustrates this process for creating HARP images which contain motion encoding in the horizontal and vertical directions.

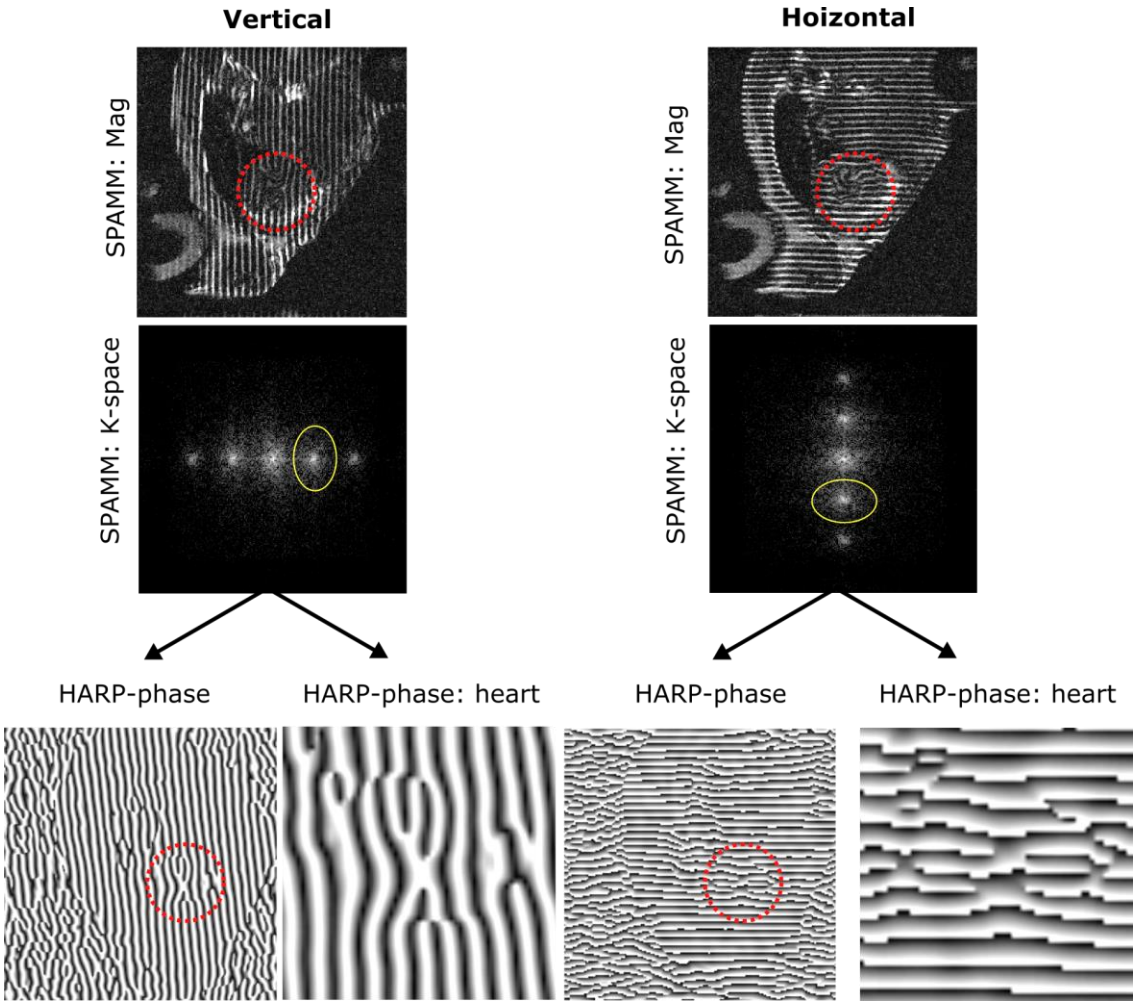

Figure 5.6 Generation of harmonic phase images. Two SPAMM acquisitions are required to describe 2D motion of the heart (red circle), one each for horizontal and vertical motion encoding. A harmonic spectral peak is isolated and undergoes an inverse Fourier transform to create HARP magnitude and phase images that contain motion information. Here only the phase images are shown since the magnitude images are typically discarded.

In simple terms these HARP images have a phase value for each pixel that is locally unique. Tracking a single phase value through consecutive image frames is done by finding the most similar value in the local region of tissue throughout an image sequence. In this way the path followed by that element of tissue can be traced through time and related to neighbouring traces to quantify myocardial function.

The following sections describe the work I have undertaken to establish SPAMM imaging with HARP processing for assessing regional function in mouse models of cardiac regeneration.

5.2 Methods

5.2.1 Methods: Motion phantom development

The development of the motion phantom was performed in two parts. The first was the design and manufacture of the physical phantom and its control system. The second part is the implementation of the same phantom simulated in Matlab that provides the ground truth for validation. First I will describe the development of the physical phantom and second I will describe the development of the simulation.

The motion phantom was designed in the Inventor computer aided design (CAD) environment (Autodesk, San Rafael, CA, U.S.A). The final CAD model design is shown in Figure 5.7. Parts were designed to be compatible with 3D printing fabrication methods allowing for fine control of dimensions and shapes during manufacture. The design features a chamber containing 3 cavities for MRI visible material of different sizes and offsets from the axis of rotation. The chamber is attached to an axial rod that extends out of the scanner bore to an external servo that provides a controllable torque. The phantom was designed to be placed in the standard mouse cradle used for in-vivo imaging with two stabilising structures either side of the agarose chamber to minimise the effect of flex in the rod and provide stability to the structure during operation.

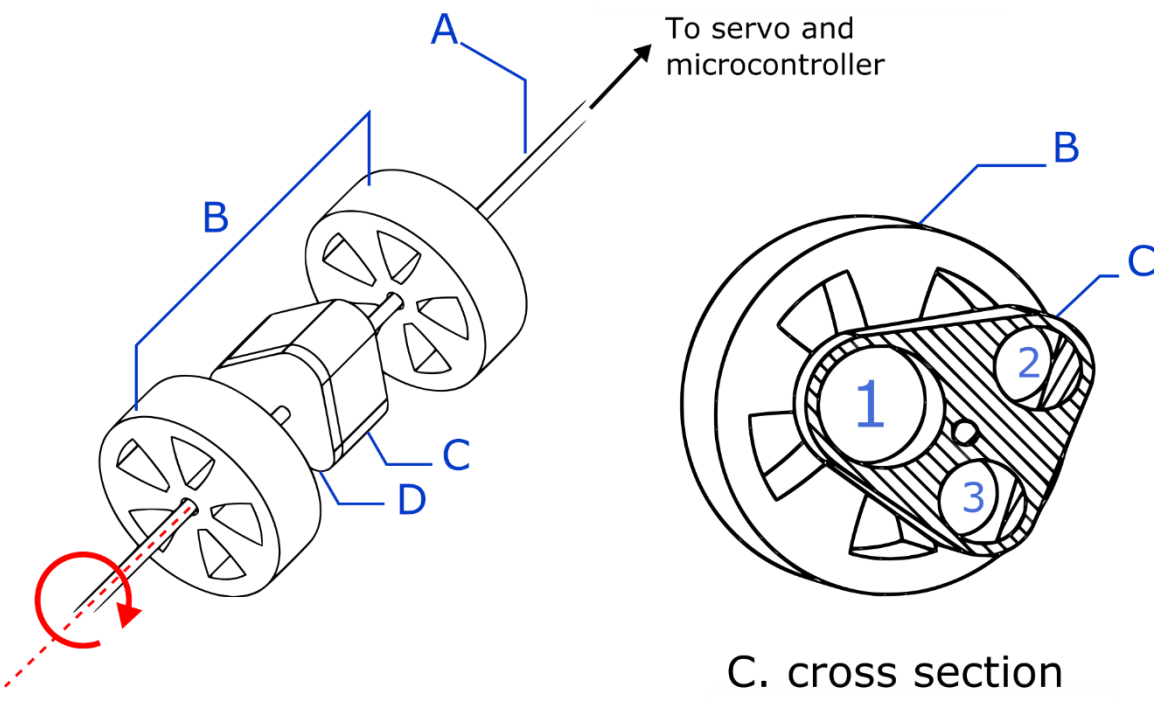

Figure 5.7. Design for motion phantom. (A) rod connected to servo (B) stationary supports (C) agarose chamber (D) chamber cap. A cross section of the agarose chamber shows 3 independent cavities for agarose ranging in size and distance from the rotation axis.

The control system for the phantom was an Arduino Uno board based on the ATmega328P microcontroller. A simple C++ program was written to produce a repetitive and controllable motion that could simulate the heart. The outline for this program is depicted in Figure 5.8. The controller initiates rotating the phantom to zero degrees of rotation a position which defined as 'diastole'. Next a transistor-transistor logic (TTL) pulse was output into the scanner gating system which was interpreted as an R-wave marking the start of contraction. The phantom then rotated in +2° increments to 10° ('systole') with a tuneable delay between each increment to modify rotation speed. Rotation was performed using a TowerPro MG995 controllable digital servomechanism (servo). Once the rotation reached +10° a delay was added to simulate end systole before the motion reversed until back at position zero. The controller emits another TTL pulse and the program looped indefinitely.

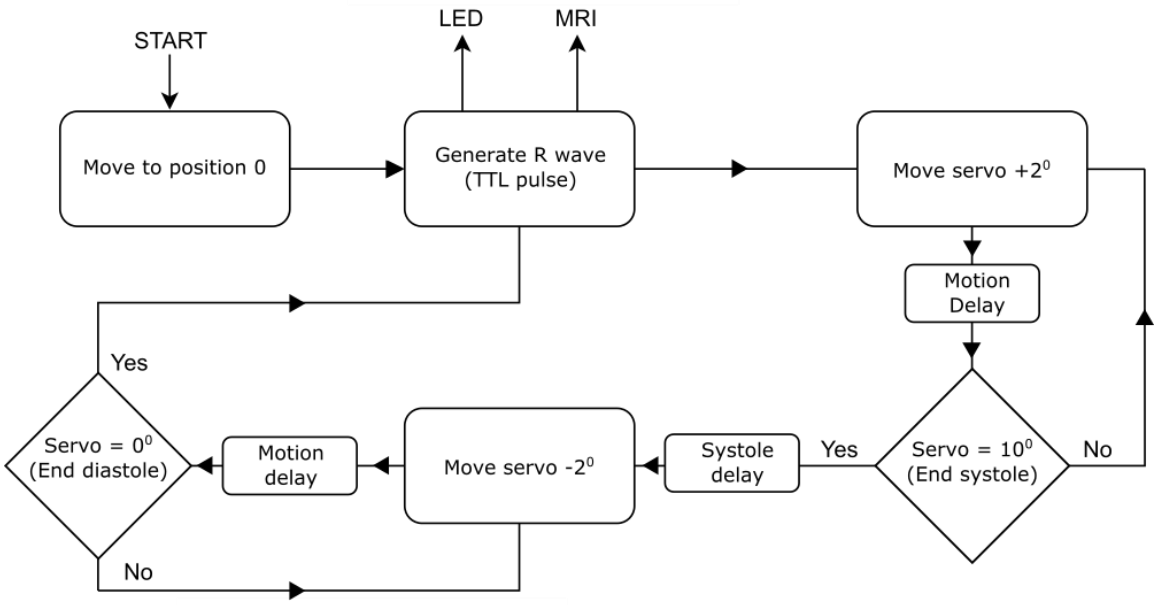

Figure 5.8 Arduino program. The motion starts by sending a TTL pulse into the MRI gating system to simulate an R wave, the servo motor then turns to 10° in 2° intervals with a tuneable delay to alter the simulated heart rate. This process then reverses until back in the original position and loops until the system is turned off.

Due to hardware limitations the highest frequency for reproducible motion was around 2.4Hz (142bpm). This was principally due to the poor performance of the servo motor. Although the servo specifications state a 3ms/° rotational velocity, when the load from the phantom is included this rate is severely reduced.

To test the phantom, the chambers were filled with 1% agarose doped with Gd-DTPA at concentrations of 23.6 and 58.5µmol/kg to match heart and liver tissue T1 respectively.[245] Since chamber 1 exhibited the widest range of motion it was chosen to contain agarose that was T1 matched to myocardium where we are most interested in measuring displacement. Chambers 2 and 3 were filled with liver T1 matched agarose. The phantom was imaged using 1000mT/m gradients and fitted inside a 39mm diameter volume resonator RF coil. A standard single slice cine sequence was performed with acquisition parameters TR=15ms; TE = 1.1ms, FA=15°; resolution=0.2×0.2×1mm. These values are typical of a mouse cine scan with an extended TR to account for the slower motion of the phantom while maintaining relative frame rates.

The second part of the motion phantom development revolved around building an accurate simulation of the phantom in Matlab. This simulation was used as a ground truth for comparing measured displacement with simulated displacement.

A synthetic model of the phantom was written in Matlab which could simulate the true displacement of the agarose in the chambers. The model inputs were image acquisition

parameters and information from the phantom control program, this includes the image acquisition matrix size, FOV, TR, cine frames, phantom rotation, motion delays and systole delays. The aim of including these input parameters was to make the simulation as versatile as possible to make it adaptable in the case of variable acquisitions. The model created a 2D grid mesh that is set to the resolution of the acquisition, it then defines the three chambers based on the CAD design files and the offset defining the centre of rotation. The three chambers are converted to a point cloud where each point defines a unique element of agarose, the dimensions of each element can be scaled by changing the resolution of the 2D mesh. The Euclidean distance separating a point in each cine frame from its position in frame 1 is then calculated and assigned this displacement. The point cloud is then converted back to an image matrix using a cubic grid interpolation method. This switching between scattered points and an image matrix allows the displacement of each pixel to take on a continuous range of values that is more representative of acquired image data. This is as opposed to defining rotation and displacement by rotating synthetic pixels where displacement can only occur in discrete intervals corresponding to the dimensions of the matrix the data is synthesised on.

In the physical phantom, the initial position included an offset in rotation and translation due to variation in how the phantom was set up on the day of scanning. To correct for this and enable direct comparison with the simulated phantom data, a registration step was included when synthesising images. The first frame of the synthesised data undergoes a rigid deformation to co-register with the first frame of the acquired data. This transformation was then applied to all subsequent image frames. This process aligns the images and by applying the same transformation to all image ensures that inaccuracies in the image acquisition are not masked by the registration step.

5.2.2 Methods: SPAMM implementation and optimisation

The vendor software on the MRI system used in this thesis does not include a SPAMM tagging sequence, opting instead to include a variation of the DANTE tagging method. The DANTE method is similar in principle to the original inefficient tagging sequence proposed by Zerhouni et al.[215] and was used in two studies later in this thesis due to the absence of a SPAMM implementation at the time (sections 7.2 and 7.3)

It was therefore necessary to create an efficient SPAMM tagging sequence, this was done by modifying the cine MRI sequence code to incorporate a SPAMM tagging module. This tagging module consists of two RF pulses separated by a modulation gradient which are followed by a

large crusher gradient in the slice select direction. The SPAMM pulse sequence is displayed in Figure 5.9. Hard shaped RF pulses were used for the tagging module high power and short duration, as this pulse shape excites a wide bandwidth of frequencies non-selectively and allows for rapid tagging to minimise tag distortion caused by movement during application.

Figure 5.9 VNMRJ pulse sequence display for SPAMM tagging cine MRI. This is the practical implementation of the pulse sequence described in Figure 5.2. Numbers describe pulse sequence feature timing (white s; yellow ms; blue µs).

The SPAMM sequence was tested on the motion phantom to evaluate sensitivity to motion. The SPAMM sequence was performed with acquisition parameters TR=15ms; TE = 1.1ms, FA=15°; resolution=0.2×0.2×1mm. The tagging module was applied with an encoding strength of $K_e = 1.1$cycles/mm created by a gradient of strength 5G/cm and a duration of 500us.

The process of optimising this sequence focussed on two properties of the tagging pattern- tag fading over the cardiac cycle and tag distortion following application. Optimising these two properties was performed by varying receiver bandwidth and tagging gradient strength in acquisitions of the motion phantom. These optimisations aimed to improve the contrast, duration and linearity of the tag lines to enable accurate quantification of displacement throughout the cardiac cycle.

Tag fading due to T1 relaxation reduces tag contrast in later cine frames limiting the information on diastolic function. Tag fading is determined by complex interactions between intravoxel dephasing, gradient readout and tagging frequency. High resolution acquisitions are less susceptible to intravoxel effects and high tag frequency but result in long acquisitions with low SNR. To characterise tag fading as a function of tagging frequency, a number of SPAMM tagging images were acquired where the duration of the wrapping gradient was kept the same but different gradient strengths were used to vary the tagging pattern frequency. This resulted in a series of identical acquisitions of the motion phantom, varying the frequency of the tagging

modulation applied as described by Equation 5.4. Four gradient strengths in total were examined at 3, 5, 7 and 9G/cm. To quantify the degree of tag fading, the mean signal intensity of the first and last images in the cine acquisition were measured in all chambers of the phantom using Equation 5.5. Where S_n represent the mean signal intensity of the line profile in frame n.

$$Tag\ fading\ [\,\%\,] = \frac{\overline{S_{last}} - \overline{S_{first}}}{\overline{S_{last}}} \times 100 \qquad \textit{Equation 5.5}$$

The second target of optimisation was the distortion of tag lines. Following an empirical observation, a shorter acquisition bandwidth was thought to reduce this distortion. The reasoning behind this was that a shorter receiver bandwidth and corresponding shorter read out gradient would sample less noise frequencies resulting in lower noise power and a less corrupted signal. Additionally, the faster readout would include less motion in the case that the phantom was moving during acquisition. To test this hypothesis acquisitions were performed while varying the spectral bandwidth of the acquisition from 50, 100, 150 and 200KHz. Other acquisition parameters remained fixed between scans with TR=15ms; TE = 1.1ms, FA=15°; resolution=0.2×0.2×1mm, $K_e = 1.1$cycles/mm created by a gradient of strength 5G/cm and a duration of 500us. Results were then analysed for distortion by drawing taking a profile across each acquisition. Image SNR was characterised as a function of bandwidth.

Tag distortion was also investigated as a function of tagging frequency. In this case the acquisitions used previously as part of the optimisation for tag fading were reanalysed. Tag distortion was therefore investigated at tagging strengths of 3, 5, 7 and 9G/cm.

5.2.3 Methods: SPAMM validation

The validation of the SPAMM sequence was performed by comparing the measured displacement from the SPAMM sequence- analysed with HARP- to the displacements produced by the phantom simulation describing the true motion.

The implementation of HARP used for this project was the HARP Matlab toolbox Version 2.1 (2013) developed by Image Analysis and Communications Lab (IACL), Johns Hopkins University.[237,246,247] The semi-automatic workflow for HARP processing using this software is outlined in Figure 5.10. The user chooses image data for each encoding direction and manually defines a bandpass filter to isolate the displacement encoded echo. The image is then passed through the user-defined filter removing all other frequency information. This filtered k-space undergoes an iFFT to reconstruct the HARP phase and magnitude images. The HARP phase

images for each direction are then passed to the point tracking algorithm where the most likely position of each point in successive frames is calculated based on distance travelled and surrounding pixels. For any element of heart tissue with a HARP phase value only one point in a later frame is the correct match. If the image sequence has an appropriately high temporal resolution relative to the heart rate and a suitable tagging frequency, then the most likely position in a later time frame for a point will be the closest point with a matching HARP value. The result of the motion tracking is a 4D numerical matrix with a size equal to $frames \times PE\ dimension \times RO\ dimension \times 2$ containing the x and y co-ordinates of each point through the image sequence. This matrix can be exported from the HARP software into the Matlab workspace for further custom analysis.

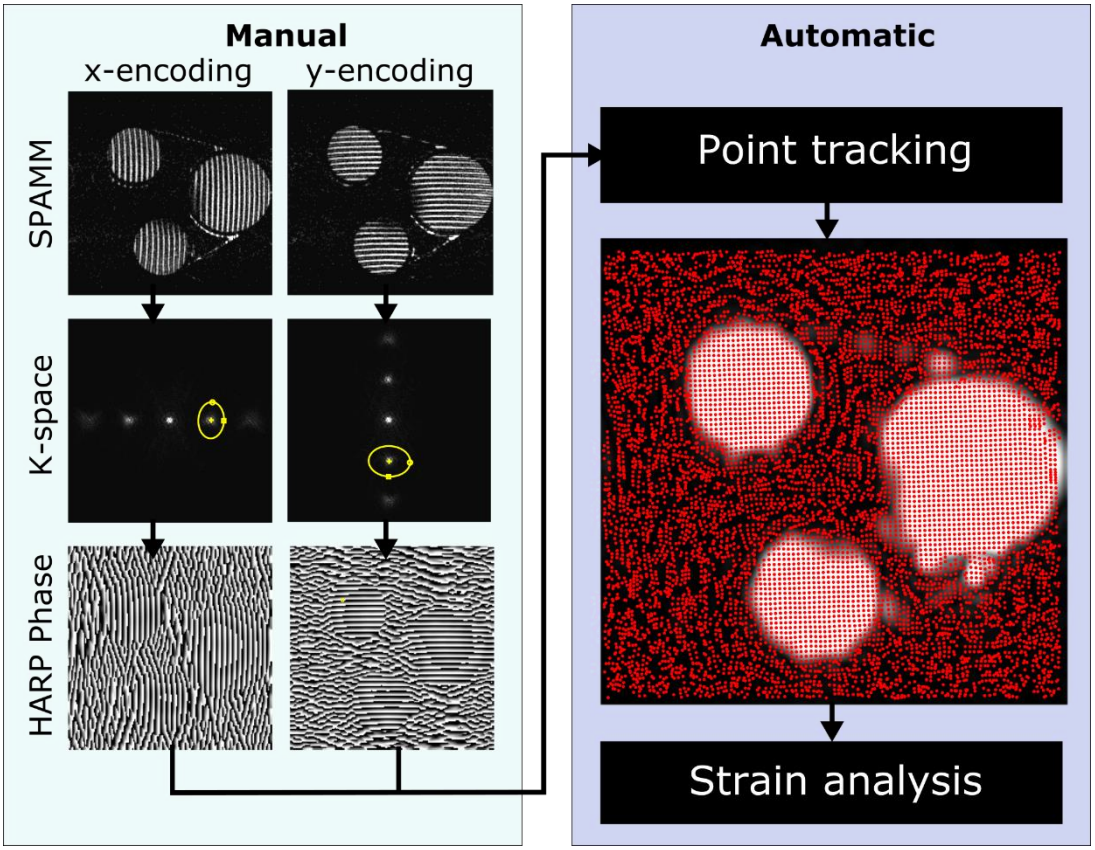

Figure 5.10 HARP software workflow. Each SPAMM encoding direction undergoes HARP processing as described in Figure 5.6. An Each point in the HARP phase images is then tracked through every image frame describing the motion of that point.

Although each tissue point has a unique phase value within its local area, due to phase wrapping the adjacent lines contain the same values meaning a large displacement can cause a tracked point to jump across adjacent phase wraps. The potential then is for this error to propagate as the mistracked point is tracked through time. This tracking error was investigated as a function

of displacement and encoding strength for validating the SPAMM acquisition over the range of motion expected in the mouse and rat heart.

SPAMM images were acquired at tagging frequencies produced by gradients of 3, 5, 7 and 9G/cm. Displacement of acquired data was calculated in the same way as with the synthesised data, defining the displacement as the Euclidean distance between a point at any time with its position in the first frame. The motion of the phantom was reproduced synthetically using the simulation described above (5.2.1) to provide the ground truth. This allowed subtraction of the two displacement maps to produce difference images that show the accuracy of the implemented SPAMM and HARP techniques for tracking motion.

5.2.4 Methods: in vivo implementation

Finally, the SPAMM sequence was tested in-vivo using the optimised acquisition protocol. SPAMM imaging was performed in a naïve wild type mouse with image acquisition parameters; TR = 5ms, TE = 1.5ms, 192×192 acquisition, with a tagging frequency of K_e = 1.4 cycles/mm corresponding to a wrapping gradient strength of 7G/cm with a duration of 0.5ms while a normal mouse heart rate ≈550bpm allowed for 20 cine frames and 10 averages within a 5 minute/direction scan.

5.3 Results

5.3.1 Results: Motion phantom development

Figure 5.11 shows the acquired cine acquisition frames of the motion phantom with the original position of the phantom in green. End systole occurs from frames 8-11 corresponding to 120-165ms after the start of systole. There is some degree of motion artefact in the phase encoding direction. These motion artefacts although visible do not seriously degrade image quality. Alternatively, these mismatches in position can be likened to the variability of the heart rate over the duration of an acquisition. The artefacts are most likely caused by the quantised nature of the servo motion. The servo incorporates an internal feedback system to ensure it reaches the position instructed by the microcontroller, a motor is turned on and off in an attempt to reach and maintain the position of the mechanism. This is the reason for including a motion delay to give the servo time to reach the desired position. Each increment of rotation therefore includes a period of motion and a stationary period in between reaching position and waiting for the next instruction. The motion artefacts in the cine image is due to acquisition occurring partially in

both of these periods depending on sequence timing. It is extremely difficult to match the sequence timing and the servo position since the servo feedback system operates independently and depends heavily on the mechanical load and position of the phantom.

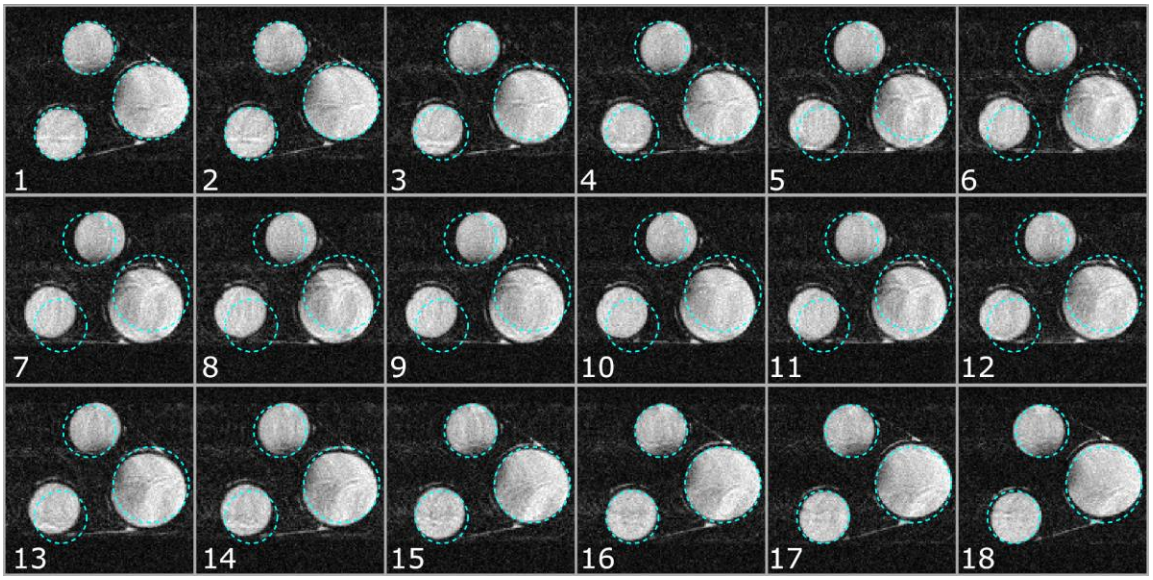

Figure 5.11 Cine MRI of motion phantom. Axis of rotation is approximately in the centre of the image with 10° of CW rotation followed by 10° CCW. Green circles represent the position of the three chambers in the first frame.

The same acquisition protocol presented in Figure 5.11 was simulated using the synthetic phantom in Matlab. This simulation is shown in Figure 5.12. The displacement of each point in the simulated data is scaled by colour for visualisation. The simulated data is comparable to the acquired cine data. The displacement is seen to be proportional to the distance from the centre of rotation as would be expected. The simulated motion described by the simulation shows a well matched motion path to the cine sequence from the physical phantom above.

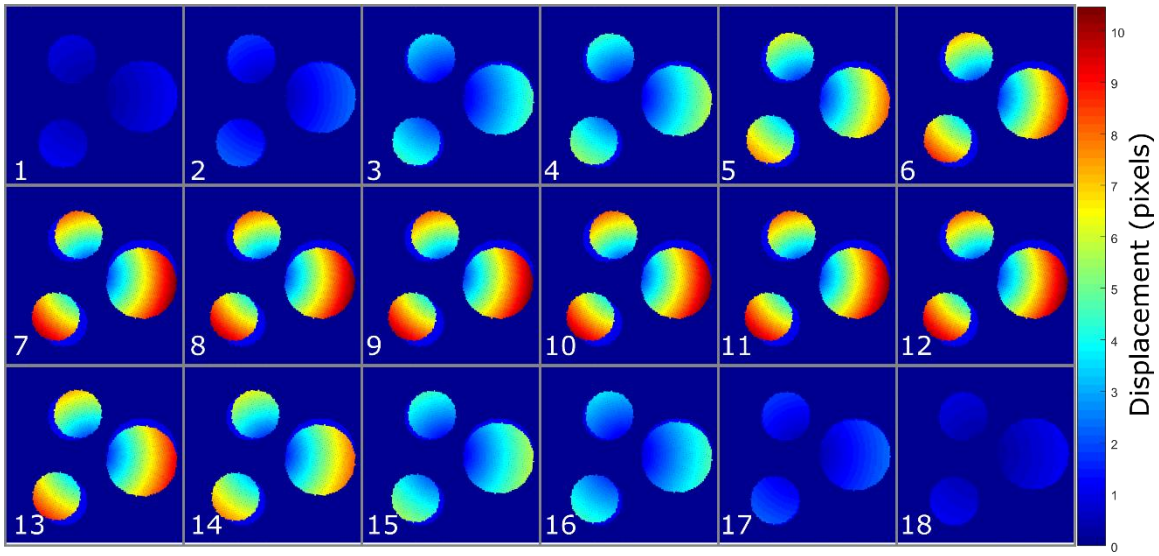

Figure 5.12 Simulation of motion phantom showing pixel-wise displacement based on image acquisition and phantom properties. Each frame shows a scatter plot with a dot representing each unique element of agarose along with a faded image of the phantom in frame 1 for reference. the colour of each point is scaled by the magnitude of its displacement from frame 1.

The range of displacements produced by the physical and simulated phantom are shown in Figure 5.13. At end systole chamber 1 is displaced by 0.64mm at the edge closest to the rotation axis and 3.67mm at the furthest edge. This covers the expected range of displacements for the contracting LV of the mouse (0 – 1.2mm) and rat (0 – 2.4 mm)[39] illustrated by the blue and green contours respectively in Figure 5.13.

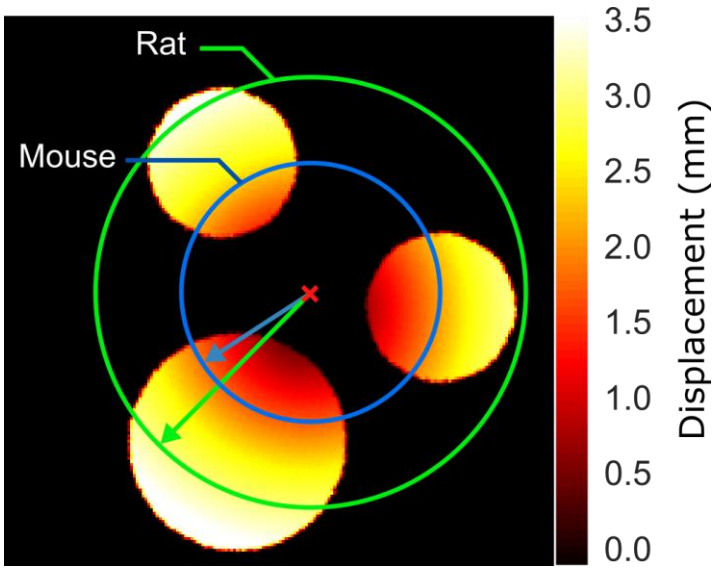

Figure 5.13 Simulated phantom displacement map at the maximum rotation overlaid with expected magnitude of motion in normal physiology for mouse and rat left ventricles during systole.

This phantom design is a good model of cardiac displacement but it is a simplification of the complex contraction of the myocardium. In the living heart the physical shape of the heart

changes during contraction, becoming shorter and thicker at systole due to the flattening of myocardial laminae. The contraction of the opposing helical myocardial fibres also induces a torsion force where the epicardium and endocardium contract in opposing helical directions, this induces a torsion (twisting) force as well as shearing forces during systole that this phantom cannot simulate. These complex motions are extremely difficult to reproduce without complex and elaborate phantom design. However, these motions play an important role in the definitions of wall thickening and fractional shortening making this phantom unsuitable for testing the cine regional morphology analysis presented in Chapter 4.

For the purpose of validating MRI measures of cardiac displacement however, these forces are not necessary, if displacement can be accurately measured using this phantom then the complex deformations in vivo can be inferred from that basic information. The following results sections describe how this motion phantom was used further for the optimisation of the SPAMM acquisition.

5.3.2 Results: SPAMM implementation and optimisation

5.3.2.1 SPAMM sequence implementation

An example SPAMM image sequence from the motion phantom is shown in Figure 5.14. Acquisition parameters were identical to the standard encoded cine sequence shown in Figure 5.11 and the original agarose chamber positions are again shown as green circles to help visualise displacement.

The acquired SPAMM images appear identical to the original cine acquisition (Figure 5.11) but with the sinusoidal modulation of signal in the vertical direction. At later frames of the imaging cycle, the modulation pattern fades according to T1 decay as described by Equation 5.3.

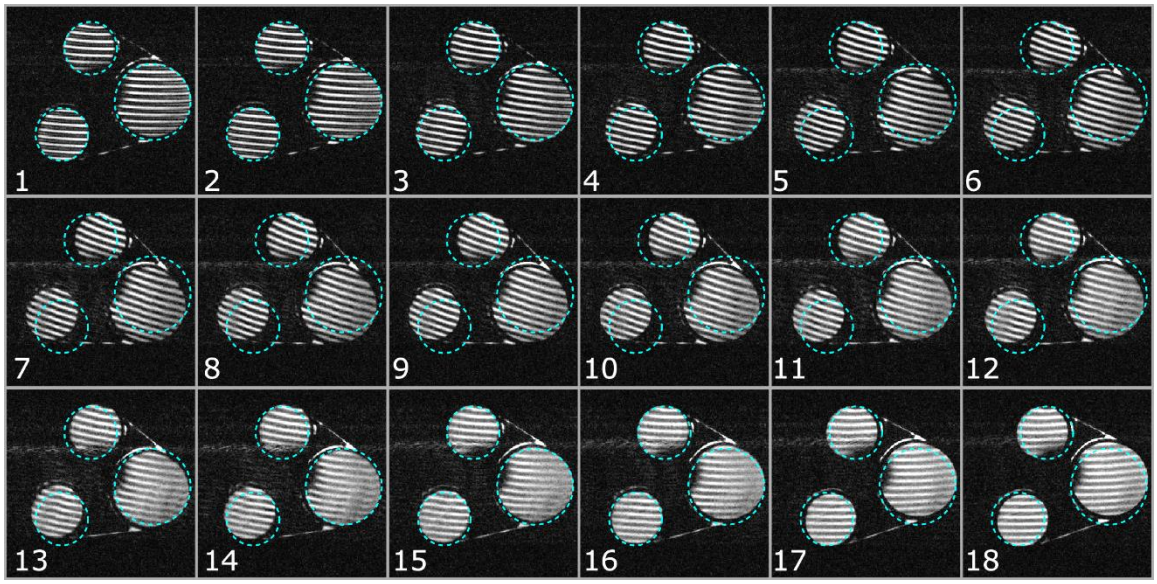

Figure 5.14 Example of acquired SPAMM tagging cine images. The motion phantom is shown using the same motion parameters as the cine sequence shown in Figure 5.11. Green circles represent the initial chamber position.

Figure 5.14 shows the first implementation of the SPAMM sequence I produced. The parameters for encoding the modulation pattern were chosen empirically. The result is that the applied tag lines exhibit some degree of unoptimised tag fading and distortion not related to deformation of the phantom. The following section describes how I optimised the acquisition and encoding parameters for imaging regional function in mice with improvements in tag fading and distortion.

5.3.2.2 SPAMM optimisation: Tag fading

The results of the acquisitions varying encoding strength to investigate the relationship between tag fading and tag frequency are shown in Figure 5.15. The variation in the tag patterns can be clearly visualised as tag lines get thinner and more tightly packed with increasing gradient strength, although tag fading appears to be accentuated at higher tag frequencies.

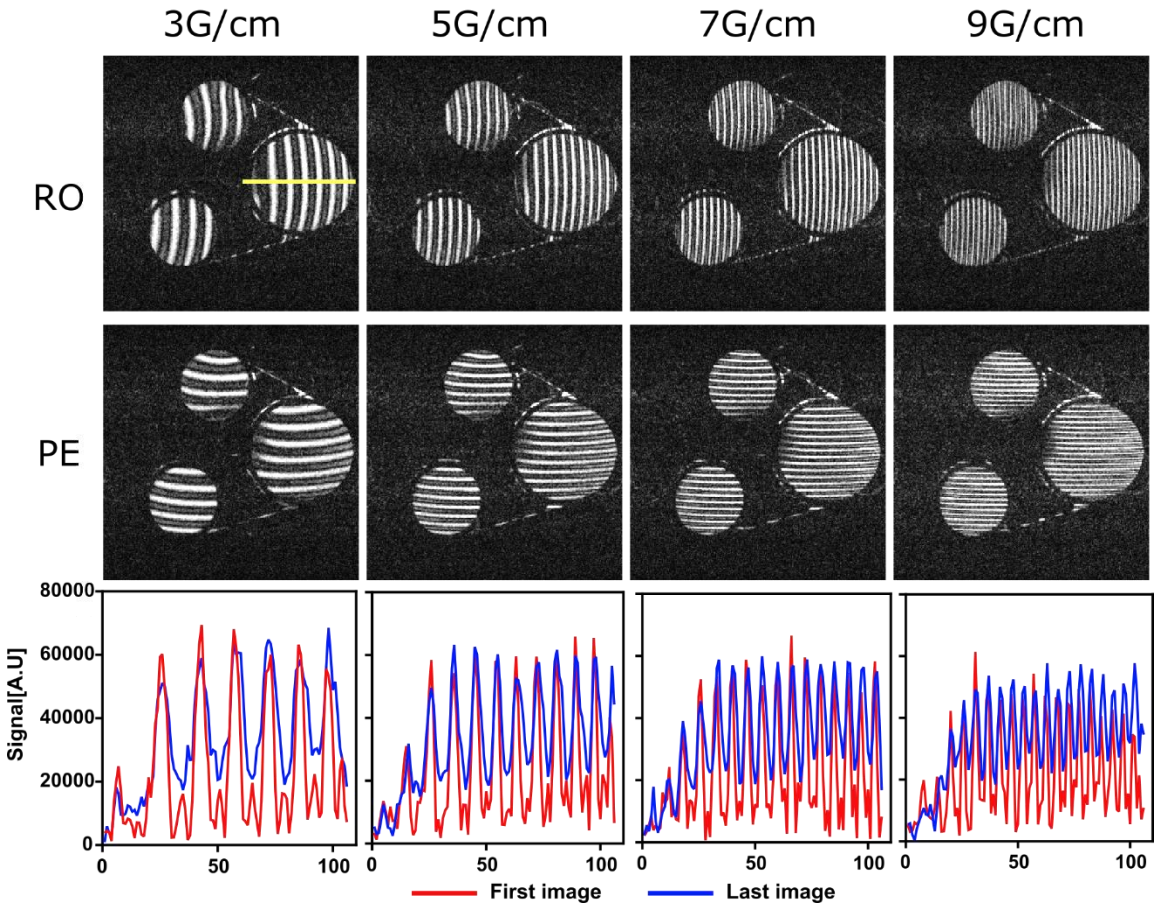

Figure 5.15 Increasing the tagging gradient strength increases tagging frequency. Encoding values shown here are G=3, 5, 7 and 9 G/cm in phase encode (PE) and readout (RO) orientations. Bottom row shows the intensity profile (yellow line, top left) for each encoding strength in the first and last image frames to illustrate the effects of tag fading with increased tag frequency.

Tag fading over the complete imaging cycle and its relationship to encoding strength is plotted in Figure 5.16. The relationship between tag fading and encoding strength is visible although there is initially increased fading at 3G/cm. When the RF flip angle (α) used to excite the tagging pattern is high, the magnetisation pattern can pass the zero line and take a negative value in the troughs. Since the scanner measures the absolute value of magnetisation this results in the small positive secondary peaks at the bottom of the troughs best seen in Figure 5.15 for 3G/cm. When these secondary peaks are wide enough relative to the spatial resolution of an image they can contribute to the mean signal and produce an artificial increase in tag fading. This relative increase in fading at at 3G/cm is likely a result of a partial sampling of the tagging pattern in this way. As tag frequency increases relative to the image resolution these small peaks are lost through partial volume effects.

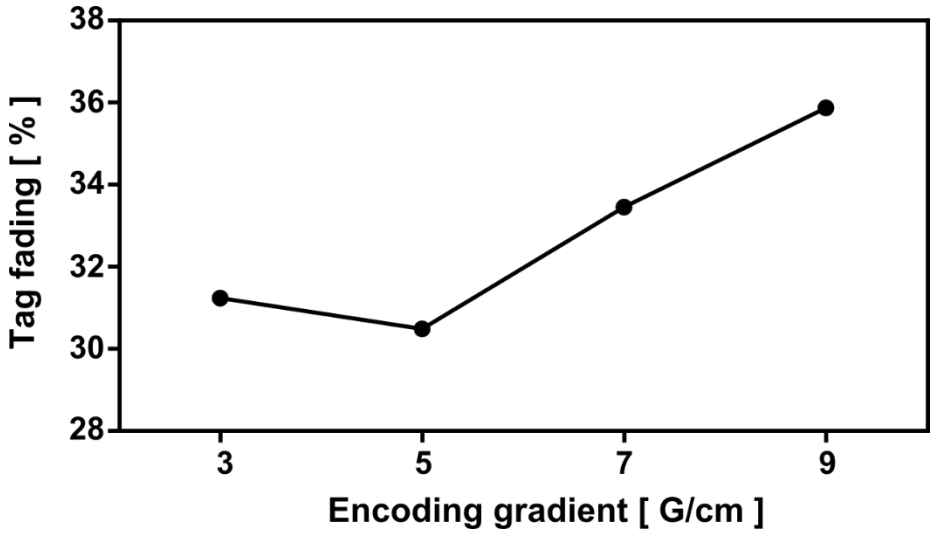

Figure 5.16 The relationship between the extent of tag fading between the first and last cine frames and SPAMM encoding gradient strength. Note the artificially increased fading at 3G/cm due to partial volume effects.

5.3.2.3 SPAMM optimisation: Tag distortion

Tag distortion was observed in the initial pilot scans for the SPAMM sequence. This distortion is not due to deformation since the phantom only exhibits rotational motion. This section describes the results of my efforts to minimise this distortion. Figure 5.17A shows the first frame of acquisitions at 5G/cm encoding with 50, 100, 150 and 200KHz receiver bandwidths. Visually tag lines appear sharper at lower bandwidths but when that is quantified by drawing a profile across a tag line (red line in Figure 5.17A insets) and plotting the pixel values (Figure 5.17B) the acquisitions show very similar curves in the tag line. There is a small reduction in tag distortion at 50KHz shown by the low signal at around position 10 (arrow) in Figure 5.17B. This improvement does not account for the larger visible distortions and so receiver bandwidth could be excluded as the primary cause of tag distortion in these images. Subsequent imaging tested distortion in terms of tag frequency.

SNR improvements with receiver bandwidth were quantified using the same data. Results are shown in Figure 5.17C. SNR improves rapidly from 200 to 100KHz with a smaller improvement at 50KHz. Following this result, the bandwidth was fixed to 50KHz for all future acquisitions.

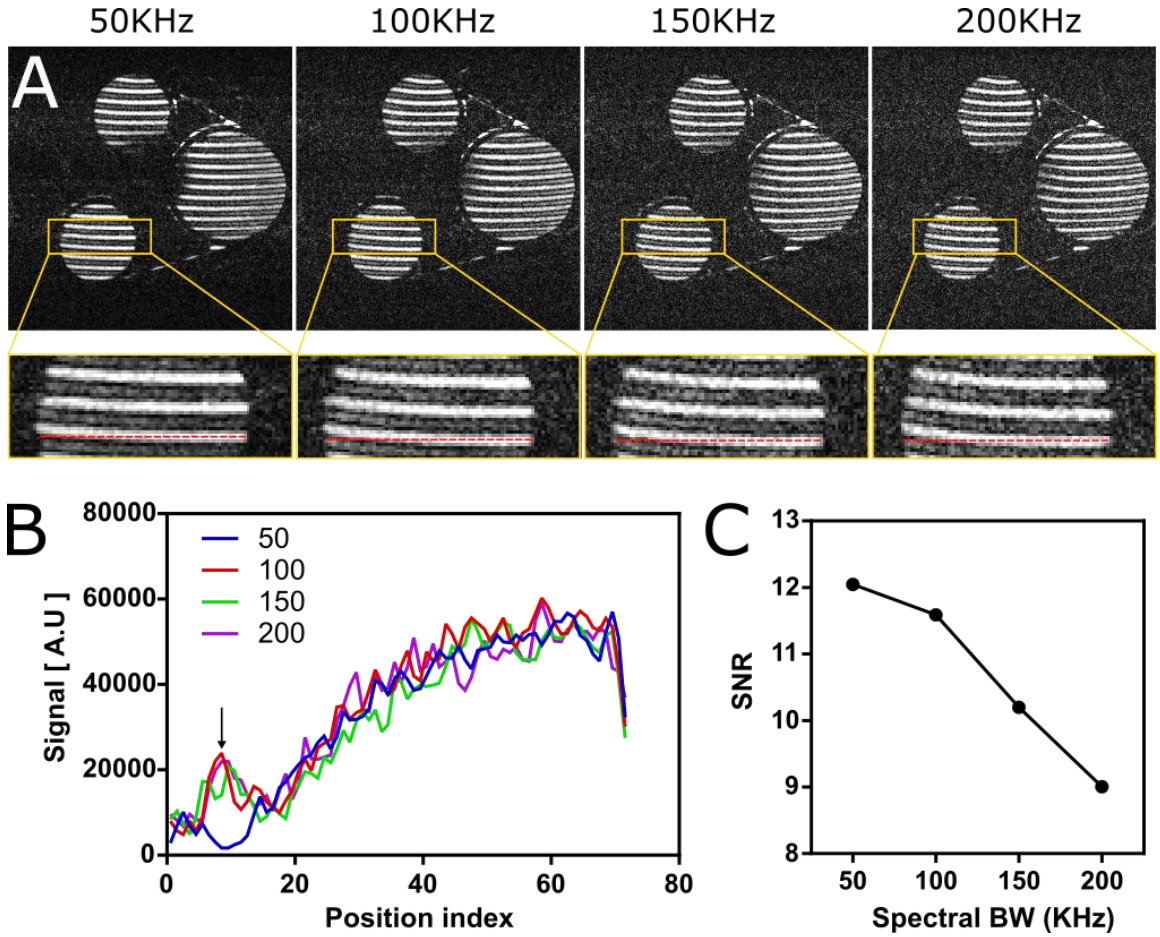

Figure 5.17 Effects of acquisition bandwidth on tag distortion and image SNR. (A) shows the first images at a number of different acquisition bandwidths. To quantify tag distortion a profile was plotted for each bandwidth (see A. insets) but showed no real change other than the inclusion of a secondary peak (arrow). Higher SNR (C) was related to lower acquisition bandwidth.

Since the presence of tag line distortion was only observed at low tagging frequencies it suggests that there may be some influence of tag separation on this artefact. To investigate this, we can observe the separation of the displacement encoded echoes in k-space. Figure 5.18 shows the central portion of k-space in the tagging direction for each gradient strength.

At low encoding strengths the displacement encoded echoes (B/B') appear close to the central T1 echo (A). This figure shows additional echoes at harmonic frequencies (C/C'). The appearance of these echoes in k-space are related to the secondary peaks we see in image space. Where B/B' represent the main tagging pattern, C/C' are created from the secondary peaks and contribute to the primary modulation pattern by superimposing a pattern with the same phase and double the frequency of the intended modulation. The superposition of the stimulated echoes with the T1 echo without sufficient spatial resolution to resolve them independently is likely the cause of the tag distortion seen in image space. As the gradient strength is increased

these peaks move further away from the central echo allowing the information in each echo to be resolved at this acquisition resolution.

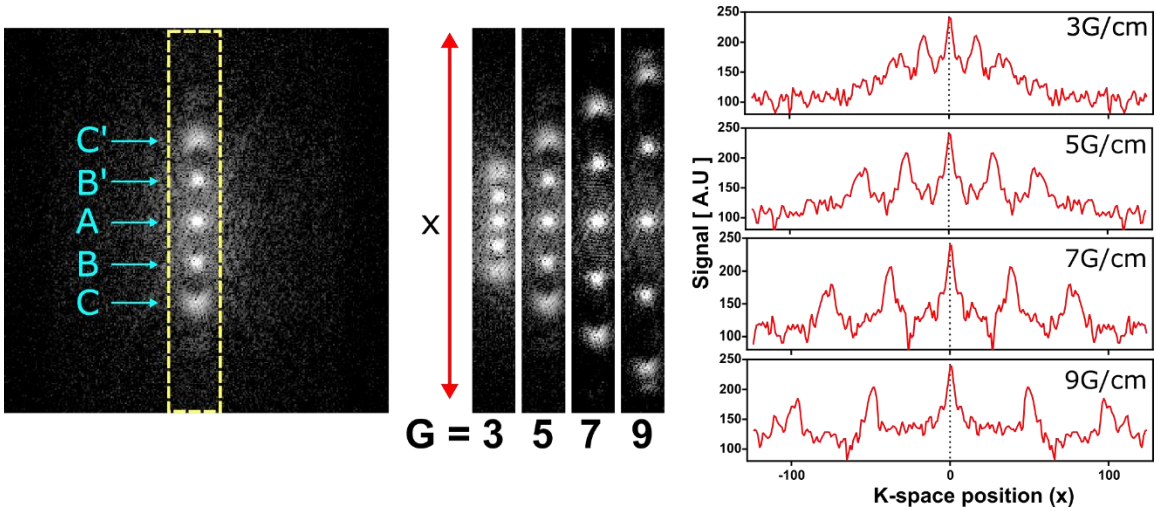

Figure 5.18 Magnitude k-space profiles for the variable tagging frequency acquisitions shown in Figure 5.15. The tagging information is encoded in peaks offset from the centre of k-space by a distance specified by encoding strength. Low frequency tag lines near the centre of k-space become distorted due to superposition of displacement encoded echoes with the central T1 peak.

5.3.3 Results: SPAMM Validation

Displacement maps for the measured and simulated motion phantom are shown in Figure 5.19B. Here the top row shows the simulated displacement map (ground truth), the second row shows the measured displacement and the third row shows the subtraction of these two maps. In these difference images a low value (dark) shows good agreement with the synthetic data while a high value (bright) shows poorly tracked regions with a high mismatch. The first frame of each image sequence is uniform.

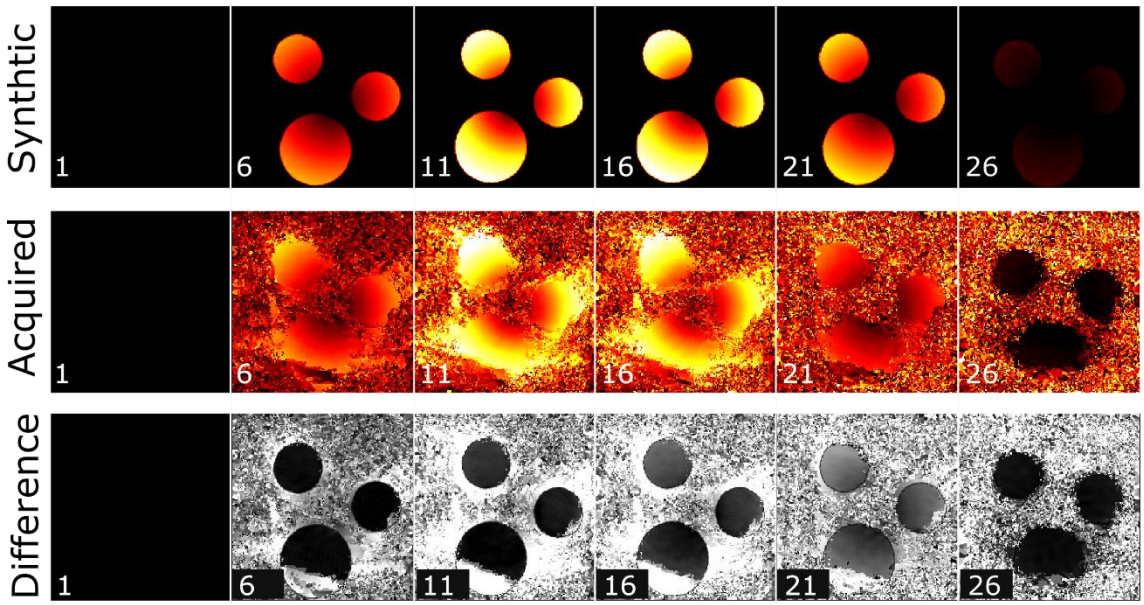

Figure 5.19 Quantifying displacement from HARP output data. The acquired displacement data can be compared to the synthetic data generated from knowledge of the phantom motion to create a difference image showing the error in measurement.

The example data shown in Figure 5.19 shows displacement errors when measuring the large motion at the edge of chamber 1. This is most easily seen in the difference images in Figure 5.19 as the bright region furthest from the centre of rotation. The onset of this error is rapid as tracking errors propagate and occurs at displacements >2.5mm. This example data was acquired using a gradient encoding strength of 7G/cm and it is likely that the tagging frequency is too high to measure large displacements. A high tagging frequency produces a dense pattern of phase wrapping in HARP phase images, if the displacement between image frames is large relative to the tagging frequency then a tracked point in these phase images may skip into an adjacent wrapped line.

The displacement maps from the data shown in Figure 5.18 for end systole are shown in Figure 5.20A. As encoding strength increases the threshold at which measurement errors occur can be seen to move radially inwards towards the centre of rotation beginning at 7G/cm. To investigate this in more detail a profile was plotted from the centre of rotation across chamber 1 for each encoding strength and the synthetic data (coloured lines in Figure 5.20A). The displacement values along these profiles are plotted against the synthetic data (black lines) in Figure 5.20B. These graphs are a clear illustration of the rapid deterioration of tracking accuracy above certain displacements. At 3-5G/cm the tracking is accurate across the range of displacements present in the phantom motion, however for encoding strengths of ≥7G/cm there is a threshold of displacement above which accuracy is severely impaired. This threshold is lower at 9G/cm relative to 7G/cm showing a dependence on tagging frequency.

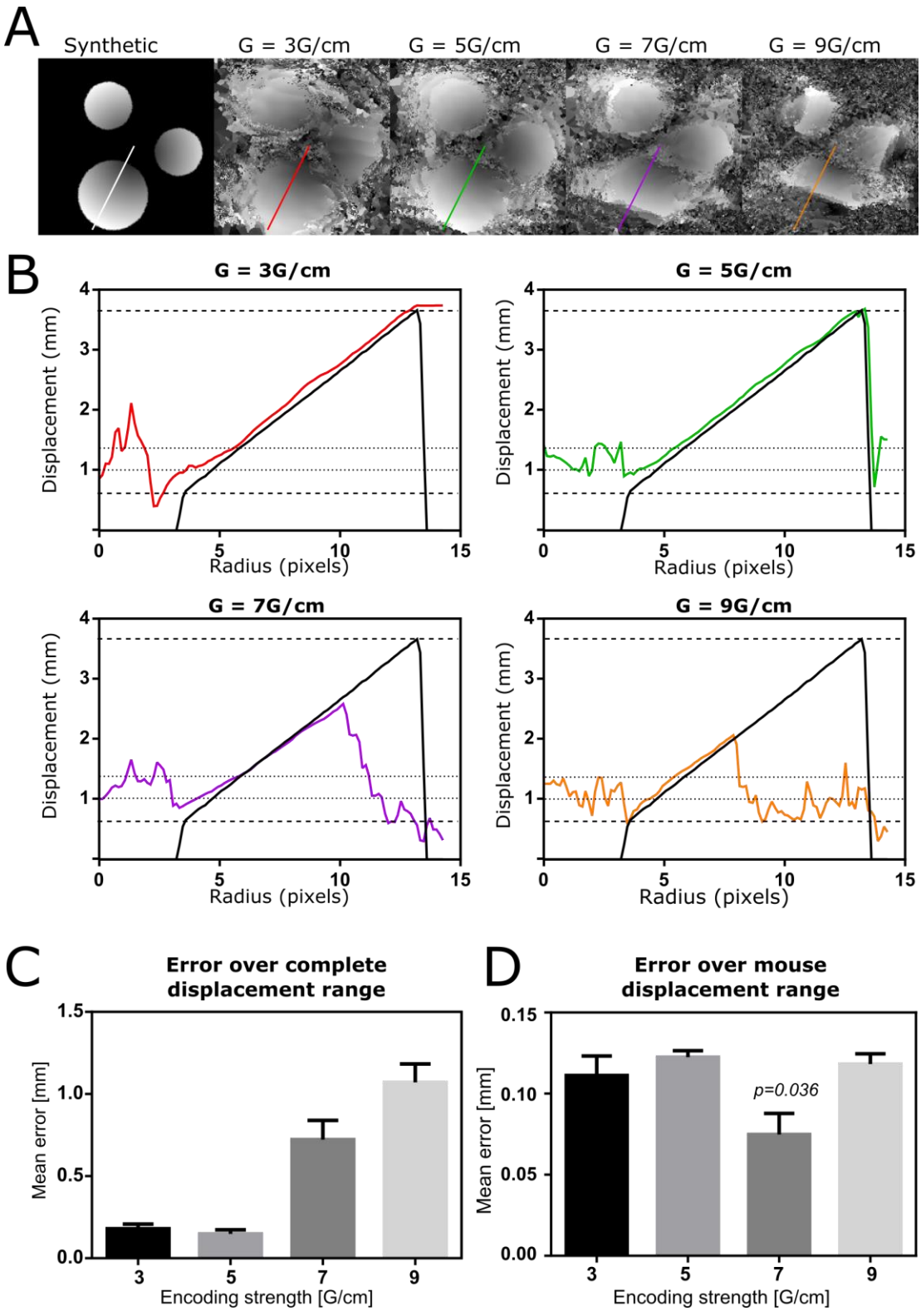

Figure 5.20 Displacement errors with encoding strength. (A) displacement images at phantom systole an overlay showing the line profile used to plot the displacement errors (B). Dashed lines show the total range of motion in the phantom, dotted lines show the expected displacement range for the mouse LV. Taking the mean error over these ranges allow the accuracy of each encoding strength to be quantified (C-D).

Figure 5.20C-D shows the mean difference between measured and synthesised displacements across the profiles to give a single value quantifying the quality of the displacement measurements for each encoding strength. If the complete range of displacements across chamber 1 are considered (dashed lines Figure 5.20B) then tagging with an encoding strength of 5G/cm produces the most accurate map of displacement with encoding at ≥7G/cm producing significantly less accurate results. However, the range of displacements produced by this phantom far exceed the expected motion of the mouse heart (see Figure 5.13). If we consider only the measurements over the expected range of displacements for the contracting mouse heart (dotted lines Figure 5.20B) then 7G/cm becomes significantly more accurate (P=0.036; one way ANOVA) than the other gradient strengths. This increased accuracy at small displacements at higher encoding strengths is the inverse effect of the cause of inaccuracies at high displacements. Higher tagging frequencies provide a higher concentration of phase wraps in HARP images, at small displacements this can provide higher resolution displacement information.

5.3.4 In vivo implementation

Figure 5.21 shows the in vivo implementation from the final optimised SPAMM tagging protocol. Tag distortion was minimal in these images thanks to a relative high encoding strength of 7G/cm. This produced a tagging frequency of $K_e = 1.4$cycles/mm that resulting in tag fading of approximately 33% as determined above. This value was slightly less in vivo however due to the more rapid heart rate of the mouse compared to the phantom motion.

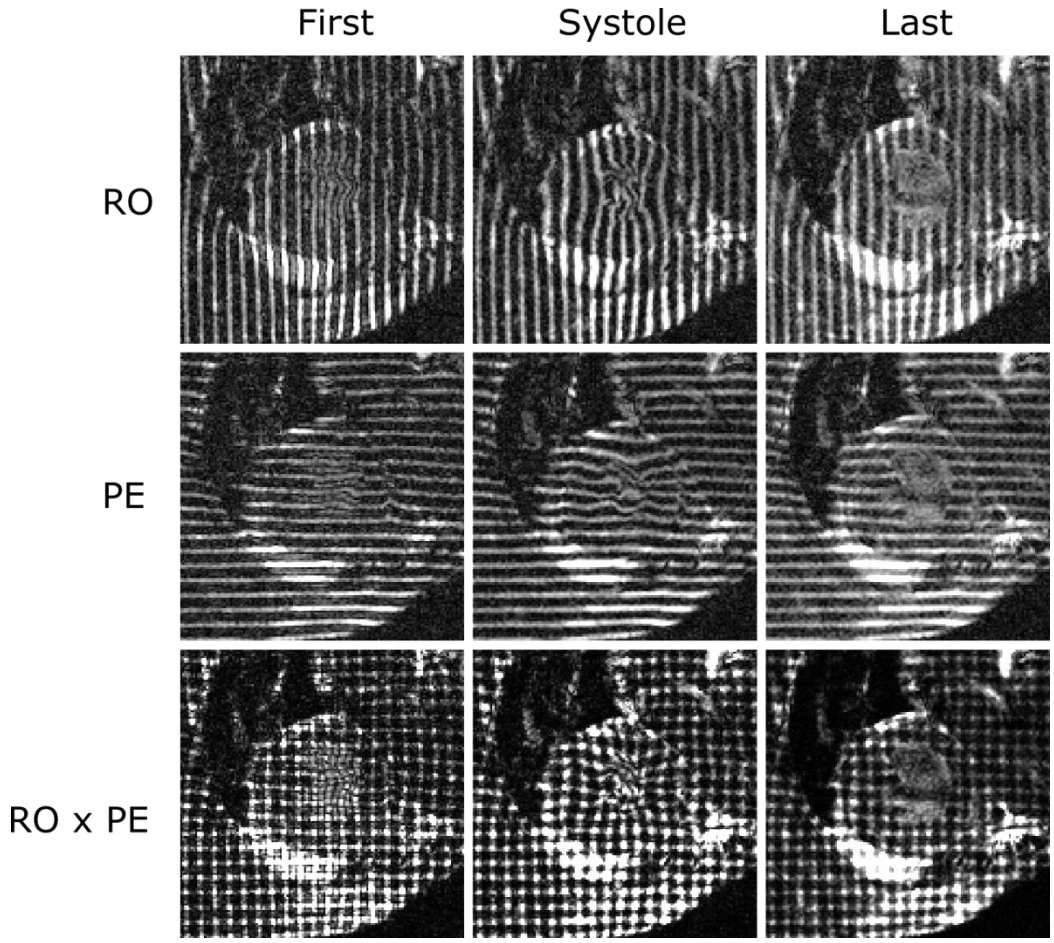

Figure 5.21 In-vivo SPAMM tagging test showing the first, end-systolic and last cine images for tagging in the readout and phase encoding direction. Also shown is the product of the RO and PE images to produce an artificial 2D tagging grid pattern.

5.4 Discussion

This chapter described the implementation and optimisation of a SPAMM cardiac cine sequence with HARP processing using a custom motion phantom. An in-vivo assessment of this technique is included in chapter 7 as part of a comparison of SPAMM and DENSE for regional function assessment in myocardial infarction following regenerative therapy.

Development of the motion phantom was important for validation of the tagging technique. A reproducible and programmable motion allowed the measurements of displacements by HARP to be compared to true displacement (Figure 5.20) determined by simulations. The contraction cycle of the mouse heart in vivo occurs around 550Hz and due to mechanical limitations of the motor controlling motion, this rapid motion could not be reproduced. The 2.4Hz that could be reproducibly achieved using available hardware is significantly slower. Although the speed of motion was limited, the displacement of the phantom was within the expected range for both

mouse and rat hearts ensuring the phantom work was a useful exercise for validation and optimising tagging properties for maximising sensitivity and image quality to this range of motion. The duration of acquisitions was, however, significantly longer using the motion phantom than in vivo imaging since each cine dataset has duration proportional to the contraction cycle duration (RR interval).

The result of the phantom optimisation was a tagging module consisting of two 90° RF pulses separated by a tagging gradient with a duration of 0.5ms and strength of 7G/cm. Inputting these values into Equation 5.1 returns an encoding strength of $K_e = 1.49$ cycles/mm.

Optimisation of SPAMM cine imaging for minimising tag fading over a contraction cycle showed that higher tagging frequencies suffer greater contrast loss compared to lower frequencies. Tag fading of 30 – 36% was observed for the phantom over a single contraction cycle lasting 410ms which is 4x longer than the mouse heart cycle. For in vivo imaging the shorter contraction cycle should result in less tag fading. However, despite matching the T1 of the agarose phantom to cardiac tissue, the relatively uniform magnetic homogeneity of the agarose makes it a non-ideal model of heart tissue. The SPAMM tagging module stores the magnetisation pattern in the T1 decay where tag fading is dependent only on the T1 of tissue as described by Equation 5.3. During cine acquisition however this magnetisation is restored to the transverse plane for gradient readout allowing T2/T2* decay to attenuate the magnetisation pattern. The effect of magnetic field inhomogeneity in the heart due to factors such as the lung/tissue boundary, motion and flow is therefore likely to cause more rapid tag fading in vivo compared to in the phantom.

Overall there was good agreement of displacement measured by HARP with true phantom motion over the range of displacements that could be accurately measured for each encoding strength (Figure 5.20D). Over the entire range of displacements performed by the phantom an encoding gradient of 5G/cm ($K_e = 1.06$cycles/mm) performed best, however, when considering only the expected range of displacements for the mouse heart, an encoding strength of 7G/cm was found to be more accurate.

An interesting idea for continuation of this work would be to produce a T1 map from SPAMM tagged images. T1 mapping and tagging are two time consuming sequences that are typically considered too long for practical use in clinical MRI. The ability to extract two useful parameters from a single acquisition may aid in the uptake of regional function assessment in the clinic. Since the tag fading (see Figure 5.15 and Figure 5.16) occurs due to the recovery of the longitudinal magnetisation it has dependence on T1 as described by Equation 5.3. However, with

tagging there are stripes in the image that do not fade since they are already fully relaxed, these are the dark bands in the tagged image. To sample T1 relaxation in these lines, a complementary SPAMM acquisition with a 90° phase offset in the modulation pattern would be required. The acquisitions can be combined for an efficient CSPAMM acquisition to reduce tag fading (complementary acquisition are discussed further in Chapter 6). To account for the motion of an element of tissue the motion path of a pixel can be traced using HARP to correct for cardiac motion during T1 relaxation. This T1 mapping concept is an exciting idea with great potential for research and clinical imaging and remains an objective for further work.

SPAMM and HARP are effective for measuring regional function in the heart but MRI sequences based on tagging such as this are inherently limited in the spatial resolution of the displacements they can resolve. This limited resolution can become a problem in studies of biomaterials where high resolution information is required. The resolution of SPAMM and HARP based techniques are limited by the tagging frequency and the k-space HARP filter. These two factors are interconnected since a higher tagging frequency will allow a wider k-space filter that will pass high frequency displacement components. Regional information is also limited by fact that the myocardial signal is intentionally suppressed to produce the saturated tag pattern. Although these resolution limits are not significant when investigating broad regional function- for example, a comparison of contraction in the anterior/septal regions- it can be a limiting factor when investigating transmural function. In cardiac tissue engineering for regenerative therapy the engraftment location of the biomaterial may have a significant effect on its efficacy and compatibility with the existing myocardium. SPAMM and HARP are limited in their ability to identify the transmural strain and an alternative technique with improved spatial resolution is required to quantify intramyocardial function in response to a therapeutic material. For this reason, the Displacement encoding using stimulated echoes (DENSE) sequence was developed in parallel with SPAMM and HARP.

5.5 Summary

This chapter described the internal development, optimisation and validation of a cine Spatial Modulation of Magnetisation (SPAMM) tagging sequence with Harmonic Phase (HARP) processing. A motion phantom was designed, manufactured and simulated in Matlab. This was used to optimise the SNR and tag fading of the sequence and validate the SPAMM sequence and HARP processing over the range of mouse and rat myocardial displacements. The result is an

optimised SPAMM sequence and processing system that is able to accurately track regional myocardial displacement.

Chapter 6 Development of Displacement ENcoding using Stimulated Echoes (DENSE) MRI

6.1 Introduction and theory

6.1.1 Study overview

This chapter describes the development of a displacement encoding using stimulated echoes (DENSE) MRI sequence for preclinical assessment of regional function. DENSE is a phase based imaging technique that can provide higher resolution displacement information than SPAMM or HARP, which may provide useful biomarkers for the efficacy and safety of cardiac regeneration therapies in transmural myocardium, such as intramyocardial injections. This chapter introduces the theory underlying DENSE and describes the experimental optimisation of a DENSE sequence, including cine DENSE imaging, phase correction, artefact suppression and fitting trajectories for improved strain analysis. The aims of this chapter can be summarised in 4 objectives.

1. Develop and optimise preclinical cine DENSE sequence
2. Apply novel method for background field removal for accelerating acquisition
3. Investigate approaches to removing artefacts echoes and determine which method is optimal for preclinical imaging.
4. Implement motion trajectory fitting and strain calculations for displacement analysis

The workflow to meet these aims is shown in Figure 6.1 and describes the outline of how the work is presented in this chapter. The chapter can be roughly split into 4 parts where each aims to develop or optimise a specific component of the DENSE acquisition and post processing pipeline. Part 1 aims to implement the DENSE sequence- first as a single phase sequence as originally described by Aletras et al.[248] before expanding it with a cine imaging capability. Part 2 aims to test a new method for phase correction in DENSE data using projection onto dipole fields. Part 3 investigates advanced methods for isolating the displacement encoded echo without k-space filtering. Finally, part 4 aims to calculate strain from the displacement field images as well as assess an optional processing step where myocardial trajectories are fitted to displacement data to produce more physiologically accurate motion.

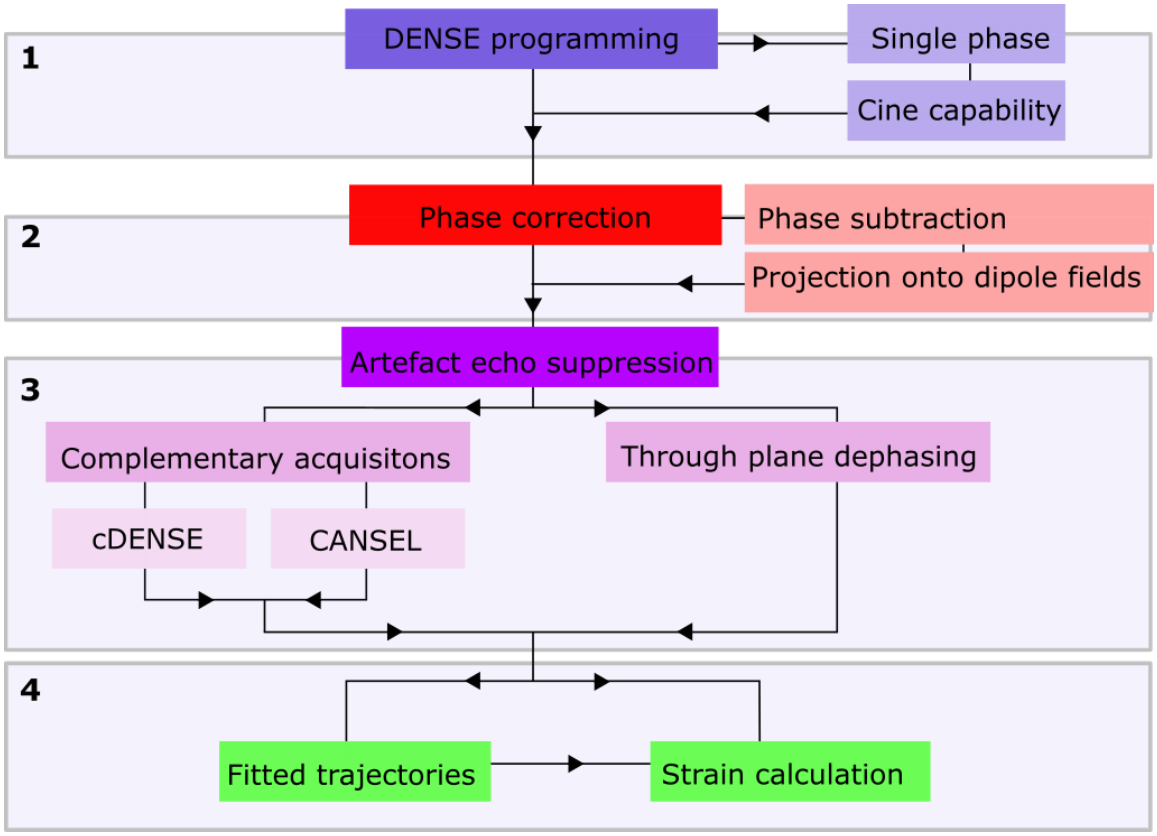

Figure 6.1 Study design for the work described in this chapter with the aim of producing a regional strain map from DENSE data. Each stage of this development process is separated by a box and a colour with the lines describing the processing steps necessary to produce the strain map. 0

6.1.2 DENSE sequence

DENSE MRI developed in parallel with HARP and the two techniques share many similarities and can be described as two approaches to phase based regional displacement tracking[249]. Both are imaging techniques for assessing regional myocardial displacement mapping based on spatial modulation of the MRI signal and are able to produce displacement maps of cardiac tissue. They differ in that DENSE has been developed as a stimulated echo acquisition scheme that aims to isolate the displacement encoded echo at the centre of k-space while HARP and SPAMM are based on filtering acquired data to perform analysis.

DENSE was introduced in 1999 by Aletras et al.[248] The original DENSE sequence was not cine-capable and imaged the displacement of the heart tissue at end systole only. This original DENSE pulse sequence is shown in Figure 6.2A. The sequence consists of 3 stages modulation, mixing and demodulation which combine to encode and decode the MRI signal with information about cardiac motion.

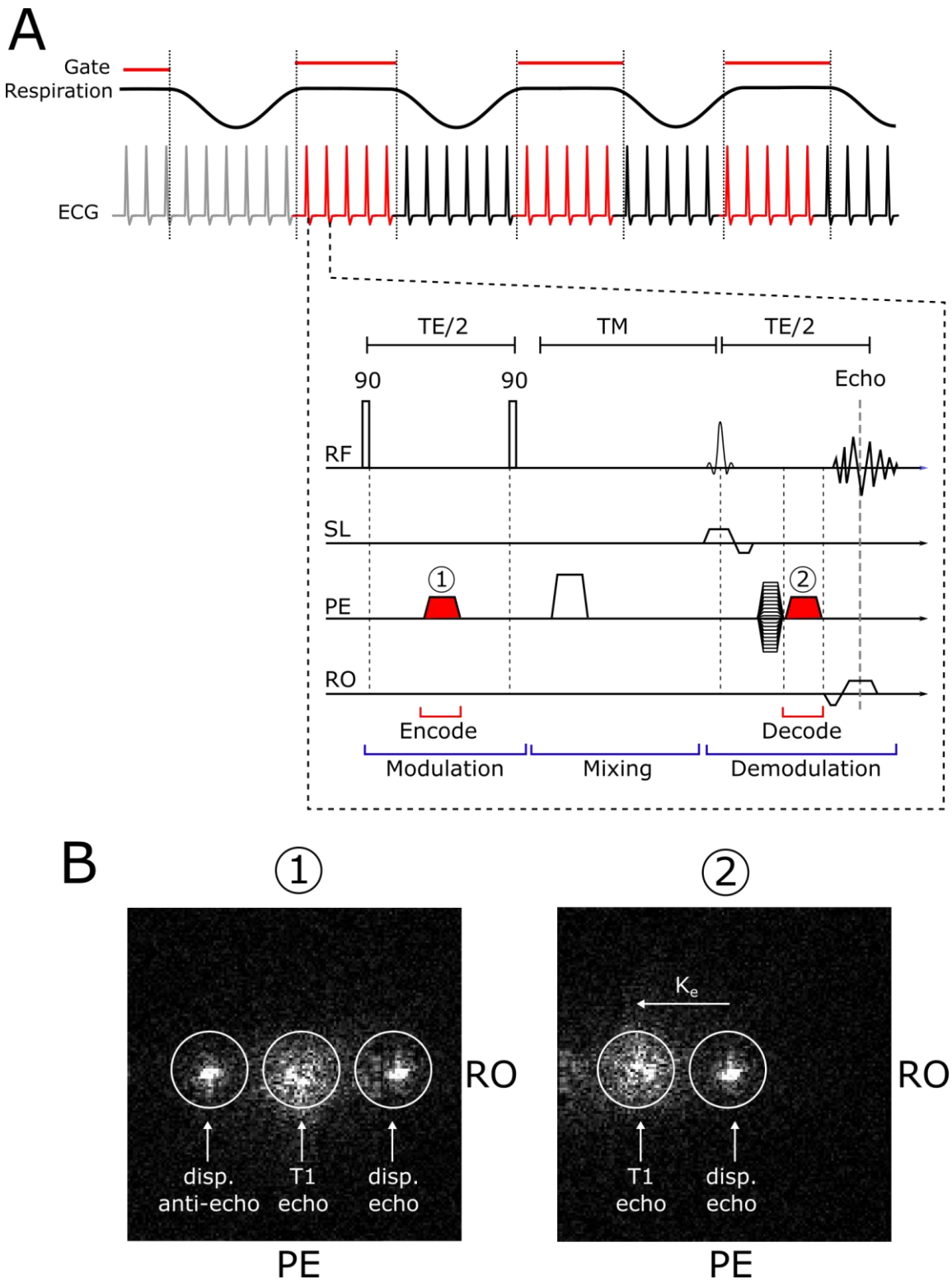

Figure 6.2 DENSE acquisition scheme (A) the pulse sequence acquires with ECG and respiration gating. The modulation stage is applied at end diastole and the echo is formed at end systole. The appearance of DENSE in k-space (B) is identical to SPAMM at the modulation stage (B1), the second demodulation gradient however shifts the final acquisition so that the displacement encoded echo forms at the centre of k-space (B2).

The modulation stage is applied immediately following detection of an R-wave trigger and is identical to a SPAMM tagging module. The magnetisation is modulated in the same way as with SPAMM (see chapter 5). This modulation produces a tagged k-space image as seen in Figure 6.2B2 with a T1 relaxation echo and a displacement encoded echo and anti-echo. Following the modulation period, the tissue acquires a phase value that is sinusoidally modulated by its position along the encoding direction. This is followed by the mixing period during which motion occurs while the magnetisation is stored in the longitudinal direction. The duration of the mixing period is designated TM. When imaging a single cardiac phase this value is typically set to the finish at end systole to capture the largest component of motion. The demodulation phase is a combined motion decoding and the image acquisition sequence. Following the selective RF excitation that tips the stored magnetisation into the transverse plane for imaging, a demodulation gradient is applied with the same gradient area as the SPAMM wrapping gradient. The effect of this demodulation gradient is to rewind phase in tissue in which no motion has occurred over the mixing time since it experiences an identical encoding and decoding gradient. In tissue that has moved during the mixing time the tissue accumulates a phase change that is proportional to the magnitude of displacement along the encoding gradient direction. To describe this mathematically a spin that has moved by a distance Δx between the application of the encoding and decoding gradients will accumulate a phase φ described by Equation 6.1.

$$\varphi = \Delta x \left[\gamma_H \int G_{enc}(t)\, dt\right] \qquad \text{Equation 6.1}$$

In k-space the demodulating gradient translates the displacement encoded echo to the centre of k-space (see Figure 6.2B.1). Depending on the tagging frequency controlled by the encoding gradient area it is possible to shift the T1 echo and complex conjugate outside of the acquisition window. The goal of shifting k-space in this fashion is to produce an acquisition in which the displacement echo is sampled without corruption from the other echoes. By centring the displacement echo at the k-space origin and removing extraneous echoes DENSE is able to produce high spatial resolution maps of displacement since there is no need to filter the encoded echo and discard corrupted k-space as is the case with SPAMM.

DENSE requires 3 acquisitions to describe 2D motion in the heart. One acquisition to image x-axis displacement one for y-axis displacement and a third identical acquisition with a different encoding strength to remove sources of background phase. The background phase image provides a reference for the encoded images. By subtracting the reference image from the

directionally encoded images the result is a phase image showing only the phase change induced by motion occurring the mixing time.

Image processing in DENSE is straightforward in comparison to HARP since tracking individual points through time is not necessary to measure displacement because pixel phase values are directly related to their displacement in DENSE. Depending on the value of K_e however it can be necessary to perform phase unwrapping if the displacement of the tissue meets the phase wrap condition (Equation 6.2).

$$\Delta x \geq {}^{1}/_{K_e} \qquad \text{Equation 6.2}$$

This condition describes the case where if the displacement Δx is large enough or the encoding strength high enough for a tissue region to accumulate a phase change $> 2\pi$ then phase wrapping will occur and require correction. In HARP the phase wrapping provides image features which aid the tracking of tissue motion however in DENSE this wrapping introduces severe errors in displacement due to sudden changes in phase values. The result of DENSE imaging are maps of the displacement of heart tissue for each encoded direction such as those shown in Figure 6.3. Plotting the values of these maps as x and y-components of a vector produces a 2D displacement field map. From this displacement field the strain tensor can be calculated based on the deformation of a uniform square grid by the measured displacement.

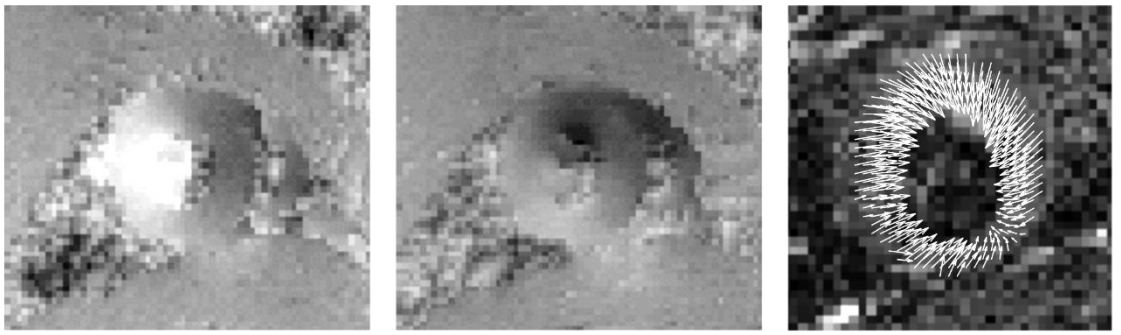

Figure 6.3 Example DENSE data encoded in 2 directions to produce a typical displacement field visualised using a small vector in each pixel defined by the x and y displacements.

6.1.3 DENSE artefact echoes

To enable extraction of useful uncorrupted displacement information from these DENSE acquisitions it is necessary to filter out or suppress the T1 relaxation echo and the complex conjugate of the displacement encoded echo. The simplest method for removing these

unwanted echoes is using a bandpass filter centred on the displacement encoded echo and zeroing all frequencies outside this band. However, this has the effect of removing high frequency spatial information removing fine detail in images and limiting the resolution of displacement maps. It is therefore desirable to supress these echoes rather remove those frequencies completely.

Before describing the different methods for supressing these echoes it is first necessary to describe how the artifactual echoes are generated during DENSE acquisition. The DENSE sequence begins with the detection of an R-wave and the application of a SPAMM tagging module that modulates the signal by a cosine function and stores it in the longitudinal magnetisation M_z as described in Equation 5.2. The modulation stored M_z then undergoes T1 relaxation according to Equation 5.3. M_z is sampled after a time t by the application of an RF excitation pulse with flip angle α that tips M_z into the transverse (xy) plane. Including this excitation and rearranging Equation 5.3 with the exponential form of cosine results in a function with 3 terms, one for each of the 3 echoes in DENSE acquisitions (Equation 6.3).[250]

$$M_{xy}(x,t) = \frac{M}{2} sin(\alpha)\, e^{-t/T1} e^{ik_e x} + \frac{M}{2} sin(\alpha)\, e^{-t/T1} e^{-ik_e x} + M_0\, sin(\alpha)\left(1 - e^{-t/T1}\right) \qquad \text{Equation 6.3}$$

The final component of each term containing the x value describes the position of the signal peak in k-space for encoding in the x direction. The first term has phase $K_e x$, the second term has phase $-K_e x$ and the third has 0 phase. These correspond to the displacement encoded echo, the complex conjugate echo and the T1 relaxation echo respectively. This describes the magnetisation state following the SPAMM module prior to the application of a DENSE unencoding gradient and is equivalent to the magnetisation in a SPAMM acquisition. The T1 echo is therefore at the k-space origin with the displacement encoded echoes at $\pm K_e$. If a DENSE demodulation gradient equal to the encoding gradient is applied immediately following RF excitation and before readout with a tissue displacement Δx between them the magnetisation takes the form described by Equation 6.4.

$$M_{xy}(x,t) = \frac{M}{2} sin(\alpha)\, e^{-t/T1} e^{-ik_e \Delta x} + \frac{M}{2} sin(\alpha)\, e^{-t/T1} e^{-ik_e \Delta x} e^{-i2k_e x} + M_0\, sin(\alpha) \left(1 - e^{-t/T1}\right) e^{-ik_e \Delta x} e^{-ik_e x} \quad \text{Equation 6.4}$$

It can be seen that the terms describing the position of the signal peaks in the x direction are shifted by the second gradient. The first term describing the displacement encoded echo now has no x component positioning it at the k-space origin. The second term describing the complex conjugate echo has shifted to $-2K_e x$ and the T1 echo now appears at $-K_e x$.

A simple method to isolate the acquisition to the displacement encoded echo without filtering is to increase encoding strength K_e until the artefact echoes are outside acquisition window, i.e. increase K_e to the point where K_e is higher than the range of sampled frequencies and all echoes are generated outside of the FOV or sample lower frequencies only. Removing echoes through this method is a compromise and results in either a loss of spatial resolution as less frequencies are sampled or a decrease in SNR due to intravoxel dephasing when K_e is large.

Three advanced methods for removing these artefact echoes are investigated in this chapter based on complementary acquisitions (cDENSE and CANSEL) and through plane dephasing. The Theory underpinning these echo suppression techniques will be described below.

6.1.3.1 Complementary acquisitions

There are two complementary acquisition schemes that have been applied to DENSE, the first is complementary DENSE (cDENSE) and the second is cosine and sine modulation to eliminate (CANSEL) artefact generating echoes. Complementary acquisitions were first proposed in the context of SPAMM tagging with complementary SPAMM (CSPAMM). A standard SPAMM tagging pulse as used in Chapter 5 and for all implementations of DENSE so far uses two 90° RF pulses for tipping the magnetisation vector. This results in a cosine modulated magnetisation as described by Equation 5.2. A complementary image is an identical acquisition where the second RF pulse is given a phase offset to shift the modulation pattern by nπ/2. Figure 6.4 illustrates the effect of changing the second RF pulse phase has on the resulting magnetisation pattern. The phase of the second RF pulse (RF2) changes the transverse orientation of the net magnetisation vector to produce a phase offset in the pattern of modulation across the tagging direction (in this example the x direction).

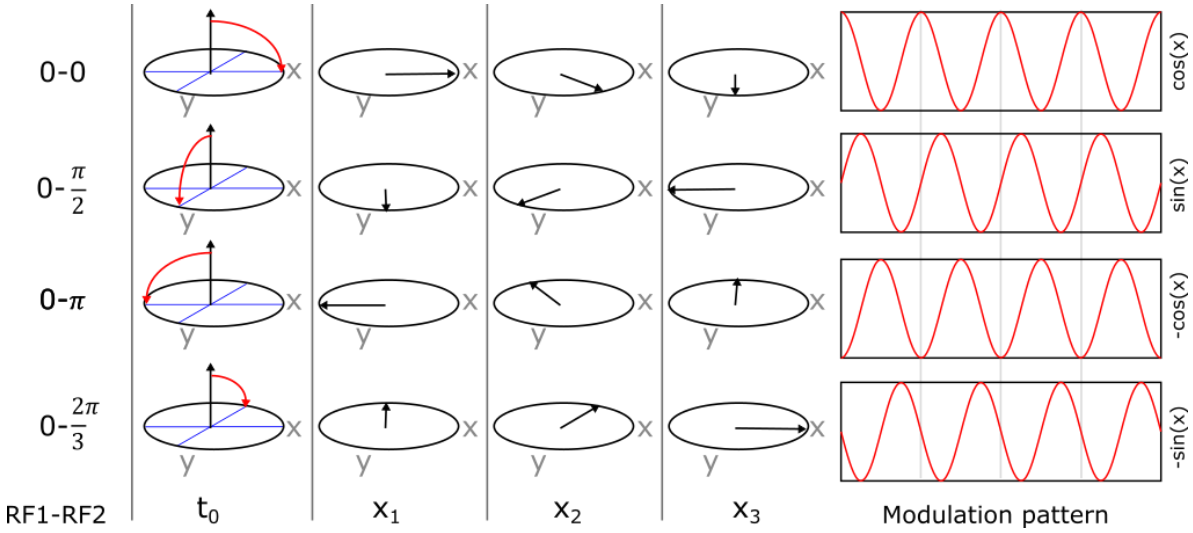

Figure 6.4 Effect of changing the phase of the second RF pulse on precessing spins for CANSEL and cDENSE. Changing the position of the magnetisation vector in the transverse xy plane creates π/2 phase shifts in the resulting SPAMM pattern.

In cDENSE the complementary image is acquired with the second RF pulse given a π phase offset resulting in a negative cosine modulation pattern. Subtraction of these images in k-space supresses the T1 relaxation echo leaving only the displacement encoded echo and the complex conjugate echo. The result of this is reduced tag fading due to the removal of the a large T1 relaxation component in the MRI signal, this subtraction process is described graphically in Figure 6.5.

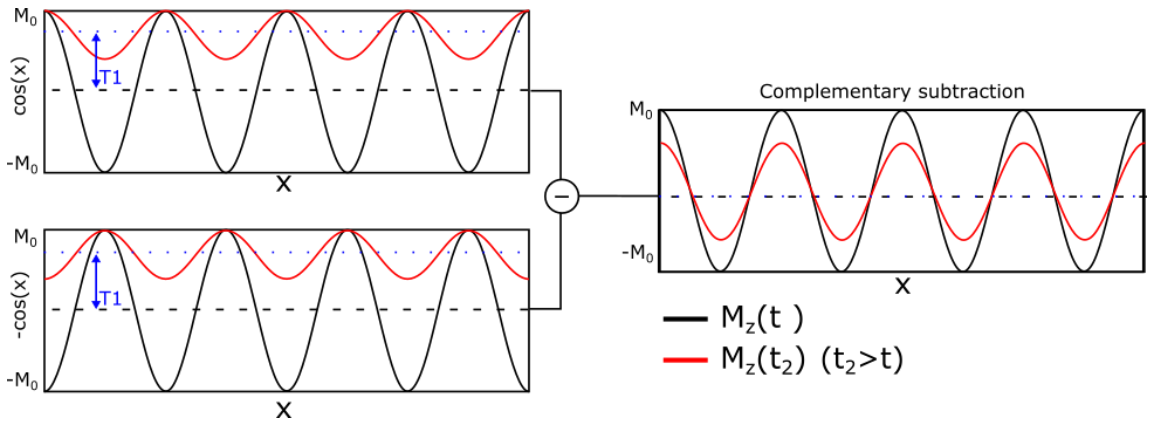

Figure 6.5 Illustration describing the effect of the complementary subtraction method on cosine modulated magnetisation in the x direction. The result is the removal of the 'DC' T1 offset decay term, reducing tag fading and providing more displacement information at later stages of the cardiac cycle.

Mathematically this subtraction process can be described as follows. If we rearrange Equation 6.4 to separate the common $sin(\alpha)$ terms we have Equation 6.5 and Equation 6.6 describing the first DENSE image and the complementary image respectively.

$$M_{xy}^{cos}(x,t) = \left[\frac{M}{2}e^{-t/T1}e^{-ik_e\Delta x} + \frac{M}{2}e^{-t/T1}e^{-ik_e\Delta x}e^{-i2k_e x} + M_0\left(1-e^{-t/T1}\right)e^{-ik_e\Delta x}e^{-ik_e x}\right]sin(\alpha) \quad \text{Equation 6.5}$$

$$M_{xy}^{-cos}(x,t) = \left[-\frac{M}{2}e^{-t/T1}e^{-ik_e\Delta x} - \frac{M}{2}e^{-t/T1}e^{-ik_e\Delta x}e^{-i2k_e x} + M_0\left(1-e^{-t/T1}\right)e^{-ik_e\Delta x}e^{-ik_e x}\right]sin(\alpha) \quad \text{Equation 6.6}$$

Subtraction of Equation 6.6 from Equation 6.5 results in the complementary image with the T1 echo at $-K_e$ offset from the k-space origin subtracted and an image that can be described by Equation 6.7.

$$M_{xy}^{subcos}(x,t) = \left[Me^{-t/T1}e^{-ik_e\Delta x} + Me^{-t/T1}e^{-ik_e\Delta x}e^{-i2k_e x}\right]sin(\alpha) \quad \text{Equation 6.7}$$

Here we have isolated the displacement encoded echo and the complex conjugate echo. If K_e is set such that $2K_e$ is greater than the range of sampled frequencies the second term inside the brackets is removed since the complex conjugate echo is outside of the acquisition window. The subtraction image then contains the desired uncorrupted displacement information. An additional advantage of this technique is that the addition of two datasets with independent noise terms yields an image with an SNR improvement of approximately 40%.[214]

The cDENSE technique is able to accurately supress the T1 echo so long as heart rate remains consistent and the two complementary images contain the same information. If K_e is not set high enough to isolate the displacement encoded echo then the complex conjugate echo can remain and corrupt motion information.

The CANSEL technique was developed to remove all artifactual echoes from DENSE images including the complex conjugate echo and can be thought of as an extension to cDENSE. CANSEL is another complementary acquisition scheme but relies on 4 acquisitions with positive and negative sine and cosine modulation patterns. In cDENSE there are two complementary acquisitions with cosine and –cosine modulation. In DENSE the second RF pulse of the SPAMM module is given a phase offset of 0, $\pi/2$, π, $2\pi/3$ relative to the first RF pulse producing

complementary cosine, sine, -cosine and –sine modulation respectively. The subtraction process to create the cDENSE image described by Equation 6.7 is repeated for the sine and –sine images. The sine and –sine images are identical to the functions described by Equation 6.5 and Equation 6.6 but including a π phase shift that is accounted for by multiplying these functions by the complex number i (Equation 6.8 - Equation 6.10).

$$M_{xy}^{sin}(x,t) = i\left[\frac{M}{2}e^{-t/T1}e^{-ik_e\Delta x} - \frac{M}{2}e^{-t/T1}e^{-ik_e\Delta x}e^{-i2k_e x} + M_0\left(1-e^{-t/T1}\right)e^{-ik_e\Delta x}e^{-ik_e x}\right]sin(\alpha) \quad \text{Equation 6.8}$$

$$M_{xy}^{-sin}(x,t) = i\left[-\frac{M}{2}e^{-t/T1}e^{-ik_e\Delta x} + \frac{M}{2}e^{-t/T1}e^{-ik_e\Delta x}e^{-i2k_e x} + M_0\left(1-e^{-t/T1}\right)e^{-ik_e\Delta x}e^{-ik_e x}\right]sin(\alpha) \quad \text{Equation 6.9}$$

$$M_{xy}^{subsin}(x,t) = i\left[Me^{-t/T1}e^{-ik_e\Delta x} - Me^{-t/T1}e^{-ik_e\Delta x}e^{-i2k_e x}\right]sin(\alpha) \quad \text{Equation 6.10}$$

Finally to remove the complex conjugate echo from the image the sine and cosine subtractions are subtracted from each with the phase offset in the sine acquisition corrected by multiplying by a factor of i according to Equation 6.11. The result of this subtraction is an isolated displacement encoded signal centred at the k-space origin described by Equation 6.12. Note that the displacement signal term is 4× greater than a single modulation image.

$$M_{xy}^{CANSL}(x,t) = M_{xy}^{subcos}(x,t) - i\,M_{xy}^{subsin}(x,t) \quad \text{Equation 6.11}$$

$$M_{xy}^{CANSEL}(x,t) = \left[2Me^{-t/T1}e^{-ik_e\Delta x}\right]sin(\alpha) \quad \text{Equation 6.12}$$

The primary advantage of using these complementary acquisitions is that it allows images to be acquired with lower encoding frequencies. When relying on k-space filtering as described previously to separate the displacement encoded echo there is a significant loss of spatial resolution due to the removal of high spatial frequencies. Using the cDENSE acquisition allows

the k-space filter to be placed at a greater radius from the displacement echo since the T1 echo is removed. In cDENSE the filter removes only the complex conjugate echoes in cases where the choice of encoding strength causes these echoes to lie within the acquisition window. In CANSEL there is no need to perform k-space filtering since all artifactual echoes are suppressed before reconstruction. Figure 6.6 illustrates this process at a low encoding frequency, $K_e = 0.5$ cycles/mm. In this example the acquisitions are from a stationary agarose phantom, the reduction in resolution due to k-space filtering is clearly visible in image space. Lower encoding strength are associated with improved SNR and greater sensitivity to large displacements.

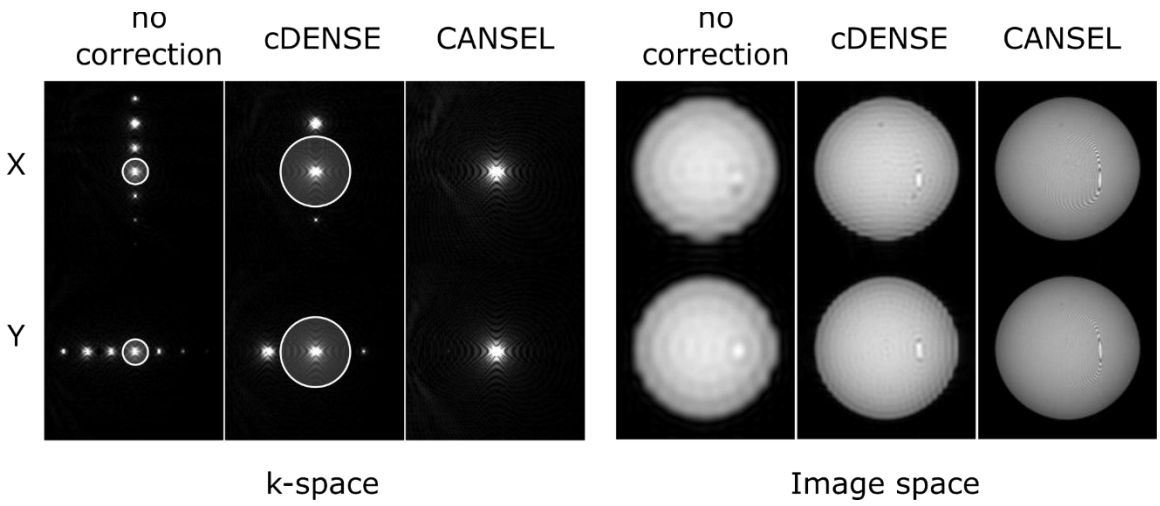

Figure 6.6 Illustrating spatial resolution improvements with complementary acquisitions at low encoding frequencies ($K_e = 0.5$ cycles/mm). The detrimental effect of k-space filtering on spatial resolution is visible in uncorrected and cDENSE images. Since CANSEL requires no filtering it offers the highest resolution displacement images at these encoding frequencies.

6.1.3.2 Through plane dephasing

TPD was developed by Zhong et al. (2006) and aimed to produce an echo suppression technique without dependence on time or displacement encoding frequency or requiring additional acquisitions.[251] TPD applies additional encoding gradients in the through plane direction in concurrence with the in plane encoding gradients. The primary mechanism of echo suppression in this case is the selective dephasing of echoes not centred at the k-space origin.

The application of TPD gradients with an encoding frequency of K_d in addition to the normal DENSE sequence parameters described above results in a magnetisation pattern described by a version of Equation 5.2 modified to include the through plane gradient term K_d and through plane position z as described Equation 6.13.

$$M_z(x,z) = M\cos(K_e x + K_d z) \qquad \textit{Equation 6.13}$$

This equation evolves following the completion of the tagging module and excitation pulse in the same way as Equation 6.4 but with the added $K_d z$ term. After including the imaging excitation term with flip angle α and converting to the Euler exponential form of cosine the transverse magnetisation can be described in a fashion very similar in form to Equation 6.4 but accounting for possible displacements in the encoding direction Δx and the through plane direction Δz. This modification is described by Equation 6.14.

$$\begin{aligned} M_{xy}(x,z,t) = {} & \frac{M}{2} sin(\alpha)\, e^{-t/T1} e^{-i(k_e \Delta x)}\, e^{-i(k_d \Delta z)} \\ & + \frac{M}{2} sin(\alpha)\, e^{-t/T1} e^{-ik_e \Delta x} e^{-i2k_e x} e^{-ik_d \Delta z} e^{-i2k_d z} \\ & + M_0\, sin(\alpha) \left(1 - e^{-t/T1}\right) e^{-ik_e \Delta x} e^{-ik_e x} e^{-ik_d \Delta z} e^{-ik_d z} \end{aligned} \qquad \text{Equation 6.14}$$

Which can be simplified to the form described by Equation 6.15 by combining the in plane and through plane terms.

$$\begin{aligned} M_{xy}(x,z,t) = {} & \frac{M}{2} sin(\alpha)\, e^{-t/T1} e^{-i(k_e \Delta x)}\, e^{-i(k_d \Delta z)} \\ & + \frac{M}{2} sin(\alpha)\, e^{-t/T1} e^{-ik_e(2x+\Delta x)} e^{-ik_d(2z+\Delta z)} \\ & + M_0\, sin(\alpha) \left(1 - e^{-t/T1}\right) e^{-ik_e(x+\Delta x)} e^{-ik_d(z+\Delta z)} \end{aligned} \qquad \text{Equation 6.15}$$

With the TPD gradients applied the artefact echoes (second and third terms of Equation 6.15) still occur at $-2k_e x$ and $-k_e x$ but also undergo a through plane dephasing of $-2k_d z$ and $-k_d z$ repectively. This is in contrast to the location of the displacement encoded echo described by the first term of Equation 6.15 that contains no z component and therefore no through plane dephasing only a phase shift of Δz. This through plane effect is analogous to introducing a through plane tilt to the magnetisation in the displacement encoding direction. This has the effect of pushing the T1 and complex conjugate echoes out of the acquisition plane attenuating their signal in the image plane. This process can be described using spin phase diagrams such as in Figure 6.7. In these figures diagonal lines represent transverse magnetisation and horizontal lines represent longitudinal magnetisation. The horizontal axis defines time and the vertical axis represents the phase. In Figure 6.7, RF1 and RF2 refer to the RF pulses of the tagging modules and RF3 refers to the RF excitation prior to imaging. Each line is this figure is a 'spin phase pathway' that represents the phase evolution of a given component of the total magnetisation.

So In the case of DENSE imaging (e.g. Equation 6.15) the magnetisation splits into 3 subpopulations following 3 distinct pathways. Each subpopulation branches from the initial magnetisation as it is acted on by RF pulses and branching of the magnetisation only occurs at the application of an RF pulse. The original of this branching arises from considering every possible evolution of the magnetisation following the RF pulse. A complete and detailed description of spin phase pathways is given by Haacke et al. (1999).[112] For this purpose it is necessary only to understand that each line represents a subpopulation of the total magnetisation and its position along the vertical axis determines the phase of the subpopulation.

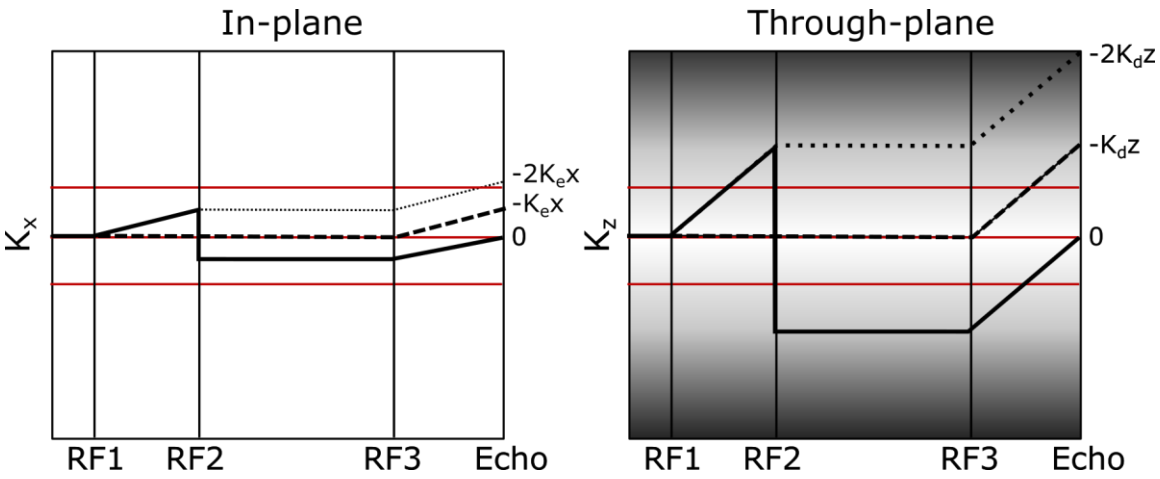

Figure 6.7 Spin diagram description of TPD. Through plane dephasing depicted by the shading in the right inset defines the degree to which an echo cannot be refocused for readout in-plane. Echoes that are further offset in the through plane direction therefore produce smaller echoes in the in plane direction. Figure modified from Zhong et al.[251]

Figure 6.7 describes the evolution of 3 spin subpopulations in the DENSE sequence for both the in plane and through plane magnetisation. Note that these are simplified diagrams that show the ideal case, i.e. no magnetisation decay, no longitudinal magnetisation following FR3 and no B0 or B1 inhomogeneity. If we first look at the in-plane magnetisation (kx), at the application of the readout gradients (labelled 'Echo') the spins refocus to form the 3 echoes described previously. The sampled portion the k-space is enclosed by the red lines in Figure 6.7 meaning that the image acquired for these spins contains information from all 3 echoes. If we apply the TPD gradients the spins also follow the through plane spin phase diagram. In this case we have echoes forming in the through plane direction (Kz). In this direction we get through plane dephasing of spins, the magnitude of this dephasing effect is depicted by the degree of shading in the spin phase diagram. Echoes experience a degree of dephasing proportional to their position along Kz determined by slice thickness and K_d. This dephasing effect prevents the

complete refocusing of spins in the transverse plane to form detectable echoes. If we observe the displacement encoded echo centred at 0 in Kx it experiences no through plane dephasing due to its position of 0 in Kz. However the T1 echo occurring at $-K_e x$ in the in plane direction experiences incomplete refocusing due to the dephasing of $-K_d z$ in the through plane direction with the complex conjugate echo experiencing a higher degree of dephasing. The result then is an image where the echoes that have a through plane component are dephased and suppressed, since the displacement echo has no through plane component it retains its signal. TPD is therefore a useful technique for selectively suppressing the artefact echoes in DENSE.

6.1.4 DENSE developments

Since the original DENSE implementation by Aletras et al. in 1999 the sequence has been under continuous development with several key improvements made including cine, 3D and multislice capabilities. The technique was adapted to a cine sequence by Kim et al. (2004)[250] who implemented a complementary acquisition strategy which was the first instance of a time independent suppression of the T1 echo making cine DENSE practical. The authors deployed a 2D echo planar imaging (EPI) DENSE sequence in humans that applied a single modulation module after the detection of an R wave followed by a demodulation gradient combined with segment EPI readout where the demodulation gradient was reapplied at each cardiac phase. This produced high spatial resolution and uncorrupted displacement information for multiple cardiac phases covering contraction and relaxation. The primary advantages of a cine sequence as opposed to a single phase sequence is the ability to observe dyssynchrony between contracting segments and greater sensitivity to time dependent components of cardiac dysfunction. The next major development of DENSE was the introduction of 3D displacement mapping. The first example of 3D DENSE was published by Gilson et al. (2005).[252] The authors produced a sequence that implemented a multislice cine gradient echo readout with displacement encoding gradients applied in the x, y and z directions where the T1 and anti-echo were suppressed using the CANSEL technique. CANSEL will be discussed in detail in 6.3.3.1. This sequence achieved multi slice imaging by sacrificing the cine component and imaging only at end systole. Following the application of DENSE modulation, a single phase encode line was read out at end systole for 3 successive slices for the next 3 successive ECG triggers. This long readout is possible due to the rapid heart rate of the mouse (RR ≈120ms) and the persistence of the modulation pattern when it is stored in the longitudinal magnetisation where it depends primarily on T1 of tissue (T1 ≈1200ms). There is an SNR penalty the longer the magnetisation has

been stored, however, with later slices having reduced signal. To extend the DENSE encoding to 3 dimensions an additional acquisition was required with the modulation gradients applied in the z direction. Since the through plane displacement in the cardiac short axis is larger than in plane, the encoding strength was smaller to provide better sensitivity to large displacements. The primary disadvantage of 3D DENSE is the requirement for additional acquisitions to encode in the longitudinal direction.

Aside from improvements to the acquisition sequence there have been developments in the field of DENSE image processing that aim to streamline processing or interpolate additional cardiac information. These include point trajectory fitting, myocardial modelling and automated LV segmentation methods. Spottiswoode et al. (2006) proposed a novel spatiotemporal unwrapping algorithm to remove phase wrapping at high encoding frequencies in a consistent fashion throughout the cardiac cycle.[235] In addition to the DENSE phase unwrapping algorithm, Spottiswoode et al. (2007) implemented a temporal fitting method to improve tissue trajectory estimates. By fitting trajectories to tissue regions it is possible to calculate strain to any temporal resolution without being limited by the image acquisition. Trajectories were fitted to the displacement data using fifth order Fourier basis functions. The result was accurate tissue displacement tracking that improved strain mapping and was able to identify infarcted regions of myocardium even in images severely affected by noise. Computational modelling of the LV is a powerful technique for expanding multislice DENSE data into a true 3D model of cardiac deformation. The goal of this expansion is to produce a whole heart view of cardiac mechanical dysfunction. Lui et al. (2009) created a patient specific finite element model of the heart that could interpolate DENSE data to provide a continuous 3D strain information.[253] The modelling provided a more complete view of cardiac contraction where each dataset is fitted to a model based on LV epi and endocardial borders making it robust to changes in heart structure, such as following infarction. However, the method is computationally intensive and mathematically complex beyond the scope of this study. Accurate LV segmentation is important in DENSE images to exclude displacement errors arising from including extra-myocardial pixels such as those in the lung that contain a large noise component. Performing this segmentation manually can be time consuming. An interesting approach by Spottiswoode et al. (2009) took a motion guided approach to semi-automated segmentation based on their trajectory fitting method described above.[254] Their approach projects the epicardial and endocardial borders defined in a single frame through time based on the trajectory information. This approach has the benefit of being limited by physiological information, robust to low contrast between blood and

myocardium in early frames and is independent of LV shape making it applicable to atrophied infarct tissue in both SA and LA views.

6.2 Methods

6.2.1 Methods: DENSE sequence development

6.2.1.1 Single-phase DENSE

This section corresponds to stage 1 of the workflow described in Figure 6.1. The aim of this section is to describe the implementation and development of single phase and cine-capable DENSE sequences.

The first implementation of DENSE I created was based on a cardiac gated 2D gradient echo imaging sequence. In normal use this sequence is used to acquire fast static images of the heart. The sequence was modified to include the additional RF and gradient components necessary for displacement encoding. A variable delay was added so that the time between application of the first and second displacement encoding gradients (TM) could be varied. For in-vivo scans this delay is tuned so that the second displacement encoding gradient is applied at end systole.

This sequence was tested on a phantom containing 1% agarose where T1 was matched to heart tissue by gadolinium doping. Three acquisitions were performed where the displacement encoding gradients were applied in the readout (RO), phase encode (PE) directions and one where the gradient amplitude was set to zero (reference image). The images were acquired using a 35mm volume resonator RF coil, with acquisition parameters; matrix size of 128×128, FOV = 25.6×25.6mm, TE = 2.5ms, TR = 500ms, 3 averages, a DENSE delay of 50ms and K_e=0.5 cycles/mm. The total duration of the tagging module was 3ms.

The resulting images were corrupted by the T1 and complex conjugate stimulated echoes, in this case the displacement encoded peak is isolated through a bandpass filter centred at the origin of k-space and was tuned to exclude all other echoes. These filtered images were then reconstructed using the iFFT to create magnitude and wrapped phase images. Phase unwrapping was performed using the graph cuts method with magnitude weighting. Subtracting the unwrapped phase of the reference images from the unwrapped phase of the RO and PE encoded images yielded maps of the phase accumulated by displacement between the two encoding gradients.

Displacement magnitude maps were produced using the quadrature sum of the X and Y displacements according to Equation 6.16. Where D is displacement and Δx and Δy are the X and Y displacements respectively.

$$D = \sqrt{(\Delta x^2 + \Delta y^2)} \qquad \text{Equation 6.16}$$

The same single phase DENSE sequence was then tested in-vivo in a wild type mouse heart. The images were acquired using a 35mm volume resonator RF coil, with acquisition parameters; matrix size of 128×128, FOV = 25.6×25.6mm, TE= 2.5ms, TR = RR interval (approx. 110ms), 3 averages, a DENSE delay of 50ms and K_e=1.3 cycles/mm.

6.2.1.2 Cine DENSE

In the same way that single phase DENSE was developed by modifying a single phase cardiac imaging sequence, cine DENSE was created by modifying a cardiac cine sequence. The cine sequence is based on a rapid low flip angle gradient echo readout. To incorporate the DENSE sequence, the SPAMM module was included immediately after the R-wave trigger and a displacement unencoding gradient was included after every slice selective excitation readout pulse.

The cine DENSE sequence was first tested on a stationary agarose phantom with T1 matched to heart tissue. Since the properties of a cine sequence must be tuned to the RR interval of the ECG signal an ECG simulator (SA Instruments, Stony Brook, NY, USA) was used to trigger the acquisition. The signal generator was programmed to produce a regular ECG signal at a frequency of 550bpm and included respiratory artefacts at approximately 40bpm to simulate normal physiology of a mouse under anaesthetic. The total duration of the tagging module was 3ms following the R-wave trigger. The images were acquired using a 35mm volume resonator RF coil, with acquisition parameters; matrix size of 128×128, FOV = 25.6×25.6mm, TE= 2.5ms, TR = 5ms, flip angle = 15°, 8 averages and K_e=1.7 cycles/mm. The scan was repeated 3 times with encoding in the RO and PE directions and with the displacement encoding gradients set to K_e=0 cycles/mm. Displacement images were filtered to remove all frequencies $> K_e/2$, .

6.2.2 Methods: Phase correction

This section corresponds to stage 2 of the workflow described in Figure 6.1. The aim of the techniques discussed below is to remove the background field sources that produce phase

measurements that are unrelated to cardiac displacement. This allows the isolation of motion due to contraction producing a more accurate displacement field map.

To solve this field removal problem and remove the offset in the in-vivo cine DENSE protocol a processing technique was adapted from the field of quantitative susceptibility mapping MRI (QSM). QSM is a quantitative parametric imaging technique that aims to map the magnetic susceptibility of tissue revealing details about underlying pathology. Magnetic susceptibility is a fundamental property of a material and can become altered in disease providing a novel contrast mechanism and biomarker for MRI. The main obstacle to overcome in QSM is the isolation of the small local magnetic field sources that arise from the susceptibility of tissue from the much larger background field sources. Contributions to the background field arise from a number of sources such as high susceptibility boundaries and imperfect shimming. This is analogous to the problem faced with DENSE where the aim is to isolate the small phase changes due to tissue motion from background sources.

Any gradient echo MRI image of a region of tissue is a convolution of the background field and local field contributions. Although QSM was theorised early on in the history of MRI by Young et al. (1987) it has only been in the last decade that the mathematical tools have come of age, making QSM a feasible tool for MRI research.[255,256] These QSM tools include mathematical methods for separating field sources and solving the ill posed inverse problem required to quantify magnetic susceptibility from the resulting field map. Projection onto dipole fields (PDF) is a tool used in QSM to remove background field contributions and isolate the local sources.[257] PDF was developed based on the observation that the field projected from any magnetic dipole outside of a region of interest is orthogonal to the magnetic dipole inside the region of interest. The total field inside the ROI can then be projected onto the background field sources outside the ROI using the projection theorem in Hilbert space. This projection can then be used to deconvolve the field inside the ROI and decompose it into two fields, one for dipoles originating within the ROI and one from outside due to background sources. For DENSE background field removal, the PDF function was applied to both the encoding directions separately. This is a valid operation since the field contribution induced by motion is independent of the background field and depends only on distance tissue has travelled between the encoding gradients applied during acquisition. The PDF function is a complex mathematical solution and so an established Matlab implementation developed by the authors of the original PDF paper was used.[257,258]

The PDF background field removal technique was tested first in a stationary agarose phantom and then on in vivo DENSE data acquired in a wild type mouse heart. The images were acquired using a 35mm volume resonator RF coil, with acquisition parameters; matrix size of 128×128,

FOV = 25.6×25.6mm, TE= 1.5ms, TR = 5ms, cine frames = 19, flip angle = 15°, 15 averages and K_e=1.7 cycles/mm. The scan was repeated twice with encoding in the RO and PE directions and displacement images were filtered to remove all frequencies $> K_e/2$.

6.2.3 Methods: Artefact echo suppression

This section corresponds to stage 3 of the workflow described in Figure 6.1. The aim of the work discussed below is to remove the unwanted T1 and complex conjugate echoes from the acquisition either through the addition of complementary acquisitions or the application of a through plane dephasing gradient. The theory behind these techniques was discussed in detail in sections 6.2.3.1 and 6.2.3.2 respectively.

6.2.3.1 Complementary acquisitions: cDENSE and CANSEL

The DENSE sequence was modified so that the second RF pulse in the tagging module could be assigned a variable phase. This allowed the generation of all the phase modulation patterns described in Figure 6.4.

In vivo pilot data were acquired using a 35mm volume resonator RF coil, with acquisition parameters; matrix size of 128×128, FOV = 25.6×25.6mm, TE= 2.6ms, TR = 10ms, flip angle = 20°, 8 averages and K_e=1.4 cycles/mm. The scan was repeated 4 times with sine, cosine-sine and –cosine modulation patterns. This allowed reconstruction of the data with either cDENSE or CANSEL echo removal. Since the aim here was to assess echo removal not displacement information the acquisition was performed with encoding in the RO direction only. In the case of the processed cDENSE acquisition, k-space was filtered to remove all frequencies $> K_e/2$. Each scan took approximately 9minutes depending on heart rate and respiration. Data were then reconstructed in Matlab using the cDENSE or CANSEL subtraction methods described above.

6.2.3.2 Through plane dephasing

Testing of the TPD technique was performed on a stationary agarose phantom consisting of 4 tubes of 1% agarose with gadolinium doping to achieve a range of T1 values consistent with physiological values, these were quantified using the inversion recovery look locker method and model fitting described in Chapter 3. The aim of the agarose phantom imaging was to determine the relationship between K_d and the effectiveness of echo suppression. Cine DENSE imaging was performed with TPD gradients of duration 0.8ms and varying gradient strengths to achieve K_d

values between 0 and 2.04 cycles/mm. In plane encoding K_e was set to a relatively low encoding strength of $K_e = 1.02$ cycles/mm to ensure acquisition of the complex conjugate echo. These data were acquired using a 35mm volume resonator RF coil, with acquisition parameters; matrix size of 128×128, FOV = 25.6×25.6mm, TE= 1.8ms, TR = 10ms, flip angle = 20°, 5 averages and a slice thickness of 1mm. Images were then reconstructed in Matlab and the centre of the k-space peaks located manually. A circular region of interest was drawn around the T1 and displacement encoded peaks including all frequencies within $K_e/4$ of the peak centroid. The values within this range were used to quantify the total energy contained in the peak as a percentage of total image energy where energy was evaluated by summing the square of the absolute values of the k-space data as described by Zhong et al. (2006). Peak energy was calculated for each cine frame in the cine DENSE sequence allowing visualisation of T1 recovery term and resulting loss of displacement encoding as a function of time from the encoding gradient.

Cine DENSE imaging was performed with TPD gradients of duration 0.8ms and varying gradient strengths to achieve K_d values between 0 and 1.36 cycles/mm. In plane encoding K_e was set to a higher encoding strength than used for the phantom study at more conventional encoding frequencies for mouse heart DENSE of $K_e = 1.36$ cycles/mm. These data were acquired using a 35mm volume resonator RF coil, with acquisition parameters; matrix size of 128×128, FOV = 25.6×25.6mm, TE= 1.8ms, TR = 10ms, flip angle = 20°, 8 averages and a slice thickness of 1mm. Data was reconstructed and the relative energy of each peak computed as described above for the phantom.

6.2.3.1 Comparison of echo removal techniques

The cDENSE, CANSEL and TPD methods all aim to remove the T1 and complex conjugate artefact echoes while retaining the displacement encoded stimulated echo at the k-space origin. To compare the capability of each technique and the spatial resolution preserved by each, a wild type mouse was imaged with DENSE encoding in a single direction and the displacement map produced by each echo removal technique compared. Comparison was performed by empirical inspection of the resolution in each displacement map, along with the SNR available in each method.

Cine DENSE imaging was performed with in plane encoding $K_e = 1.36$ cycles/mm. These data were acquired using a 35mm volume resonator RF coil, with acquisition parameters; matrix size of 128×128, FOV = 25.6×25.6mm, TE= 1.8ms, TR = 10ms, flip angle = 20°, 8 averages and a slice thickness of 1mm with 12 cine frames. Data was acquired with cos, sine,-cosine and –sine

modulation patterns as well as one TPD dataset with cosine modulation and $K_e = 1.02$cycles/mm.

These acquisitions allow 4 different echo suppression techniques to be tested. The first is a standard cosine modulated DENSE dataset filtered with a circular bandpass filter with a radius of $K_e/2$. The second is a cSPAMM dataset, this requires a combination of cosine and –cosine acquisitions to supress the T1 echo meaning the centre of the bandpass filter can be extended to $3K_e/2$ to remove only the complex conjugate echo. The third combines all complementary datasets to remove both echoes and requires no filter. The fourth dataset using the TPD acquisition to suppress the echoes and also requires no filtering.

6.2.4 Methods: Trajectories and strain

6.2.4.1 Myocardial trajectories

DENSE displacement maps describe the phase accumulated by a pixel due to its displacement between the application of two displacement encoding gradients. This means that every point refers back to the position of that pixel at diastole. The trajectory of a myocardial element through time follows a path defined by the cardiac function of that region. DENSE data is subject to noise and tracing the trajectory can result in discontinuous and non-physiological path of motion. The periodic contraction of the heart is naturally suited to fitting with a periodic Fourier function. Creating these trajectories starts by converting the cine displacement maps to a motion path originating at the centre of each pixel within the myocardium at the beginning of diastole. The value of each pixel in the sequential x and y displacement maps can be used to describe the raw 2D trajectory. Equation 6.17 describes the Fourier basis function used to describe the periodic trajectory of a single myocardial element.

$$f_{x,y}(t) = \frac{1}{2}a_0 + \sum_{n=1}^{K}(a_K \cos(\mathrm{n}\omega\mathrm{t}) + b_K \sin(\mathrm{n}\omega\mathrm{t})) \qquad \text{Equation 6.17}$$

Where $f_{x,y}$ is the motion path of the tissue in either the x or y direction fitted using least squares minimisation, a_K and b_K are the fitted coefficients of the Kth order Fourier series and $\omega = 2\pi/T$ where T is the cardiac period or RR interval. Fitting was performed using a nonlinear least squares optimisation function. Fitting the Fourier coefficients of the x displacement followed by the y displacement independently relative to time produces a time dependent 2D trajectory of the cardiac motion.

6.2.4.2 Strain calculation

A custom strain calculating function was implemented in Matlab based on the displacement images. This function was also made applicable to the HARP data by converting the point tracking result of HARP to displacement maps. This enabled data from HARP and DENSE could be readily processed using the same functions.

Strain was calculated by calculating the differential of the x and y displacement maps in the x and y direction to produce the 4 components of the displacement gradient tensor $\boldsymbol{F}$. This tensor was then converted to the strain tensor $\boldsymbol{E}$ by Equation 4.1. The resulting 2D tensor contained two components in x and y, however a more physiological coordinate system for cardiac strain is cylindrical with circumferential and radial components. The tensors were therefore converted to their projections onto the cylindrical axis to allow calculation of circumferential (Ecc) and radial (Err) strain components.[259] This was done by rotating the strain matrix by the angle made to the centroid of the LV (θ) to produce the transformed strain tensor $\dot{\boldsymbol{E}}$ as described in Equation 6.18. In this coordinate system negative values of strain represent contraction while positive values indicate stretching.

$$\dot{\boldsymbol{E}} = \boldsymbol{Q}\boldsymbol{E}\boldsymbol{Q}^{\boldsymbol{T}} \qquad \textit{Equation 6.18}$$

$$\boldsymbol{Q} = \begin{bmatrix} cos\theta & sin\theta \\ -sin\theta & cos\theta \end{bmatrix}$$

6.3 Results

6.3.1 Results: DENSE sequence development

6.3.1.1 Single phase DENSE

The result of the single phase DENSE sequence applied to a stationary phantom is shown in Figure 6.8. The ideal displacement images for this phantom would show zero motion in the agarose and artifactual displacement in the surrounding space. In a stationary phantom we see minimal displacement within the phantom and relatively large artifactual displacements in the surrounding space. The colourmap in the displacement images is the magnitude of motion calculated by adding the displacement vectors in quadrature. The displacement measurements in Figure 6.8 are reasonable for a stationary phantom, with an average displacement within the agarose of 0.33±0.31mm (mean ± standard deviation). There is also a clear ring of artifactual displacement around the perimeter of the agarose phantom, this is due to the low spatial resolution of the filtered acquisition. Although the uncertainty in measurements its fairly high

the displacement is low making this example adequate but requires optimisation. The main issue with this acquisition and processing scheme is the k-space filtering. The majority of spatial information is thrown away when using the bandpass filter method, more sophisticated methods of removing the artefact echoes and preserving spatial information are investigated in section 6.3.3.

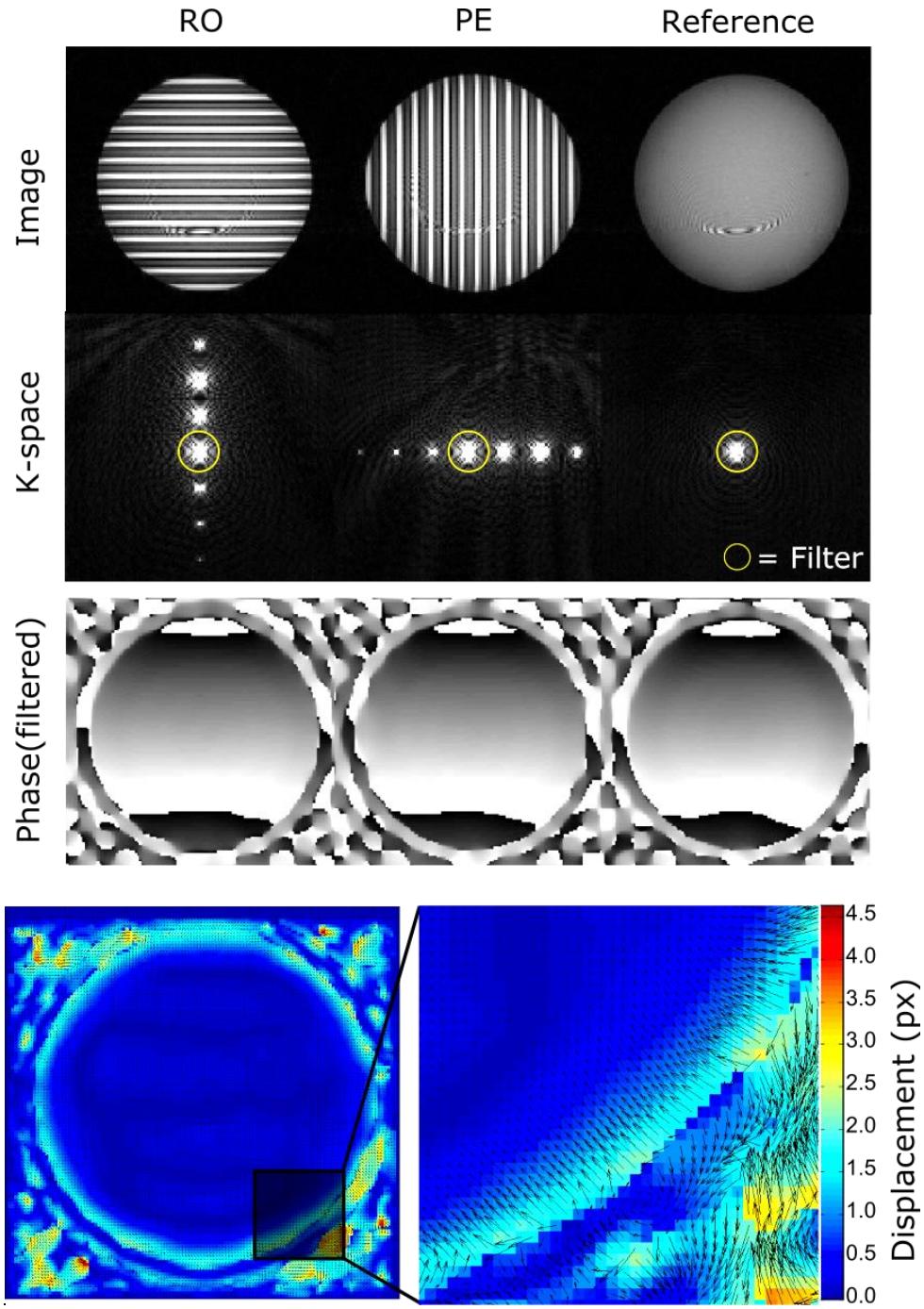

Figure 6.8 Single phase DENSE of stationary agarose phantom. Magnitude images (top row) show the banding artefacts resulting from the T1 and complex conjugate echoes, these are present in k-space (second row) as stimulated echoes offset from the k-space origin. Isolating the central displacement encoded peak with bandpass filter results in wrapped phase maps (third

row) these can be unwrapped and background phase removed with the reference acquisition to produce maps of 2D displacement (bottom row).

The results of the in-vivo acquisition are presented in Figure 6.9. The higher encoding strength relative to the stationary phantom acquisition pushed the artefact echoes further towards the edge of k-space meaning that the displacement encoded echo could be isolated using a larger filter, therefore excluding less spatial frequencies and preserving more spatial information than in the case of the stationary phantom. This higher resolution information can be seen when comparing the phase maps of the stationary phantom acquisition and the in vivo acquisition.

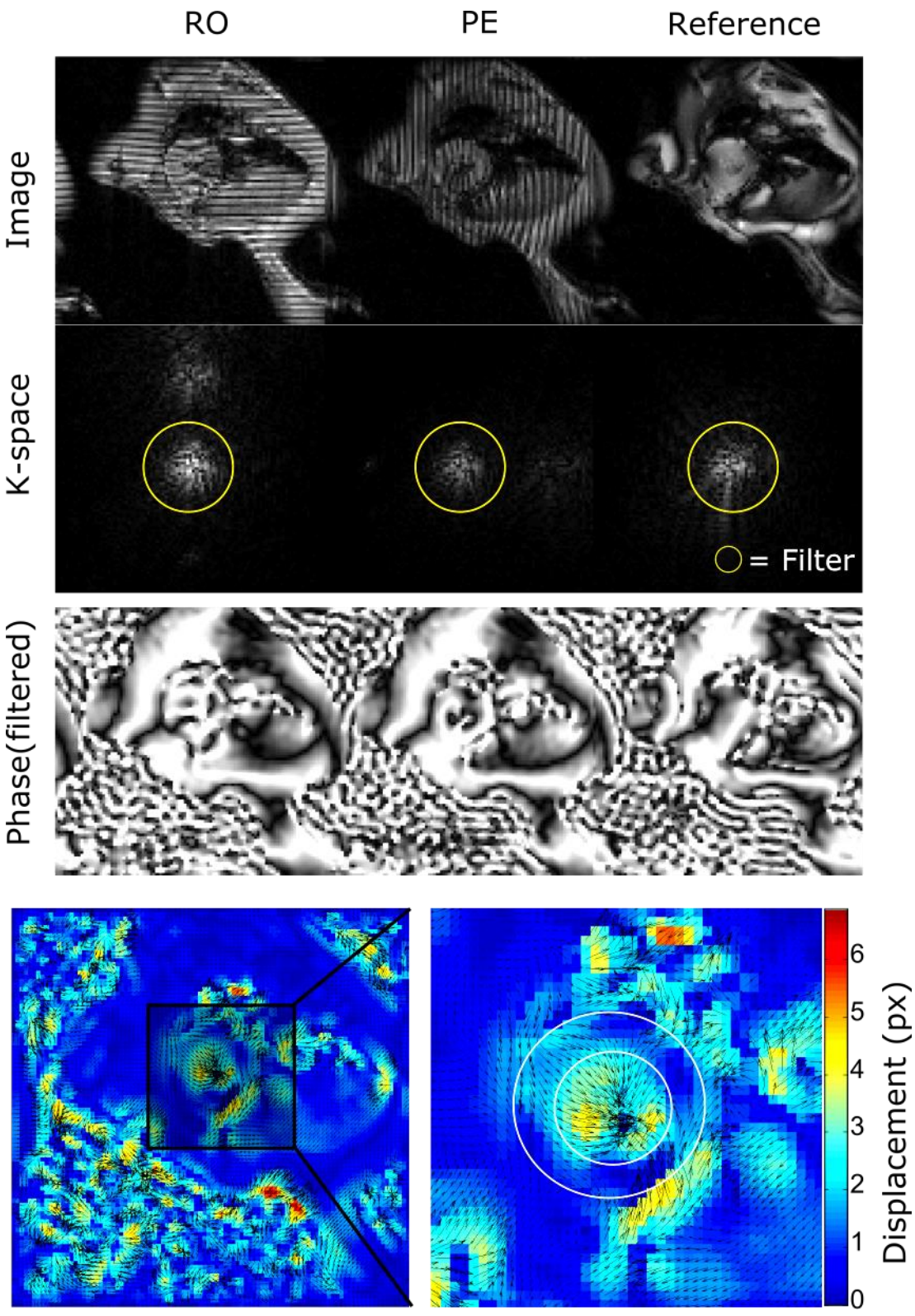

Figure 6.9 In-vivo single phase DENSE. As above the image is filtered to isolate the displacement encoded echo, in this case the filter can include more frequencies since the high encoding strength offsets the artefact echoes. Phase unwrapping provides displacement magnitude and direction maps (bottom row). White contours indicate LV myocardium.

The displacement fields in Figure 6.9 show consistent and small displacements in tissue such as the liver, fat and muscle regions while regions of noisy or corrupted signal such as the pulmonary cavity, blood pool and extra corporeal space show highly variable displacements. If we apply a mask to the displacement maps to isolate only the displacement of the LV myocardium we find that the average displacement to systole in the LV is 1.31±0.68mm. This is consistent with previous myocardial displacement studies demonstrating the accuracy of this sequence.[39] However, although the average displacement is within the physiological range, the ability of DENSE to image regional displacement reveals that there is uncertainty in specific regions of myocardium. The vector plots in Figure 6.10 show the masked myocardial displacements to illustrate this point.

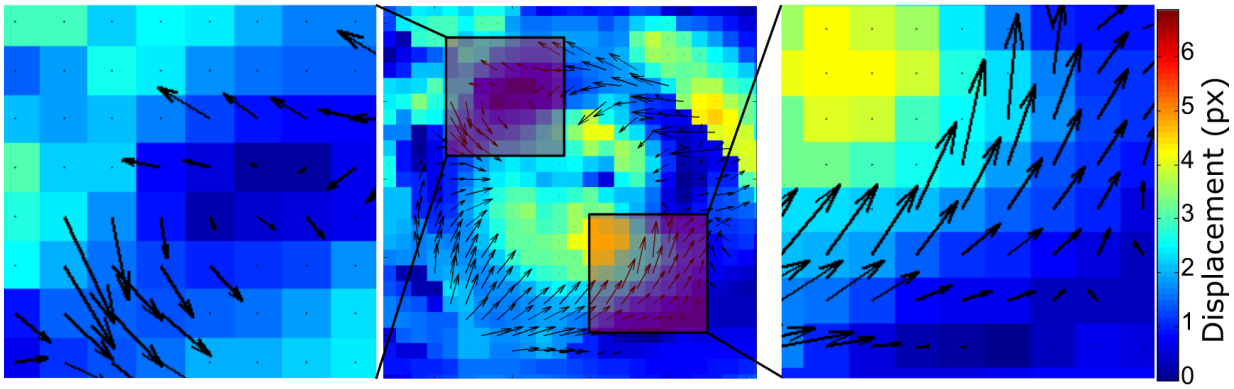

Figure 6.10 Heart displacement only (90° rotation CCW from Figure 6.9). Some regions of heart tissue show physiologically accurate displacements (right inset) while others appear effected by phase errors (left inset). The reasons for this variability are due to background field contributions that have not been accurately removed in the phase subtraction step.

The region shown in Figure 6.10(Left inset) is the inferior wall of the LV bordering the pulmonary cavity. The magnetic field homogeneity is lowest in this region due to the high magnetic susceptibility boundary with the cavity. The result of this is decreased DENSE signal intensity due to intravoxel dephasing, as was the case with SPAMM tagging, at higher encoding frequencies this dephasing becomes more. This is a recognised issue associated with all stimulated echo acquisitions in the heart.[260] This region of low signal causes displacement errors due to the ineffective removal of background field contributions to image phase during the phase subtraction step. Steps taken in future acquisitions to minimise this dephasing effect were more homogenous shimming gradients and the use of lower encoding frequencies of around K_e=1.1cycles/mm for in vivo imaging, this value was chosen based on previous mouse DENSE literature as a good compromise between displacement sensitivity in the range of motion for the mouse heart and reduced intravoxel dephasing.

Single phase DENSE was a useful starting point to establish the processing pipeline and identify initial implementation issues with the in-vivo DENSE sequence however cine DENSE offers far more useful information about the dynamic motion of the heart and developing this was the next logical step for improvement of the DENSE implementation.

6.3.1.2 Cine DENSE

The result of the cine DENSE sequence in a stationary phantom is shown in Figure 6.11. The data in Figure 6.11A were filtered using the illustrated bandpass filter with an identical filter applied to every frame in the cine sequence resulting in displacement maps for each direction (Figure 6.11B). This sequence would be expected to measure zero displacement throughout the imaging sequence, however, these displacement maps suffer from a significant offset. The mean x and y displacements within the stationary agarose are -21.5±1.7mm and -14±1.6mm respectively. This offset is caused during the phase subtraction step since the unwrapped phase in the reference image is much higher than in the directionally encoded images resulting in a large offset after phase subtraction. The most likely cause of this is the automated graph cuts phase unwrapping algorithm. The graph cuts technique is weighted by image magnitude meaning the phase of pixels with a high signal content strongly effect the assigned phase in nearby darker pixels. In the agarose phantom a uniform signal is expected throughout, however image magnitude was not always uniform, as seen in the example image of the reference scan in Figure 6.11A. The cause of this non-uniformity is complex and due to a number of factors. A major contribution to signal inhomogeneity is from insufficient B0 shimming before the acquisition. This would also explain the distorted tag lines observed in the encoded images. The filtering necessary to isolate the displacement encoded peak must be applied in the reference image as well as the displacement encoded images to maintain consistent spatial information between images. This has the effect of removing a large fraction of the acquired signal in the reference image. The sensitivity of this field removal method to accurate shimming and acquisition properties makes it impractical for in vivo cardiac cine DENSE, where shimming is limited by persistent flow, susceptibility boundaries and cardiac and respiratory motion. These phase removal errors led to the development of a novel phase removal method based on the PDF method.

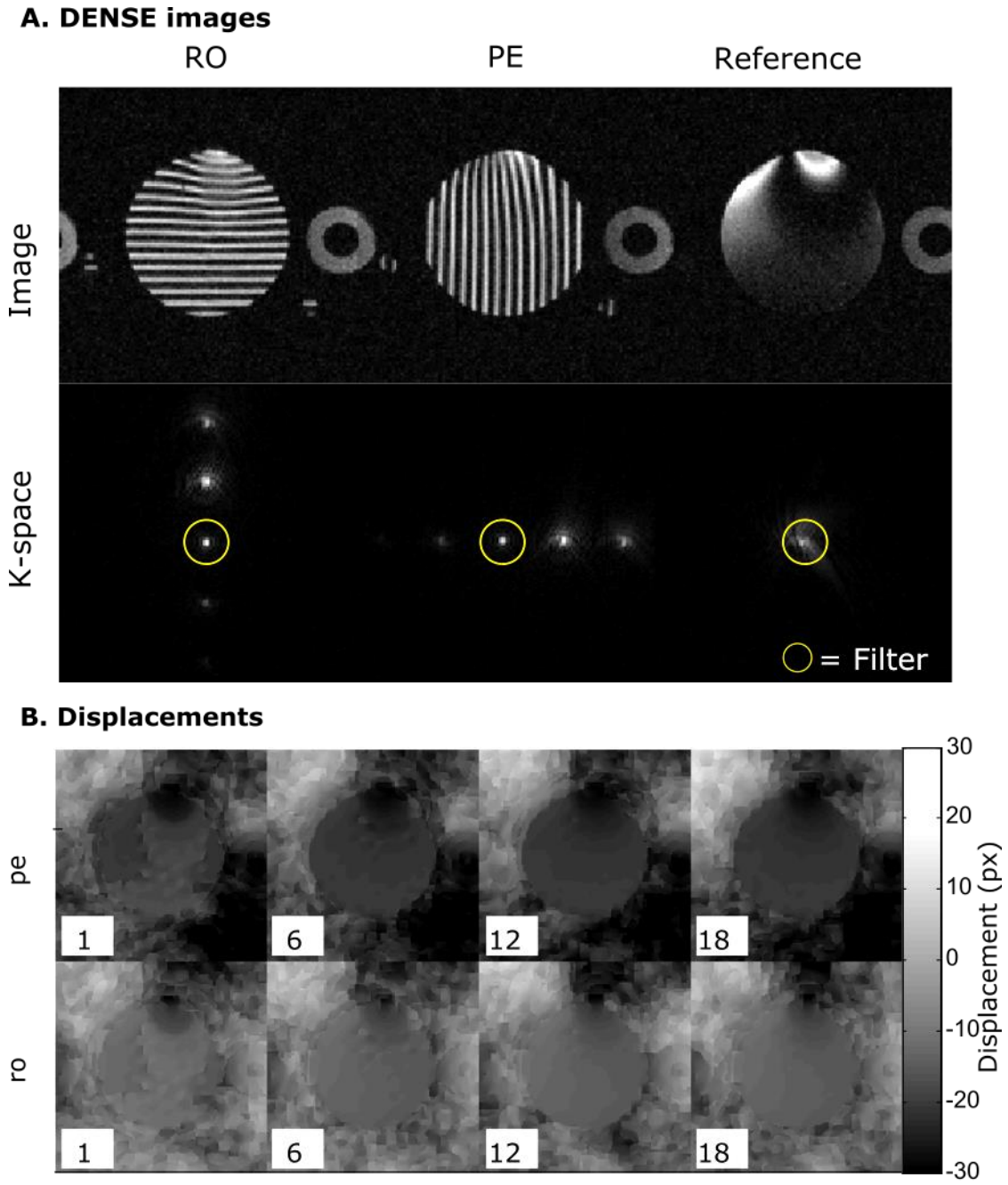

Figure 6.11 Example cine DENSE images acquired with a stationary agarose phantom.(A) cine DENSE image data was produced to be similar in appearance to the stationary single phase DENSE images. The k-space filter removing frequencies >Ke/2 was propagated through the time dimension to remove artefact echoes in all frames. Displacement maps for the RO and PE directions (B) are produced by phase unwrapping and reference phase subtraction of the DENSE data, shown here are cine frames 1,6,12 and 18.

6.3.2 Results: Projection onto dipole fields phase correction

The results of the PDF field removal algorithm applied to the data shown in Figure 6.11 as well as the original field removal method for comparison are shown below in Figure 6.12.

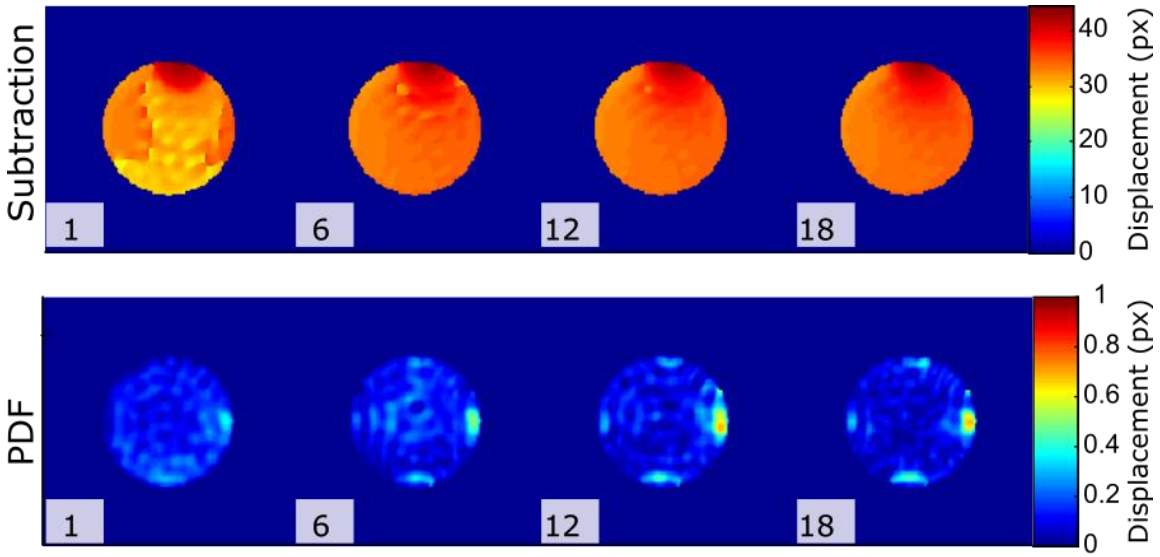

Figure 6.12 PDF is an effective method for removing background field contributions from DENSE data without the need for a reference scan (second row). The PDF method is significantly closer to the zero motion expected for the stationary phantom than the previously used phase subtraction method (first row). Numbers indicate cine frame index.

The mean 2D displacement magnitude in the phantom when field removal was performed by the subtraction method was 26.0±2.1mm while the PDF method performed much better with a mean displacement of 0.12±0.04mm, much closer to the true value of zero. The PDF subtraction images show some image artefacts, there is a speckled texture to the displacement and some small regions of high displacement near the top, bottom, left and right edges of the agarose. The lack of high frequency image information due to the DENSE filtering process is likely to contribute to both of these artefacts. The high displacement regions near the boundary of the agarose could also be affected by the inaccuracy of the PDF technique near ROI boundaries. Near the boundaries of the ROI the field originating from inside the ROI and outside the ROI have a significant correlation making them more difficult to deconvolve since they do not satisfy the PDF assumption that the fields are orthogonal.[261] To counter this effect for in vivo data the ROI for PDF was made to cover the entire corporeal body including lungs and blood pool. Although this removes the ability of PDF to remove field contributions from high susceptibility boundaries it prevents the generation of boundary errors since the heart is well inside the ROI.

A secondary advantage of the PDF field removal method is that it makes the acquisition of a reference image redundant. Since the PDF function operates only on the directionally encoded images there is no need to acquire a separate reference scan reducing acquisition time equal to the time required to acquire one volume. Since the assumption of PDF is that all external field contributions arise from outside the region of interest this method corrects only for phase

changes due to B0 inhomogeneity. This means that field perturbations due to high susceptibility boundaries such as between the myocardium and lungs are not corrected.

The application of PDF phase correction to in vivo cine DENSE data in the wild type mouse heart is shown in Figure 6.13. The results show physiologically realistic concentric twisting displacement around the circumference of the LV over the duration of the cardiac cycle.

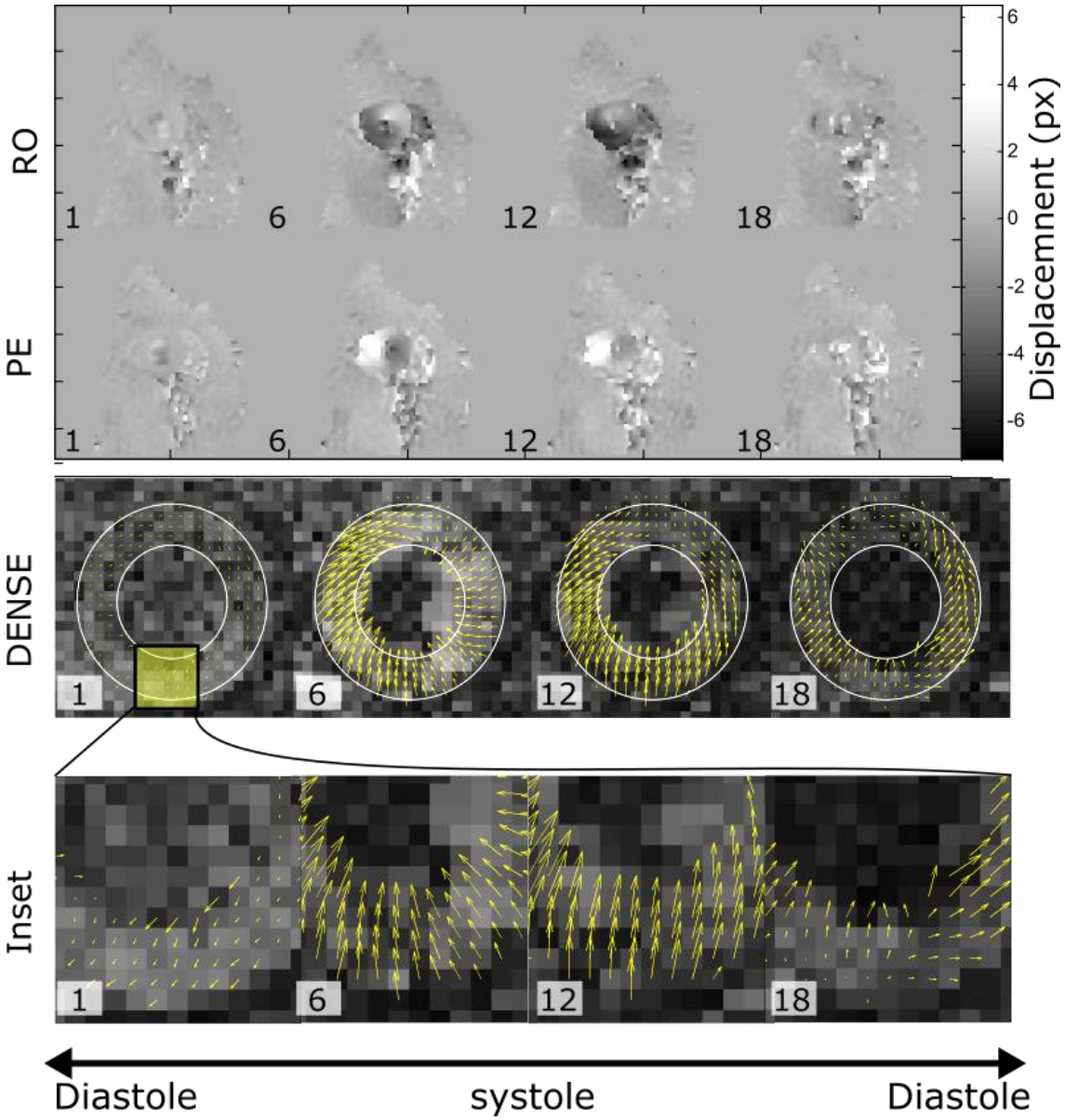

Figure 6.13 in vivo cine DENSE testing using the PDF field removal technique. Displacement maps from unwrapped and PDF corrected phase are shown in the top two rows. The heart, lungs and blood pool are clearly visible by their variation through time. Numbers indicate cine frame index .

The displacement can be seen to increase in magnitude to systole and return to baseline during diastole. This cycle is plotted in Figure 6.14A. The displacement is smallest at the anterior and septal walls and largest at the lateral and posterior regions of myocardium consistent with other studies of regional myocardial function.[218] This can most easily be seen in maps of the maximum

displacement that in normal physiology occurs at end systole (Figure 6.14B) and the variance of displacement over the cardiac cycle (Figure 6.14C). Figure 6.14C shows bright regions where there is a high degree of motion while dark regions show little motion. In this map the heart and lungs show high variance due to cardiac motion and artifactual signal respectively while the stationary body shows low variance as expected.

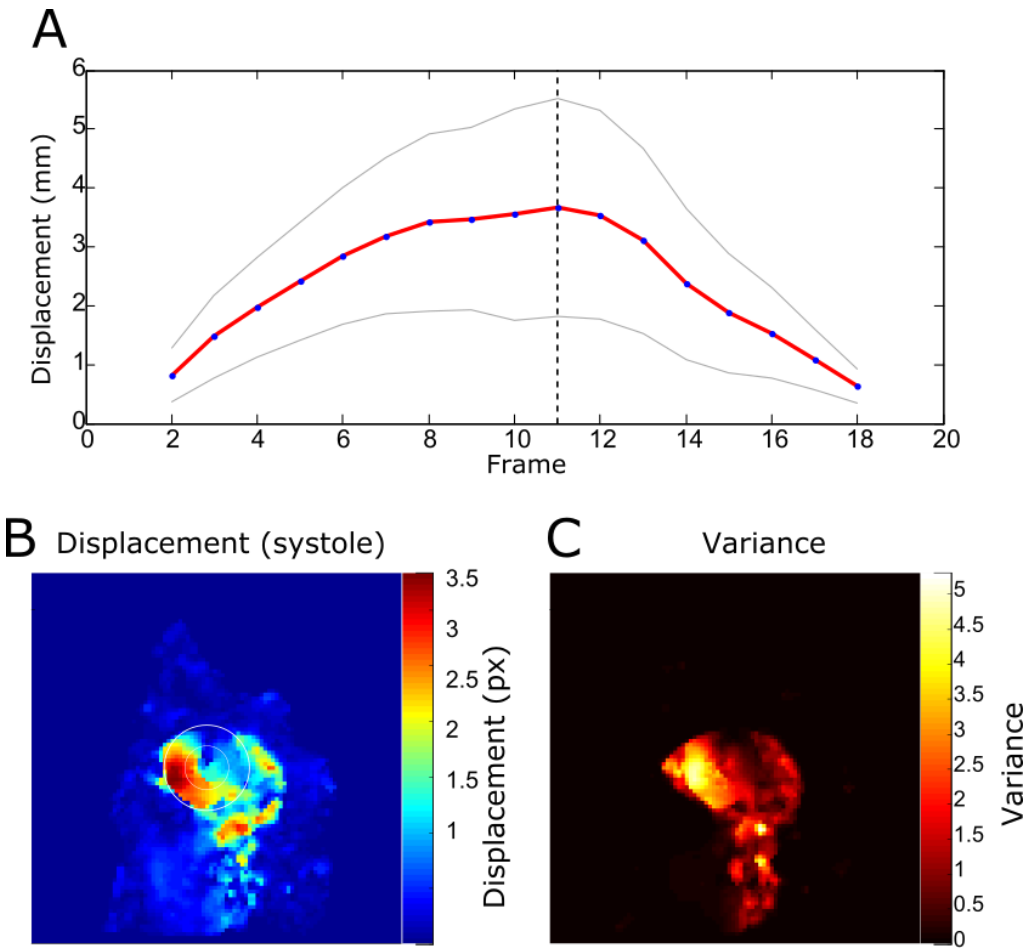

Figure 6.14 plot of mean myocardial displacement ±SD over the cardiac cycle. Showing contraction and relaxation either side of end systole (dashed line). Also shown are the displacement map for end systole and the variance of the displacement over the cardiac cycle.

A key advantage of DENSE imaging over tagging methods such as HARP is its higher spatial resolution. In HARP the displacement encoded echo is isolated by use of a bandpass filter removing much of the high frequency spatial information. All DENSE developments up to this point have used the same filtering method to remove the T1 and complex conjugate echoes. This type of filtering severely limits spatial resolution and negates the primary advantage of using DENSE. The following section investigates the development and implementation of advanced techniques for removing artefact echoes while retaining higher frequencies and spatial information.

6.3.3 Results: Artefact echo suppression

6.3.3.1 Complementary acquisitions: cDENSE and CANSEL

The in vivo example of the two complementary DENSE acquisition schemes are shown in Figure 6.15. It can be seen that both cDENSE and CANSEL are able to achieve this goal in-vivo despite complications such as heart rate variability (541±31 bpm over acquisition duration).

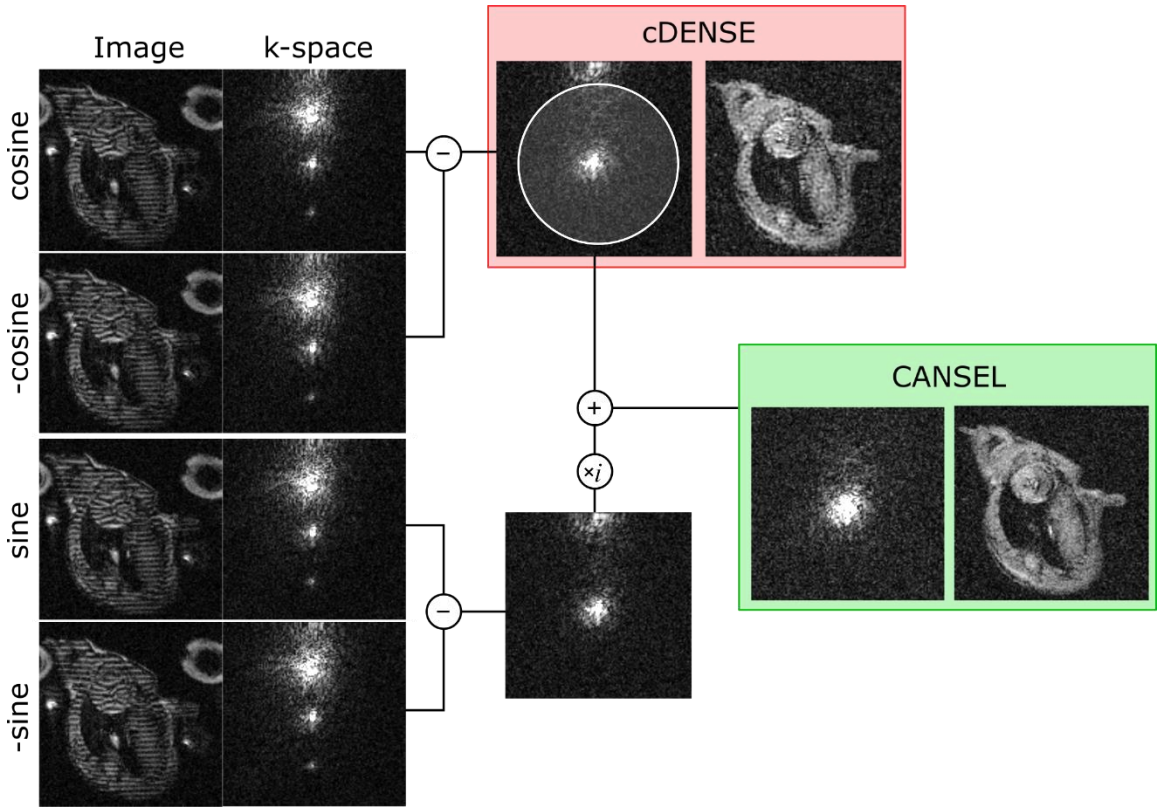

Figure 6.15 CANSEL and cDENSE in vivo example. Representative images of systole for all 4 modulations required to create a CANSEL dataset. To achieve removal of the T1 echo only the positive and negative cosine modulations are required. To remove the residual complex conjugate echo at the edge of k-space either a bandpass filter (white circle) or additional sine modulations are required.

Note that despite the almost identical appearance of the different modulations in k-space there is a significant difference in the data. The similarities arise from the complications of displaying complex data, here we follow convention and display k-space data as the magnitude of the complex number describing that point.

The primary trade-off between these two complementary schemes is between time and removal of the complex conjugate echo. cDENSE is faster to acquire but requires higher encoding strengths to remove the complex conjugate without implementing a filter. CANSEL acquisition times may be prohibitively long, acquisitions using the parameters described here took

approximately 9 minutes per volume. To describe 2D motion 2 volumes are required with orthogonal encoding, introducing the multiplicative factors of 2x acquisition time for cDENSE and 4x acquisition time for CANSEL can lead to acquisition times of 36 minutes and 72 minutes respectively. Long scan durations such as these are ill suited to studies of cardiac regeneration therapy or other preclinical imaging projects that are typically multiparametric in nature. Preclinical studies often aim to quantitatively image as many relevant features as possible, requiring multiple acquisitions for each. Combined with a requirement for high study populations to ensure statistical robustness it is difficult to justify a 72-minute imaging sequence. These are factors that have led to the development of through plane dephasing (TPD) as a technique to accelerate complete DENSE dataset acquisitions.

A full quantitative comparison of cDENSE and CANSEL as well as the through plane dephasing technique is performed in section 6.3.3.3 following the description of the development of TPD.

6.3.3.2 Through-plane dephasing

The results of this investigation into the influences of K_d on TPD DENSE imaging are shown in Figure 6.16. Results are displayed in both a graphical form on the left and quantitated on the right. At $K_d = 0$ we see no change in the tagging pattern and no suppression of artifactual echoes. This can be seen in k-space by the large T1 and complex conjugate echoes that can be seen to increase in proportional magnitude to the displacement echo over the RR interval duration.

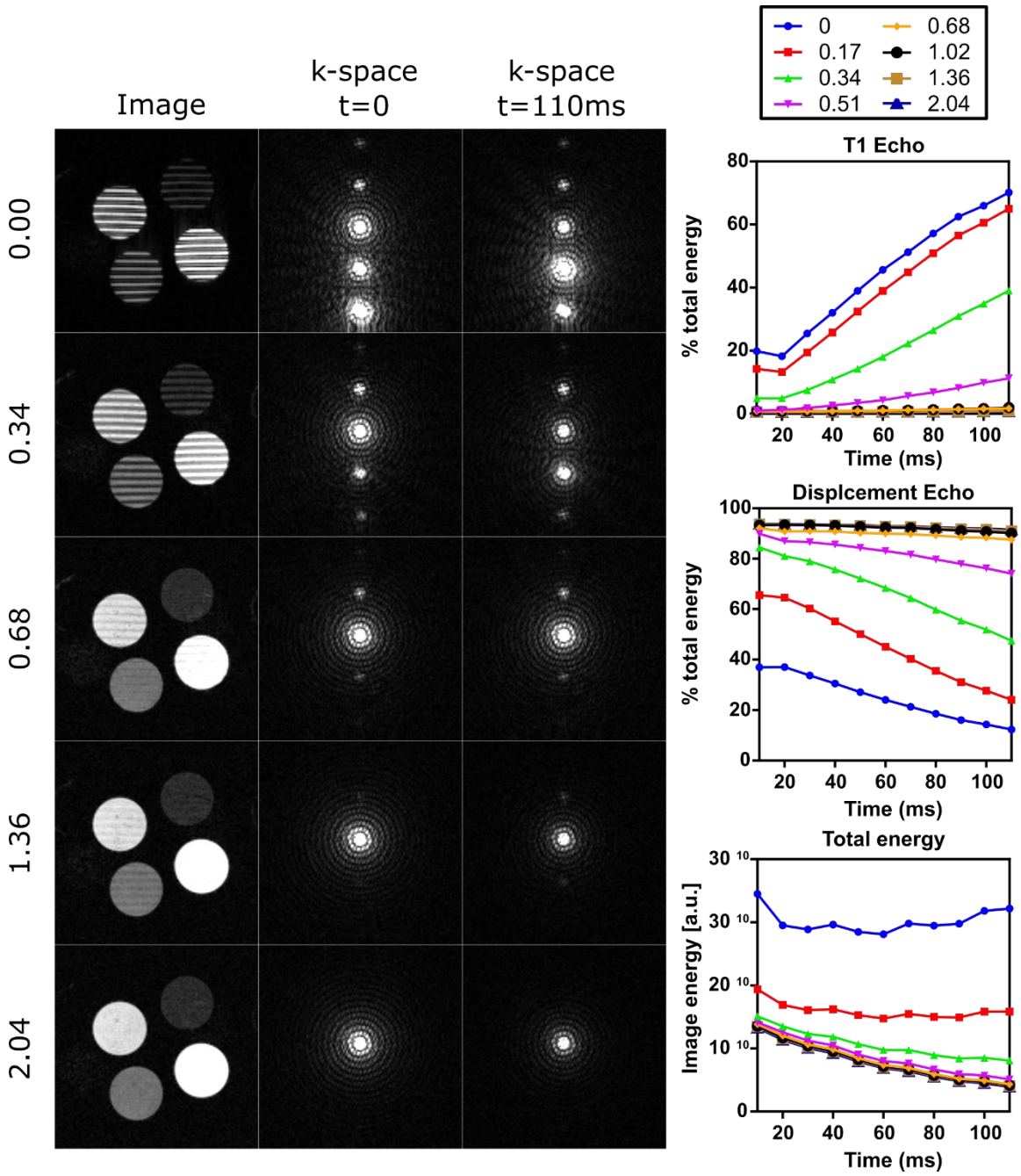

Figure 6.16 TPD testing in a multiple T1 phantom. Values describe the degree of through plane dephasing K_d. As K_d is increased the artefact echoes that are offset from the centre of k-space are suppressed proportionally resulting in the removal of the banding pattern in the DENSE images. The proportion of total image energy contained in the displacement echo becomes more consistent with K_d, however the increased K_d can be related to a decrease in total image energy reducing the available signal. All images are displayed using the same windowing.

As K_d is increased there is a visible reduction in the appearance of the tagging planes in images space. In k-space this is shown by the reduced magnitude of the artefact peaks. Additionally the relative amplitude of the displacement encoded peak vs the artefact echoes is seen to be more consistent as K_d increases. At $K_d = 2.04$ we see no significant artefact echoes and no visible tagging planes. However, there is a noticeable reduction in total acquired image energy as K_d

increases. This suggests that there is an SNR trade off with stronger artefact suppression. The plots on the right of Figure 6.16 show the variation of echo energy with time. The recovery of the T1 echo with $K_d = 0$ follows a multi exponential where each term is of the form described by Equation 2.3, and a term exists for each value of T1 in the acquisition. The 4 chambers in this case then make the recovery of the T1 echo a quad-exponential recovery. Once $K_d > 0$ this relationship is no longer true due to the through plane dephasing terms. The displacement echo as a fraction of total image energy can be seen to decay in cases where K_d does not sufficiently supress the artefact echoes i.e. where $K_d < 1.02$. These figures are a good example of why these echoes need to be suppressed. Since only the displacement encoded echo contains information about tissue displacement it is important for this information to be isolated. The displacement encoded echo with $K_d = 0$ shows that at its peak the displacement echo only accounts for 38% of total image energy. Meaning the other 62% is artifactual information.

Although a useful examination of the effects of K_d on DENSE images these data are not fully relatable to the in-vivo case due to the absence of motion and physiological effects. The effect of K_d on echo suppression was next tested in vivo by imaging healthy mouse heart. Results are shown in Figure 6.17.

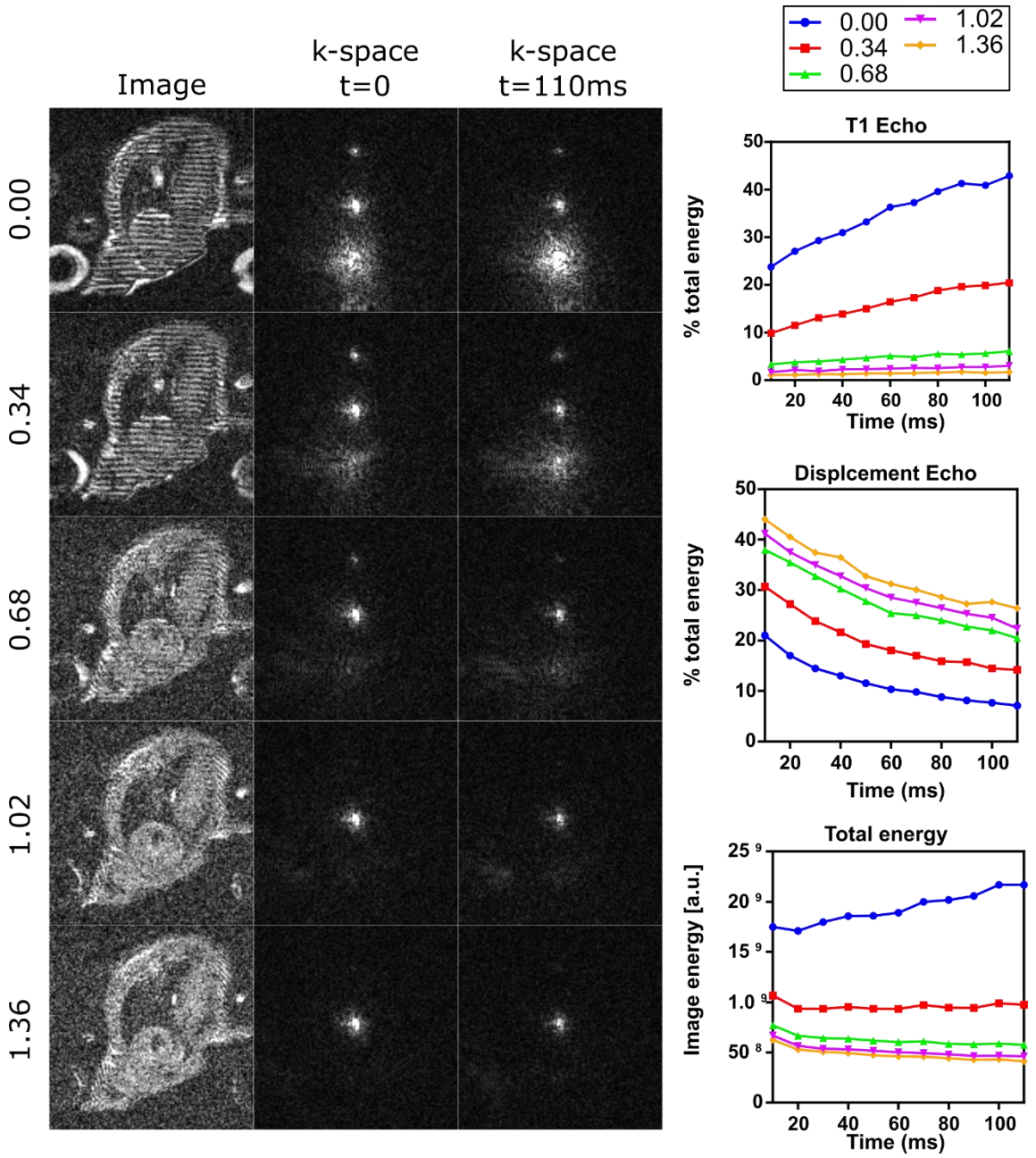

Figure 6.17 TPD in vivo testing in the wild type mouse heart. Values describe the degree of through plane dephasing K_d. SNR is an order of magnitude lower in vivo relative to the phantom. Increasing K_d however shows a consistent relationship with the suppression of the T1 echo. All images are displayed using the same windowing.

The echo suppression in vivo is similar to the phantom case. With the echoes sufficiently supressed from approximately $K_d = 1$ cycles/mm. The recovery of the T1 echo follows a complex exponential recovery relative to the phantom example due to the wide range of T1 values present in the in-vivo case. The displacement echo appears to be far more susceptible to signal decay for the in vivo case relative to the phantom tests potentially limiting the accuracy of DENSE later in the cardiac cycle.

The most significant change when implementing TPD DENSE to in vivo is the marked decrease in SNR at higher values of K_d. This is partially due to the presence of a higher TPD gradient although the primary cause of SNR at higher values of K_d is the removal of the T1 echo. The DENSE technique is limited to relatively low SNR due to the isolation of a single stimulated echo that contains all image information. The majority of image energy tends to be contained within the T1 echo, by suppressing this there is a significant SNR penalty. The additional SNR penalty of introducing the TPD gradient is assessed below (6.3.3.3) as part of a comparison of echo removal techniques. Figure 6.18 shows the SNR in TPD images as a function K_d for both the phantom and in vivo case. SNR in the phantom was largely unaffected by K_d following a short period of decreasing SNR at low encoding strengths and the SNR plateaued after around $K_d = 0.5$ cycles/mm. For the in vivo case the SNR is approximately an order of magnitude lower and over the range of K_d tested the SNR continued to decline with increased K_d. This suggests that the ideal value of K_d for TPD DENSE in vivo is the smallest value that can sufficiently suppress the artefact echoes. In this case that was found to be around $K_d = 1.3$ cycles/mm.

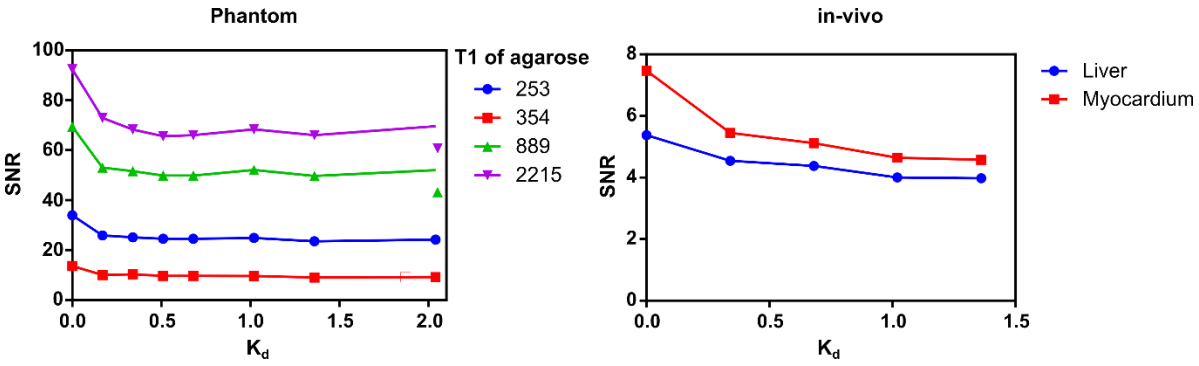

Figure 6.18 SNR vs K_d for the phantom the SNR penalty for increased K_d plateaus at around $K_d = 0.5$. Over the range tested in vivo the SNR continued to decrease in the liver and myocardium. The ideal value of K_d therefore is the lowest that is able to suppress the artefact echoes.

The key advantage of TPD relative to the other echo removal techniques is that it only requires a single acquisition for each direction removing the requirement for additional complementary acquisitions. It is worth noting however that the complementary acquisition methods cDENSE and CANSEL care compatible with the TPD method. Although the TPD gradients induce a phase shift in the magnetisation pattern, so long as the TPD gradients are consistent the phase shift represents a relative offset and does not limit the application of complementary subtraction methods. This suggests that there may be an optimised echo removal technique that utilises complementary acquisitions to remove the majority of the artefact echo signal and a smaller TPD component with a low value of K_d to remove the residual information induced by variations in animal physiology and hardware non uniformities. This may offer accurate artefact

echo removal while reserving displacement encoding and SNR. This remains an objective for future work.

6.3.3.3 Comparison of echo removal techniques for DENSE

Representative images for each dataset with the heart at end systole are shown in Figure 6.19. It can be seen that the techniques that implement a k-space filter suffer from reduced spatial resolution in the image domain resulting in smooth and blocky images. Since CANSEL and TPD do not require a filter they maintain the spatial resolution of the acquisition.

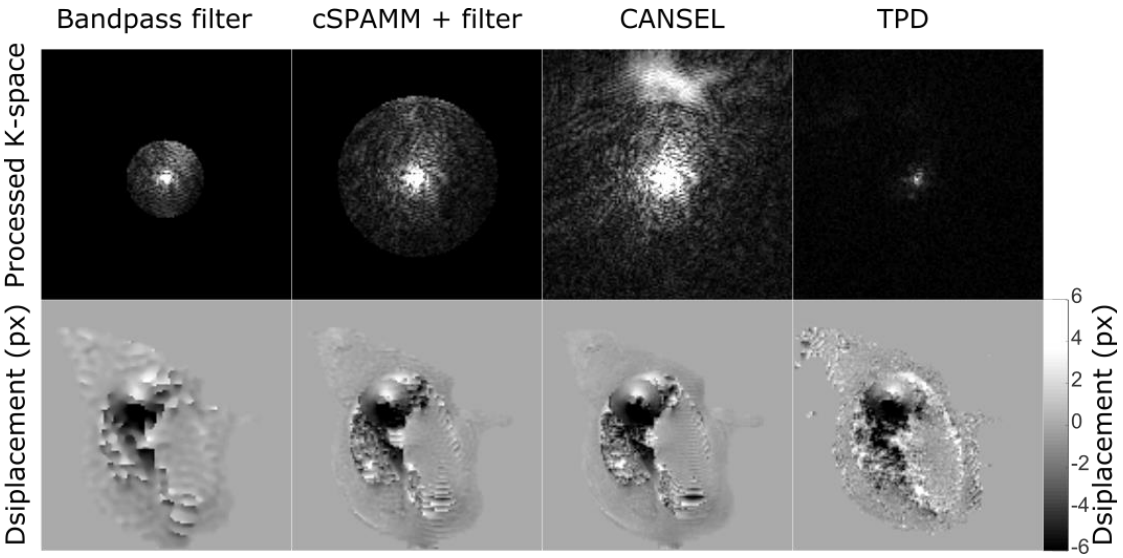

Figure 6.19 Comparison of DENSE echo removal techniques. Top row shows the k-space images following each respective processing method all with the same windowing. Bottom row shows the respective displacement maps (y direction) all with the same windowing.

All acquisitions in Figure 6.19 are displayed with the same windowing, this allows visualisation of the increase in displacement echo signal with echo combination. Recall that cDENSE offers a two-fold increase in displacement echo signal (Equation 6.7) and CANSEL improves the signal by 4x (Equation 6.12). The SNR for each technique plotted against time to show the decay of the displacement encoded echo is shown in Figure 6.20. SNR was calculated from the absolute values in image domain. It can be seen that as expected the CANSEL technique offers the best SNR, although this is only marginally better than the cDENSE method that is twice as fast. The filtering method also provides good SNR but the necessary loss of resolution from the filtering in this method makes it mostly unsuitable to identifying changes in myocardial function. The TPD method requires only one acquisition per direction but has the lowest SNR of all techniques. Due in partially to the dephasing of the signal but the single acquisition nature of this method puts it as a disadvantage relative to the complementary acquisitions that take multiple images.

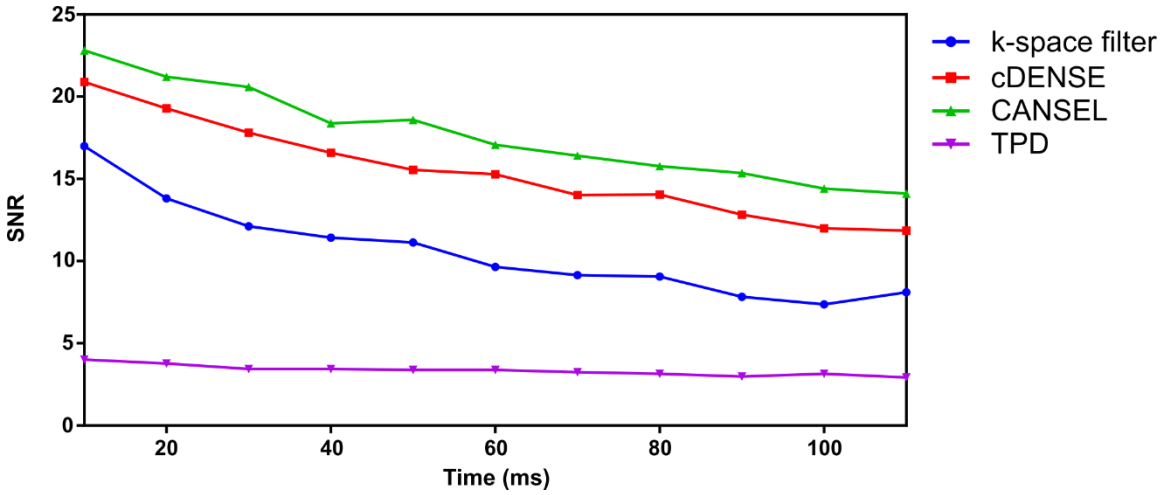

Figure 6.20 Comparison of SNR available with each echo removal technique. CANSEL offers the best SNR but requires 4 acquisitions/direction. cDENSE is close behind but requires only 2, k-space filtering is unsuitable due to its low resolution and phase errors and TPD has the lowest SNR but maintains resolution and requires only one acquisition/direction.

Looking at this information the techniques that provides the best DENSE information is CANSEL, however the long acquisition time makes it impractical. The effect of SNR on the ability of these images to detect changes in heart function is difficult to quantify since DENSE relies on unwrapped phase data. So long as the noise is not sufficient to effect the effectiveness of the unwrapping algorithm it is unlikely to have a noticeable effect on the displacement maps. Table 6.1 summarises the key points for all 4 techniques.

Table 6.1 Summary of DENSE artefact echo removal techniques

Technique	Mechanism	Advantages	Disadvantages
k-space Filtering	Bandpass filter isolates displacement echo	▪ Simple and fast ▪ No extra acquisitions	▪ Removes all high frequencies ▪ Lowers resolution ▪ Prone to errors
cDENSE	Subtraction of positive and negative sines	▪ Removes T1 echo ▪ Does not require filtering until $+2K_e$	▪ Requires consistent heart rate ▪ Requires 2 acquisitions per direction ▪ Does not remove complex conjugate
CANSEL	Subtraction of positive and negative sines and cosines	▪ Removes all artefact echoes ▪ No filtering required	▪ Requires 4 acquisitions per direction ▪ Requires consistent heart rate

TPD	Supress artifactual echoes in-plane	▪ Removes all artefact echoes ▪ No filtering required ▪ No extra acquisitions	▪ Low SNR ▪ No through plane DENSE

The low resolution of the k-space filtering technique makes it unsuitable for use in studies investigating regional heart function in detail. In tissue engineering it is important to maintain the high resolution of MRI acquisition data of identify subtle changes in regional function. CANSEL is also unsuited to multiparametric imaging due to its long scan time, it is difficult to incorporate it in large studies involving multiple acquisitions. cDENSE and TPD are both suitable however. cDENSE has a slightly limited resolution due to the filter removing the complex conjugate echo although this has a minimal effect on displacement maps. The 2 acquisitions per direction is not excessively long and allows for accurate suppression of the T1 echo while maintaining a high SNR. TPD is the fastest imaging technique and its low SNR has a limited effect on displacement maps.

6.3.4 Results: Myocardial trajectories and strain

This section corresponds to stage 4 of the workflow described in Figure 6.1. The aim of the techniques discussed below is to calculate the mechanical strain of tissue based on the displacement fields produced by DENSE. An additional post processing step whereby myocardial trajectories are calculated is described with the goal of improving temporal strain resolution and producing more physiological motion.

Extracting useful and quantifiable values from DENSE images is vital to making the data useful for identifying cardiac dysfunction or recovery. Previous examples in this chapter have used the myocardial displacement as a quantitative value and although this is useful for visualisation and establishing the sequence it is not necessarily related to cardiac function due to factors such as the tethering effect. For this reason, a processing step was included to calculate the myocardial strain tensor from displacement information.

Examples of fitted LV trajectories are shown in Figure 6.21. Figure 6.21A shows the paths traced by these trajectories where each yellow path corresponds to a single pixel, the overall path follows what is expected of the heart tissue with a twisting and contracting component. The benefits of these smoothed trajectories can be seen in Figure 6.21B where the yellow fitted trajectories are overlaid on the red raw trajectories. The raw trajectories follow jagged paths due

to image noise and phase errors, by utilising a fitting algorithm the motion can be smoothed and any non-physiological roughness in the motion suppressed. Figure 6.21C and D show the vector field plots for a frame in mid-systole for the raw and fitted trajectories respectively.

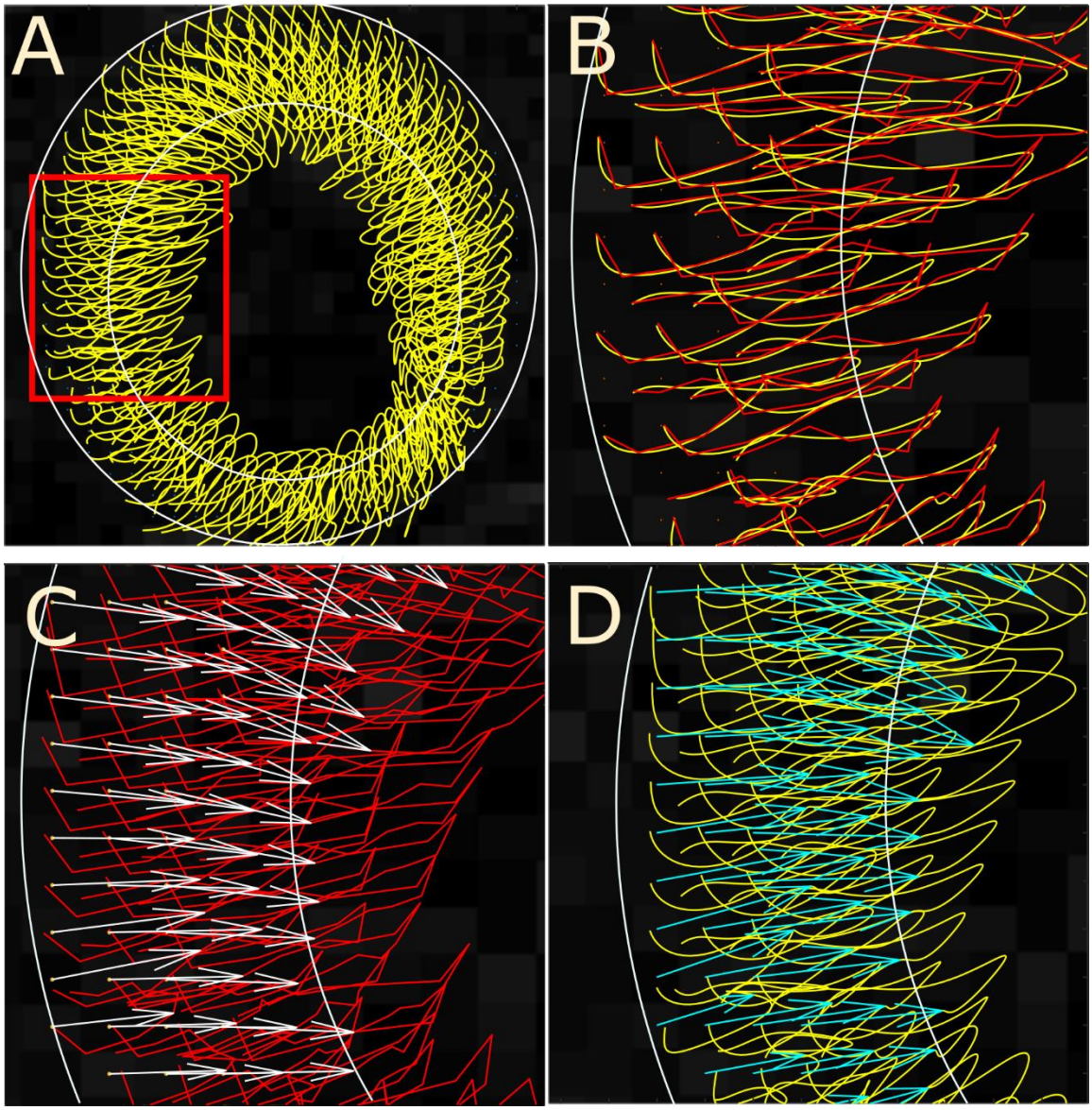

Figure 6.21 (A) fitted trajectories traced in yellow with epicardial and endocardial borders in white. (B) inset showing overlay of raw (red) and fitted (yellow) trajectories. (C) Inset of raw trajectories with mid-systole vector displacement. (D) Inset with fitted trajectories and mi-systole vector displacement map.

Strain values can be calculated from fitted trajectories in the same way as the raw displacement information. Strain fitted to trajectories was found to be smoother and closer to what was expected from previous studies of regional function.[235] Figure 6.22 shows a comparison of raw and fitted strain curves for a naïve mouse in 3 regions. The rough motion of the raw motion

curve over the cardiac cycle causes a jagged strain curve following strain calculations. This strain is not physiological and it is useful to apply the trajectories calculation to remove these rapid transient displacement errors.

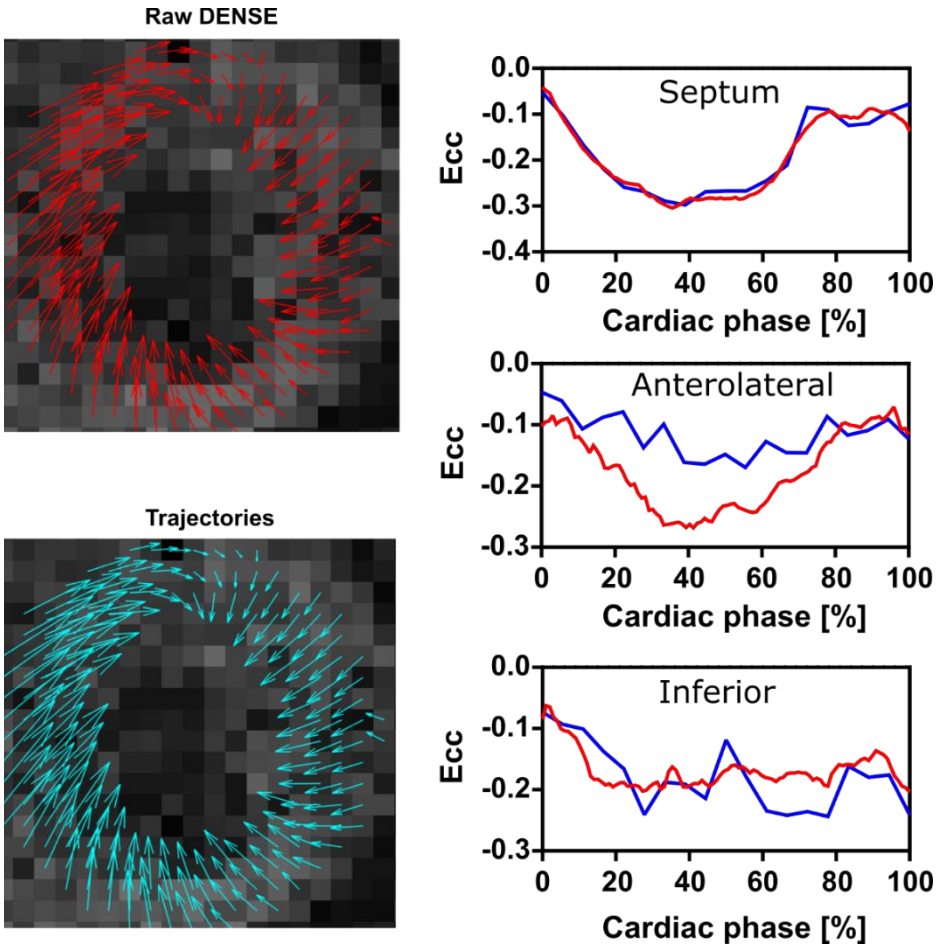

Figure 6.22 Comparison of strain curves in the septal, anterolateral and inferior regions of LV. The fitted trajectories (red) show much smoother strain response compared to the raw motion paths (blue). The fitted trajectories are likely to be more accurate since the strain calculations based on fitted trajectories are less susceptible to phase errors during contraction.

6.4 Discussion

As a measure of regional myocardial function DENSE offers a high resolution alternative to SPAMM and HARP processing. This increased resolution however comes at a cost of scan time, processing time and image noise. A direct comparison between SPAMM and DENSE for investigating regional function will be included as part of a later study on the efficacy of regenerative alginate microspheres in myocardial infarction (7.3).

In this chapter, I develop and optimise a DENSE protocol for preclinical imaging. The result is a cine DENSE sequence that can image displacement over the whole cardiac cycle and a novel PDF

method for removing background field contribution, making this accelerated approach highly attractive for preclinical imaging. An appropriate encoding strength for mouse heart imaging determined heuristically was k_e =1.7 cycles/mm. Through plane dephasing was chosen as the best technique to remove the T1 and complex conjugate artefact echoes due to its shortened acquisition time. The associated SNR penalty with TPD does not appear significant at a through plane encoding of $k_d = 1.3$cycles/mm.

This is the first application of PDF to DENSE field removal and in this case it has proven to be significantly more reliable than subtraction methods to isolate phase changes due to displacement from background sources. Future work would be to further validate this method and find the optimal masking method to minimise the effects of flow and susceptibility boundaries on displacement images without causing excessive boundary artefacts.

A limitation of this sequence is that it currently only supports 2D displacement in a single slice. This is suitable for locating regions of higher or lower contraction in disease models with regional pathology but is not suited to assessing the whole heart. Whole heart assessment will be a valuable tool in assessing the effects of a biomaterial or cell therapy in remote tissue. The long scan time of the DENSE sequence makes it unsuited to performing in multiple slices in its current form and particularly in any study where many scans are performed for a multiparametric outcome. Although accelerating the technique with TPD and PDF goes some way to making this a practical goal the scan time for the finalised protocol was still around 25minutes for a single slice encoded in two directions. Clinical DENSE imaging has been extended to a multislice sequence by Gilson et al. (2005) who used a single modulation phase to read out a phase encode step in 3 short axis slices in each RR interval.[252] The result is a multislice acquisition that sacrifices the cine capability of the sequence. In some cases, the peak strain at systole may be sufficient to describe cardiac function and in these cases this single phase multislice may be useful.

This sequence measures 2D strain by applying the DENSE encoding gradients in the x and y directions sequentially. Each direction requires the acquisition of a single image volume. It is possible to extend the acquisition and acquire an additional image volume where encoding is applied in the through plane z-direction. This allows a single slice acquisition to completely describe 3D motion for all tissue within that slice. This results in a circumferential, radial and longitudinal strain measurement through a 3×3 strain tensor

6.5 Conclusion

In this chapter I have implemented and optimised a DENSE sequence for mapping myocardial strain. The sequence is capable of cine imaging of myocardial displacement with a novel phase correction method that can measure displacement in 2 in-plane dimensions. This sequence will be utilised in a later study on the engraftment of regenerative biomaterials. Future work would aim to extend this sequence to 3D whole heart coverage to produce complete strain maps of the LV.

In chapters 5 and chapter 6 I have described my development of two advanced preclinical imaging techniques for assessing regional heart function in mouse models of cardiac disease. These sequences provide pixel wise maps of 2D myocardial motion that can be converted to full mechanical descriptions of cardiac contraction using measures such as displacement, twist and strain. These sequences add to the MRI imaging toolbox that I have developed over this work for the assessment of regeneration therapies. In chapter 7 I demonstrate the application of these sequences to 3 studies of regenerative biomaterials in myocardial infarction.

Chapter 7

Applications of imaging in cardiac regeneration therapy

7.1 Introduction

Over the course of this thesis I have been performing imaging studies into the efficacy and safety of biomaterial regeneration therapy in parallel with the method developments that have been the focus of previous chapters. This chapter describes three key proof-of-concept studies I performed and demonstrates the evolving protocol that I have developed for assessing preclinical myocardial regeneration therapy. Three separate imaging studies are presented in chronological order:

1. Global and regional cardiac function measurements in scaffoldless cell transplants
2. MRI visible hydrogel with mechanical matching for reduced dysfunction in engraftment region
3. MRI measurements of extracellular, global and regional function changes following alginate microspheres engrafted to the infarcted myocardium

Each study has its own short introduction, methods, results and discussion sections, as well as the key results from that study that led to the development of the subsequent study.

7.1.1 Global and regional cardiac function measurements in scaffoldless cell transplants

7.1.2 Introduction

As discussed in 1.2.5 tissue engineered approaches to cardiac regeneration have many advantages over the more common approach of direct injection of cells in liquid suspension. Following myocardial infarction, regions of heart tissue exhibit changes such as inflammation and hypoxia that make them hostile to cell growth. Transplanting regenerative cells for regeneration into this region results in a high proportion of therapeutic cells undergoing rapid apoptosis following engraftment due to this hostile environment.[262] Promoting the survival of transplanted cells following engraftment is a key field of research for improving cell retention and efficacy in cardiac regeneration therapy.[78] One avenue of research for improving therapeutic cell survival is transplanting cells in scaffoldless cell sheets or monolayers.[263] These are single cell thick patches that are grown in-vitro and can be layered to create a viable 3D construct. The individual layers can be of the same cell type or contain a mixture of cell types. It is also possible

to layer different cell types together. Layered cell types provides a means to tune the properties of the construct and allow additional control over the mechanisms by which the layers interact. This targeted approach allows more direct control of the tissue formation process, allowing therapy to be tuned to the morphological and cellular architecture of the treatment region allowing for more effective therapy.[264] The growth of cellular monolayers became possible following the work of Okano et al. in 1995, developing a process for coating standard polystyrene cell culture dishes with a temperature sensitive Poly(N-isopropylacrylamide) (PIPAAm) film.[265] This film exhibits hydrophobic surface properties at incubation temperature (37°C) but transitions to a hydrophilic state at around 32°C. Cells will adhere to a hydrophobic surface during culture but not to a hydrated hydrophilic surface.[40] This allows whole cell sheets to be lifted from the culture dish intact. Photographs of the lifting process for a cell sheet composed of neonatal rat fibroblasts is shown in Figure 7.1. This lifting process is what makes monolayers an appealing cell delivery strategy. During cell culture neighbouring cells form a complex intercellular microenvironment, comprising cell-cell signalling molecules, surface proteins and accumulated growth factors. Standard practice for extracting cells from culture takes an enzymatic approach such as trypsinization that destroy these intercellular contacts and isolate the cells in suspension. Lifting cultured cell sheets allows the sheet to be transplanted with this microenvironment intact, providing a local beneficial cellular environment that enhances cell survival after engraftment.[266] Cell sheets also overcome several complications associated with other tissue engineering therapies which utilise a biodegradable scaffold as a temporary support and artificial environment for the cells, such as biocompatibility of the ECM and controlled degradation of the scaffold.[267]

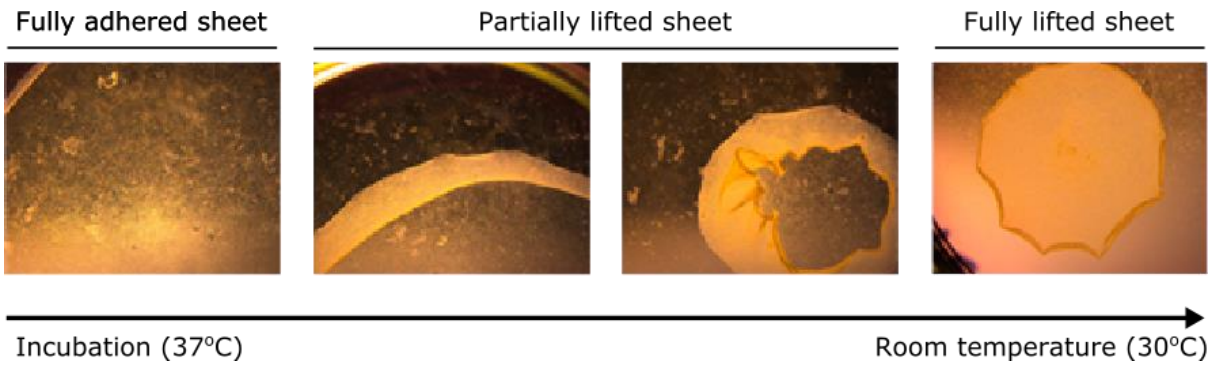

Figure 7.1 The PIPAAm coating on the culture dish is hydrophobic at incubation temperature (37°C) and the cells will actively adhere to the surface. As the temperature is decreased the coating becomes hydrophilic and the cells change shape to detach themselves from the surface while PBS solution is attracted into the space beneath them.

Cellular monolayers have been cultured in vitro using cardiomyocytes by Shimizu et al (2002).[268] The authors produced multiple monolayers cultured from neonatal rat cardiomyocytes and layered 4 sheets together to create viable 3D engineered cardiac tissue. These constructs were observed to mechanically pulse spontaneously demonstrating a contraction mechanism that could potentially be used to restore lost function following MI. The authors then transplanted these cell sheets into subcutaneous tissue of nude rats. Three weeks after engraftment surface ECG electrodes detected electrical pulsatility originating from the graft and macroscopic beating motion could be observed. Histological analysis then showed that the cell sheets had developed into subcutaneous tissue similar to myocardium. This demonstrated the potential for the regeneration of both cardiac tissue structure and electrical activity from transplantations of these monolayers.

Subsequent in vivo studies have engrafted these contractile constructs to the infarcted heart in rodent and porcine models of infarction and have produced promising results. Sekine et al. (2008) transplanted sheets consisting of neonatal cardiomyocytes and endothelial cells in a 6:1 ratio to the infarcted rat heart.[269] The authors demonstrated a significant improvement in capillary density in the infarcted tissue along with increased presence of growth factors VEGF, HGF and basic fibroblast growth factor (bFGF). In another rat study, Narita et al. (2013) demonstrated that skeletal myoblast (SM) cell sheets reduce the impact of arrhythmias in infarcted hearts relative to direct injection of SMs suspended in saline.[270] They propose that this is due to the increased control over transplanted cellular architecture, specifically, preventing the formation of cell clusters which can disrupt electrical conduction. The cellular monolayers have also been validated as a therapy in large animals. A study by Miyagawa et al. (2010) cultured autologous skeletal cells into monolayers and engrafted them to the epicardium in a porcine model of MI.[271] The authors used echocardiography to show that cardiac function was significantly improved following therapy, with increased ejection fractions, fractional shortening and preserved LV architecture.

In this first study I aimed to familiarise myself with the basic imaging techniques for the quantification of infarct size as well as global and regional heart function in rat hearts following neonatal rat fibroblast monolayers as a therapy for myocardial infarction.

7.1.3 Methods

7.1.3.1 Cell sheet preparation

Cell sheets were cultured by Dr Vassilis Georgiadis (University College London).[78] 300,000 neonatal rat cardiac fibroblasts were seeded into temperature sensitive dishes and cultured for 14 days in DMEM with 10% FBS at 37˚C in 5% CO2. Fibroblasts were chosen for the culture of the cell sheets for their availability and known paracrine effects.[272] The cell culture was labelled with the fluorescent membrane stain DiL (molecular probes) 549/565nm excitation/emission to enable fluorescent imaging at the study end. Example OPT images showing labelled and unlabelled cell sheets suspended in 1% agarose are shown in Figure 7.2.

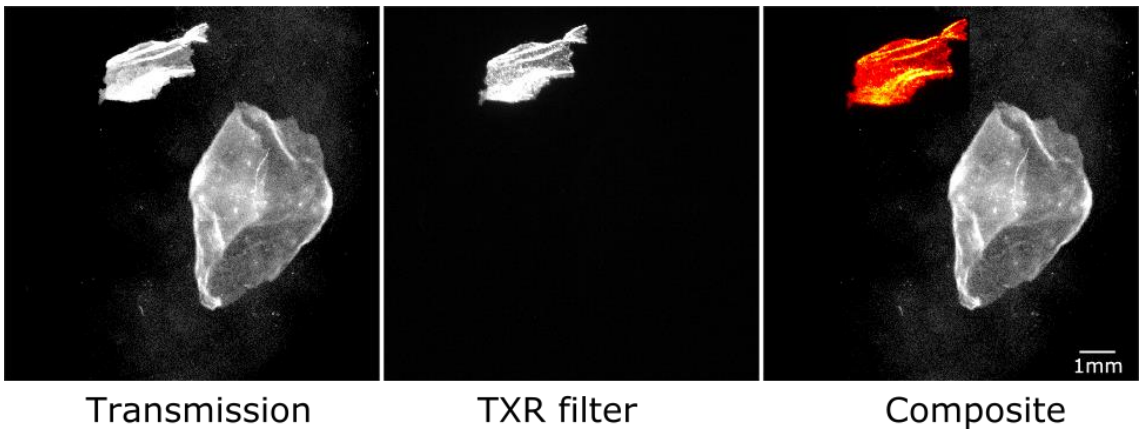

Figure 7.2 Example OPT images showing cell sheets in agarose suspension. Transmission images show attenuation of light through monolayers, TXR filter isolates fluorescent emissions at 560/20nm from the DiL membrane stain. Combining these images in a composite allows visualisation of fluorescent cells.

On the day of engraftment, the temperature of the dishes was reduced to 30˚C to induce the thermal change in culture surface affinity. The cells were left to lift form the dish for 1 hour to ensure complete separation of the sheet from the culture surface. Sheets were transferred to a standard 12 well plate in culture medium and stored at 37˚C to await engraftment. Cell sheets were engrafted to the myocardium within 5 hours of lifting.

7.1.3.2 Animal preparation

Coronary ligation surgery and cell sheet engraftment was performed by Valerie Taylor (University College London). Adult Wistar rats were anaesthetised in an induction chamber using 3% isoflurane in oxygen before intubation so that respiration could be artificially maintained by an external ventilator with a stroke volume of 500µL at a rate of 40 breaths per minute and 2% isoflurane in oxygen. The rat was placed on a heated operating surface with body temperature maintained at 37±0.5°C. The heart was accessed through the fourth intercostal space where an

incision was made through the skin and pericardium to expose the anterior wall of the LV. The LAD was identified and a suture placed underneath the vessel at the point of ligation before being tied off around a piece of sterile tubing placed above the vessel. During this 40-minute occlusion period, 3 individual cell sheets were removed from suspension in PBS and layered directly over the epicardium at the anticipated anteroapical infarct region. Sheets were adhered to the epicardium by the preserved cell surface proteins, an inherent advantage of this cell lifting technique. Following the desired ligation time, the tubing was removed and the suture severed to reperfuse the tissue. Animals were monitored during recovery to ensure welfare. Animals were allowed to recover for 7 days prior to imaging, this allowed time for myocardial remodelling in the presence of the cell sheets.

Groups included sham surgery with no infarction (n=3) to act as controls, infarcted hearts with no cellular monolayers (n=6) and infarcted hearts with cellular monolayers (n=4).

7.1.3.3 MRI methods

In-vivo imaging was performed with a 9.4T Agilent system (Agilent Technologies Inc., CA, US) equipped with a 72mm volume transmit coil and a 4 channel surface receive array. Rats were anesthetised under a mixture of isoflurane and oxygen and ECG, respiration and temperature monitored for image gating and to maintain depth of anaesthesia.

Following slice localisation, a stack of cardiac short axis slices were acquired to measure global heart function. Cine images were analysed by segmenting the LV borders using Segment software.[185] Following cine imaging, a Gd-DTPA infusion was delivered via intraperitoneal injection at a dose of 46.9mg/g with 20 minutes allowed for circulation and imaged using a LGE inversion recovery sequence.

The cell sheet therapy is a regional treatment and so an in-vivo regional analysis tool is required to assess the local influence of the therapeutic cells. Global assessment using cine MRI only partially describes the complex contraction of the heart and cannot measure myocardial twist or differentiate quantitatively between akinetic scar tissue and actively contracting regions. This study was performed prior to my development of SPAMM/HARP or DENSE at our facility meaning that these techniques were unavailable. For this reason, the standard tag-cine sequence provided with the Agilent imaging system was used. This sequence was a DANTE prepared tagged-cine sequence that produced a tagging pattern similar in appearance to SPAMM tagging, however the modulation of magnetisation is not sinusoidal with uneven spacing between tag places. A tagged cine image for assessing the contractility of the LV was

acquired with FOV = 5.2cm^2; pixel size = 0.13×0.13×1mm; TE = 2ms; tag spacing= 0.3mm; averages=2 with 27 cine frames at a standard rat heart rate. This tagged cine was acquired through a slice containing the infarcted/treated myocardium. The uneven tag spacing in these images means that the HARP tissue tracking technique cannot be used. Therefore, tagged images were analysed using an alternative method implemented through the inTag plugin for Osirix. The tag analysis software inTag tracks tag lines using a sine wave modelling approach (SinMod).[273] In this approach a sine wave model is fitted to each pixel so the moving line of hyperintensity is treated a moving wavefront. From this model the displacement can be measured to sub pixel resolution based on interpolating the deformations provided by this model. SinMod has been shown to give favourable results with respect to HARP and was chosen for the availability of a commercial implementation at the time of this study. inTag data was used to assess regional circumferential strain over the cardiac cycle.

7.1.3.4 Optical projection tomography

For ex vivo imaging such as optical projection tomography it is necessary to excise the tissue and prevent decay to maintain internal structures. This was achieved through perfusion fixation as described by Gage et al. (2012).[274] In brief the perfusion fixation protocol consisted of a terminal administration of sodium pentobarbital. Once unresponsive and in a surgical plane of anaesthesia the chest was opened by incision beneath the sternum and the diaphragm pierced to expose the pleural cavity. The left and right side ribs were then cut through up to the collarbone and the chest wall pulled back to expose the heart. A 27G needle was then passed into the LV through the apex and the right atrium cut to provide an outflow tract for the perfusate. Heparinised phosphate buffered saline (PBS) was pumped through the LV at a constant flow rate provided by a syringe pump. This removed all blood from the specimen. Following sufficient exsanguination, the perfusate was switched to 4% paraformaldehyde (PFA) to fix the tissue. The heart was then extracted and immersed in 4% PFA for at least 8 hours to finalise fixation.

Heart tissue was then dehydrated in 3:2 ethanol and dimethyl sulfoxide (DMSO) for 14 days with daily changes of solution, then transferred to 1:2 mixture of benzyl alcohol and benzyl benzoate (BABB) for 7 days, changing the solution every two days. Imaging was performed using a commercial OPT system (Bioptonics, MA, USA) using a Texas Red filter (560nm) to image DiL membrane fluorescence and GFP+ filter (470nm) to image long wavelength tissue autofluorescence for anatomical reference. Projections were acquired over 360° with 0.45° steps

and the tomographic volume reconstructed using a filtered back projection (FBP) algorithm as described in 2.4.

7.1.3.5 Statistical tests

All results are presented as mean value ± standard error. All data were tested for normality using the Kolmogorov-Smirnov test and significance values were calculated by one-way analysis of variance corrected for multiple comparisons using the Holm-Šídák method. In all cases a p-value of less than 0.05 was considered significant.

7.1.4 Results

Results from cardiac MRI are shown in Figure 7.3. Due to low group numbers it would not be fully accurate to determine the distribution of data for this reason individual data points are plotted on graphs to aid interpretation. End systolic and end diastolic volumes showed no significant differences.

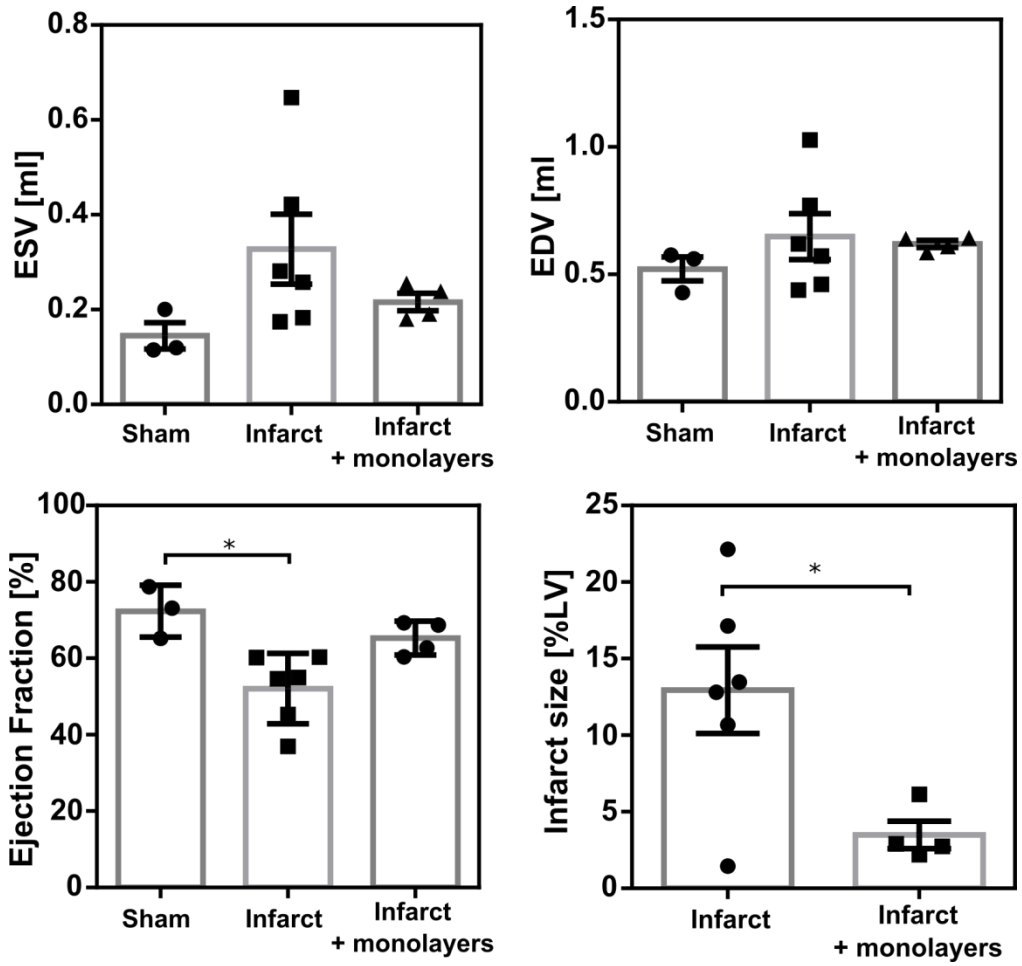

Figure 7.3 Results of cine MRI. End systolic volume (ESV), end diastolic volume (EDV) and ejection fraction were quantified from cine MRI imaging and infarct size was quantified from LGE inversion recovery imaging.

Ejection fraction was significantly (p=0.015) lower in infarcted untreated rats (52±4%) versus sham surgery rats (72±4%), this is consistent with the loss of contraction and remodelling effect following MI. The treated monolayer group however had an ejection fraction (65±2%) that although lower was not significantly different from the sham group. This may indicate improvement in global heart function in the treated group suggests that the monolayers may provide some therapeutic benefit to global heart function.

The scar size was quantified from inversion recovery images in the infarcted and treated groups, representative LGE images are shown in Figure 7.4. The control group were not assessed as no regions of myocardial enhancement were visible. There was a significant (p=0.015) reduction in infarct scar size as a percentage of the total LV in the monolayer treated group (3.5±0.9%) versus infarction with no treatment (12.9±2.8%).

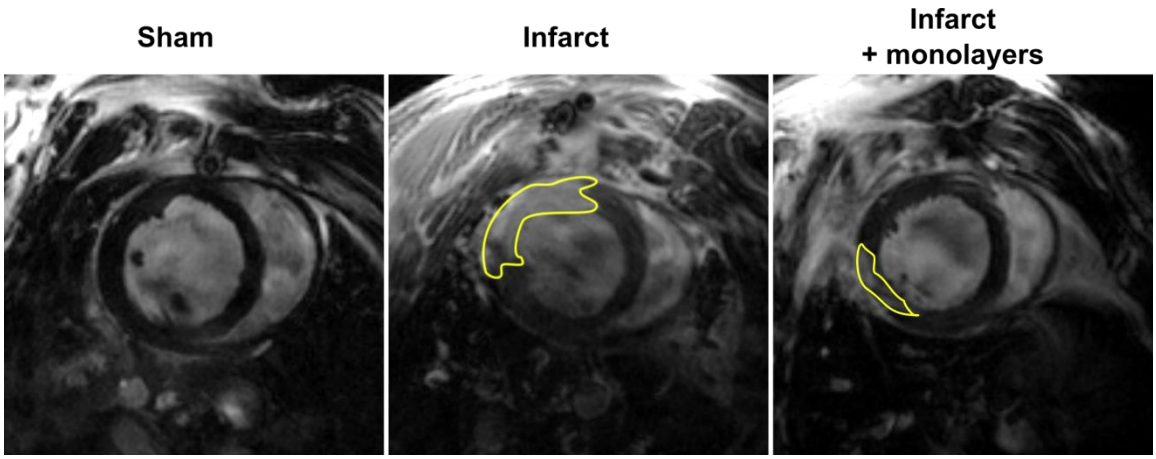

Figure 7.4 Representative LGE images showing the approximate LV scar boundary (yellow) in the infarct and treated group. Sham group shows no scar tissue.

Regional function measurements are shown in Figure 7.5. The plots here show the mean circumferential strain as a function of time for a 6 segment model of the LV as was the case with the cine structure assessment in Chapter 4. The curves plotted in these figures are a fitted 5th order polynomial function to aid in visualisation of the strain-time curves. These segments are further characterised by the infarct region in the surgery. The anterolateral region developed the infarct, the neighbouring anterior and inferolateral segments were characterised as border zone and the inferior, inferoseptal and anteroseptal segments were classified as remote.

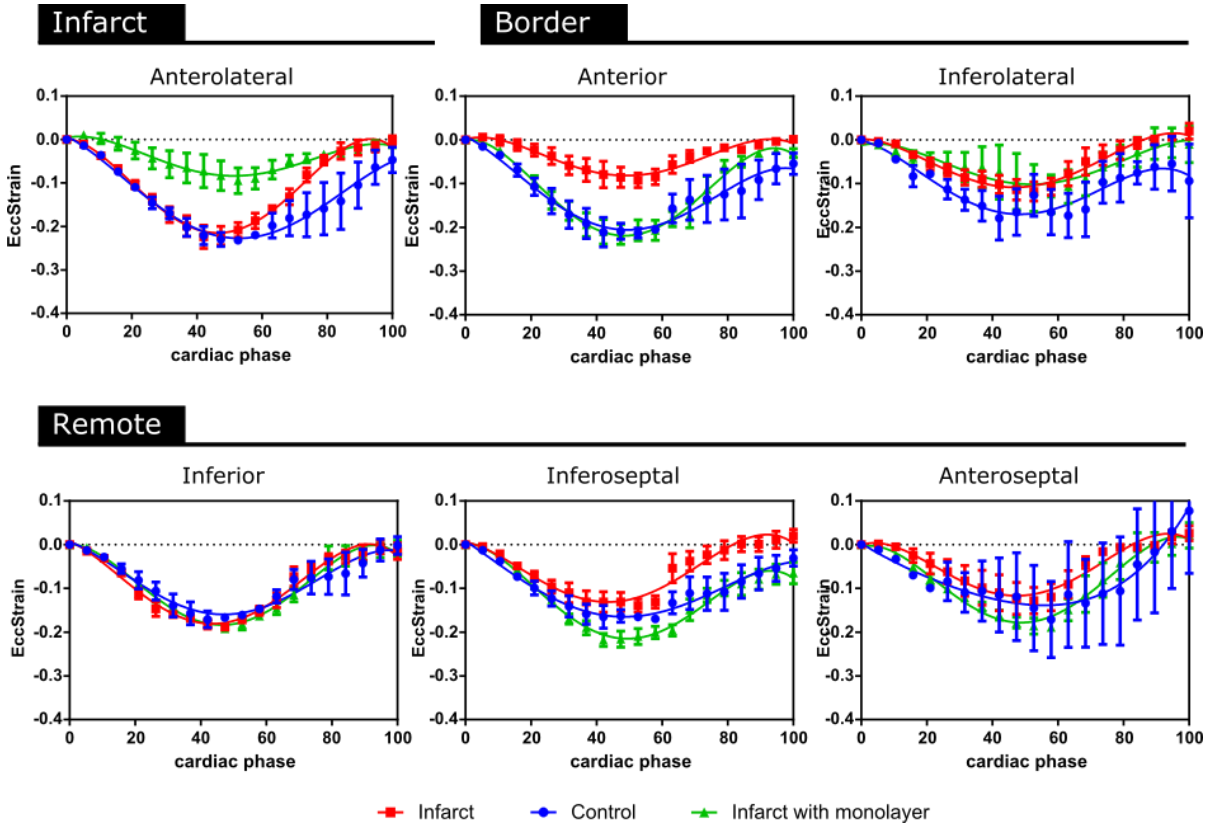

Figure 7.5 Regional function assessment of monolayer therapy with tagged MRI. Strain curves are plotted for each group for comparison in each segment of LV. The segments are characterised as infarct regions, border zone or remote tissue. Polynomial curves are fitted to the data to aid visualisation.

In the infarcted region the contraction strain is lower in the monolayer treated group relative to the sham and infarct groups, suggesting that the cell therapy was not effective at improving function at the site of infarction and reduced contraction in this region. In the anterior infarct border zone however, the strain did appear to be improved by the application of the monolayer therapy. Remote tissue showed mostly similar results in all groups suggesting that distant uninfarcted tissue was not affected. There was increased variability in strain measurement of the anteroseptal region for the sham surgery group. This was due to poorly tracked regions of tissue in the inTag software.

Further quantification of the relative contraction in each segment can be provided by the peak strain that can be a useful measure to summarise the contraction of a segment of LV. Peak strain is compared for infarcted, neighbouring and remote (posterior) segments in Figure 7.6. The inferoseptal region was chosen to act as the remote tissue since it receives the smallest relative blood supply from the LAD and is therefore least likely to suffer an infarction injury from LAD ligation surgery.

The infarcted group without treatment showed the smallest peak strain values in the infarct zone and border zone segments with similar values across groups in remote myocardium. Strain was only significantly different between the infarcted and sham groups (p=0.027) in the neighbouring regions (p=0.027). In this region, the peak strain in the infarct group was reduced (-0.11±0.01) relative to the sham group (-0.21±0.03) but the treated group showed improved strain that was not significantly different from the sham group (-0.17±0.05). There was no significant difference between peak strains in these segments between the sham and monolayer treated group. These results are consistent with the global functional measurements, showing the monolayer treated group has similar properties to the sham groups indicating the therapy may be effective. The additional information provided by the regional assessment tagged MRI techniques has shown that this improved contractility originates from increased contraction in the infarct border zone.

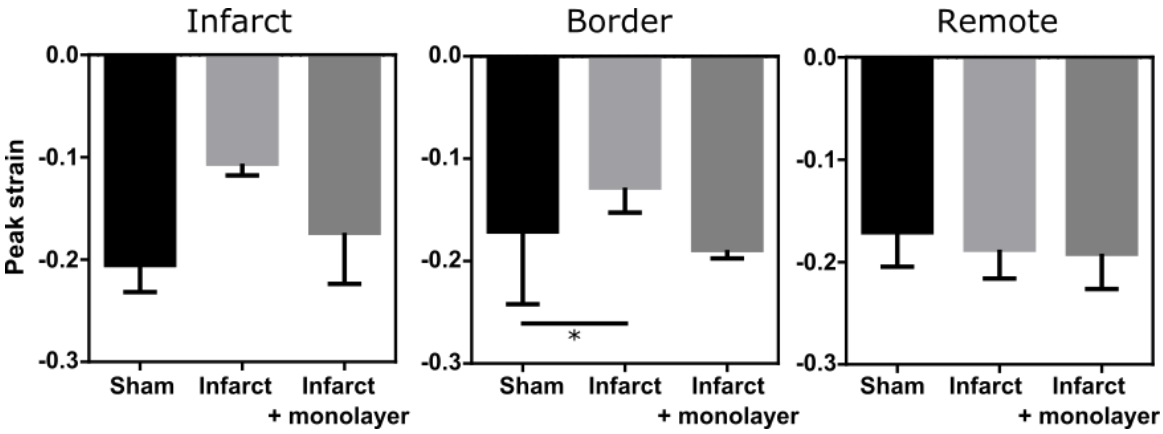

Figure 7.6 Comparison of peak strains in infarcted, neighbouring and remote myocardium. The infarcted group shows the smallest peak strain in each segment, the monolayer group however shows no significant difference compared to the sham surgery.

To be able to reliably attribute any functional change in the heart to the treatment it is necessary to demonstrate the continued presence of the treatment cells. Cell loss is an issue in many cardiac regeneration therapies and successful engraftment is essential for the cells to stimulate recovery. In this case fluorescent labelled cell membranes allowed tracking of the

cardiac fibroblasts using optical projection tomography (OPT). Representative OPT data is shown in Figure 7.7.

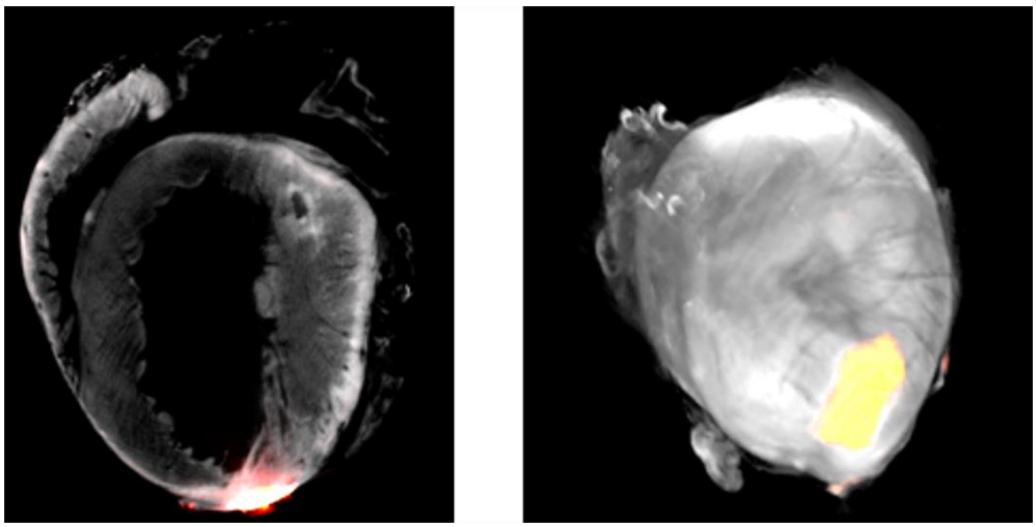

Figure 7.7 Representative OPT imaging (L) tomographic reconstruction of a single slice showing fluorescence from DiL labelled cells in apical region. (R) 3D surface rendering showing distribution of fluorescence on surface of the heart.

These images show that there in fluorescence at the epicardium 21 days post engraftment, suggesting that the treatment cells adhered successfully with the myocardium. OPT is not a technique ideally suited to rat hearts due to their relatively large size. The tissue clearing process requires good penetration of the dehydration and clearing agents and this can be challenging for tissue with a thickness >1mm. The result is that deeper tissues do not clear as well as surface tissue and produces and edge enhancement artefact in reconstructions. This is visible as hyperenhancement at the tissue surface in reconstruction and a loss of signal in deep tissue in Figure 7.7.

7.1.5 Discussion

This study has established the basic imaging techniques required for quantification of cardiac function and viability in myocardial infarction. The imaging techniques were applied to in the context of investigating a novel cellular monolayer therapy in rats. The data presented here suggests that cell patches composed of neonatal cardiac fibroblasts may help limit the damage suffered by the rat heart during infarction. In-vivo analysis of cardiac function shows an improvement in ejection fraction when compared to untreated hearts and a regional improvement in circumferential contraction in the infarct border zone following engraftment. The continued presence of fluorescent membrane stains at 21 days post-engraftment suggests

that the cells are adhering to the myocardium. Improved contraction in the infarcted and neighbouring regions suggest that the presence of the cell sheet is beneficial to the heart. Although fibroblasts do not have the regenerative potential of progenitor cells for cellular integration, these results show that a fibroblast patch may stimulate regenerative or damage limiting effects through paracrine factors. Over the short timescale of this study regeneration of tissue is not expected to occur, making these paracrine effects the most likely factor producing therapeutic benefit.

As this study was powered towards establishing imaging techniques the study has a number of limitations that must be discussed in the context of making a conclusion about therapeutic effect. The low sample sizes of the infarct with monolayer therapy group (N=4) was due to the complexity of producing the cellular monolayers. The cell sheets are inherently delicate and were frequently torn and disintegrated during the lifting procedure making engrafting them impossible. Despite this some positive outcomes were observed in the animals that did receive the therapy. The lack of statistical significance in the ESV and EDV measurements may be in part due to the variability in the myocardial infarction surgery. Investigating the distribution of values in the infarct group in Figure 7.3 shows that there is a wide range of scar sizes from a minimum scar of 1.4% up to 22.1% of the LV. This variability is not only limited to scar size but also scar location. The vasculature in the LV is complex with a dense network of collateral venous and arterial vessels, meaning that depending on the exact nature of the induced myocardial injury will determine the scar properties and this may not be sufficiently reproducible between animals. This can be seen by the varying infarct locations in Figure 7.4, the infarct in the untreated group example develops in the anterior wall, while in the treated group example it develops in the posterolateral wall. An additional consequence of this variability is that improvements in cardiac metrics in the treatment group must be treated with caution as there is a possibility that in the MI surgery produced only minor infarctions in these animals. Minor infarctions in these animals would appear similar to a successful therapy. Monolayers were grafted during infarction surgery to negate the need for a complex second thoracotomy to enable sheet attachment at a later time point. This meant there was no way to determine whether the initial infarction surgery was successful or similar between groups. Ideally LGE and cine imaging would be performed post infarction surgery and prior to therapy to establish the existence and extent of MI in each animal. A future study developing this therapy would require larger sample sizes to minimise the statistical power of this variability.

Although OPT can produce a high resolution 3D map of cell distribution this technique is non-quantitative and represents only the presence of cells and cannot provide an accurate

quantification of cell population or importantly whether the cells are viable. The signal depends only on the presence of the fluorescent molecule DiL and so viable cells and residual fluorescent molecules from dead or displaced cells cannot be differentiated. Bioluminescence imaging (BLI) was introduced in later studies to allow for imaging of cell viability due to the limitations presented here with OPT. The fluorescent cells at the epicardium indicate the cell adhesion has occurred between the monolayers and the host tissue but does not confirm full integration. Confirming integration would require additional histological staining methods and high resolution microscopy such as fluorescence microscopy imaging. However, the OPT chemical clearing process makes tissue samples unsuitable to further processing so this could not be performed. The OPT quantification of biomaterial location has an additional disadvantage in that it is an ex-vivo imaging technique. The OPT tissue clearing process may potentially remove therapeutic cells or material that has not fully adhered to the heart. This limitation was recognised in this study and led to the development of techniques for the in-vivo detection of transplanted biomaterials using gadolinium agents to provide MRI contrast these materials are discussed further in 7.3.

This sheet of a single cell type was able to successfully adhere to the epicardium. However, a patch with a more complex structure such as a contractile sheet of cardiomyocytes and endothelial cells may offer more scope for regeneration. More advanced patches and constructs will come with more complex integration requirements of the construct with the existing tissue. For example, orientation and engraftment location will become important if the construct is to produce contractile motion. The imaging techniques developed with this study are a valuable tool for assessing the position or detrimental effect of engrafted biomaterials. Cell patches as a treatment have advantages in terms of regenerative therapy are viable for small animals such as rodents but scaling them to be suitable for clinical use has a number of obstacles. The patches used in this case were composed of layers approximately 1cm across, scaling layers up to the size required for a human heart would require developments to the growth method. Growing larger patches makes it more difficult to lift the cell sheet off in one piece due to the likelihood of variable cell densities across the monolayer. The thickness of patches is currently limited by the diffusion of oxygen to cells. Without integrated vasculature, oxygen can diffuse to a depth of approximately 150μm,[78] beyond this depth the tissue construct would require its own blood supply that is successfully integrated with the host coronary circulation.

This study proved to be a promising pilot study in establishing cellular monolayers as an effective therapy for MI in rats. However, with the departure of Dr Vassilis Georgiadis the technical expertise required to grow the monolayers was gone, effectively terminating this avenue of

research. Future investigations would have applied the monolayer therapy to larger groups of animals to improve statistical power. It would also have been interesting to grow cell sheets from cell lines known to have more potential in regenerative medicine such as cardiac stem cells or bone marrow mononuclear cells.

To conclude, this study has established techniques and demonstrated the value of imaging in the assessment of regenerative therapy. MRI was able to quantify functional changes in LV contraction and structure in MI following the engraftment of a cell sheet composed of neonatal rat fibroblasts. Improvements in ejection fraction were observed as well as a reduction in scar size. MRI tagging showed that contraction is improved in the cell sheet treated hearts in the infarct border zone relative to untreated infarction. OPT found that fluorescence from the engrafted cells was detectable at 21-days post engraftment suggesting that adhesion between the cellular monolayer and the native epicardium has successfully occurred.

7.1.6 Key results

- Imaging techniques developed for assessing global and region heart function and structure.
- Rats treated with cell sheets showed reduced scar by LGE size as well as improved contraction in the infarct border zone from MRI tagging.
- Cell adhesion 21-days post engraftment was demonstrated using optical projection tomography.
- In situ imaging of viable cells may offer more information about success of engraftment

7.2 MRI visible hydrogel with mechanical matching for reduced dysfunction in engraftment region

Some of the work described in this section forms part of the paper Multi-modal hydrogel platform to enhance and monitor cardiac progenitor/stem cell engraftment. (under review) by Alessondra T. Speidel, Daniel J. Stuckey, Lesley W. Chow, **Laurence H. Jackson**, Michela Noseda, Marta Abreu Paiva, Michael D. Schneider and Molly M. Stevens.

7.2.1 Introduction

An alternative cell delivery strategy to the surgical engraftment of monolayers method described above is suspension of the cells an injectable medium (e.g. saline, alginate, collagen) and engrafting the cells by injection. The advantage of this technique is its versatility. The monolayer technique described in Part 1 allows for the engraftment of cells with a pre-established cellular microstructure but the development of these sheets is technically complex and requires specialist materials and skills to manufacture. Injectables are technically simpler to manufacture, engraft and are able to be delivered to the transmural myocardium potentially increasing their efficacy. The practical advantages of injectable therapies have helped them become widespread in clinical and preclinical trials investigating cardiac regeneration.[108] The most common method for cell delivery in clinical trials has been via intracoronary injection, although a few opt for a more direct transendocardial intramyocardial injection delivered through a needle catheter. However, injection as a method for delivery of cells can result in a high proportion of the injected material being lost immediately following injection due to the contractions of the heart.[275] The injected material is physically forced from the heart by the contraction of the myocardium displacing the material into the pericardial space. The optimal delivery method for stem cell therapy remains unknown and remains an area of investigation.[276]

As discussed in1.2.5 there are a huge number of variables to consider when designing a biomaterial for cardiac regeneration. This study investigated the safety and retention of an advanced hydrogel based on poly (ethylene glycol) (PEG) polymers cross linked with dithiol and heparin binding peptides functionalised with bound gadolinium contrast and luciferase expressing cardiac stem cells (CSCs). This study was performed in collaboration with researchers at Imperial College London who provided the stem cells and biomaterial. This study used the MR imaging techniques developed in previous chapters to assess the safety of engrafting this

functionalised PEG hydrogel by performing ultrasound guided injections of hydrogel into healthy hearts in the absence of MI.

Poly (ethylene glycol) is a hydrophilic polyether molecule (H−(O−CH2−CH2)n−OH) that can be crosslinked to form variable 3D polymer networks with a high water content (hydrogel). PEG is a synthetic polymer; both synthetic and natural polymers have been utilised in cell therapy research and both have their relative advantages. PEG based hydrogels have a wide range of biomedical applications such as controlled release platforms for drug or bioactive molecules, cell delivery mediums and physical support.[277-279] The properties of PEG which make it so widely applicable to biomedical fields is its biocompatibility, biodegradability, temperature responsiveness, non-ionic properties and versatility in polymerisation. The biocompatibility of PEG hydrogels results in a minimal immune reaction following engraftment to the host tissue which maximises the survival of transplanted cells. PEG hydrogel microenvironments are highly permissible and readily allow diffusion of gases, biomolecules and nutrients. This property makes them ideally suited to transplanting cells and aids in the regenerative effect from paracrine signalling. However, this same property is seen as a hindrance for controlled release of biomolecules since the gel networks are equally permeable to the therapeutic molecules controlling their release is a major challenge. PEG hydrogels can be manufactured to gelate at physiological temperatures. Jeong et al. (2000) produced a PEG based hydrogel that was aqueous at room temperature but solidified at 37°C.[280] The authors injected the polymer solution in its liquid state subcutaneously into rats. The gel solidified in-situ and maintained mechanical integrity up to 1-month post engraftment.

Controlled degradation of the hydrogel is important for allowing native tissue to regenerate and replace the engineered graft. The biodegradation profile of the PEG hydrogel can be changed through altering the polymerisation reaction e.g. incorporating a bond breaking reaction at a later time point to induce degradation. The most commonly used mechanism is hydrolysis where a molecule of water adds to the polymer backbone and breaks a link in the polymer network. Alternatively hydrogels can be degraded by enzymatic degradation or photodegradation.[281-284]

Gelation of PEG polymers is typically performed through chemical or covalently bonded crosslinking that leads to stable and controllable polymerisation. By changing the type, concentration or mixture of available crosslinkers allows the manufacture of hydrogels with varying permeability, mechanical properties, water content and degradation profiles. As the density of cross-linking increases the network mesh size decreases, swelling ratio due to water uptake decreases and the stiffness increases. This relationship is roughly described in Figure 7.8.

The gelation of PEG hydrogel can be performed at temperatures and pH levels that are hospitable to cell culture allowing for live cells to be encapsulated with the hydrogel.

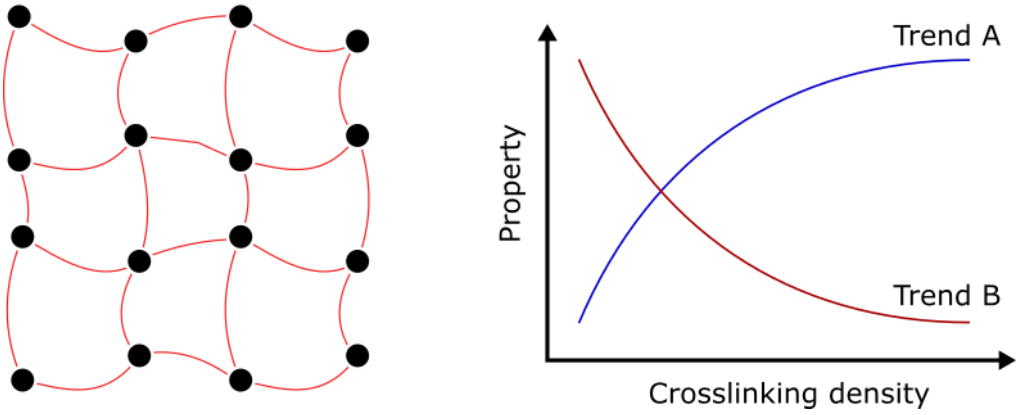

Figure 7.8 Simplified PEG hydrogel where black circle indicate crosslinking points and red lines indicated PEG polymers. Changing the density of crosslinking points in the PEG gel allows tuning of the hydrogel properties. Properties such as modulus, stiffness and hydrophobicity approximately follow trend line A (blue) while permeability, diffusivity, water content, swelling ratio follow trend B (red).

In the field of cardiac regeneration PEG hydrogels have been commonly used as mechanical support, injectable cell matrices and bioactive molecule transporters. A study by Jiang et al. (2009) showed that the presence of PEG hydrogel even without stem cells or doping with bioactive molecules could be beneficial following myocardial infarction.[285] The authors induced MI in rabbits and injected 200µL of either PEG hydrogel or PBS into the infarcted tissue. Twenty-eight days later, the hydrogel treated group showed reduced wall thinning and smaller infarcts versus the PBS group measured by histology and echocardiography showed higher ejection fractions in the hydrogel group. The authors propose the therapeutic mechanism is the presence of the hydrogel prevents the infarction induced systolic bulging that leads to adverse remodelling. In a study from the same group by Wang et al. (2009) assessed the efficacy of PEG based hydrogel in improving bone marrow stem cell (BMSC) survival and retention as well as minimising structural damage in the infarcted myocardium of rabbits.[286] Echocardiography showed that animals that received injections of BMSCs in hydrogel had significantly higher LVEF at 4 weeks relative to animals that received BMSCs in PBS and control infarctions. US imaging also showed that adverse LV remodelling was reduced with the LV end diastolic diameter smallest in the hydrogel group indicating reduced wall thinning. Histology showed reduced scar volume in the hydrogel group relative to the BMSC only group with increase vessel density around the infarct. The authors suggest that this is a survival enhancing effect due to the presence of the stem cells that are retained better in the PEG hydrogel. In a rodent study by Rane et al. (2011) injected an inert PEG hydrogel or PBS into the infarcted rat myocardium.[287]

Despite the PEG group showing increased wall thickness at 7-weeks post infarction relative to PBS controls, cardiac function assessed by MRI and quantified by LVEF, EDV and ESV showed no significant difference to the PBS group. This is in contradiction to the previous study by Jiang et al. (2008) who measured improved LVEF by echocardiography. The author propose that the biodegradation of the hydrogel is the key parameter effecting the preservative effects of passive biomaterial in myocardial infarction. The cell and bioactive molecule penetration into the degraded hydrogel is proposed as a mechanism for inert material as a therapy.

The PEG hydrogel developed for this study was produced and optimised in-vitro by Dr Allie Speidel (Imperial College London). The hydrogel was composed of a 4-arm PEG-acrylate molecule terminating in thiol chains that was crosslinked with heparin binding peptides (HBP). The HBP crosslinkers were chosen due to their demonstrated ability to delivery growth factors and promote angiogenesis.[288,289] The HBP crosslinkers were further functionalised by binding a chelated Gd(III) ion for T1 weighted contrast in MRI. A simplified diagram of the PEG hydrogel structure is shown in Figure 7.9.

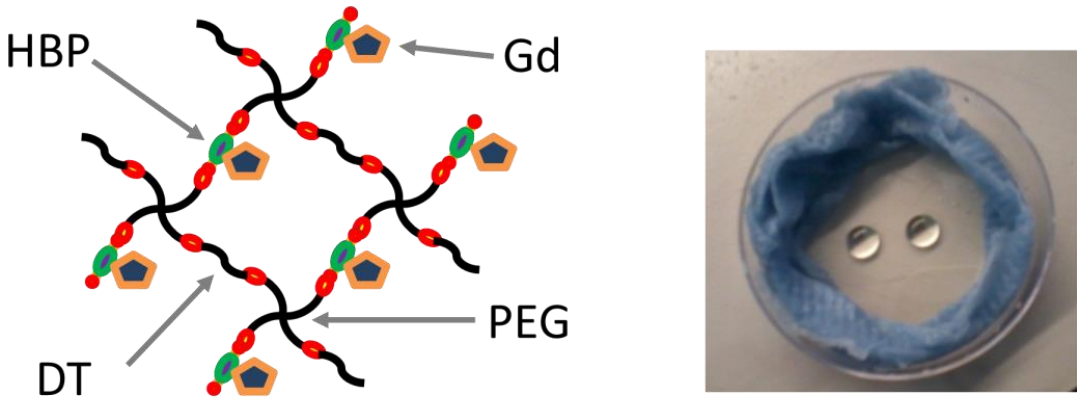

Figure 7.9 Functionalised PEG hydrogel utilised in this study. PEG- 4-arm poly (ethylene glycol); DT- dithiol crosslinker; Gd- chelated gadolinium ion; HBP- heparin binding peptide. Macroscopically these hydrogels have a gel like colourless and transparent appearance.

The development of injectable hydrogels based on natural and synthetic polymers has grown into a large body of research with attempts to optimise the properties of the hydrogel for cell retention ongoing.[290-292] The benefits of making this hydrogel MRI visible has several advantages by enabling in situ and non-invasive quantification 1) allowing the degradation profile of the hydrogel bioscaffold to be quantified 2) locating the engraftment site to confirm procedure 3) associate functional change with presence of material 4) image guided computational modelling of outcome. A number of approaches have been taken to make hydrogels MRI visible, this involves bestowing a contrast mechanism to the hydrogel through the introduction of contrast agents or chemical exchange saturation transfer (CEST) MRI methods. MRI has frequently been

used to image the distribution of iron oxide labelled regenerative cells in cell therapy[293-296] but few have attempted to directly image the hydrogel delivery scaffold. Liu et al. (2015) developed a Gd-DTPA doped chitosan based hydrogel for stem cell delivery.[297] The authors demonstrated the visibility of the hydrogel following subcutaneous engraftment using T1 weighted MRI imaging. Visibility of the hydrogel was preserved up to 35 days post engraftment. This study is a valuable proof of principle in producing a functionalised hydrogel with contrast agents for biomaterial tracking. However, imaging the hydrogel following subcutaneous injection is relatively simple compared to intracardiac injection due to the static tissue environment and large hydrogel volumes injected. Engrafting hydrogels to the heart and maintaining visibility from the smaller volumes will be more challenging. An alternative technique for producing MRI contrast from hydrogels is the CEST MRI acquisition scheme. CEST produces MRI contrast without exogenous contrast agents and is based on the exchange of saturated protons between molecules with different resonant frequencies. CEST hydrogel tracking has been demonstrated previously by Liang et al (2015) and Dorsey et al (2015).[298,299] These studies have validated CEST tracking of biomaterial, with the main advantage relative to contrast agents being the specificity in identifying a particular biomaterial non-invasively. CEST is an interesting and powerful technique for this purpose but due to the very long acquisition times required for CEST imaging, that can be prohibitively long with cardiac gating this method was deemed unsuitable to the multiparametric imaging platform that was developed in this work.

This hydrogel platform underwent several in-vitro experiments prior to the in-vivo implementation described here. These in-vitro tests included monitoring gel degradation, mechanical properties and cell retention and viability. The Gel presented in this study- consisting of 50% dithiol and 50% HBP crosslinkers- was optimised to increase cell retention and have similar mechanical properties to myocardium.

The cell type chosen for these experiments were $Sca1^{+}$ cardiac stem cells that were isolated and derived as described by Noseda et al. (2015).[300] These cardiac stem cells represent an attractive therapeutic cell for cardiac regeneration since they have been shown to differentiate into cardiomyocyte, endothelial and smooth muscle cells.[301-303] A study by Liang et al. (2010) investigated the fate of these cells following transplantation into the myocardium.[304] Transplanted $Sca1^{+}$ CSCs were shown to differentiate into cardiomyocytes and endothelial cells and were shown to migrate from healthy regions of tissue to damaged myocardium. CSCs have been used previously in preclinical studies of regenerating the myocardium following infarction. A study by Porrello et al. (2010) showed that when the neonatal mouse heart suffers a severe injury by surgical resection of apical tissue it has the ability to regenerate.[46] This regeneration of

tissue was characterised by cardiomyocyte proliferation and minimal fibrosis making it true regeneration as opposed to remodelling processes. The native CSC population is theorised to provide this transient regenerative ability. Autologous CSCs have been deployed in clinical studies of myocardial regeneration in the CArdiosphere-Derived aUtologous stem CElls to reverse ventricUlar dySfunction (CADUCEUS) trial where they were found to reduce scar size and increase contractility and wall thickening in the infarct tissue.[305]

Due to its optimal balance of durability, mechanical matching and cell retention the 50% HBP crosslinked PEG hydrogel was carried forward for use in the in vivo experiment described below. The aims of this study were to assess the safety and efficacy of the injectable PEG hydrogel in the healthy mouse heart as a preliminary study establishing this PEG hydrogel platform as a tailored, in vivo, detectable cell delivery system for enhancing cell and biomaterial retention in the mouse heart.

7.2.2 Methods

7.2.2.1 Cell culture and Hydrogel manufacture

Cell culture and hydrogel manufacture was performed by Dr Allie Speidel (Imperial College London). In brief CSCs were isolated as Sca-1 positive side population cells from adult mouse hearts and then deposited as single cells so that clonogenic lines could be harvested and expanded to passage 10. The CSC population were cultured at 37°C with 5% CO2 on collagen I coated polystyrene dishes. CSCs were passaged at 70% confluence every 7 days by trypsinisation. CSCs were transduced with pLenti-III-PGK-Luc2 luciferase lentivirus (Applied Biological Materials, Richmond, CAN) so that they would produce the firefly luciferase protein to enable bioluminescent imaging for measuring cell retention and viability as described in 2.6. PEG hydrogel was then formed by crosslinking the PEG polymer chains with a 50:50 ratio of dithiol bonds and heparin binding peptide (HBP). The HBP bonds also included a chelated gadolinium ion to provide MRI imaging contrast.

7.2.2.2 Engraftment

This study was performed in mice due to the availability of murine cardiac stem cells with collaborators at Imperial College London. The goals of this study were to examine the safety and retention of this material in-vivo and develop the engraftment procedures. For this reason, experiments were performed in healthy mice without myocardial infarction to assess damaged

caused by the engraftment procedure without the confounding factor of infarction induced fibrosis and remodelling.

CSCs were harvested on the day of engraftment by disassociation and separated by centrifugation before being suspended in PBS. Two groups of animals were produced, one received intramyocardial injections of PBS with CSCs (n=6) and the other received intramyocardial injections of PEG hydrogel with CSCs (n=8). For the PEG hydrogel group, these cells were encapsulated in 50% HBP solution containing 2mM Gd (III)-HBP at a concentration of 1.4×10^6 CSC-Luc2 cells in 160µL of PEG acrylate solution.

Ultrasound guided injections were performed by Dr Daniel Stuckey (University College London), the US guided procedure was performed on a Visualsonics Vevo 2100 system equipped with a 25 MHz rat imaging transducer in b-mode with an 18mm FOV. A schematic of the setup used is shown in Figure 7.10. Wild type mice were anaesthetised under 2.5% isoflurane in oxygen and the hair over the chest removed as described in 2.5 to allow unimpeded imaging through the parasternal short axis view of the heart for injection. A 27G needle was inserted through the intercostal space into the anteroapical region of the heart. Once the position within the anteroapical region was confirmed by US b-mode imaging 20µL of PEG was injected. The needle was then retracted so that it was outside the myocardium but within the chest wall, the needle was then repositioned and another nearby injection site determined for another 20µL injection. This process was repeated for a total of 4 localised injection sites.

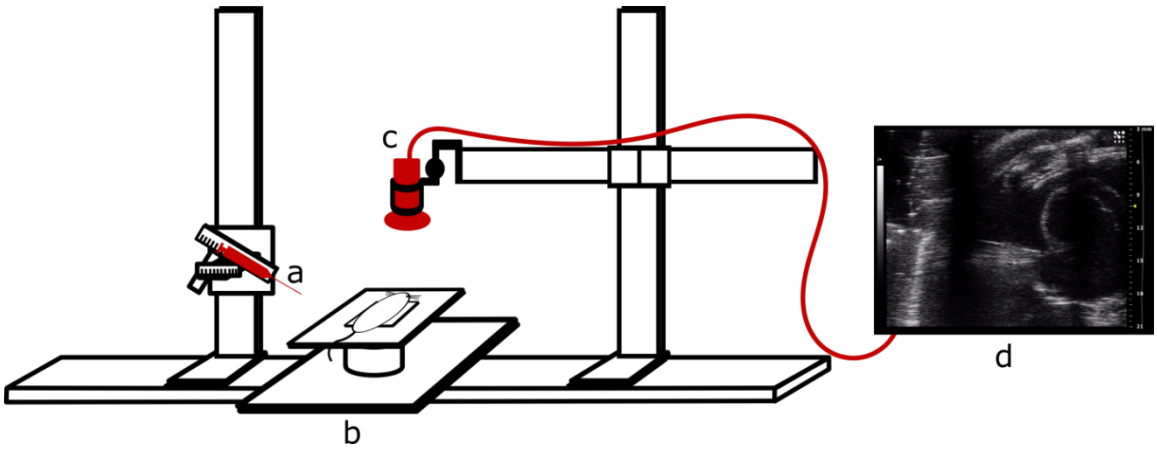

Figure 7.10 Schematic of the setup used for intramyocardial injections. Each component of the setup could be positioned independently on rails (a) syringe containing CSC loaded PEG had translational and rotational freedom allowing for accurate needle positioning (b) the animal bed could similarly be repositioned and incorporated physiological monitoring and anaesthetic delivery. The ultrasound transducer (c) was placed above the animal when prone and was positioned to image through the parasternal window producing an image showing both the needle and SA view (d).

7.2.2.3 Imaging

Bioluminescence imaging was performed for assessing cell viability and retention. BLI was performed as described in 2.6 using the Biospace PhotonImager system. Animals were imaged immediately following the US guided injections to provide a baseline cell engraftment population, this provided a way to normalise cell retention across animals regardless of initial engraftment variability. Imaging was subsequently performed at 1, 3, 7 and 14-days post engraftment.

Magnetic resonance imaging was performed at 1, 7 and 14-days post engraftment to assess changes in cardiac function and assess biomaterial retention. For global cardiac function assessment, a standard short axis cine stack was acquired and processed using the standard protocol. LGE images were acquired pre-contrast and post-contrast and analysed as described in 2.3.5 to assess biomaterial retention by utilising the T1 shortening effect in the presence of the Gd(III)-HBP. Regional function was assessed using the DANTE tagging sequence with equally spaced bright and dark bands resulting in a magnetisation modulation that can be approximated as sinusoidal meaning that the HARP processing methods developed as part of this thesis described in Chapter 5 can be used. Tagged imaged were acquired in a short axis slice through the approximate injection site with imaging parameters; resolution = 0.13×0.13×1mm; TE = 1.7ms; tag spacing = 0.3mm; and TR = 5ms that in a typical RR interval of 110ms allowed for 20 cine frames. Tagged imaged were analysed using the HARP toolbox and were reconstructed with identical bandpass filtering of the stimulated echoes. Strain tensors were calculated from the gradient deformation tensors calculated using a custom Matlab script and translated to cylindrical co-ordinates centred at the centre of the LV to produce circumferential and radial strains.

7.2.2.4 Statistical tests

All results are presented as mean value ± standard error. All data were tested for normality using the Kolmogorov-Smirnov test and significance values were calculated by one-way analysis of variance corrected for multiple comparisons using the Holm-Šídák method. In all cases a p-value of less than 0.05 was considered significant.

7.2.3 Results

Inversion recovery T1 weighted images were acquired pre-contrast and post-contrast (LGE). Representative images can be seen in Figure 7.11 for mice injected with PBS and PEG hydrogel. It

was theorised that the Gd(III) bound to the HBP cross linkers within the gel would provide T1 contrast that would allow for biomaterial quantification. The pre contrast images however did not consistently show any visible enhancement in biomaterial injected regions in the PEG or PBS groups. As pre contrast images were found to provide no capability to detect the gadolinium doped hydrogel, this imaging sequence was removed from the protocol after day 1. The post contrast groups however consistently show regions of hyperenhancement. These hyerpenhanced regions could arise from two mechanisms. The first case is that the injected material has created a space within the myocardium and the Gd bolus injected via the IP route is occupying this volume. This would suggest that the gadolinium bound to the hydrogel and PEG is not providing sufficient T1 contrast for imaging. This could be caused by low concentrations of contrast during manufacture, immediate loss of material from the injection site or the volumes injected may be too small to effectively alter the T1 of surrounding tissue. The second case would be that the Gd contrast bolus is occupying tissue damaged by the engraftment procedure. An example of the second case is given by the example given in Figure 7.11B. Here the hydrogel injection has damaged the myocardium. This is visually different to the majority of the PEG injection images in that it has a clearly defined infarct region and crucially the enhanced region develops over time to show characteristics of infarcted myocardium such as wall thinning and reduced contraction. This is an isolated case and the remaining PEG gel injections (n=7) do not exhibit this clear enhancement or remodelling over time suggesting that they are not undergoing the same degree of damage from engraftment. The visibility of enhancement up to 14 days in the representative PEG animal shown in Figure 7.11A, without adverse myocardial remodelling, indicates that the space occupied by the hydrogel is visible and better retained than the PBS injection over time.

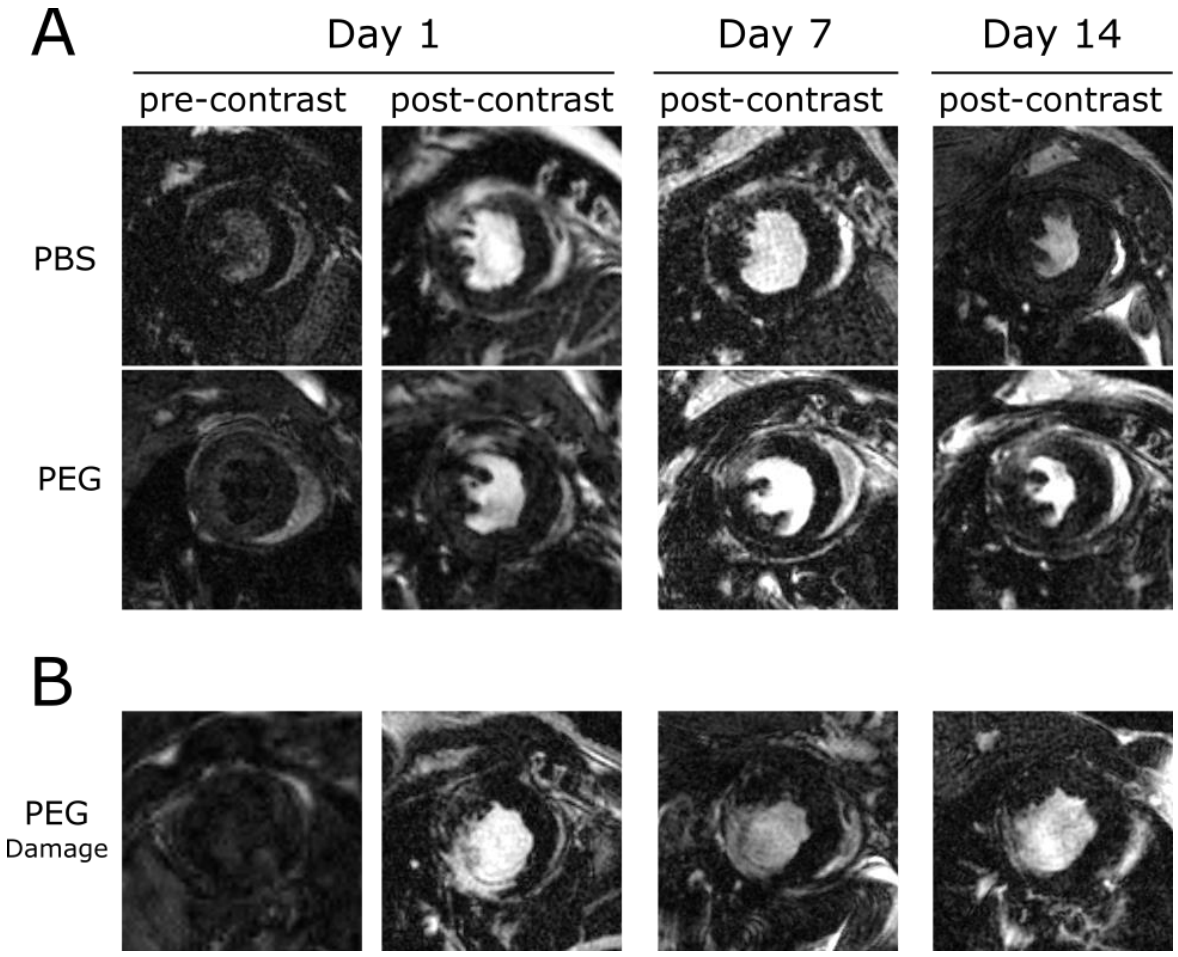

Figure 7.11 Representative LGE images for mice that received the PBS and PEG with CSC injections. (A) Shows representative PBS and PEG injected animals. The post contrast images show regions of hyperenhancement in both at day 1 and these diminish over time- although hyperenhancement in the PEG appears to be better defined. (B) Shows a noteworthy case where the injection appeared to induce an inferoseptal infarct that persisted through time and produced myocardial remodelling and wall thinning by day 14. The regional function in this enhanced tissue is assessed below.

Global function was assessed using cine MRI and quantified by left ventricular ejection fraction (LVEF), these results are shown in Figure 7.12. No significant differences were found over 14 days for either the PEG hydrogel or the PBS injections. This is a positive result suggesting that injections of this biomaterial are mechanically comparable to PBS injections. Despite the single instance of major damage shown in Figure 7.11B, the overall trend for the developed intramyocardial injection protocol induces no global function change. The PBS injections showed little variation with time with a low of 68±3% at day 7 and a high of 70±4% at day 1. The PEG group was more variable with a low of 62±2% at 14-days post engraftment but this was that significantly different from the day 7 where ejection fraction was measured to be highest at 71±4%.

Quantification of the representative LGE images shown in Figure 7.11 are shown in Figure 7.12. These images were quantified by the same semi-automated methods as used for quantification of myocardial scarring but with no assumptions about blocked coronary arteries allowing quantification of all hyperenhanced regions. Here, increased volumes of gadolinium enhancement are given as a measure of retention of the injected material. The PBS injected animals showed little variation in enhancement and no significant variation with time with enhancement of around 3-4% of the LV volume. The PEG injected animals however had a larger volume of enhancement on day 1 of 8.4±3.4% decreasing to 4.0±1.4% on day 7 and dropping to 3.4±0.7% on day 14. This may indicate better retention of biomaterial at day 1 and day 7 before dropping to PBS levels at day 14. Although this trend is promising it did not reach statistical significance and observing the plotted data in Figure 7.12 the averages may be partially affected by outliers.

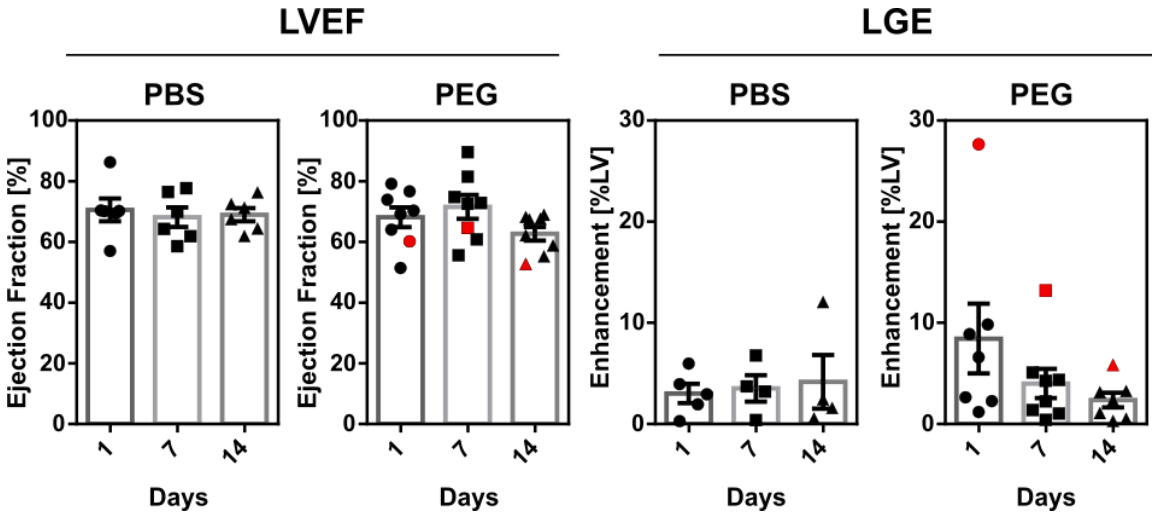

Figure 7.12 Results of CMR assessment of PEG hydrogel vs PBS. LVEF is not significantly different over 14 days for either PBS of PEG injections. Red markers indicate the animal where the LV was damaged during engraftment (Figure 7.11B). Regional enhancement appears higher in the PEG group at day 1 indicating better retention of material but does not reach statistical significance and may be affected by outliers.

BLI showing the retention and viability of cells within engrafted hearts are shown in Figure 7.13. Representative BLI data is shown in Figure 7.13A showing the BLI signal is largely localised to the left-side thorax suggesting that the majority of cells are retained within the region of the heart. This could mean that the cells have successfully grafted to the myocardium or the injection has leaked into the pericardial space or both. However, having the signal clearly localised to the heart is a promising sign for retention of injected material. Figure 7.13B quantifies the bioluminescence to assess the cell retention within each group with results presented as mean counts ± standard deviation. Relative to the BLI signal at day 0 the PEG gels express higher

bioluminescence relative to PBS at day 3 ($p = 0.0028$) where there is a 6.5x higher BLI signal for the PEG injected group relative to PBS. This suggests that a higher proportion of the cells that were viable at engraftment are retained over time in the PEG hydrogel relative to the PBS.

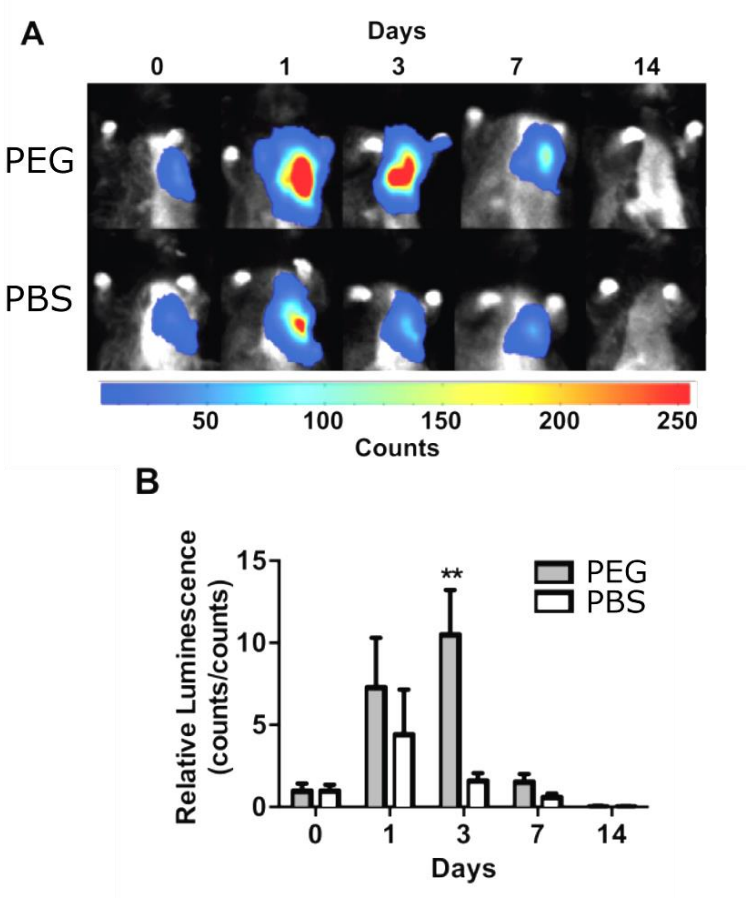

Figure 7.13 BLI results comparing PBS and PEG (A) representative images showing the bioluminescent signal from CSCs suspended in PEG gel or PBS at 0, 1, 3, 7 and 14 days. Figure reproduced with permission from Speidel et al. Unpublished.

Results from regional function assessment are shown in Figure 7.14. For each segment of myocardium, the circumferential strain for both PBS and PEG injections are plotted at 1,7 and 14 days with the injection site region and neighbouring regions displayed in groups.

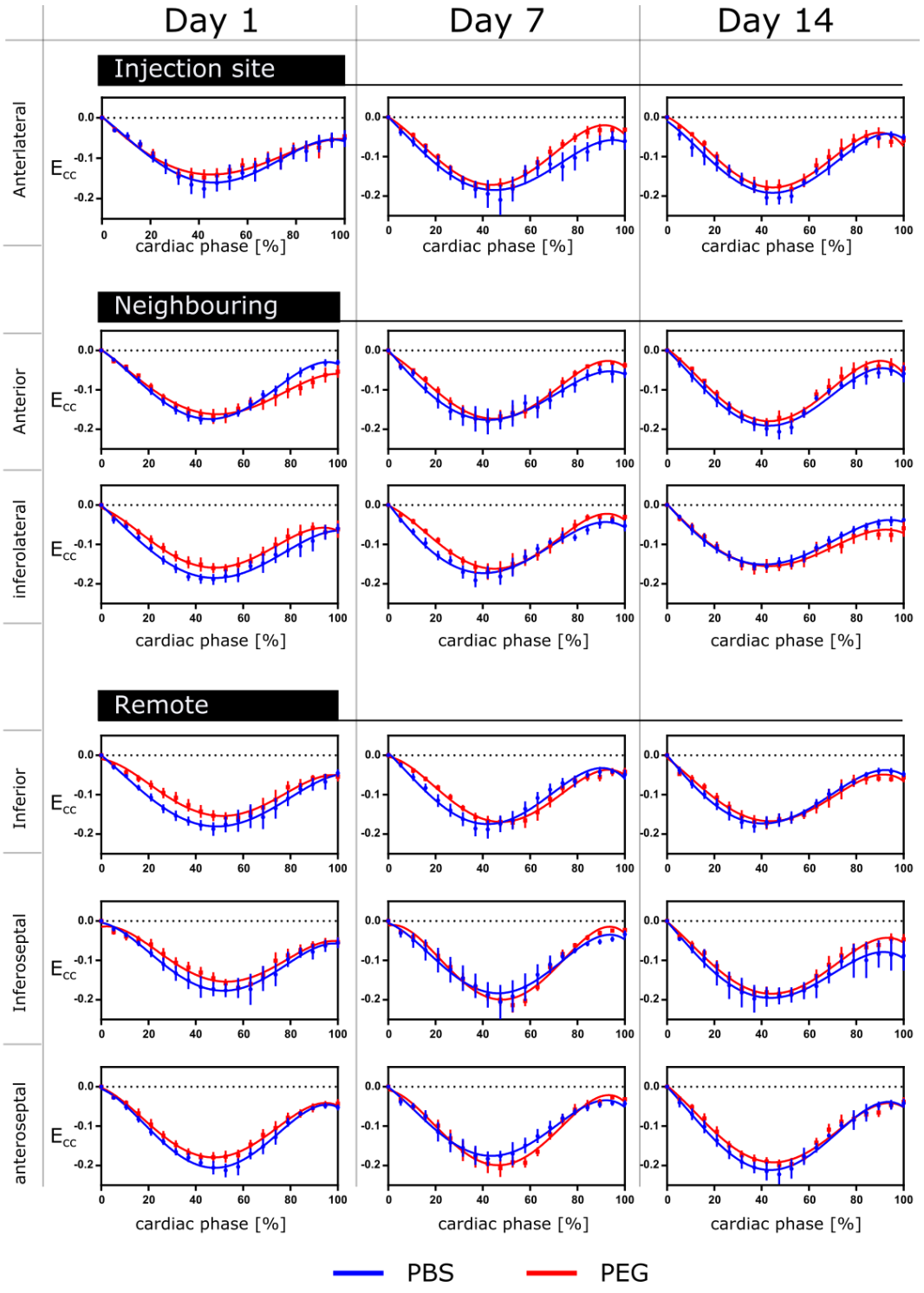

Figure 7.14 Regional circumferential strain (E_{cc}) assessment using SPAMM cine MRI analysed using HARP for PEG and PBS cell suspension at 1, 7 and 14 days post engraftment to healthy mice. The injection site, neighbouring regions and remote regions are shown separately to help identify the segments of myocardium that should be affected by the presence of the engrafted PBS/PEG.

No significant changes were observed between the two groups in any regions. Despite the lack of statistical significance some observations can be made about the mean data trends. The peak strain- occurring at the lowest point on the strain curves, appears to be consistently lower at day

1 in the PEG group relative to the PBS group suggesting a smaller contraction in this group at 24 hours. This relative difference appears to diminish at later time points with the two curves taking on very similar shapes by 14 days. The PBS (blue) curves appear to be consistent in time, with similar shapes and peaks in injected and neighbouring segments suggesting that the PBS injection has had minimal effect on contraction as would be expected. The variation in the PEG group strain curves over time shows some level of disruption to normal contraction following engraftment. The transient nature of this disruption can be seen by the return of the PEG strain curves to more closely match the PBS injections by 14 days. This return to normal function could be attributed to either the degradation of the PEG gel or the heart adapting to the presence of the material.

Regional function information from tagging can be applied to the problem presented above where we are uncertain whether myocardial enhancement in LGE images are due to tissue damage or hydrogel accumulation. In Figure 7.15 shows the strain curves in the infarcted posterior region of myocardium for the same mouse shown in Figure 7.11B. The magnitude of the strain can be seen to be consistently lower in the damaged tissue relative to the mean strain curves for the PEG or PBS injections.

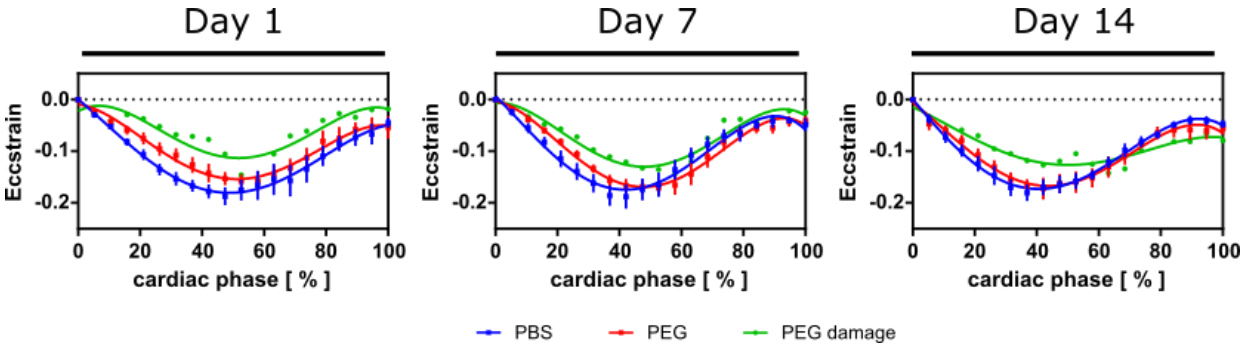

Figure 7.15 Tagging results including the infarcted animal shown in Figure 7.11B (green). Strain curves are shown for the posterior region where LGE images (Figure 7.11B) indicate a region of tissue damage and remodelling. Strain was found to be lower than the mean for that group throughout the cardiac cycle suggesting the regional function imaging is sensitive to the presence of this tissue damage.

The abnormal strain values observed in the damaged myocardium (Figure 7.15), suggest that the presence of hyperenhancement in the LGE images can be attributed to either the presence of hydrogel or regions of tissue damage based on this regional assessment technique. In cases where hyperenhancement is present but the tissue shows no dysfunction the enhancement is probably hydrogel. When the hyperenhancement coincides with reduced strain it may be due to tissue damage.

7.2.4 Discussion

The extensive in-vitro experiments performed to establish and optimise the mechanical characteristics and tailor the degradation profile of this PEG hydrogel makes it an exciting candidate for cardiac regeneration therapy. This study has shown that the majority of its in-vitro characteristics have carried through to the in-vivo case. The key in-vitro experiments aimed to optimise mechanical properties, cell retention and MRI visibility. This study has investigated each of these optimisations in-vivo.

Preliminary rheology experiments identified optimal proportions of HBP and DT crosslinking to produce a hydrogel with similar mechanical stiffness to the mouse heart. The objective of this was to minimise adverse effects following engraftment. The beneficial effect of mechanical support provided by an engrafted biomaterial following infarction has been well established as discussed in 7.2.1. The benefit provided by this support will be optimal when the stiffness of the supporting material is matched to the stiffness of the surrounding tissue and the tissue it is intended to replace. The injection of the mechanically matched biomaterial was found to have no significant effect on regional contraction at the injection site or neighbouring segments at up to 14-days post engraftment to healthy mice. This is evidence that the hydrogel is compatible with supporting heart function and is unlikely to be detrimental to contraction when transplanted as a therapeutic. This is a vital characteristic for a successful biomaterial for cardiac regeneration.

One of the most common criticisms of cardiac cell therapy studies is the low retention of cells following engraftment, this is a major limiting factor to their potential as a therapeutic. The retention of viable CSCs was shown to be significantly higher in the PEG hydrogel at 3 days post engraftment, relative to the same cells in PBS suspension. This increased retention will give the transplanted CSCs a greater chance of providing a therapeutic benefit. The increased retention is only significant at 3 days, meaning that this increased retention is relatively short lived. There is evidence however that the most beneficial effects of transplanted cells are from paracrine factors and not from full integration of transplant cells and replacement of lost tissue. These paracrine effects will be most beneficial in the first days following infarction. An important caveat to the increased cell viability is that this may not be the case in myocardial infarction. The hostile cellular environment following infarction due to factors such as inflammation and fibrosis are likely to limit the lifetime of transplanted cells. Additionally, the matched mechanical properties of the hydrogel will no longer be true in highly fibrotic scar tissue meaning that the time from infarction to engraftment will be an important factor. The PEG gel has been shown to

increase retention in the healthy myocardium but a future study would be required to investigate its capacity to prolong cell viability in the infarcted myocardium.

The introduction of chelated Gd(III) to the hydrogel was intended to provide MRI visibility to enable tracking of the biomaterial retention. In combination with the BLI for tracking the encapsulated cell retention and viability this would provide a comprehensive non-invasive technique for tracking the retention of the therapy with high spatial resolution. Unfortunately, inversion recovery imaging was not able to delineate the Gd doped biomaterial from the normal myocardium. The most likely reason for this that the Gd was unable to effectively alter T1 of surrounding tissue. Low concentration of Gd ions in the gel or the tiny volumes injected may be the cause of this. A potential solution is to increase the Gd concentration within the gel, the alternative of injecting more may be damaging to heart tissue. An external Gd bolus via IP injection was able to detect regions of myocardial enhancement. As discussed above this is likely to be accumulating in space occupied by the hydrogel providing an alternative means of detection. However, when applied as a therapeutic this LGE approach to locating the biomaterial will be unable to differentiate between biomaterial and myocardial scarring. Alternative techniques are therefore required to locate the biomaterial in-vivo using MRI. T1 mapping in combination with ECV mapping may be a possible solution. A T1 map of tissue before and after the IP Gd injection will provide information about where Gd accumulates and the fraction of space it occupies within each pixel. This technique is discussed in more detail and implemented for this purpose in the following section (7.3).

This study therefore has demonstrated the safety of a PEG hydrogel crosslinked by 50/50 dithiol and HBP/Gd(III) as a therapeutic cell-loaded biomaterial for injection into the heart. The hydrogel was shown to improve cell retention and viability without have a detrimental effect on cardiac function. In this study the role of imaging in establishing the safety of transplanted material is demonstrated. The MRI methodologies implemented here are directly translatable to investigating clinical cardiac tissue engineering and their use in future clinical studies would be a powerful tool for validation of safety. PEG is an FDA approved biomaterial and further development of hydrogels based on this synthetic polymer has significant clinical potential.[306] The next step in development of the PEG hydrogel platform discussed here would be to investigate therapeutic benefits in a mouse model of myocardial infarction. It is necessary to demonstrate that the improved cell retention and minimal functional impact are not limited to healthy hearts.

7.2.5 Key results

- PEG gel retains viable CSCs better than PBS following intramyocardial engraftment
- Established ultrasound guided injection protocol for biomaterial delivery
- Multiparametric approach using regional function and LGE can attribute enhancement to damaged tissue or biomaterial retention
- Significantly, PEG gel has no effect on regional function relative to PBS indicating well matched mechanical properties and a suitable delivery platform for cells

7.3 MRI measurements of extracellular, global and regional function changes following alginate microspheres engrafted to the infarcted myocardium

7.3.1 Introduction

A major limitation of injectable polymer hydrogels such as the functionalised PEG based hydrogel (7.2) is that structurally hydrogels are two component systems. They are composed of polymer chains and a cross linking reagent. The result is that for the biomaterial to remain injectable the cross-linking process must be only partially complete and the hydrogel remaining aqueous until the injection is complete and ideally solidifying in-situ. This means that there is significant uncertainty about the mechanical properties of the material immediately following injection. If an injection has not solidified sufficiently, it is likely to be immediately displaced by the beating heart. This disperses the material and negates the advantage of encapsulating cells within the hydrogel. Conversely if the material has solidified too much it will block the syringe and prevent engraftment, requiring another engraftment procedure. An alternative to this approach is to pre-form the biomaterial in the form of microspheres that are small enough to remain injectable while maintaining the beneficial effects of the scaffold.

Microspheres, are small spheres or beads, typically composed of polymer compounds such as alginate or PEG on the order of micrometres. As regenerative structures, microspheres are appealing due to their relatively simple fabrication processes, the ability to create multiple functional 'shells' within them and several advantages associated with their discrete nature.[307] These points will be discussed further in the following section. This study aimed to investigate the therapeutic efficacy of macrophages encapsulated in alginate microspheres in myocardial infarction. The study aimed to combine all previously developed imaging techniques such as HARP and DENSE to establish MRI and BLI imaging protocols for assessing cell and biomaterial retention as well as global and regional heart function.

Microspheres can be manufactured from a single type or combinations of natural and synthetic polymers. Various techniques are able to induce the polymer to form spherical forms of various sizes. Microspheres have previously been fabricated through electrospraying, phase separation, emulsion and cryogenic atomisation techniques.[308-311] These methods aim to separate the unlinked hydrogel solution into elements that are smaller than the droplets they naturally form to the surface tension of the liquid. These smaller droplets form spherical shapes under surface

tension and can then be solidified by immersion in cross-linking solution. The size of the microsphere is determined by factors such as the concentration of the polymer solution, the cross-linker used and the size of the droplets. The concentration of the polymer solution is the factor that has the greatest influence on microsphere size.[312] Higher concentrations of polymer increase the surface tension of the liquid resulting in higher viscosity and larger droplets.

The discrete nature of microspheres offers several advantages over regular single body biomaterials applied to cardiac regeneration. Firstly, the packing of the spheres will always leave an interstitial space between adjacent spheres. This space offers room for surrounding regenerating tissues to infiltrate the microsphere mass.[313] This void also offers highly permissive space for the diffusion of bioactive molecules secreted from cells encapsulated with the spheres, enabling them to reach and effect surrounding host tissue. Discrete spheres also offer a level of control by making it simple to combine multiple microspheres within a treatment with each tailored to different functions. This simplifies the process of manufacturing a biomaterial that possesses all the desired properties. Producing one biomaterial that is able to support multiple cell types and predictably release a range of growth factors and drugs would be a complex task whereas, producing a single type of microsphere to possess a certain property is comparatively simple. It is then possible to combine different types of microsphere within an injection or engraftment that is then a combination of the desired properties.

Microspheres are most commonly used as a controlled drug release platform. The relatively predictable degradation from hydrolytic reactions in vivo make microspheres ideal for this purpose. As the microsphere is broken down, the encapsulated drug or active molecules are released into the surrounding space where they can produce local effects or disperse throughout the body.[314] Microspheres have previously been used to deliver vaccines, insulin and bioactive glass to regions of the body not typically assessable.[315-317] For example, orally administered microspheres are able to deliver bioactive molecules to the highly permissive gut wall. The advantage of encapsulating these drugs within microspheres is that their release can be tailored to the needs of an application. Molecules can be released at a constant rate, or in a pulsatile fashion dependent on the degradation profile of the sphere. The encapsulation of these molecules within the microspheres also protects them from being absorbed or cleared by the immune system.[318]

When cells are encapsulated within microspheres the encapsulation protects the cells from hostile cellular processes such as the inflammation in tissue following myocardial infarction during the remodelling phase. To aid cell retention following myocardial transplant it is possible to manufacture a microstructure within the microspheres that is conducive to cell growth by

making it similar to the extracellular matrix. Using natural polymers such as alginate or collagen produce internal microstructure that is similar to the ECM and promotes cell growth and survival. When cell-loaded microspheres are transplanted to the infarcted myocardium, the principle mechanism through which they interact with the host tissue will be through paracrine signalling. The cells secrete cytokines and other bioactive molecules that are conducive to cell survival and have been shown to be beneficial following myocardial infarction. As discussed in chapter 1, paracrine signalling is thought to be the most beneficial aspect of transplanting cells to the infarcted heart. Encapsulating cells within protective microspheres is thought to aid cell retention and viability therefore extending the duration of paracrine factor release.

Microsphere encapsulated cells have been used previously for therapy in myocardial infarction. Yu et al. (2010) produced calcium alginate microspheres encapsulating human mesenchymal stem cells (hMSCs) and engrafted them to the rat heart by ultrasound guided injection at 1-week post infarction.[319] Echocardiography assessment at 10 weeks post injection showed the alginate spheres retained LV shape and reduced adverse remodelling effects. Compared to cells suspended in PBS the microspheres enhanced survival and retention of encapsulated cells within the heart. Cell loaded microspheres have also been demonstrated as a therapy in larger animals with MRI for assessment of efficacy and microsphere retention. Gomez-Mauricio et al. (2013) encapsulated adipose derived stem cells within alginate microspheres coated with superparamagnetic iron oxide nanoparticles (SPIONs).[320] The authors injected these microspheres into the myocardium of the porcine heart during surgical ligation of the LAD. MRI assessment was performed at up to 30 days later to measure global heart function, scar size and T2*. The SPION nanoparticles allowed in vivo monitoring of microsphere retention by regions of hypointensity and microspheres were shown to be well retained. LVEF showed no significant change with the authors suggesting low cell density within the microspheres was the cause.

The larger hearts of rats and pigs make them more appealing to investigations of myocardial regeneration due to the relative simplicity of ligation surgery and engraftment, and their similarity to the human heart. However, regeneration studies in mice are valuable for the availability of genetically modified mice that can accurately mimic human disease, for example the mouse model of β thalassemia discussed in chapter 3. The only previous example of intramyocardial injection of alginate microspheres into a mouse model of myocardial infarction was performed by Lee et al. (2013).[321] The authors created an alginate/hydrogel hybrid for the controlled release of heat shock proteins as a therapy for MI. The sustained release of the proteins due to the microporous microspheres was shown to improve ejection fraction, reduced diastolic dysfunction and increase the pressure produced by the heart during contraction.

Alginate microspheres were produced using an electrostatic encapsulator (Nisco, Zurich, SUI). This system is illustrated in Figure 7.16. An electrostatic potential is applied between a narrow nozzle (<1mm) and the surface the cross linking solution creating an electric field. This E field induces a charge at the surface of the liquid proportional to the square of the applied voltage.[322] This charge interferes with intramolecular attraction, reducing surface tension and causes droplets to fall under gravity in much smaller particles than they would without the electric field.

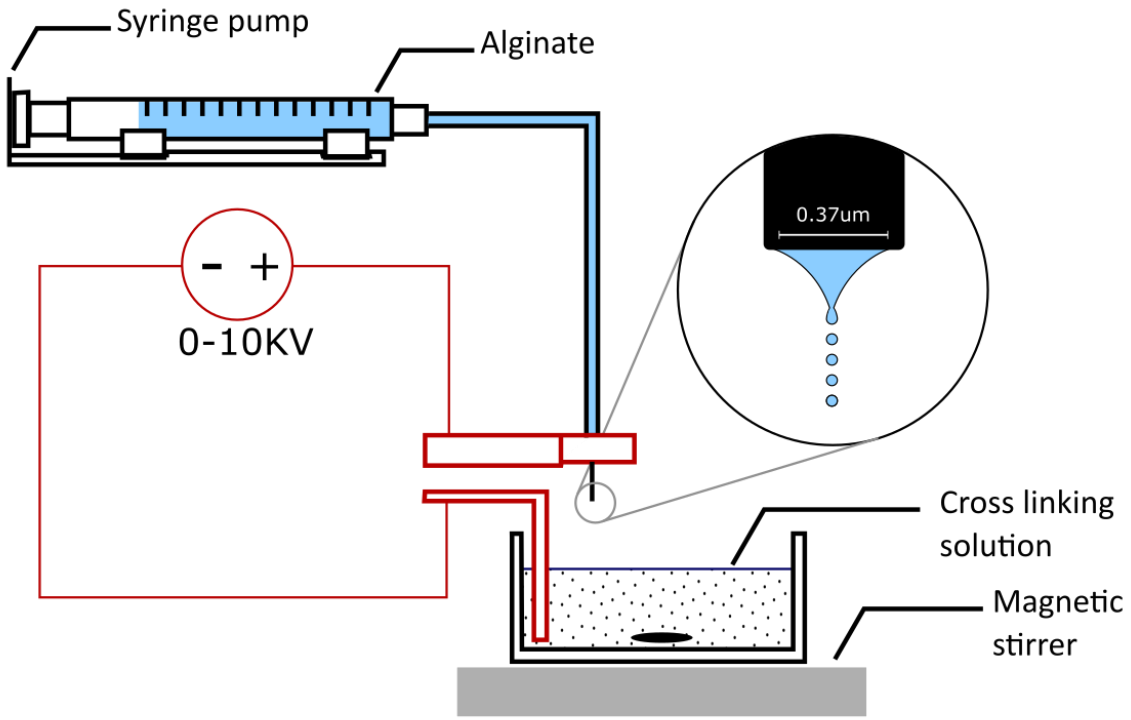

Figure 7.16 Electrostatic encapsulator. A syringe pump pumps sodium alginate solution through a narrow nozzle suspended above a cross-linking solution bath. The electrostatic potential reduces the surface tension of the liquid and causes it to fall under gravity in small droplets. These droplets fall into the cross-linking solution and solidify.

Luciferase transduced resident macrophages were chosen for encapsulation due in part to their availability, but also their regenerative potential and relative robustness compared to stem cells lines.[323] Macrophages are known to control inflammation by secreting a variety of cytokines, pro-inflammatory and trophic mediators that beneficially modulate the inflammatory response.[324] Macrophages have also been shown to clear apoptotic leukocytes to limit the extent of inflammatory injury and attenuate progressive collateral tissue damage from extended inflammation.[325] Since the primary mechanism for macrophage regeneration is through release of paracrine factors, they make an ideal candidate for microsphere encapsulation to increase retention and survival following engraftment to prolong and localise the release of these factors in the heart.

7.3.2 Methods

7.3.2.1 Pilot study

An initial pilot study was performed in which 4 mice received ultrasound guided injections of microspheres without cell loading. These microspheres were fabricated using what became the final fabrication protocol described below. The aim of this pilot study group was to confirm that the procedure could be performed safely, to practise the fabrication and engraftment procedure and to establish the final imaging protocols. Optimised imaging protocols included establishing the ECVF mapping technique using segmented k-space acquisitions, determining suitable values for the SPAMM and DENSE acquisitions to provide sufficient spatial encoding with sufficient SNR and timing the full imaging procedure to ensure all animals could be imaged within the experimental timeframe.

The result of this study was that all mice survived and were engrafted with the microspheres described below without macrophage encapsulation. They were imaged using several different protocols while seeking optimisation, meaning that the pilot study data cannot be included with the main study data due to differences in acquisition technique. This pilot study resulted in an optimised protocol developed for engraftment and imaging that is described below in the context of the full study.

7.3.2.2 Cell preparation and microsphere encapsulation

Macrophages were cultured by Dr Stephen Patrick (University College London). Cells were harvested no more than 1 hour before encapsulation and no more than 4 hours before engraftment. Cells were lifted from the culture flask by scraping and the culture medium and cells separated by centrifugation to form a macrophage pellet. The cells were then resuspended in 2ml 1% sodium alginate PBS solution using pipette agitation.

Encapsulation was then performed using an electrostatic encapsulation system (Nisco, Zurich, SUI) with an alginate flow rate of 0.5ml/min, potential difference of 9KV and a cross-linking solution of 100mM calcium chloride solution. Encapsulation and microsphere size was then confirmed by optical microscopy. A sample of the produced microspheres were taken into a syringe and passed through a 27G needle to confirm compatibility with injection, shape and cell loading of microspheres. Examples of these images are shown in Figure 7.17. The microspheres were found to take on approximately spherical shapes and were well seeded with macrophage

cells. However, after passing the microspheres through a 27G needle there was reduced sphere density within the solution suggesting a fraction of larger spheres were blocking the needle.

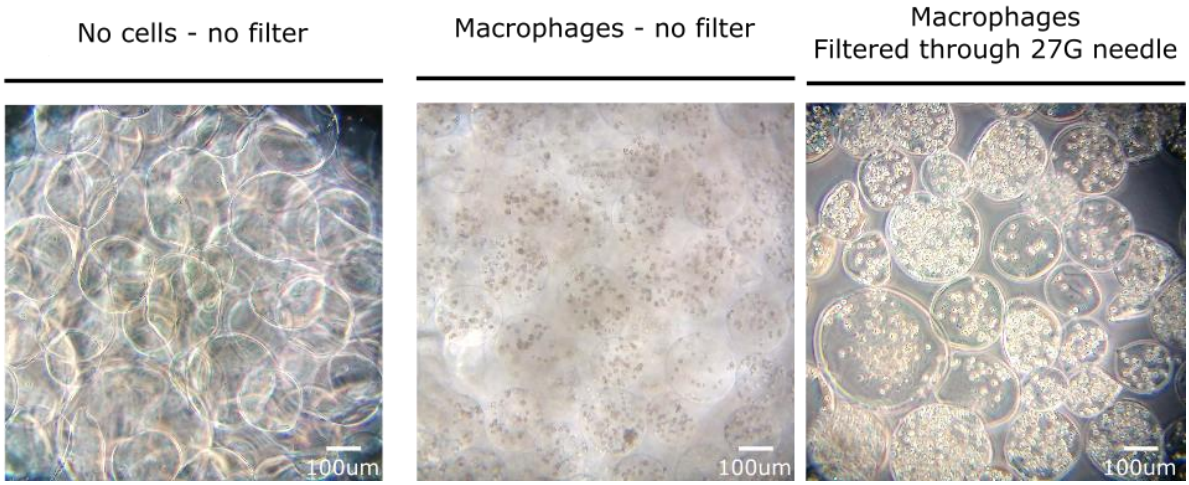

Figure 7.17 Visual inspection of encapsulated microspheres. Cells are visible within encapsulated microspheres with variable densities. Spheres have roughly spherical shapes and are shown to pass through a 27G needle, although with some loss of spheres. Images shown at 20x magnification.

The viability of the encapsulated macrophages in each batch of microspheres was tested after fabrication and prior to engraftment. By taking a 100µL sub sample of the microsphere solution and adding 20µL luciferase to induce light bioluminescent emission in viable cells. An example BLI cell viability test is shown in Figure 7.18.

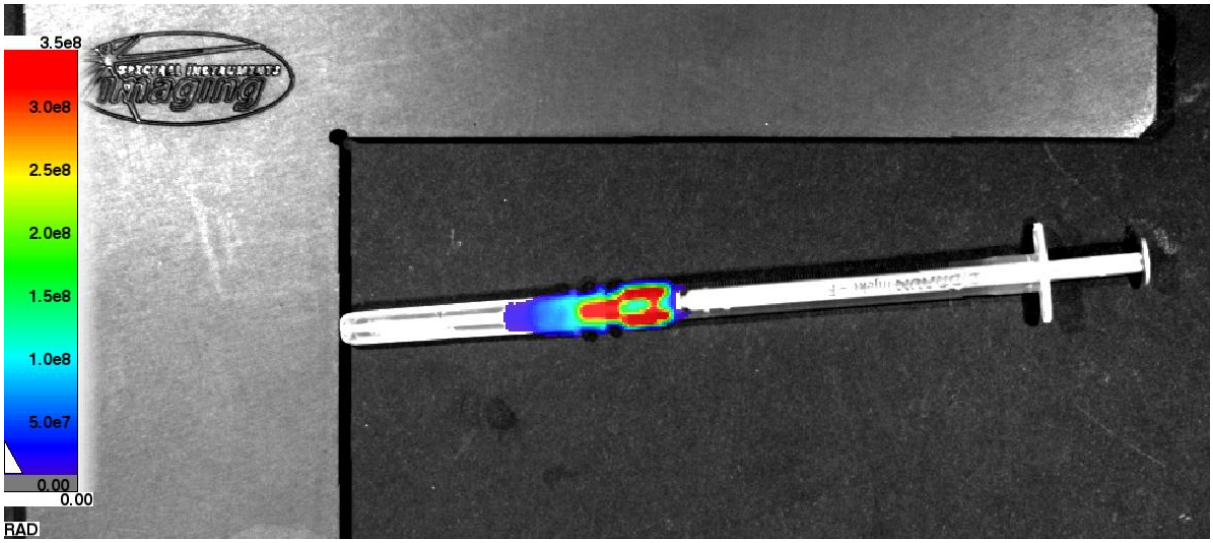

Figure 7.18 Example BLI acquisition showing that the macrophages remain viable after the encapsulation process and are alive immediately prior to engraftment to the mouse myocardium.

Identically cultured and harvested macrophage pellets were also resuspended in 0.9% saline. The cell loaded PBS and the cell loaded microsphere solutions were manufactured on the day of engraftment and stored on ice until ready for injection.

7.3.2.3 Myocardial infarction and engraftment

In total MI was induced in 32 C57/BL/6 wild type mice using the permanent suture ligation technique described in 1.2.3.4. During the open chest phase of the suture ligation intramyocardial injections of 20µL were delivered by manually under magnification using a 27G needle and low dead space syringe. One group of animals (N=8) received injections of saline only, a second group (N=8) received injections of saline + cells, the third group (N=8) received injections of microspheres without macrophages and the final group (N=8) received injections of macrophage encapsulated microspheres. Very low survival rates were observed following this surgery. From the saline group 3/8 mice survived up to the first MRI imaging point at 1-week post infarction and engraftment surgery. Survival in other groups was lower, in the cell group 2/8 mice survived, from the microsphere group 0/8 animals survived and from the cell encapsulating microsphere group 2/8 survived. The success of engraftment in the initial pilot study (7.3.2.1) suggests that the cause of mortality here was related to the infarction surgery. A full discussion of potential causes for this extremely poor outcome are hypothesised in the discussion of this section. The consequence of this is that there was a fundamental lack of statistical significance when comparing groups. In the results section trends will be observed but statistical testing is inappropriate when investigating such small populations.

7.3.2.4 Imaging

This study utilised two imaging modalities. BLI was performed regularly to assess the survival and retention of macrophages following engraftment and MRI was performed to assess myocardial structure and global and regional function.

BLI imaging was performed at 0, 2, 5 and 9 days post engraftment. Mice were anaesthetised under 2% isoflurane in oxygen and received 20µL intraperitoneal injections of luciferin. BLI was then performed and an identical square region of interest placed over the left thorax of each mouse to quantify the bioluminescent radiance from cells retained in the heart.

MRI was performed at 7 and 14 days post infarction and engraftment. The first scan performed was a segmented k-space T1 look locker acquisition this scan was performed to quantify native T1 of myocardium to allow calculation of the extracellular volume fraction (7.3.2.5). A Gd-DTPA

bolus was then delivered via IP line to the mouse in a standard LGE protocol. While the Gd was circulating a cine scan was performed to measure global function in the whole heart. A T1 scout image was then acquired, followed by a full resolution LGE acquisition to locate regions of hyperenhancement. A second segmented k-space T1 look locker acquisition was then acquired to quantify the T1 in tissue with Gd uptake in the interstitial space. Next a SPAMM tagging sequence was acquired in the x and y directions with a pixel size of 0.13×0.13×1mm, TE = 1.5ms, TR = 3.8ms, 20 cine frames and 10 averages. The tagging frequency for the SPAMM acquisition was set to $K_e = 1.49$cycles/mm as this was found to be optimal in the development of the SPAMM/HARP sequence. This was followed by a second regional function assessment with DENSE imaging. DENSE images were acquired with encoding in the x and y directions with a pixel size of 0.2×0.2×1mm, TE = 2.2ms, TR = 5ms, 20 cine frames and 15 averages. The artefact echo removal technique of choice was through plane dephasing with a strength of $K_d = 1.27$ cycles/mm and an in plane encoding strength of $K_e = 1.7$cycles/mm. Cine and LGE image analysis was performed in segment, T1 mapping, ECVF, HARP and DENSE reconstruction and analysis was performed in Matlab as described previously.

7.3.2.5 ECVF mapping

Structural changes such as diffuse or focal fibrosis and oedema are known to occur in myocardial infarction and can be quantified by changes to the extracellular volume fraction.[326] Measuring ECVF requires acquisition of quantitative T1 maps of the heart before and after the application of a gadolinium contrast agent. The ECVF is measured as the percent of tissue comprised of extracellular space. Since the contrast agent is known to only occupy the extracellular space we can make measurements of pre and post contrast T1 to assess the fraction of each pixel containing gadolinium/ extracellular matrix. ECV was introduced in this study to aid in the quantification of myocardial infarction. The regenerative paracrine properties of the macrophages were hypothesised to mediate the inflammation and resulting apoptosis following myocardial infarction. LGE is used to quantify infarct size thanks to its high resolution and positive contrast, but it is not quantitative of the tissue within the infarct due to variability in gadolinium bolus dosage, infarct size and signal intensity. ECVF mapping is a reliable quantitative method to assess the severity of infarcted tissue that is independent of these parameters.

The ECV is estimated by acquiring in the dynamic steady state phase following contrast uptake in the extracellular matrix. At this point post contrast there is a constant exchange between tissue and blood which is faster than the clearance of contrast from the blood. The ECVF is calculated from T1 values using Equation 7.1.

$$ECVF = (1 - hemacrit)\frac{\left(\frac{1}{T1_{myo-post}} - \frac{1}{T1_{myo-pre}}\right)}{\left(\frac{1}{T1_{blood-post}} - \frac{1}{T1_{blood-pre}}\right)}$$ Equation 7.1

Where hematocrit is the proportion by volume of the red blood cells within the blood, this value is unchanged in MI and is assigned a standard value of 44%.[327] The result of this calculation is a pixel wise map of ECVF with values in the range of 0 to 1. Examples from a healthy mouse are shown in Figure 7.19.

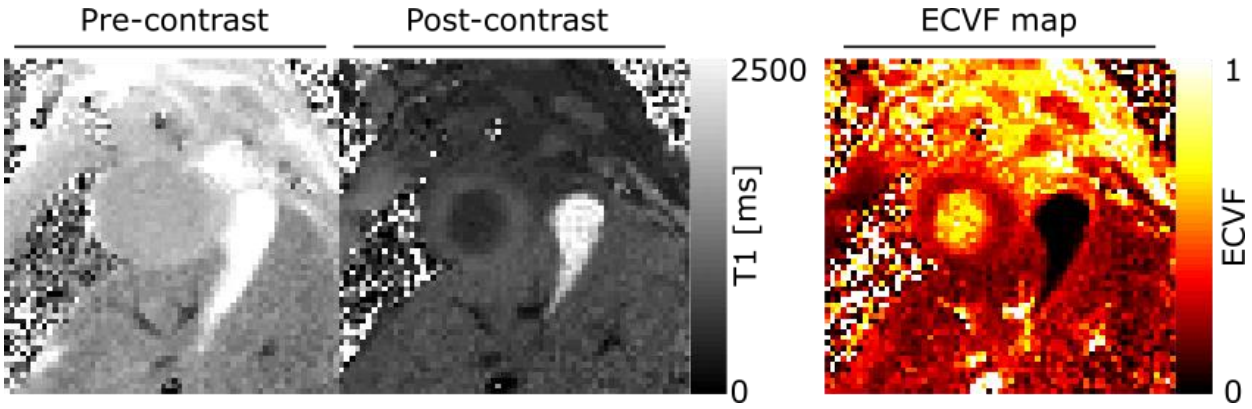

Figure 7.19 Example ECVF calculation from pre and post contrast T1 maps. In a healthy mouse heart, the ECVF is circumferentially uniform and in the region of around 0.2. It is important that the mouse does not move between T1 measurements pre and post contrast to prevent partial volume effects between maps.

7.3.3 Results

7.3.3.1 Cell retention

Bioluminescence imaging was used to track the retention of macrophages and their viability over the course of 9 days. The results are shown in Figure 7.20. Note that the scale in this figure is a Log10 scale, this was necessary to make the microspheres bioluminescence signal visible since the BLI signal was much greater in the saline injections. Initial BLI radiance at day 0 for the saline + cells group was 1164±37.8×10^2 counts/s/cm2/sr while the microspheres +cells group began at 1734±941 counts/s/cm2/sr.

Since the low BLI signal exists at in the microsphere group from day zero this is not a result of lower cell viability in the microspheres, the low signal indicates that the intial engraftment of cells to the infarct was much lower than the cells in saline. There are two possible reasons for

this 1) the cell density was much higher in the saline injections or 2) the microspheres were not being deposited in the heart and were become immediately displaced.

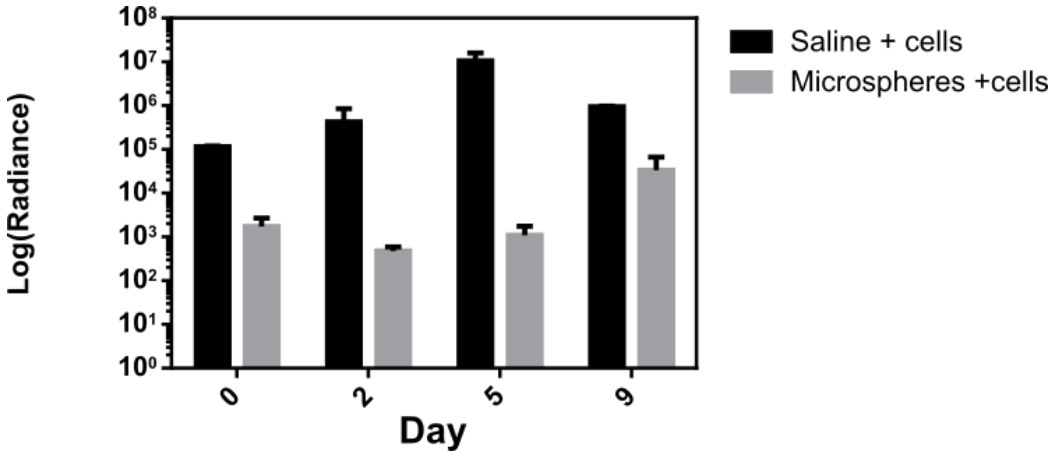

Figure 7.20 Bioluminescence from macrophages suspended in saline was higher than the signal measured from the macrophages encapsulated in microsphere. This is likely due to a lower cell density within the microsphere relative the saline injections.

7.3.3.2 Infarct quantification

The quantification of myocardial infarction took two approaches. First the LGE images were used to quantify the volume of the hyperenhanced scar region as a fraction of LV myocardium as performed is previous studies. Secondly the ECVF maps were used to assess the internal severity of these regions of hyperenhancement. Representative LGE and ECVF images from each group at 7 and 14 days can be seen in Figure 7.21.

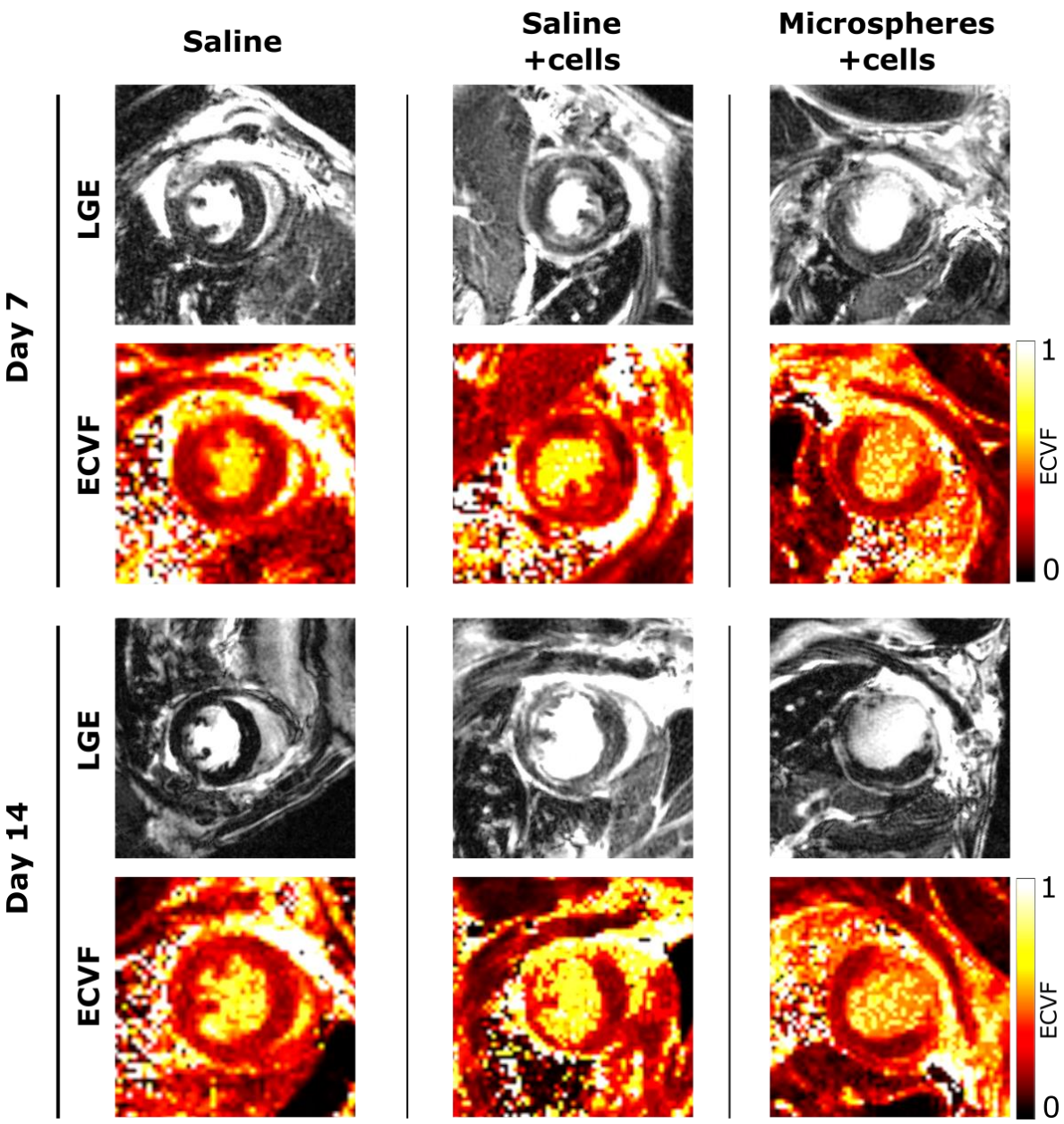

Figure 7.21 Representative LGE image and ECV maps. For each time point and group, it is clear that regions of increased signal intensity in LGE imaging correlate with regions of increased ECVF. The key advantage of using both of these techniques is that LGE provide high resolution quantification of scare size and ECVF reveals details about the underlying tissue structure.

The LGE and ECV maps show good agreement when identifying regions of myocardial infarction. Scar size from LGE images was quantified using the semi-automated EWA method described previously (Chapter 2) and these results are presented in Figure 7.22. The volume of LV scar in each animal is plotted at 7 and 14 days to show the evolution of the infarction with time. Interestingly the saline group without cells showed a decrease in scar size from 7.2±4.5%LV at 7 days to 1.8±0.4%LV at 14 days. The saline with cells group showed a moderate increase in scar volume from 12.0±10.6%LV to 19.8±3.4%. This increase however is visibly skewed by one animal who rapidly develops infarction over the measurement period. This is an interesting example

and the other measurements in ECV, LVEF and CO all show this same animal rapidly deteriorating. It is worth noting however that this animal skews the saline + cells group due to the small sample population. The mice treated with the encapsulated macrophages showed no overall change with a scar volume of 12.8±7.7%LV at 7 days and 11.5±5.3%LV at 14 days. Also shown in Figure 7.22 is the quantification of ECVF in infarcted and remote tissue from 7 to 14 days. The overall trend observed here shows an increase in ECVF in infarcted tissue from 7 to 14 days in the macrophage and saline treated group (0.34±0.09 to 0.64±0.08) and the microsphere encapsulated macrophage group (0.38±0.10 to 0.68±0.12) with no real change in the saline only group (0.26±0.01 to 0.24±0.02). Remote tissue remained largely unchanged overall in all groups. The consistent measurement of ECVF in remote tissue at 7 and 14 days in all groups is an encouraging sign that the ECVF technique is reproducible.

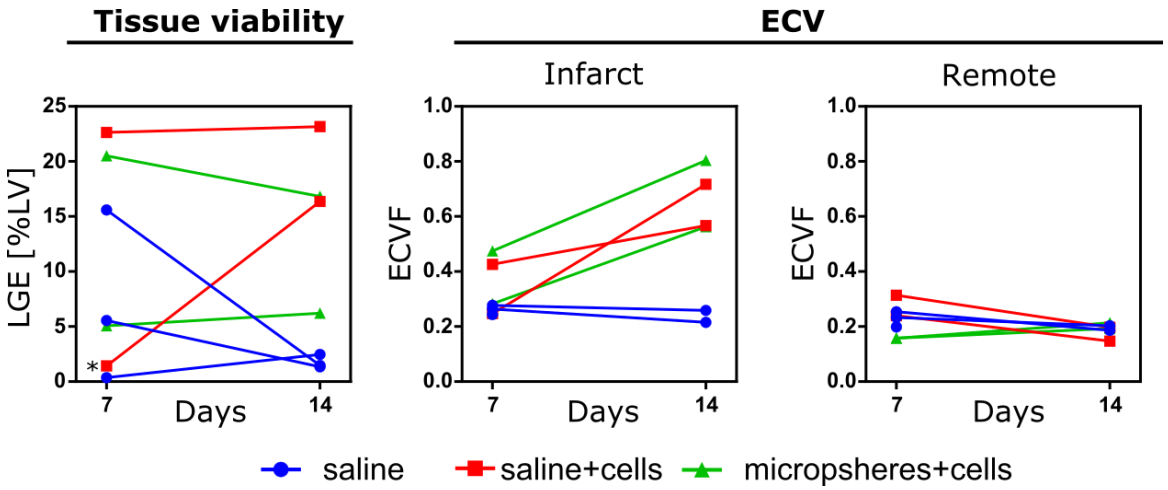

Figure 7.22 Quantification of LGE scar volume and ECVF in infarcted and remote tissue. Each line represents an animal over time and colour indicates the experimental group. Infarct severity appeared to increase in macrophage treated groups although overall scar volume was consistent for most of these animals. For animal showing rapid increase in LGE from 7-14 days (*) contrast did not enter system in this mouse producing an artifactual increase.

This increase in infarcted tissue ECVF over time suggests that the infarct is still developing and that cardiac remodelling along with inflammatory processes, are causing apoptosis in myocardial tissue resulting in increased ECVF. The increasing ECVF of the macrophage treated group is the opposite of what was hypothesised. In the case of the encapsulated macrophages it was observed from the BLI results that very few macrophages were retained within the heart. Low retention could be a possible explanation for this group, low cells counts are unlikely to be able to produce the beneficial cytokines and cofactors in sufficient quantities to modulate the inflammatory response.

7.3.3.3 Global heart function

Global heart function measured by LVEF and cardiac output is shown in Figure 7.23. Overall, LVEF appears to be maintained over the imaging period, this is despite increases in ECVF shown above for the macrophage treated groups. The saline treated group maintained the highest LVEF over the imaging period (61.3±5.5% - 63.0±2.4%). The saline treated group suffered a large drop overall (61.1±4.8% - 44.3±7.3%), although this is heavily affected by the rapidly deteriorating animal that also showed increased scar volume and ECVF. The encapsulated macrophage group had consistently lower LVEF over the imaging period (45.8±16.3% – 44.4±13.3%).

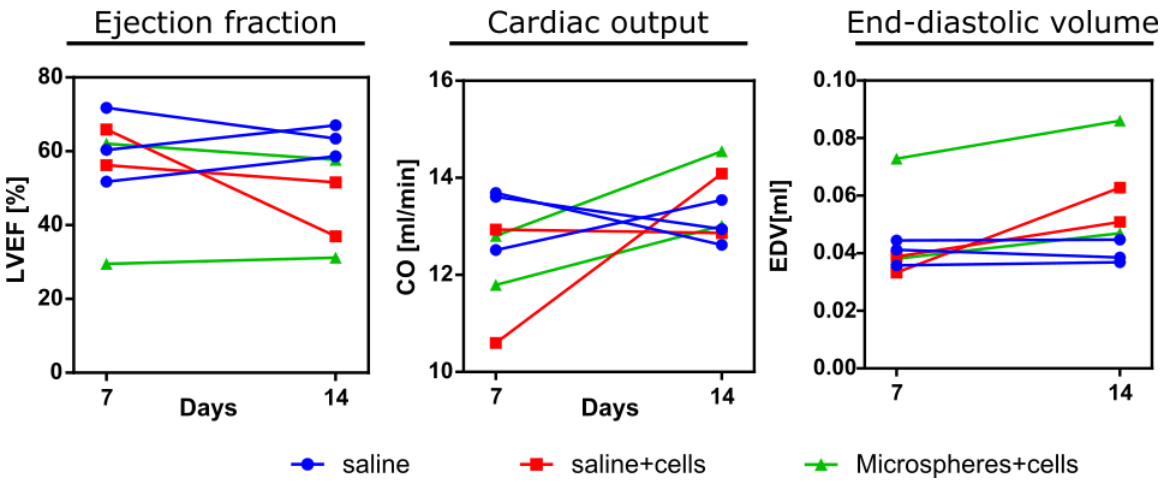

Figure 7.23 LVEF, cardiac output and end diastolic volume measurements. LVEF is most maintained between groups. CO recovers over time as the heart adapts to the remodelled myocardium. The principle mechanism by which CO is maintained is by expanded end diastolic volume.

Cardiac output (CO) is another measure of global cardiac function. CO is the product of stroke volume and heart rate and quantifies the amount of blood pumped per minute. Maintaining cardiac output is important to maintain systemic blood flow requirements. There are four major factors determining CO and dysfunction in one typically leads to the modulation of the others to maintain the same output.[328] Heart rate, contractility, preload and afterload are all variables in CO. The CO data presented in Figure 7.23 shows initially lowered CO in the cell + saline group and the encapsulated cell group (11.8±1.1 and 12.3±0.5 ml/min respectively) relative to the saline group where CO is maintained (13.3±0.4ml/min). After 14 days of cardiac remodelling the cell treated groups show that CO is adapting the presence of increased ECVF infarct severity and scar size with the CO increased to 13.5±0.6 ml/min in the saline + cells group and 13.8±0.8ml/min in the microsphere group. Measurements of end systolic volume and heart rate appear unchanged overall but the end diastolic volume (Figure 7.23) is increased in the macrophage groups suggesting that the heart is increasing preload to account for lost function and maintain cardiac output.

7.3.3.4 Regional heart function

This was the first study over the course of this project where both SPAMM and DENSE were developed to the point they could be compared. Figure 7.24 shows a comparison of the SPAMM and DENSE based measurements of regional circumferential strain in each segment of myocardium at day 7 and day 14. Along the vertical axis plots are ordered from injection site to neighbouring regions to remote regions, the horizontal axis indicated time and imaging technique used.

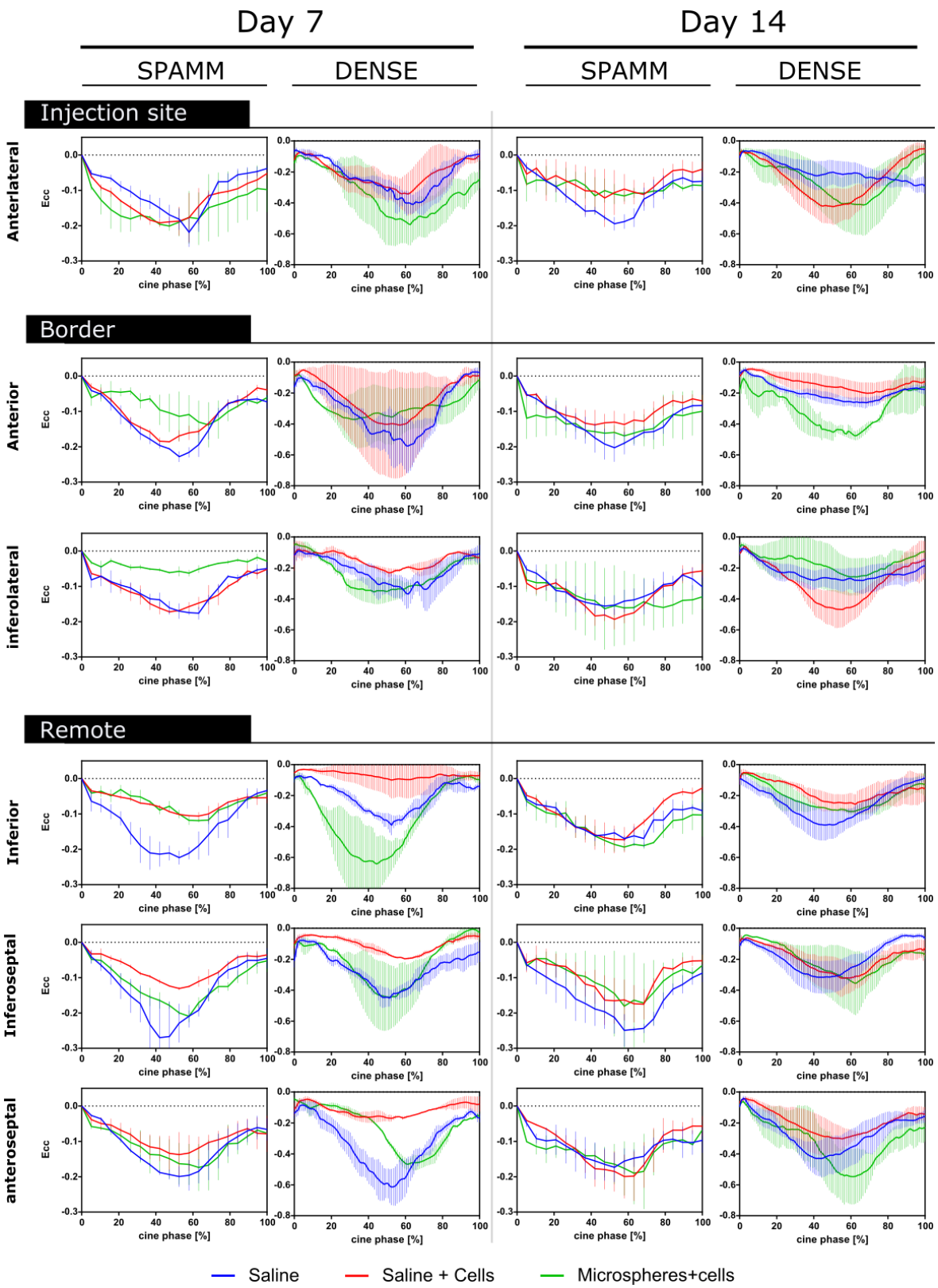

Figure 7.24 Comparison of regional circumferential strain measurements (Ecc) by SPAMM and DENSE. Each strain time curve shows the circumferential strain through the cardiac cycle in 6 segments of heart tissue measured either using the SPAMM technique (chapter 5) or DENSE (chapter 6). Regions are separated in injections site, neighbouring and remote tissue to aid visualisation.

Overall the circumferential strain curves were of similar shapes when measured by SPAMM or DENSE. The small sample size results in comparatively large error bars compared to the previous functionalised hydrogel study (7.3). The denser temporal sampling in DENSE results in smoother curves which may provide subtler information about cardiac mechanics for example, the comparison between the anteroseptal region at 14 days shows delayed contraction in the microspheres group. This is easily visible in the DENSE dataset but appears obscured by lower spatial and temporal resolution in the SPAMM data.

Figure 7.25 shows example regional assessment data from a single animal. This mouse is from the saline + cell group and was selected arbitrarily. The LGE image shows hyperenhancement in the lateral wall corresponding to a region of infarction, confirmed by ECVF mapping. The displacement fields show the 2D displacement of each pixel produced from both the SPAMM/HARP processed data and the DENSE dataset in the same slice. The higher density of displacement vectors in the SPAMM data is due to the higher resolution of the acquisition. However, the lower resolution of the displacement information in SPAMM is visible from the high degree of smoothness in the vector field. Conversely the DENSE data has lower acquisition resolution due to signal restraints but offers higher displacement resolution. This is visible in the circumferential strain data; the DENSE dataset is able to isolate 3 regions of reduced contraction within the infarct area. The SPAMM dataset however can resolve only a single broad area of dysfunction. Whether the added resolution of DENSE provides better information than the smoother SPAMM data is a question that is specific to application. The SPAMM data also identifies regions of reduced contraction in the septal wall which do not manifest themselves in the LGE of ECVF maps suggesting that this is the result of poorly tracked pixels. Since DENSE does not rely on pixel tracking in the post processing but encodes displacement within the measured signal DENSE is less susceptible to this kind of error.

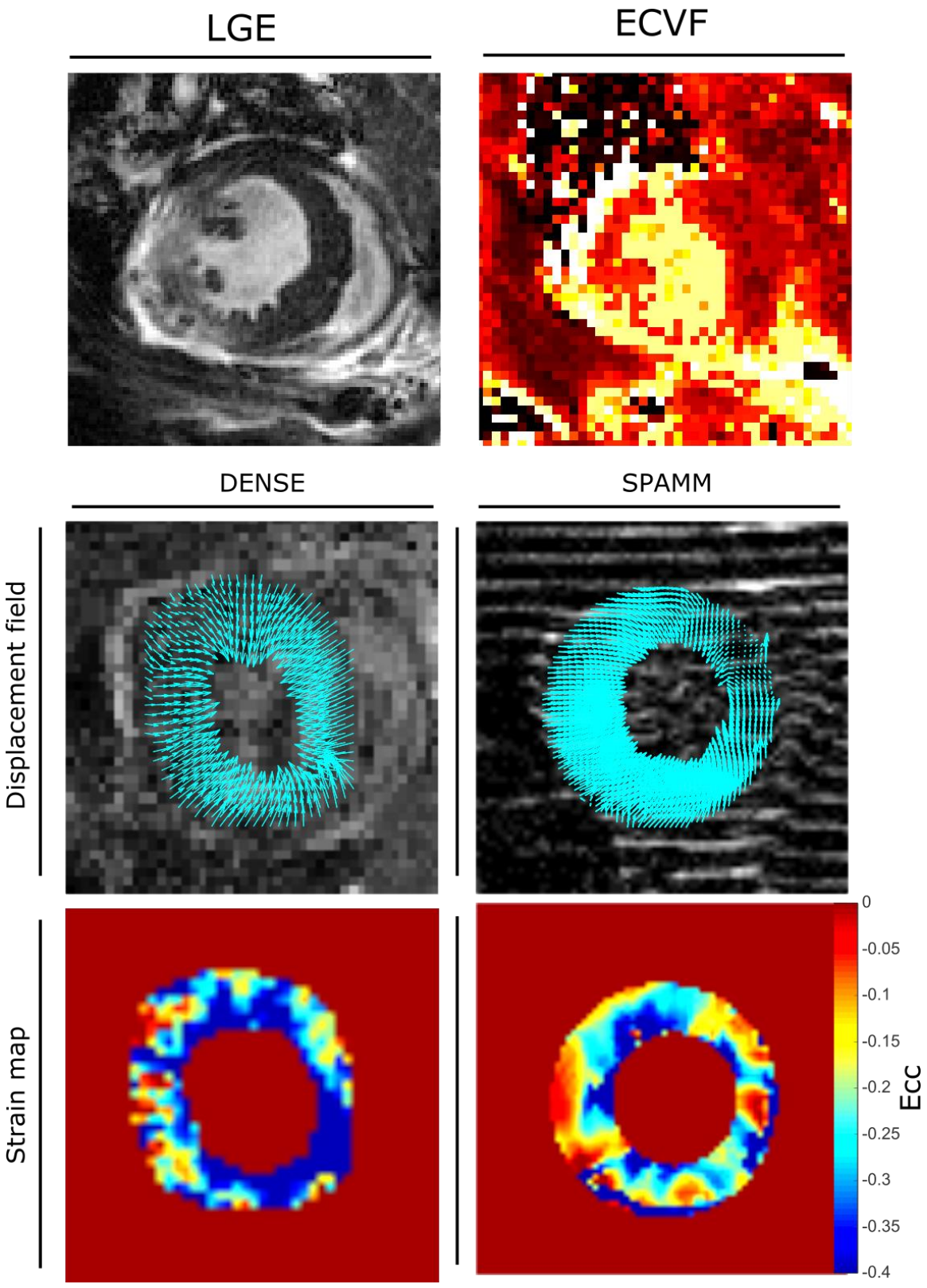

Figure 7.25 Example images in the same mouse from SPAMM and DENSE. LGE and ECVF maps are provided for structural information. Both techniques identify the region of LGE hyperenhancement by enhanced strain in the lateral wall. However, SPAMMs information, although a better match to the LGE data in the lateral wall is lower resolution more prone to tissue tracking errors than DENSE.

To further compare the two techniques, the peak strain for each animal was measured and segments assigned to either infarct (anterior, anterolateral, inferolateral) or remote (inferior, inferoseptal, inferoseptal). These were then compared for each group at day 7 and day 14. The results are shown in Figure 7.26.

In terms of measuring peak strain SPAMM and DENSE provide very similar relationships between groups. SPAMM and DENSE both give the same results when investigating which group has higher or lower strain. In terms of absolute values DENSE returns higher strain. This is likely due to the higher resolution strain information provided by DENSE. The raw displacement information is much coarser than the smooth, filtered HARP analysis technique. The result is DENSE displacement maps have a higher displacement gradient at boundaries between neighbouring pixels that causes increased strain measurements.

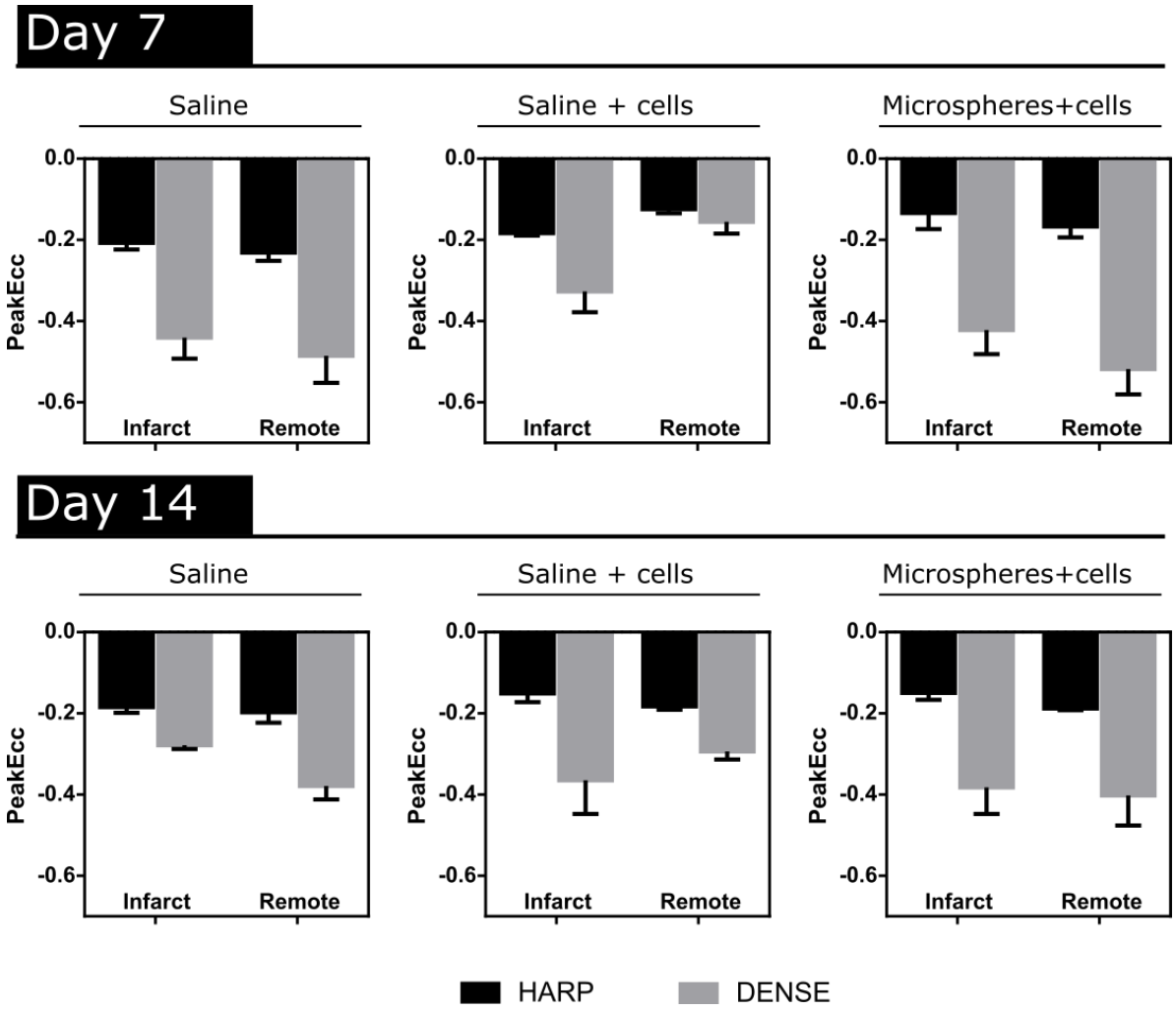

Figure 7.26 Comparison of peak strains in infarct tissue and remote tissue. HARP and DENSE provided similar results in terms of the relationships between groups but gave much higher strain magnitude relative to HARP.

Finally, to compare the two a correlation plot of peak circumferential strain measured by SPAMM and by DENSE is shown in Figure 7.27 along with a Bland-Altman analysis of peak strain. There was a no real correlation (R^2 = 0.07) between HARP and DENSE measures of peak circumferential strain in this case. The Bland-Altman analysis shows an increasing difference with increasing average. This suggests that the similarities between the two techniques is poorest at high strain values. All of the points in the Bland Altman plot show positive differences which corresponds to the positive bias where strain values measured by DENSE are higher relative to SPAMM.

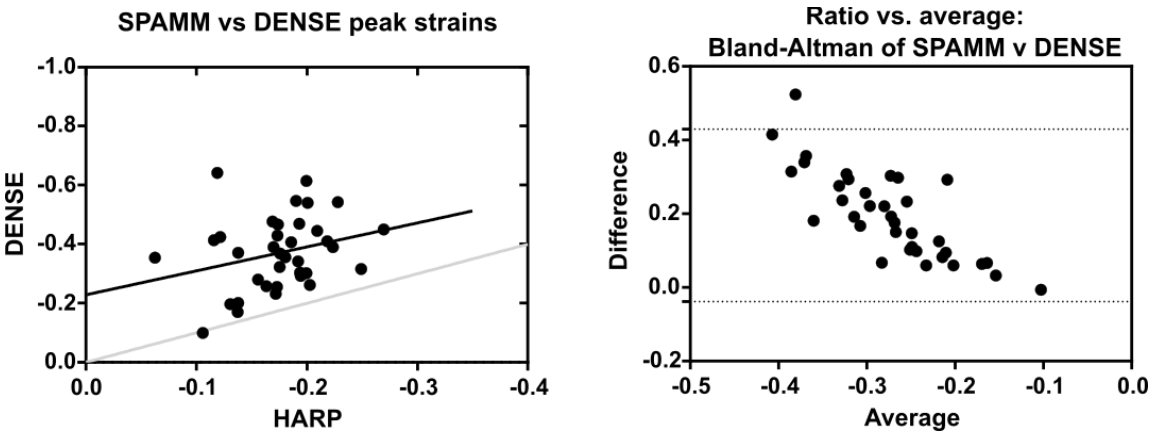

Figure 7.27 Comparison of HARP and DENSE measurements of peak circumferential strain. The solid black line indicates the line fitted by least squares regression and the light grey represents the 1-1 line. Bland-Altman analysis showed increased differences at high strain peaks suggesting there is a magnitude dependence on the correlation.

The lack of correlation between the two measures may be partly explained by the different resolutions of the strain information. The strain maps produced by SPAMM are convolved by the bandpass filter used in k-space to isolate the displacement encoded peak. This means that the relative displacement between neighbouring elements of tissue is smoothed, with the true pixel wise displacement masked by the poor resolution. The use of DENSE where full resolution pixel wise displacement is available produces maps where each pixel is measured independently from the surrounding tissue. The result of this is more variation in the displacements measured since each corner of the quadrilateral strain element can move independently.

To validate the sensitivity of DENSE or HARP to regional dysfunction the circumferential strain in the infarct segments and the remote segments were compared to the ECVF in the infarct and remote segments. The results of this comparison are shown in Figure 7.28. The circumferential strain measurements made by HARP show no dependence on ECVF in the infarct or remote tissue. The DENSE measurements of strain show a relationship in the infarct zone, and no relationship in the remote tissue. The suggests that the ECVF changes present in the infarct

myocardium are creating regional variations in circumferential strain that DENSE regional imaging is sensitive to.

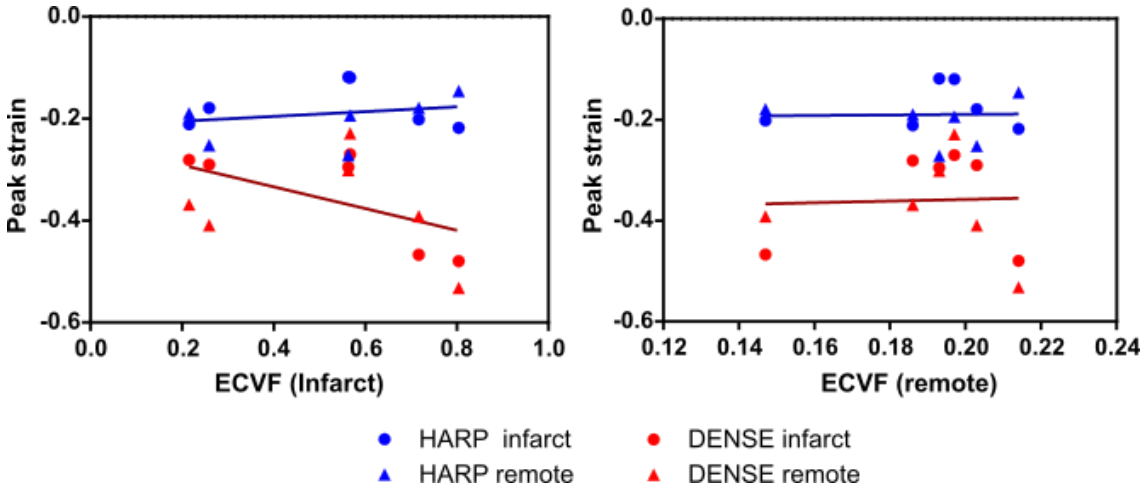

Figure 7.28 Correlation of DENSE and HARP measurements of circumferential strain against ECVF measurements in the infarct and remote tissue. DENSE shows a higher sensitivity to the ECVF induced changes in circumferential strain in the infarcted myocardium.

7.3.4 Discussion

This study has investigated the engraftment of macrophages encapsulated within calcium alginate microspheres for regenerative therapy in the heart. Overall, the results showed no benefit to engrafting microspheres or macrophages in terms of cardiac function, myocardial scar size or scar evolution. The results from the surviving animals seems to suggest that injecting saline into the infarcted myocardium is more beneficial than delivering cells microspheres. The evidence for this conclusion is weak due to low sample populations. However, it may be best to consider the infarct and infarct + microsphere encapsulated macrophages as the same group since the retention of cells is very low in this group. The saline injection group consistently showed the smallest infarcts at 7 and 14 days- this may indicate mild infarctions rather than an effective therapy. The main problem with this study is the small sample sizes and the poor survival of animals following engraftment. The pilot study described in (7.3.2.1) showed survival in all animals following engraftment of identical microspheres. This pilot study used ultrasound guided injection to deliver the microspheres to the non-infarcted heart. For the full study the microspheres were engrafted using two modifications to the engraftment procedure 1) microspheres were delivered to the infarcted heart and 2) injections were performed by hand during surgery. The decision to inject by hand rather than using the ultrasound guidance was taken due to the difficulty in performing cardiac injection in the infarcted heart. The complex

infarct environment produces multiple reflective boundaries that can make resolving the myocardium difficult, especially during the early remodelling phase of MI. The decision to inject during the surgery was justified by providing the optimal conditions for the macrophages to provide a therapeutic effect, before the inflammatory response was triggered. These two decisions are likely to be the cause of the poor engraftment process. The engraftment of the microspheres to the myocardium at the same time as the induction of MI appears to place too much pressure on the heart at once and results in acute heart failure. Previous studies that have engrafted microspheres to the infarcted heart have allowed 7 days for the infarct to develop and cardiac remodelling to begin before performing the injection.[319] Injections by hand were performed during surgery since this reduced the number of invasive procedures the mice would need to undergo. The problem with manual injections is that it relies heavily on the skill of the surgeon and the small dimensions of the mouse heart make the procedure extremely difficult. If this study were repeated, the engraftment procedure would more closely mimic the pilot study and previous published work by engrafting via ultrasound guidance and performing the engraftment after allowing the myocardium time to adapt to infarction.

The discrete nature of microsphere although beneficial in many ways, has several consequences. Mechanically the behaviour of microspheres is less predictable than a single interconnected bolus of biomaterial. Additionally, the smaller that the microspheres are manufactured the more likely they are to become displaced following engraftment. A study by Teng et al. (2006) showed that injected microspheres are liable to become immediately displaced following intracardiac injection. This mechanical leakage could account for the lack of microsphere retention following injection shown by the BLI data. Key to the success of the microsphere approach is finding ways to increase this microsphere retention. Microsphere size and location of engraftment are likely to be important factors in optimising retention. Larger microsphere will be less likely to be displaced but will be harder to engraft. Some studies have taken the approach of engrafting a cluster of microspheres to the epicardium where they are unlikely to be affected by myocardial contraction but are also limited in their ability to regenerate transmural myocardium.

Regional function was assessed by measuring the peak strain for each animal, this is the conventional way to summarise the strain-time curve with a single value and quantifies the maximum deformation. Whether this is the best value for this purpose is debatable, the area of the strain-time curve may offer a more complete value of contraction over the whole cardiac cycle. The lack or correlation in circumferential strain measurements in HARP and DENSE is interesting. Since they are measuring the same mechanical property of tissue it would be expected that a strong correlation would exist between them. Indeed, this has been

demonstrated in previous DENSE development papers, where they have compared the relatively new DENSE technique to the gold standard SPAMM and HARP methods.[329] The most likely reasons for this variation are the spatial and displacement resolution of the acquisitions. The DENSE acquisition had a lower acquisition resolution compared to the SPAMM sequence since the additional SNR provided by larger pixels was required however it provided a higher displacement resolution since it does not require filtering in k-space that removes a large fraction of the spatial information. Observing the displacement field examples given in Figure 7.25, the DENSE displacement field appears more physiological and a closer match to the expected motion paths compared to the SPAMM data. The smoothness of the SPAMM data leads to low resolution strain maps that are unable to reveal the finer details of the strain field that may be important in a repeated biomaterial experiment with higher samples sizes. Another important factor that may be affecting strain calculations is the masking applied to isolate displacement of the LV form the large artifactual displacements in the pulmonary cavity and blood pool. A binary mask is applied to separate these values, in the current processing pipeline these are drawn manually based on SPAMM and DENSE images. SPAMM and DENSE images are both poorly suited to isolating myocardial boundaries due to the presence of tag lines and low SNR respectively. It was not possible to apply the same mask due to differences in the sizes of the acquisitions. A solution to this that would be an important modification to future work comparing the sequences would be to acquire a standard cine image in the same slice orientation with the same dimensions as the SPAMM and DENSE acquisitions. This could be segmented to provide an independent mask for both acquisitions and remove this variability.

To date, this experiment has utilised the largest fraction of the complete preclinical cardiac MRI assessment toolset developed over the course of this thesis. Global heart function was assessed with cine MRI, quantified by LVEF, CO and EDV. Regional heart structure was assessed using both LGE and ECVF mapping, the use of ECVF requires two T1 maps of the heart but these are not shown due to the more standardised nature of ECVF. Regional heart function was then assessed using both the advanced SPAMM and DENSE sequences I developed during this work. This study was intended to be a final exhibition of the imaging techniques developed.

Despite the setbacks in this experiment microspheres are an exciting prospect for cardiac regeneration therapy. The versatility and theoretical reproducibility of this therapy is a key advantage compared to in-situ formed hydrogels. If this experiment were repeated the engraftment procedure would be refined as described above to enable a higher graft acceptance and DENSE would be chosen as the regional function measure of choice due to the higher resolution strain information it provides. Additional refinements to the microspheres could also

include the inclusion of additional bioactive molecules such as VEGF or HGF. Mechanical validation of the microspheres by rheology could also improve the therapy. The PEG hydrogel discussed in 7.3 was tuned to myocardial tissue and showed little mechanical impact on the contraction in these hearts. Forming this functionalised PEG hydrogel into microspheres may be the most promising regenerative biomaterial to take forward for further investigation.

7.3.5 Key results

- Poor surgical outcome from microsphere engraftment in myocardial infarction
- DENSE shows a relationship to the degree of extracellular volume fraction in infarcted tissue and is more sensitive to this dysfunction than SPAMM
- SPAMM and DENSE provide different information where SPAMM is susceptible to mistracked myocardium and DENSE data suffers from image noise

7.4 Summary

This chapter has described 3 of the experiments I performed over the course of this thesis to validate the developing MRI imaging toolset. Part 1 described the imaging of scaffoldless fibroblast cell sheets in myocardial infarction. Results showed improved LVEF and reduced scar size in treated hearts. Basic regional assessment tools were used to show contractile improvements in the border zone of infarcts.

In part 2 I discuss a collaborative project in which I assessed the safety of a highly optimised synthetic hydrogel for CSC transplant. This study also introduced the field of injectable biomaterials and the developed protocol for ultrasound guided intramyocardial injection. Despite covalently bound contrast agents the hydrogel could not be visualised. However, the hydrogel was shown to increase in-vivo cell retention and the engraftment was shown to have no significant effect in any segment of myocardium demonstrating that the in-vitro optimisation for mechanical properties was successful and that the gel is ready for further studies in cardiac regeneration.

Finally, in part 3 I discuss a study that aimed to bring the separate imaging components of this thesis together to assess the regenerative potential of cell encapsulating alginate microspheres. Due to poor engraftment and infarction outcome this experiment was limited in assessing

regenerative potential. However, the imaging tools that will enhance studies such as this in the future were exhibited and the value of such techniques demonstrated.

The central role of imaging in these studies shows its value as in imaging of regeneration therapy. The non-invasive and in vivo nature of MRI allows it to be used to monitor myocardial structure and function serially as in part 1 and 2. Restoration of contractile function is a target of all cardiac regenerative therapies and MRI offers the gold standard in global and regional function assessment. It is hoped that the demonstration of these techniques will help in the uptake of these imaging tools in future clinical and preclinical studies of cardiac regeneration.

Chapter 8 Final discussion

This thesis has described my work in developing preclinical MRI acquisition techniques for the assessment of myocardial structure and function for applications in regenerative medicine.

Cardiovascular disease remains the number one cause of death worldwide, the WHO attributed 30% of all deaths to cardiovascular disease in 2005.[330] Over the past 20 years therapies for cardiac disease have come of age. Treating coronary heart disease in particular has seen a revolution in new treatments such as statins, stents and beta blockers. These therapies have slowed death rates and are able to minimise ischemic heart damage following myocardial infarction. Crucially however, they are unable to recover the lost heart function due to cardiomyocyte death resulting in poor prognosis for patients.[331] Myocardial regeneration therapy is a new strategy towards treating cardiac disease that engrafts regenerative cells and biomaterials to the myocardium to stimulate repair of tissue and restoration of contractile function.[332] Cardiac regeneration therapy has made a rapid translation from preclinical research to clinical trials as early as 2001.[333] Clinical results in the years since however have been underwhelming[108] and there is a general consensus that further preclinical optimisation utilising powerful non-invasive imaging data will be key to the future success of regenerative medicine in humans.

Medical and biomedical imaging techniques will play a central role in the optimisation into the safety and efficacy of future regenerative therapies. Imaging across scales will provide crucial information for the development of regenerative therapies over the next decade. Modern microscopy techniques such as two-photon fluorescence microscopy offer unparalleled views of the cellular architecture at sub-cellular resolutions with high sensitivity and specificity for characterising dynamic changes at micron scales. This information is valuable for in-vitro optimisation studies but it will be the imaging of whole organ systems using in-vivo techniques such as ultrasound, SPECT/PET, X-ray CT and MRI that will give the best insight into regenerative efficacy. In vivo imaging provides powerful information on the internal physiological changes induced by disease and in response to therapeutic intervention that cannot be provided by in vitro experiments. The practicality and availability of ultrasound imaging systems make them widely used in clinical and preclinical research. They offer high temporal and spatial resolution as well as allowing high throughput and cost effective imaging studies to be performed and are well suited to imaging the heart. The sensitivity and specificity of SPECT and PET imaging make them the gold standard for quantitative cell tracking and these modalities will provide valuable data

for enhancing cell retention following engraftment. Magnetic resonance imaging is unparalleled in providing non-invasive multiparametric imaging of both global and regional cardiac structure and function. MRI provides high spatiotemporal resolution and multiple contrast mechanisms revealing information about molecular changes in the myocardium. These imaging abilities make MRI a versatile and powerful tool in the preclinical optimisation of cardiac regeneration therapies. Over the chapters presented in this thesis I have established a set of MR imaging protocols that enable valuable in vivo characterisation of cardiac function and structure in mouse models of regenerative therapy.

In chapter 3, a set of multiparametric MRI imaging sequences were used to characterise a mouse model of cardiac disease and quantify how it affected cardiac function. Also investigated was how the accumulation of pathological iron within the heart and other organs could be quantified using appropriate MRI relaxometry. The disease model that was imaged was a mouse model of beta thalassemia expressing cardiac iron overload. I have established imaging tools to quantify the disease characteristics for applications in novel gene and chelation therapies. This is similar to the overall research goals in this thesis, where we aim to develop imaging tools for the assessment of novel cardiac regeneration therapies. The imaging data found that iron sequestration in the heart, liver and spleen could be quantified using a combination of T1, T2 and T2* relaxometry techniques. Global cardiac function quantified by cine MRI was found to be unchanged, despite the pathological iron overload in these organs. It is known that iron accumulation in iron metabolising organs such as the liver and spleen predisposes a patient to heart failure. This study has produced early imaging biomarkers for identifying iron overload prior to cardiac dysfunction using multiparametric MRI techniques. The experience gained from this study in terms of NMR relaxation model fitting, quantification of global cardiac function and experimental process were carried through to the biomaterial regeneration studies outlined in chapter 7. The next step for continuation of this work is the application of these MRI techniques for the assessment novel therapies. The characterisation of this mouse model in disease and iron overload pathology enables development of new therapies such as correcting the defective beta globin gene in utero or producing novel iron chelation agents.

Chapter 4 introduced the vital importance of quantification of regional function in myocardial regeneration. MI is characterised by the formation of non-contractile scar region as well as a border zone of damaged but salvageable tissue. Using global functional measurements such as ejection fraction limit the scope of an investigation. Global function is a commonly used clinical diagnostic measure but in clinical and preclinical research the function of individual segments of heart tissue provides more powerful information of the efficacy of a therapy or the extent of

damage. This chapter discusses the limitations of global cardiac function and presents key studies that make use of regional function measurements in cardiac pathology and cardiac regeneration. Regional techniques developed over the course of this thesis were used in Chapter 7 to demonstrate improved function in border zone tissue that could not be identified from global cine MRI. Chapter 4 also introduces the assessment of regional function from standard cine MRI. Assessment of a mouse model of myocardial infarction without therapy showed that the cine MRI analysis was able to quantify regional loss of wall thickening in the infarcted region and a whole LV reduced fractional shortening. This information is limited in that it describes only the radial 1 dimensional dysfunction of the LV segments. There is therefore a requirement for more powerful 2D and 3D displacement measuring tools that are able to fully characterise the complex motion of the contracting heart which led to my development of the SPAMM and DENSE sequences in subsequent chapters. The greatest potential of the wall thickening and fractional shortening measurements I produced in this chapter is in retrospective analysis. It is standard practice to acquire a cine MRI scan to visually assess the contraction of the heart during a cardiac MRI procedure. The ability to go back to data and reanalyse it for regional dysfunction will enable new interpretation of data. A future study is planned to use the methods developed here to retrospectively improve upon a study of diastolic dysfunction in myocardial infarction.

Chapter 5 described the development of a spatial modulation of magnetisation (SPAMM) MRI acquisition technique and the associated harmonic phase (HARP) tissue tracking method. SPAMM is an MRI tagging based technique that saturates the heart in a 1D sinusoidal pattern allowing tracking of regions of tissue by the deformation of the sinusoid. SPAMM has been successfully used in clinical research since the development of the HARP technique that greatly facilitates the post processing of data.[237] SPAMM and HARP were developed and optimised over the course of this chapter and were validated against a programmable motion phantom. This motion phantom could be programmed to simulate a range of periodic displacements that were imaged using an evolving SPAMM acquisition protocols and processed with HARP to demonstrate accurate displacement mapping. A limitation of this sequence is the relatively low spatial resolution of displacement information. A high fraction of the MRI acquisition is discarded during the HARP technique when the displacement encoded information is isolated. This loss of information may be important in cardiac regeneration therapy at the boundaries of regenerative biomaterials where mechanical matching will play a crucial role in engraftment safety. The SPAMM technique is recognised as the clinical standard for regional function measurements and so it is an essential imaging tool to have available in the MR imaging toolbox

I was developing for tracking regenerative therapy. However, the low spatial resolution led me to the development of the displacement encoding using stimulated echoes (DENSE) imaging protocol that provides higher resolution spatial information at a cost of image SNR.

Chapter 6 followed the development, validation and optimisation of the high resolution DENSE protocol for assessing regional cardiac mechanics. DENSE is presented as a natural evolution of the HARP processing method, it uses similar mathematical principles to encode spatial information within a single displacement echo. However, rather than use a frequency filter to remove spatial information it uses a decoding magnetic gradient during acquisition. This shifts this echo to the centre of k-space where it can be isolated while keeping the high frequency information intact. A novel application of the projection onto dipole field phase correction technique was applied to DENSE acquisitions to correct for background phase due to poor magnetic homogeneity in the heart and reducing the acquisition time by a third. A number of different techniques for isolating the displacement echo were presented including two different complementary acquisition methods and through plane dephasing. These echo removal techniques were compared and the through plane dephasing method chosen as the optimal balance of artefact suppression and acquisition time. Due to malfunction the motion phantom used to validate the SPAMM and HARP sequences was not available for validation of DENSE. Future development of DENSE would involve redevelopment of the phantom and using it to optimise and validate the DENSE sequence. With a fully optimised DENSE acquisition sequence the next step would be to use it in a full study of cardiac regeneration. Unfortunately, it was not available until the final study presented in chapter 7 where the study population was severely limited.

With the development of DENSE and SPAMM as well as the functional, relaxometry and viability imaging techniques described in chapters 3 and 4 a complete set of imaging tools were established for assessment of myocardial mechanics, structure and composition using non-invasive imaging with in vivo methods. These imaging techniques were then applied in mouse models of cardiac regeneration therapy in chapter 7. The three experiments described in this chapter were performed over the 4 years taken to develop the work in this thesis. Consequently, not all of the imaging techniques I developed over this time were available at the time of the study. However, following each experiment, experience was gained and guided my decision as to what imaging tool would require development next to improve upon the study. In this way this final chapter presents the evolving regenerative imaging platform I have been developing over the course of this work and provides examples of experiments in which they are applicable.

Future applications of the work presented in this thesis would be the incorporation of these imaging techniques into large preclinical studies of cardiac regeneration therapy. The imaging techniques presented here are applicable to any cardiac regeneration study that requires knowledge of changes in heart structure and function. The non-invasive nature of MRI makes it a powerful tool for serial assessment of potential therapies. The ability to serially monitor cardiac structure (e.g. ECV mapping, relaxometry) and function at a global (cine) and regional level (e.g. DENSE, HARP) is of huge benefit to optimisation of regenerative medicine. Future work resulting from this thesis would be to repeat one of the pilot studies presented in Chapter 7 with the developments produced from the pilot data. This repeated study would serially monitor a statistically robust study population with wild type, infarct, treated with cells + biomaterial and treated with biomaterial only groups. Imaging tools could include the full range of structural/relaxometry sequences and high resolution DENSE for regional function. A study with this structure would be able to determine the therapeutic effect of a cell loaded biomaterial relative to the benefits provided by the biomaterial alone. Of the biomaterials investigated in Chapter 7 the most likely candidate for further study are the alginate microspheres. The highly versatile microsphere platform allows widely customisable therapy that can be highly optimised by variation in microsphere size and structure. Crucially any type of microspheres can easily be combined with another in a single injection. An example of this may be the combination of cell laoded microspheres combined with tailored microspheres for releasing bioactive molecules (e.g. VEGF) to support the transplanted cells.

There is scope for further developments of the techniques developed here. Of particular interest would be development of the PDF technique for removal of background phase contributions in DENSE. Alternative methods for phase removal may provide a more efficient method for removing this contribution e.g. incorporating a solution to the Laplacian boundary value problem (LBV). Establishing the benefit of these alternative techniques would be a subject for future work. As discussed in chapter 5 the use of the tag fading present in tagged images for cardiac T1 mapping is also of particular interest. A sequence that is able to simultaneously quantify regional function and T1 is a useful tool and provides a highly efficient use of scan time.

Cardiac regeneration therapy is an exciting field of rapid development. Clinicians can be cautiously optimistic regarding the modest response to therapy seen in clinical trials. Successful translation represents a long term goal and extensive preclinical validation work will be required with many challenges remaining open. These challenges include optimisations in cell type, delivery method, timing of delivery and biomaterial properties. The role of preclinical imaging in this optimisation process will provide the valuable validation of methods and will be essential to

successful translation to clinical practice. It is hoped that the methods developed over the course of this thesis aid in the uptake of imaging applications in studies of regenerative medicine and that the wide range of imaging tools deployed help to bring regenerative medicine closer to practical clinical therapy.

Chapter 9 References

1 WHO. *Cardiovascular diseases (CVDs) fact sheet*, 2016).

2 Hausenloy, D. J. & Yellon, D. M. Myocardial ischemia-reperfusion injury: a neglected therapeutic target. *The Journal of clinical investigation* **123**, 92-100 (2013).

3 Nascimento, B. R., Brant, L. C., Moraes, D. N. & Ribeiro, A. L. Global health and cardiovascular disease. *Heart* **100**, 1743-1749, doi:10.1136/heartjnl-2014-306026 (2014).

4 Leal, J., Luengo-Fernández, R., Gray, A., Petersen, S. & Rayner, M. Economic burden of cardiovascular diseases in the enlarged European Union. *European heart journal* **27**, 1610-1619 (2006).

5 Mathers, C. D. & Loncar, D. Projections of global mortality and burden of disease from 2002 to 2030. *Plos med* **3**, e442 (2006).

6 Lopez, A. D., Mathers, C. D., Ezzati, M., Jamison, D. T. & Murray, C. J. Global and regional burden of disease and risk factors, 2001: systematic analysis of population health data. *The Lancet* **367**, 1747-1757 (2006).

7 Heidenreich, P. A. *et al.* Forecasting the future of cardiovascular disease in the United States a policy statement from the American heart association. *Circulation* **123**, 933-944 (2011).

8 Health, N. I. o. in *Bethesda (MD): US Department of Health & Human Services* (2011).

9 Katz, A. M. *Physiology of the Heart*. (Lippincott Williams & Wilkins, 2010).

10 Sietsema, K. E. *et al.* Dynamics of oxygen uptake during exercise in adults with cyanotic congenital heart disease. *Circulation* **73**, 1137-1144 (1986).

11 Roger, V. L. *et al.* Heart disease and stroke statistics—2012 update a report from the American heart association. *Circulation* **125**, e2-e220 (2012).

12 Didangelos, A., Simper, D., Monaco, C. & Mayr, M. Proteomics of acute coronary syndromes. *Current atherosclerosis reports* **11**, 188-195 (2009).

13 Czarny, M. J. & Resar, J. R. Diagnosis and management of valvular aortic stenosis. *Clinical Medicine Insights. Cardiology*, 15 (2014).

14 Thaden, J. J., Nkomo, V. T. & Enriquez-Sarano, M. The global burden of aortic stenosis. *Progress in cardiovascular diseases* **56**, 565-571 (2014).

15 Pasupathy, S., Air, T., Dreyer, R. P., Tavella, R. & Beltrame, J. F. Systematic review of patients presenting with suspected myocardial infarction and non-obstructive coronary arteries (MINOCA). *Circulation*, CIRCULATIONAHA. 114.011201 (2015).

16 Thygesen, K., Alpert, J. S. & White, H. D. Universal definition of myocardial infarction. *Journal of the American College of Cardiology* **50**, 2173-2195 (2007).

17 Reimer, K. A., Lowe, J. E., Rasmussen, M. M. & Jennings, R. B. The wavefront phenomenon of ischemic cell death. 1. Myocardial infarct size vs duration of coronary occlusion in dogs. *Circulation* **56**, 786-794 (1977).

18 Rochitte, C. E. & Azevedo, C. F. The myocardial area at risk. *Heart*, heartjnl-2011-301332 (2011).

19 Cuculich, P. S. *et al.* The electrophysiological cardiac ventricular substrate in patients after myocardial infarction: noninvasive characterization with electrocardiographic imaging. *Journal of the American College of Cardiology* **58**, 1893-1902 (2011).

20 Rubart, M. & Zipes, D. P. Mechanisms of sudden cardiac death. *The Journal of clinical investigation* **115**, 2305-2315 (2005).

21 Wit, A. L. & Janse, M. J. *The ventricular arrhythmias of ischemia and infarction*. (Futura Publ, 1993).

22 Sheridan, D., Culling, W. & Penny, W. Electrophysiological disturbances associated with acute myocardial infarction. *European heart journal* **7**, 11-18 (1986).

23 Bunch, T. J., Hohnloser, S. H. & Gersh, B. J. Mechanisms of Sudden Cardiac Death in Myocardial Infarction Survivors Insights From the Randomized Trials of Implantable Cardioverter-Defibrillators. *Circulation* **115**, 2451-2457 (2007).
24 Cohn, J. N., Ferrari, R. & Sharpe, N. Cardiac remodeling--concepts and clinical implications: a consensus paper from an international forum on cardiac remodeling. Behalf of an International Forum on Cardiac Remodeling. *J Am Coll Cardiol* **35**, 569-582 (2000).
25 Korup, E. *et al.* Comparison of degrees of left ventricular dilation within three hours and up to six days after onset of first acute myocardial infarction. *The American journal of cardiology* **80**, 449-453 (1997).
26 Weisman, H. F., Bush, D. E., Mannisi, J. A. & Bulkley, B. H. Global cardiac remodeling after acute myocardial infarction: a study in the rat model. *Journal of the American College of Cardiology* **5**, 1355-1362 (1985).
27 Hutchins, G. M. & Bulkley, B. H. Infarct expansion versus extension: two different complications of acute myocardial infarction. *The American journal of cardiology* **41**, 1127-1132 (1978).
28 McKay, R. G. *et al.* Left ventricular remodeling after myocardial infarction: a corollary to infarct expansion. *Circulation* **74**, 693-702 (1986).
29 Sabbah, H. & Goldstein, S. Ventricular remodelling: consequences and therapy. *European heart journal* **14**, 24-29 (1993).
30 Antman, E. M. *et al.* ACC/AHA guidelines for the management of patients with ST-elevation myocardial infarction—executive summary: a report of the American College of Cardiology/American Heart Association Task Force on Practice Guidelines (Writing Committee to Revise the 1999 Guidelines for the Management of Patients With Acute Myocardial Infarction). *Journal of the American College of Cardiology* **44**, 671-719 (2004).
31 Van de Werf, F. *et al.* Management of acute myocardial infarction in patients presenting with persistent ST-segment elevation. *European heart journal* **29**, 2909-2945 (2008).
32 Morel, O. *et al.* Pharmacological approaches to reperfusion therapy. *Cardiovascular research*, cvs114 (2012).
33 Gelfand, E. & Cannon, C. Myocardial infarction: contemporary management strategies. *Journal of internal medicine* **262**, 59-77 (2007).
34 Sans, S., Kesteloot, H. & Kromhout, D. o. The burden of cardiovascular diseases mortality in Europe. *European heart journal* **18**, 1231-1248 (1997).
35 Minicucci, M. F. *et al.* Infarct size as predictor of systolic functional recovery after myocardial infarction. *Arquivos brasileiros de cardiologia* **102**, 549-556 (2014).
36 Nijveldt, R. *et al.* Functional recovery after acute myocardial infarction: comparison between angiography, electrocardiography, and cardiovascular magnetic resonance measures of microvascular injury. *Journal of the American College of Cardiology* **52**, 181-189 (2008).
37 Ou, L. *et al.* Animal models of cardiac disease and stem cell therapy. *The open cardiovascular medicine journal* **4** (2010).
38 Cohen, M. V., Yang, X.-M., Liu, Y., Snell, K. S. & Downey, J. M. A new animal model of controlled coronary artery occlusion in conscious rabbits. *Cardiovascular research* **28**, 61-65 (1994).
39 Fox, J. G. *et al. The Mouse in biomedical research: diseases*. Vol. 2 (Academic Press, 2006).
40 Chagoya de Sànchez, V. *et al.* Sequential changes of energy metabolism and mitochondrial function in myocardial infarction induced by isoproterenol in rats: a long-term and integrative study. *Canadian journal of physiology and pharmacology* **75**, 1300-1311 (1997).

41 ARNOLDA, L., McGRATH, B., COCKS, M., SUMITHRAN, E. & JOHNSTON, C. Adriamycin cardiomyopathy in the rabbit: an animal model of low output cardiac failure with activation of vasoconstrictor mechanisms. *Cardiovascular research* **19**, 378-382 (1985).
42 van den Bos, E. J., Mees, B. M., de Waard, M. C., de Crom, R. & Duncker, D. J. A novel model of cryoinjury-induced myocardial infarction in the mouse: a comparison with coronary artery ligation. *American Journal of Physiology-Heart and Circulatory Physiology* **289**, H1291-H1300 (2005).
43 Ma, N. *et al.* Intramyocardial delivery of human CD133+ cells in a SCID mouse cryoinjury model: Bone marrow vs. cord blood-derived cells. *Cardiovascular research* **71**, 158-169 (2006).
44 Michael, L. H. *et al.* Myocardial ischemia and reperfusion: a murine model. *The American journal of physiology* **269**, H2147-2154 (1995).
45 Baddour, J. A., Sousounis, K. & Tsonis, P. A. Organ repair and regeneration: an overview. *Birth Defects Research Part C: Embryo Today: Reviews* **96**, 1-29 (2012).
46 Porrello, E. R. *et al.* Transient regenerative potential of the neonatal mouse heart. *Science* **331**, 1078-1080, doi:10.1126/science.1200708 (2011).
47 Michalopoulos, G. K. Principles of liver regeneration and growth homeostasis. *Compr Physiol* **3**, 485-513, doi:10.1002/cphy.c120014 (2013).
48 Beltrami, A. P. *et al.* Evidence that human cardiac myocytes divide after myocardial infarction. *New England Journal of Medicine* **344**, 1750-1757 (2001).
49 Bergmann, O. *et al.* Evidence for cardiomyocyte renewal in humans. *Science* **324**, 98-102, doi:10.1126/science.1164680 (2009).
50 Laflamme, M. A. & Murry, C. E. Regenerating the heart. *Nat Biotechnol* **23**, 845-856, doi:10.1038/nbt1117 (2005).
51 Beltrami, A. P. *et al.* Adult cardiac stem cells are multipotent and support myocardial regeneration. *Cell* **114**, 763-776 (2003).
52 Poss, K. D., Wilson, L. G. & Keating, M. T. Heart regeneration in zebrafish. *Science* **298**, 2188-2190, doi:10.1126/science.1077857 (2002).
53 Dimmeler, S., Zeiher, A. M. & Schneider, M. D. Unchain my heart: the scientific foundations of cardiac repair. *J Clin Invest* **115**, 572-583, doi:10.1172/jci24283 (2005).
54 Assmus, B. *et al.* Transplantation of Progenitor Cells and Regeneration Enhancement in Acute Myocardial Infarction (TOPCARE-AMI). *Circulation* **106**, 3009-3017 (2002).
55 Gimble, J. M., Katz, A. J. & Bunnell, B. A. Adipose-derived stem cells for regenerative medicine. *Circ Res* **100**, 1249-1260, doi:10.1161/01.res.0000265074.83288.09 (2007).
56 Planat-Bénard, V. *et al.* Spontaneous cardiomyocyte differentiation from adipose tissue stroma cells. *Circ Res* **94**, 223-229, doi:10.1161/01.res.0000109792.43271.47 (2004).
57 Schäffler, A. & Büchler, C. Concise review: adipose tissue-derived stromal cells--basic and clinical implications for novel cell-based therapies. *Stem Cells* **25**, 818-827, doi:10.1634/stemcells.2006-0589 (2007).
58 Segers, V. F. M. & Lee, R. T. Stem-cell therapy for cardiac disease. *Nature* **451**, 937-942, doi:10.1038/nature06800 (2008).
59 Barile, L. *et al.* Cardiac stem cells: isolation, expansion and experimental use for myocardial regeneration. *Nature Clinical Practice Cardiovascular Medicine* **4**, S9-S14 (2007).
60 Winter, E. & Gittenberger-de Groot, A. Cardiovascular development: towards biomedical applicability. *Cellular and molecular life sciences* **64**, 692-703 (2007).
61 Menasché, P. *et al.* Myoblast transplantation for heart failure. *Lancet* **357**, 279-280, doi:10.1016/s0140-6736(00)03617-5 (2001).
62 Dib, N. *et al.* Safety and feasibility of autologous myoblast transplantation in patients with ischemic cardiomyopathy: four-year follow-up. *Circulation* **112**, 1748-1755, doi:10.1161/circulationaha.105.547810 (2005).

63 Menasché, P. *et al.* The Myoblast Autologous Grafting in Ischemic Cardiomyopathy (MAGIC) trial: first randomized placebo-controlled study of myoblast transplantation. *Circulation* **117**, 1189-1200, doi:10.1161/circulationaha.107.734103 (2008).
64 Baraniak, P. R. & McDevitt, T. C. Stem cell paracrine actions and tissue regeneration. *Regenerative medicine* **5**, 121-143 (2010).
65 Caplan, A. Why are MSCs therapeutic? New data: new insight. *The Journal of pathology* **217**, 318-324 (2009).
66 Schinköthe, T., Bloch, W. & Schmidt, A. In vitro secreting profile of human mesenchymal stem cells. *Stem cells and development* **17**, 199-206 (2008).
67 Liu, C.-H. & Hwang, S.-M. Cytokine interactions in mesenchymal stem cells from cord blood. *Cytokine* **32**, 270-279 (2005).
68 Mirotsou, M., Jayawardena, T. M., Schmeckpeper, J., Gnecchi, M. & Dzau, V. J. Paracrine mechanisms of stem cell reparative and regenerative actions in the heart. *Journal of molecular and cellular cardiology* **50**, 280-289 (2011).
69 Duan, H.-F. *et al.* Treatment of myocardial ischemia with bone marrow-derived mesenchymal stem cells overexpressing hepatocyte growth factor. *Molecular therapy* **8**, 467-474 (2003).
70 Simón-Yarza, T. *et al.* Vascular endothelial growth factor-delivery systems for cardiac repair: an overview. (2012).
71 Ye, L. *et al.* Transplantation of nanoparticle transfected skeletal myoblasts overexpressing vascular endothelial growth factor-165 for cardiac repair. *Circulation* **116**, I-113-I-120 (2007).
72 Malliaras, K. & Marbán, E. Cardiac cell therapy: where we've been, where we are, and where we should be headed. *British medical bulletin* **98**, 161-185 (2011).
73 Kraitchman, D. L. *et al.* Dynamic imaging of allogeneic mesenchymal stem cells trafficking to myocardial infarction. *Circulation* **112**, 1451-1461 (2005).
74 Freyman, T. *et al.* A quantitative, randomized study evaluating three methods of mesenchymal stem cell delivery following myocardial infarction. *European heart journal* **27**, 1114-1122 (2006).
75 Johnston, P. V. *et al.* Engraftment, differentiation, and functional benefits of autologous cardiosphere-derived cells in porcine ischemic cardiomyopathy. *Circulation* **120**, 1075-1083 (2009).
76 Hou, D. *et al.* Radiolabeled cell distribution after intramyocardial, intracoronary, and interstitial retrograde coronary venous delivery implications for current clinical trials. *Circulation* **112**, I-150-I-156 (2005).
77 Boudoulas, K. D. & Hatzopoulos, A. K. Cardiac repair and regeneration: the Rubik's cube of cell therapy for heart disease. *Disease Models and Mechanisms* **2**, 344-358 (2009).
78 Georgiadis, V., Knight, R. A., Jayasinghe, S. N. & Stephanou, A. Cardiac tissue engineering: renewing the arsenal for the battle against heart disease. *Integr Biol (Camb)* **6**, 111-126, doi:10.1039/c3ib40097b (2014).
79 Chimenti, I. *et al.* Relative roles of direct regeneration versus paracrine effects of human cardiosphere-derived cells transplanted into infarcted mice. *Circulation research* **106**, 971-980 (2010).
80 Eschenhagen, T. & Zimmermann, W. H. Engineering myocardial tissue. *Circulation research* **97**, 1220-1231 (2005).
81 Zimmermann, W. H. *et al.* Three-dimensional engineered heart tissue from neonatal rat cardiac myocytes. *Biotechnol Bioeng* **68**, 106-114 (2000).
82 Wang, F. & Guan, J. Cellular cardiomyoplasty and cardiac tissue engineering for myocardial therapy. *Advanced drug delivery reviews* **62**, 784-797 (2010).

83 Perea-Gil, I., Prat-Vidal, C. & Bayes-Genis, A. In vivo experience with natural scaffolds for myocardial infarction: the times they are a-changin'. *Stem cell research & therapy* **6**, 1 (2015).
84 Reis, L. A. *et al.* Hydrogels with integrin-binding angiopoietin-1–derived peptide, QHREDGS, for treatment of acute myocardial infarction. *Circulation: Heart Failure* **8**, 333-341 (2015).
85 Xu, G. *et al.* Injectable biodegradable hybrid hydrogels based on thiolated collagen and oligo (acryloyl carbonate)–poly (ethylene glycol)–oligo (acryloyl carbonate) copolymer for functional cardiac regeneration. *Acta biomaterialia* **15**, 55-64 (2015).
86 Blackburn, N. J. *et al.* Timing underpins the benefits associated with injectable collagen biomaterial therapy for the treatment of myocardial infarction. *Biomaterials* **39**, 182-192 (2015).
87 Gaballa, M. A. *et al.* Grafting an acellular 3-dimensional collagen scaffold onto a non-transmural infarcted myocardium induces neo-angiogenesis and reduces cardiac remodeling. *The Journal of heart and lung transplantation* **25**, 946-954 (2006).
88 Kim, P.-H. & Cho, J.-Y. Myocardial tissue engineering using electrospun nanofiber composites. *BMB Rep* **49**, 26-36 (2016).
89 Yashiro, B., Shoda, M., Tomizawa, Y., Manaka, T. & Hagiwara, N. Long-term results of a cardiovascular implantable electronic device wrapped with an expanded polytetrafluoroethylene sheet. *Journal of Artificial Organs* **15**, 244-249 (2012).
90 Barozzi, L. *et al.* Side-to-side aorto-GoreTex central shunt warrants central shunt patency and pulmonary arteries growth. *The Annals of thoracic surgery* **92**, 1476-1482 (2011).
91 Doble, M., Makadia, N., Pavithran, S. & Kumar, R. S. Analysis of explanted ePTFE cardiovascular grafts (modified BT shunt). *Biomedical Materials* **3**, 034118 (2008).
92 Miyazaki, T. *et al.* Expanded polytetrafluoroethylene conduits and patches with bulging sinuses and fan-shaped valves in right ventricular outflow tract reconstruction: multicenter study in Japan. *The Journal of thoracic and cardiovascular surgery* **142**, 1122-1129 (2011).
93 Ghanta, R. K. *et al.* Adjustable, physiological ventricular restraint improves left ventricular mechanics and reduces dilatation in an ovine model of chronic heart failure. *Circulation* **115**, 1201-1210 (2007).
94 Mann, D. L. *et al.* Beneficial effects of the CorCap cardiac support device: five-year results from the Acorn Trial. *The Journal of thoracic and cardiovascular surgery* **143**, 1036-1042 (2012).
95 Rosano, J. M. *et al.* Targeted delivery of VEGF after a myocardial infarction reduces collagen deposition and improves cardiac function. *Cardiovascular engineering and technology* **3**, 237-247 (2012).
96 Silva, E. & Mooney, D. Spatiotemporal control of vascular endothelial growth factor delivery from injectable hydrogels enhances angiogenesis. *Journal of Thrombosis and Haemostasis* **5**, 590-598 (2007).
97 Rodness, J. *et al.* VEGF-loaded microsphere patch for local protein delivery to the ischemic heart. *Acta Biomaterialia* **45**, 169-181 (2016).
98 Lee, S., Yang, S. C., Heffernan, M. J., Taylor, W. R. & Murthy, N. Polyketal microparticles: a new delivery vehicle for superoxide dismutase. *Bioconjugate chemistry* **18**, 4-7 (2007).
99 Fiore, V. F. *et al.* Polyketal microparticles for therapeutic delivery to the lung. *Biomaterials* **31**, 810-817 (2010).
100 Tomoda, H., Morimoto, K. & Aoki, N. Superoxide dismutase activity as a predictor of myocardial reperfusion and salvage in acute myocardial infarction. *American heart journal* **131**, 849-856 (1996).

101 Uraizee, A., Reimer, K. A., Murry, C. E. & Jennings, R. B. Failure of superoxide dismutase to limit size of myocardial infarction after 40 minutes of ischemia and 4 days of reperfusion in dogs. *Circulation* **75**, 1237-1248 (1987).
102 Li, Q. *et al.* Gene therapy with extracellular superoxide dismutase protects conscious rabbits against myocardial infarction. *Circulation* **103**, 1893-1898 (2001).
103 Zimmermann, W.-H., Melnychenko, I. & Eschenhagen, T. Engineered heart tissue for regeneration of diseased hearts. *Biomaterials* **25**, 1639-1647 (2004).
104 Eschenhagen, T. *et al.* Three-dimensional reconstitution of embryonic cardiomyocytes in a collagen matrix: a new heart muscle model system. *The FASEB Journal* **11**, 683-694 (1997).
105 Liu, J., Wang, Y., Du, W. & Yu, B. Sca-1-positive cardiac stem cell migration in a cardiac infarction model. *Inflammation* **36**, 738-749 (2013).
106 Cheng, Z. *et al.* Targeted migration of mesenchymal stem cells modified with CXCR4 gene to infarcted myocardium improves cardiac performance. *Molecular Therapy* **16**, 571-579 (2008).
107 Shkand, T. V. *et al.* Assessment of alginate hydrogel degradation in biological tissue using viscosity-sensitive fluorescent dyes. *Methods and Applications in Fluorescence* **4**, 044002 (2016).
108 Fisher, S. A., Doree, C., Mathur, A. & Martin-Rendon, E. Meta-analysis of cell therapy trials for patients with heart failure. *Circulation research* **116**, 1361-1377 (2015).
109 DONNDORF, P. & WEISS, B. Monitoring myocardial functional regeneration following cardiac stem cell application. *Cardiac Regeneration and Repair: Pathology and Therapies*, 196 (2014).
110 Sugeng, L. *et al.* Quantitative assessment of left ventricular size and function side-by-side comparison of real-time three-dimensional echocardiography and computed tomography with magnetic resonance reference. *Circulation* **114**, 654-661 (2006).
111 Stuckey, D. J., Carr, C. A., Tyler, D. J. & Clarke, K. Cine-MRI versus two-dimensional echocardiography to measure in vivo left ventricular function in rat heart. *NMR in Biomedicine* **21**, 765-772 (2008).
112 Haacke, E. M., Brown, R. W., Thompson, M. R. & Venkatesan, R. *Magnetic resonance imaging: physical principles and sequence design*. Vol. 82 (Wiley-Liss New York:, 1999).
113 Lauterbur, P. C. Image formation by induced local interactions: examples employing nuclear magnetic resonance. (1973).
114 Mansfield, P. Multi-planar image formation using NMR spin echoes. *Journal of Physics C: Solid State Physics* **10**, L55 (1977).
115 Lang, R. M. *et al.* Recommendations for chamber quantification. *European Heart Journal-Cardiovascular Imaging* **7**, 79-108 (2006).
116 Deichmann, R. & Haase, A. Quantification of T 1 values by SNAPSHOT-FLASH NMR imaging. *Journal of Magnetic Resonance (1969)* **96**, 608-612 (1992).
117 Campbell-Washburn, A. E. *et al.* Cardiac arterial spin labeling using segmented ECG-gated Look-Locker FAIR: Variability and repeatability in preclinical studies. *Magnetic resonance in medicine* **69**, 238-247 (2013).
118 Ramasawmy, R. *Measurements of Pre-Clinical Liver Perfusion Using Arterial Spin Labelling MRI*, UCL (University College London), (2015).
119 Lohrke, J. *et al.* 25 Years of Contrast-Enhanced MRI: Developments, Current Challenges and Future Perspectives. *Advances in therapy* **33**, 1-28 (2016).
120 Sherry, A. D., Caravan, P. & Lenkinski, R. E. Primer on gadolinium chemistry. *Journal of Magnetic Resonance Imaging* **30**, 1240-1248 (2009).
121 Cheng, K. T., Cheng, H. & Leung, K. Clinical use of gadobutrol for contrast-enhanced magnetic resonance imaging of neurological diseases. *Rep Med Imaging* **2012**, 15-22 (2012).

122 Engblom, H. *et al.* A new automatic algorithm for quantification of myocardial infarction imaged by late gadolinium enhancement cardiovascular magnetic resonance: experimental validation and comparison to expert delineations in multi-center, multi-vendor patient data. *Journal of Cardiovascular Magnetic Resonance* **18**, 1 (2016).
123 Zhu, D., Larin, K. V., Luo, Q. & Tuchin, V. V. Recent progress in tissue optical clearing. *Laser & photonics reviews* **7**, 732-757 (2013).
124 Tuchin, V. V. *et al.* Light propagation in tissues with controlled optical properties. *Journal of biomedical optics* **2**, 401-417 (1997).
125 Tuchin, V. V. Optical clearing of tissues and blood using the immersion method. *Journal of Physics D: Applied Physics* **38**, 2497 (2005).
126 Sharpe, J. Optical projection tomography. *Annu. Rev. Biomed. Eng.* **6**, 209-228 (2004).
127 Sharpe, J. *et al.* Optical projection tomography as a tool for 3D microscopy and gene expression studies. *Science* **296**, 541-545 (2002).
128 Zhao, X. *et al.* Optical projection tomography permits efficient assessment of infarct volume in the murine heart postmyocardial infarction. *American Journal of Physiology-Heart and Circulatory Physiology* **309**, H702-H710 (2015).
129 Stuckey, D. J., Carr, C. A., Tyler, D. J. & Clarke, K. Cine-MRI versus two-dimensional echocardiography to measure in vivo left ventricular function in rat heart. *NMR Biomed* **21**, 765-772, doi:10.1002/nbm.1268 (2008).
130 Singh, S. & Goyal, A. The Origin of Echocardiography? *Texas Heart Institute Journal* **35**, 88 (2008).
131 Firestone, F. A. The supersonic reflectoscope, an instrument for inspecting the interior of solid parts by means of sound waves. *The Journal of the Acoustical Society of America* **17**, 287-299 (1946).
132 Edler, I. & Hertz, C. H. The use of ultrasonic reflectoscope for the continuous recording of the movements of heart walls. *Clinical physiology and functional imaging* **24**, 118-136 (2004).
133 Salomon, L. *et al.* Practice guidelines for performance of the routine mid-trimester fetal ultrasound scan. *Ultrasound in Obstetrics & Gynecology* **37**, 116-126 (2011).
134 Chaussy, C., Brendel, W. & Schmiedt, E. Extracorporeally induced destruction of kidney stones by shock waves. *The Lancet* **316**, 1265-1268 (1980).
135 Koski, J. M. & Hammer, H. B. Ultrasound-guided procedures: techniques and usefulness in controlling inflammation and disease progression. *Rheumatology* **51**, vii31-vii35 (2012).
136 Foster, F. *et al.* A new ultrasound instrument for in vivo microimaging of mice. *Ultrasound in medicine & biology* **28**, 1165-1172 (2002).
137 Moran, C. M., Thomson, A. J., Rog-Zielinska, E. & Gray, G. A. High-resolution echocardiography in the assessment of cardiac physiology and disease in preclinical models. *Experimental physiology* **98**, 629-644 (2013).
138 McElroy, W. & Green, A. Function of adenosine triphosphate in the activation of luciferin. *Archives of biochemistry and biophysics* **64**, 257-271 (1956).
139 Tromberg, B. J. *et al.* Non-invasive in vivo characterization of breast tumors using photon migration spectroscopy. *Neoplasia* **2**, 26-40 (2000).
140 Clark, A. J., Fakurnejad, S., Ma, Q. & Hashizume, R. Bioluminescence Imaging of an Immunocompetent Animal Model for Glioblastoma. *Journal of visualized experiments: JoVE* (2016).
141 Close, D., Xu, T., Ripp, S. & Sayler, G. Real-Time Bioluminescent Tracking of Cellular Population Dynamics. *Bioluminescent Imaging: Methods and Protocols*, 107-116 (2014).
142 Di Rocco, G. *et al.* Analysis of biodistribution and engraftment into the liver of genetically modified mesenchymal stromal cells derived from adipose tissue. *Cell transplantation* **21**, 1997-2008 (2012).

143 Zhao, D., Richer, E., Antich, P. P. & Mason, R. P. Antivascular effects of combretastatin A4 phosphate in breast cancer xenograft assessed using dynamic bioluminescence imaging and confirmed by MRI. *The FASEB Journal* **22**, 2445-2451 (2008).
144 Yang, G. *et al.* Therapeutic effects of induced pluripotent stem cells in chimeric mice with beta-thalassemia. *haematologica*, haematol. 2013.087916 (2014).
145 Jagannath, V. A., Fedorowicz, Z., Al Hajeri, A. & Sharma, A. Hematopoietic stem cell transplantation for people with ß-thalassaemia major. *The Cochrane Library* (2014).
146 Pennell, D. J. *et al.* Cardiovascular function and treatment in β-thalassemia major: a consensus statement from the American Heart Association. *Circulation* **128**, 281-308, doi:10.1161/CIR.0b013e31829b2be6 (2013).
147 Weed, R. I., Reed, C. F. & Berg, G. Is hemoglobin an essential structural component of human erythrocyte membranes? *Journal of Clinical Investigation* **42**, 581 (1963).
148 Costanzo, L. S. (Elsevier, 2003).
149 Wood, W. Haemoglobin synthesis during human fetal development. *British Medical Bulletin* **32**, 282-287 (1976).
150 Bunn, H. F. & Forget, B. G. *Hemoglobin--molecular, genetic, and clinical aspects*. (WB Saunders Co., 1986).
151 Borgna-Pignatti, C. *et al.* Survival and complications in thalassemia. *Ann N Y Acad Sci* **1054**, 40-47, doi:10.1196/annals.1345.006 (2005).
152 Rochette, J., Craig, J. E. & Thein, S. L. Fetal hemoglobin levels in adults. *Blood Rev* **8**, 213-224 (1994).
153 Kremastinos, D. T. & Farmakis, D. Iron overload cardiomyopathy in clinical practice. *Circulation* **124**, 2253-2263 (2011).
154 Origa, R. *et al.* Liver iron concentrations and urinary hepcidin in beta-thalassemia. *Haematologica* **92**, 583-588 (2007).
155 Charafeddine, K. *et al.* Survival and complications of beta-thalassemia in Lebanon: a decade's experience of centralized care. *Acta Haematol* **120**, 112-116, doi:10.1159/000171088 (2008).
156 Galanello, R. & Origa, R. Beta-thalassemia. *Orphanet J Rare Dis* **5**, 11, doi:10.1186/1750-1172-5-11 (2010).
157 Aessopos, A. *et al.* Hemodynamic assessment of splenomegaly in beta-thalassemia patients undergoing splenectomy. *Ann Hematol* **83**, 775-778, doi:10.1007/s00277-004-0934-z (2004).
158 Aessopos, A. *et al.* Cardiovascular effects of splenomegaly and splenectomy in beta-thalassemia. *Ann Hematol* **84**, 353-357, doi:10.1007/s00277-004-1002-4 (2005).
159 Ehlers, K. H., Giardina, P. J., Lesser, M. L., Engle, M. A. & Hilgartner, M. W. Prolonged survival in patients with beta-thalassemia major treated with deferoxamine. *J Pediatr* **118**, 540-545 (1991).
160 Huo, Y. *et al.* Humanized mouse models of Cooley's anemia: correct fetal-to-adult hemoglobin switching, disease onset, and disease pathology. *Ann N Y Acad Sci* **1202**, 45-51, doi:10.1111/j.1749-6632.2010.05547.x (2010).
161 Zurlo, M. G. *et al.* Survival and causes of death in thalassaemia major. *Lancet* **2**, 27-30 (1989).
162 Yang, B. *et al.* A mouse model for beta 0-thalassemia. *Proc Natl Acad Sci U S A* **92**, 11608-11612 (1995).
163 Perkins, A., Peterson, K., Stamatoyannopoulos, G., Witkowska, H. & Orkin, S. Fetal expression of a human Aγ globin transgene rescues globin chain imbalance but not hemolysis in EKLF null mouse embryos. *Blood* **95**, 1827-1833 (2000).
164 Ciavatta, D. J., Ryan, T. M., Farmer, S. C. & Townes, T. M. Mouse model of human beta zero thalassemia: targeted deletion of the mouse beta maj- and beta min-globin genes in embryonic stem cells. *Proc Natl Acad Sci U S A* **92**, 9259-9263 (1995).

165 Shehee, W. R., Oliver, P. & Smithies, O. Lethal thalassemia after insertional disruption of the mouse major adult beta-globin gene. *Proc Natl Acad Sci U S A* **90**, 3177-3181 (1993).
166 Jamsai, D. *et al.* A humanized mouse model for a common beta0-thalassemia mutation. *Genomics* **85**, 453-461, doi:10.1016/j.ygeno.2004.11.016 (2005).
167 Vadolas, J. *et al.* Humanized beta-thalassemia mouse model containing the common IVSI-110 splicing mutation. *J Biol Chem* **281**, 7399-7405, doi:10.1074/jbc.M512931200 (2006).
168 Huo, Y., McConnell, S. C. & Ryan, T. M. Preclinical transfusion-dependent humanized mouse model of beta thalassemia major. *Blood* **113**, 4763-4770, doi:10.1182/blood-2008-12-197012 (2009).
169 Stark, D. *et al.* Nuclear magnetic resonance imaging of experimentally induced liver disease. *Radiology* **148**, 743-751 (1983).
170 Anderson, L. J. *et al.* Comparison of effects of oral deferiprone and subcutaneous desferrioxamine on myocardial iron concentrations and ventricular function in beta-thalassaemia. *The Lancet* **360**, 516-520 (2002).
171 Pennell, D. J. *et al.* Efficacy of deferasirox in reducing and preventing cardiac iron overload in β-thalassemia. *Blood* **115**, 2364-2371 (2010).
172 Anderson, L. *et al.* Cardiovascular T2-star (T2*) magnetic resonance for the early diagnosis of myocardial iron overload. *European heart journal* **22**, 2171-2179 (2001).
173 Papakonstantinou, O. *et al.* Assessment of iron distribution between liver, spleen, pancreas, bone marrow, and myocardium by means of R2 relaxometry with MRI in patients with beta-thalassemia major. *J Magn Reson Imaging* **29**, 853-859, doi:10.1002/jmri.21707 (2009).
174 Tanner, M. A. *et al.* Multi-center validation of the transferability of the magnetic resonance T2* technique for the quantification of tissue iron. *Haematologica* **91**, 1388-1391 (2006).
175 Voskaridou, E. *et al.* Magnetic resonance imaging in the evaluation of iron overload in patients with beta thalassaemia and sickle cell disease. *Br J Haematol* **126**, 736-742, doi:10.1111/j.1365-2141.2004.05104.x (2004).
176 Wood, J. C. *et al.* MRI R2 and R2* mapping accurately estimates hepatic iron concentration in transfusion-dependent thalassemia and sickle cell disease patients. *Blood* **106**, 1460-1465, doi:10.1182/blood-2004-10-3982 (2005).
177 Carpenter, J.-P. *et al.* Calibration of myocardial T2 and T1 against iron concentration. *J Cardiovasc Magn Reson* **16**, 62, doi:10.1186/s12968-014-0062-4 (2014).
178 Carpenter, J.-P. *et al.* On T2* magnetic resonance and cardiac iron. *Circulation* **123**, 1519-1528, doi:10.1161/circulationaha.110.007641 (2011).
179 Wood, J. C. Impact of iron assessment by MRI. *ASH Education Program Book* **2011**, 443-450 (2011).
180 Anderson, L. J. *et al.* Myocardial iron clearance during reversal of siderotic cardiomyopathy with intravenous desferrioxamine: a prospective study using T2* cardiovascular magnetic resonance. *British journal of haematology* **127**, 348-355 (2004).
181 Pennell, D. J. *et al.* Deferasirox for up to 3 years leads to continued improvement of myocardial T2* in patients with β-thalassemia major. *Haematologica* **97**, 842-848 (2012).
182 Stuckey, D. J. *et al.* T_1 mapping detects pharmacological retardation of diffuse cardiac fibrosis in mouse pressure-overload hypertrophy. *Circ Cardiovasc Imaging* **7**, 240-249, doi:10.1161/circimaging.113.000993 (2014).
183 Yushkevich, P. A. *et al.* User-guided 3D active contour segmentation of anatomical structures: significantly improved efficiency and reliability. *Neuroimage* **31**, 1116-1128 (2006).

184 Lagarias, J. C., Reeds, J. A., Wright, M. H. & Wright, P. E. Convergence properties of the Nelder--Mead simplex method in low dimensions. *SIAM Journal on optimization* **9**, 112-147 (1998).
185 Heiberg, E. *et al.* Design and validation of Segment--freely available software for cardiovascular image analysis. *BMC Med Imaging* **10**, 1, doi:10.1186/1471-2342-10-1 (2010).
186 Stuckey, D. J. *et al.* In vivo MRI characterization of progressive cardiac dysfunction in the mdx mouse model of muscular dystrophy. *PLoS One* **7**, e28569, doi:10.1371/journal.pone.0028569 (2012).
187 Bothwell, T. H., Charlton, R., Cook, J. & Finch, C. Iron metabolism in man. *Iron metabolism in man.* (1979).
188 Wood, J. C. *et al.* Cardiac iron determines cardiac T2*, T2, and T1 in the gerbil model of iron cardiomyopathy. *Circulation* **112**, 535-543, doi:10.1161/circulationaha.104.504415 (2005).
189 He, T. *et al.* Development of a novel optimized breathhold technique for myocardial T2 measurement in thalassemia. *Journal of Magnetic Resonance Imaging* **24**, 580-585 (2006).
190 He, T. *et al.* Multi-center transferability of a breath-hold T2 technique for myocardial iron assessment. *Journal of Cardiovascular Magnetic Resonance* **10**, 1 (2008).
191 Wood, J. C. *et al.* Physiology and pathophysiology of iron cardiomyopathy in thalassemia. *Ann N Y Acad Sci* **1054**, 386-395, doi:10.1196/annals.1345.047 (2005).
192 Tanner, M. A. *et al.* A randomized, placebo-controlled, double-blind trial of the effect of combined therapy with deferoxamine and deferiprone on myocardial iron in thalassemia major using cardiovascular magnetic resonance. *Circulation* **115**, 1876-1884, doi:10.1161/circulationaha.106.648790 (2007).
193 Higgs, D. R., Engel, J. D. & Stamatoyannopoulos, G. Thalassaemia. *Lancet* **379**, 373-383, doi:10.1016/s0140-6736(11)60283-3 (2012).
194 Imren, S. *et al.* Permanent and panerythroid correction of murine beta thalassemia by multiple lentiviral integration in hematopoietic stem cells. *Proc Natl Acad Sci U S A* **99**, 14380-14385, doi:10.1073/pnas.212507099 (2002).
195 May, C., Rivella, S., Chadburn, A. & Sadelain, M. Successful treatment of murine beta-thalassemia intermedia by transfer of the human beta-globin gene. *Blood* **99**, 1902-1908 (2002).
196 Rivella, S., May, C., Chadburn, A., Rivière, I. & Sadelain, M. A novel murine model of Cooley anemia and its rescue by lentiviral-mediated human beta-globin gene transfer. *Blood* **101**, 2932-2939, doi:10.1182/blood-2002-10-3305 (2003).
197 Poggiali, E., Cassinerio, E., Zanaboni, L. & Cappellini, M. D. An update on iron chelation therapy. *Blood Transfus* **10**, 411-422, doi:10.2450/2012.0008-12 (2012).
198 Neufeld, E. J. *et al.* A phase 2 study of the safety, tolerability, and pharmacodynamics of FBS0701, a novel oral iron chelator, in transfusional iron overload. *Blood* **119**, 3263-3268, doi:10.1182/blood-2011-10-386268 (2012).
199 Bergeron, R. J., Wiegand, J., McManis, J. S., Bharti, N. & Singh, S. Design, synthesis, and testing of non-nephrotoxic desazadesferrithiocin polyether analogues. *J Med Chem* **51**, 3913-3923, doi:10.1021/jm800154m (2008).
200 Ferrer, P. *et al.* Antimalarial iron chelator, FBS0701, shows asexual and gametocyte Plasmodium falciparum activity and single oral dose cure in a murine malaria model. *PLoS One* **7**, e37171, doi:10.1371/journal.pone.0037171 (2012).
201 Marmor, A., Jain, D. & Zaret, B. Beyond ejection fraction. *Journal of Nuclear Cardiology* **1**, 477-486 (1994).
202 Paulus, W. J. *et al.* How to diagnose diastolic heart failure: a consensus statement on the diagnosis of heart failure with normal left ventricular ejection fraction by the Heart

Failure and Echocardiography Associations of the European Society of Cardiology. *European heart journal* (2007).
203 Cain, P. A. *et al.* Age and gender specific normal values of left ventricular mass, volume and function for gradient echo magnetic resonance imaging: a cross sectional study. *BMC medical imaging* **9**, 1 (2009).
204 Stegger, L. *et al.* Quantification of left ventricular volumes and ejection fraction in mice using PET, compared with MRI. *Journal of Nuclear Medicine* **50**, 132-138 (2009).
205 Minicucci, M. F., Azevedo, P. S., Polegato, B. F., Paiva, S. A. & Zornoff, L. A. Heart failure after myocardial infarction: clinical implications and treatment. *Clinical cardiology* **34**, 410-414 (2011).
206 Curtis, J. P. *et al.* The association of left ventricular ejection fraction, mortality, and cause of death in stable outpatients with heart failure. *Journal of the American College of Cardiology* **42**, 736-742 (2003).
207 Gottdiener, J. S. *et al.* Outcome of congestive heart failure in elderly persons: influence of left ventricular systolic function: the Cardiovascular Health Study. *Annals of Internal Medicine* **137**, 631-639 (2002).
208 Bogaert, J. *et al.* Remote myocardial dysfunction after acute anterior myocardial infarction: impact of left ventricular shape on regional function: a magnetic resonance myocardial tagging study. *Journal of the American College of Cardiology* **35**, 1525-1534 (2000).
209 Kramer, C. M. *et al.* Remote noninfarcted region dysfunction soon after first anterior myocardial infarction A magnetic resonance tagging study. *Circulation* **94**, 660-666 (1996).
210 Brower, R. W., Harald, J. & Meester, G. T. Direct method for determining regional myocardial shortening after bypass surgery from radiopaque markers in man. *The American journal of cardiology* **41**, 1222-1229 (1978).
211 Villarreal, F. J., Waldman, L. K. & Lew, W. Technique for measuring regional two-dimensional finite strains in canine left ventricle. *Circulation research* **62**, 711-721 (1988).
212 Rankin, J. S. *et al.* The three-dimensional dynamic geometry of the left ventricle in the conscious dog. *Circulation Research* **39**, 304-313 (1976).
213 Ho, C. Y. & Solomon, S. D. A clinician's guide to tissue Doppler imaging. *Circulation* **113**, e396-e398 (2006).
214 Ibrahim, E.-S. H. Myocardial tagging by cardiovascular magnetic resonance: evolution of techniques--pulse sequences, analysis algorithms, and applications. *J Cardiovasc Magn Reson* **13**, 36, doi:10.1186/1532-429x-13-36 (2011).
215 Zerhouni, E. A., Parish, D. M., Rogers, W. J., Yang, A. & Shapiro, E. P. Human heart: tagging with MR imaging--a method for noninvasive assessment of myocardial motion. *Radiology* **169**, 59-63 (1988).
216 Clark, N. R. *et al.* Circumferential myocardial shortening in the normal human left ventricle. Assessment by magnetic resonance imaging using spatial modulation of magnetization. *Circulation* **84**, 67-74 (1991).
217 Azhari, H. *et al.* Noninvasive quantification of principal strains in normal canine hearts using tagged MRI images in 3-D. *American Journal of Physiology-Heart and Circulatory Physiology* **264**, H205-H216 (1993).
218 Bogaert, J. & Rademakers, F. E. Regional nonuniformity of normal adult human left ventricle. *American Journal of Physiology-Heart and Circulatory Physiology* **280**, H610-H620 (2001).
219 Cupps, B. P., Taggar, A. K., Reynolds, L. M., Lawton, J. S. & Pasque, M. K. Regional myocardial contractile function: multiparametric strain mapping. *Interactive cardiovascular and thoracic surgery* **10**, 953-957 (2010).

220 Saber, N. R. & Wen, H. in *Engineering in Medicine and Biology Society, 2004. IEMBS'04. 26th Annual International Conference of the IEEE.* 3670-3673 (IEEE).
221 Rodriguez, I., Ennis, D. B. & Wen, H. Noninvasive measurement of myocardial tissue volume change during systolic contraction and diastolic relaxation in the canine left ventricle. *Magnetic resonance in medicine* **55**, 484-490 (2006).
222 McKinnon, G., Fischer, S. & Maier, S. Non invasive measurement of myocardial motion using magnetic resonance tagging. *Australasian physical & engineering sciences in medicine/supported by the Australasian College of Physical Scientists in Medicine and the Australasian Association of Physical Sciences in Medicine* **14**, 189-196 (1991).
223 Hu, Z., Metaxas, D. & Axel, L. In vivo strain and stress estimation of the heart left and right ventricles from MRI images. *Medical image analysis* **7**, 435-444 (2003).
224 Maier, S. E. *et al.* Evaluation of left ventricular segmental wall motion in hypertrophic cardiomyopathy with myocardial tagging. *Circulation* **86**, 1919-1928 (1992).
225 Sandstede, J. J. *et al.* Cardiac systolic rotation and contraction before and after valve replacement for aortic stenosis: a myocardial tagging study using MR imaging. *American Journal of Roentgenology* **178**, 953-958 (2002).
226 Donofrio, M. T. *et al.* Regional wall motion and strain of transplanted hearts in pediatric patients using magnetic resonance tagging. *American Journal of Physiology-Regulatory, Integrative and Comparative Physiology* **277**, R1481-R1487 (1999).
227 Prinzen, F. W., Arts, T., Hoeks, A. P. & Reneman, R. S. Discrepancies between myocardial blood flow and fiber shortening in the ischemic border zone as assessed with video mapping of epicardial deformation. *Pflügers Archiv* **415**, 220-229 (1989).
228 Lima, J. *et al.* Segmental motion and deformation of transmurally infarcted myocardium in acute postinfarct period. *American Journal of Physiology-Heart and Circulatory Physiology* **268**, H1304-H1312 (1995).
229 Ivancevic, M. K. *et al.* High-resolution complementary spatial modulation of magnetization (CSPAMM) rat heart tagging on a 1.5 Tesla Clinical Magnetic Resonance System: a preliminary feasibility study. *Investigative radiology* **42**, 204-210 (2007).
230 Rickers, C. *et al.* Applications of magnetic resonance imaging for cardiac stem cell therapy. *Journal of interventional cardiology* **17**, 37-46 (2004).
231 Karantalis, V. *et al.* Autologous mesenchymal stem cells produce concordant improvements in regional function, tissue perfusion, and fibrotic burden when administered to patients undergoing coronary artery bypass grafting: The Prospective Randomized Study of Mesenchymal Stem Cell Therapy in Patients Undergoing Cardiac Surgery (PROMETHEUS) trial. *Circ Res* **114**, 1302-1310, doi:10.1161/circresaha.114.303180 (2014).
232 Macarthur, J. W. *et al.* Preclinical evaluation of the engineered stem cell chemokine stromal cell-derived factor 1α analog in a translational ovine myocardial infarction model. *Circ Res* **114**, 650-659, doi:10.1161/circresaha.114.302884 (2014).
233 Hopp, E. *et al.* Regional myocardial function after intracoronary bone marrow cell injection in reperfused anterior wall infarction-a cardiovascular magnetic resonance tagging study. *J Cardiovasc Magn Reson* **13**, 22 (2011).
234 Morgan, J., Raposo, L., Clague, J., Chow, W. & Oldershaw, P. Restrictive cardiomyopathy and constrictive pericarditis: non-invasive distinction by digitised M mode echocardiography. *British heart journal* **61**, 29-37 (1989).
235 Spottiswoode, B. S. *et al.* Tracking myocardial motion from cine DENSE images using spatiotemporal phase unwrapping and temporal fitting. *IEEE Transactions on medical imaging* **26**, 15-30 (2007).
236 Axel, L. & Dougherty, L. MR imaging of motion with spatial modulation of magnetization. *Radiology* **171**, 841-845, doi:10.1148/radiology.171.3.2717762 (1989).

237 Osman, N. F., Kerwin, W. S., McVeigh, E. R. & Prince, J. L. Cardiac motion tracking using CINE harmonic phase (HARP) magnetic resonance imaging. *Magnetic resonance in medicine: official journal of the Society of Magnetic Resonance in Medicine/Society of Magnetic Resonance in Medicine* **42**, 1048 (1999).
238 Kraitchman, D. L., Young, A. A., Chang, C.-N. & Axel, L. Semi-automatic tracking of myocardial motion in MR tagged images. *IEEE Transactions on Medical Imaging* **14**, 422-433 (1995).
239 Guttman, M. A., Prince, J. L. & McVeigh, E. R. Tag and contour detection in tagged MR images of the left ventricle. *IEEE transactions on medical imaging* **13**, 74-88 (1994).
240 Montillo, A., Axel, L. & Metaxas, D. Automated correction of background intensity variation and image scale standardization in 4D cardiac SPAMM-MRI. *Proceedings of International Society for Magnetic Resonance in Medicine; Toronto, Canada* **708** (2003).
241 Ozturk, C. & McVeigh, E. R. Four-dimensional B-spline based motion analysis of tagged MR images: introduction and in vivo validation. *Physics in medicine and biology* **45**, 1683 (2000).
242 Young, A. A. & Axel, L. Three-dimensional motion and deformation of the heart wall: estimation with spatial modulation of magnetization--a model-based approach. *Radiology* **185**, 241-247 (1992).
243 Kumar, S. & Goldgof, D. Automatic tracking of SPAMM grid and the estimation of deformation parameters from cardiac MR images. *IEEE Transactions on Medical Imaging* **13**, 122-132 (1994).
244 Osman, N. F., Kerwin, W. S., McVeigh, E. R. & Prince, J. L. Cardiac motion tracking using CINE harmonic phase (HARP) magnetic resonance imaging. *Magn Reson Med* **42**, 1048-1060 (1999).
245 Kato, H. *et al.* Composition of MRI phantom equivalent to human tissues. *Medical physics* **32**, 3199-3208 (2005).
246 Osman, N. F., McVeigh, E. R. & Prince, J. L. Imaging heart motion using harmonic phase MRI. *IEEE transactions on medical imaging* **19**, 186-202 (2000).
247 Liu, X. & Prince, J. L. Shortest path refinement for motion estimation from tagged MR images. *IEEE transactions on medical imaging* **29**, 1560-1572 (2010).
248 Aletras, A. H., Ding, S., Balaban, R. S. & Wen, H. DENSE: displacement encoding with stimulated echoes in cardiac functional MRI. *J Magn Reson* **137**, 247-252, doi:10.1006/jmre.1998.1676 (1999).
249 Kuijer, J. *et al.* DENSE and HARP: Two views on the same technique of phase-based strain imaging. *Journal of Magnetic Resonance Imaging* **24**, 1432-1438 (2006).
250 Kim, D., Gilson, W. D., Kramer, C. M. & Epstein, F. H. Myocardial Tissue Tracking with Two-dimensional Cine Displacement-encoded MR Imaging: Development and Initial Evaluation 1. *Radiology* **230**, 862-871 (2004).
251 Zhong, X., Spottiswoode, B. S., Cowart, E. A., Gilson, W. D. & Epstein, F. H. Selective suppression of artifact-generating echoes in cine DENSE using through-plane dephasing. *Magnetic resonance in medicine* **56**, 1126-1131 (2006).
252 Gilson, W. D., Yang, Z., French, B. A. & Epstein, F. H. Measurement of myocardial mechanics in mice before and after infarction using multislice displacement-encoded MRI with 3D motion encoding. *American Journal of Physiology-Heart and Circulatory Physiology* **288**, H1491-H1497 (2005).
253 Liu, Y. *et al.* Reconstruction of myocardial tissue motion and strain fields from displacement-encoded MR imaging. *American Journal of Physiology-Heart and Circulatory Physiology* **297**, H1151-H1162 (2009).
254 Spottiswoode, B. S. *et al.* Motion-guided segmentation for cine DENSE MRI. *Medical image analysis* **13**, 105-115 (2009).

255 Young, I. *et al.* Clinical magnetic susceptibility mapping of the brain. *Journal of computer assisted tomography* **11**, 2-6 (1987).
256 Wang, Y. & Liu, T. Quantitative susceptibility mapping (QSM): decoding MRI data for a tissue magnetic biomarker. *Magnetic resonance in medicine* **73**, 82-101 (2015).
257 Liu, T. *et al.* A novel background field removal method for MRI using projection onto dipole fields (PDF). *NMR in Biomedicine* **24**, 1129-1136 (2011).
258 de Rochefort, L. *et al.* Quantitative susceptibility map reconstruction from MR phase data using bayesian regularization: validation and application to brain imaging. *Magnetic Resonance in Medicine* **63**, 194-206 (2010).
259 Qian, Z., Liu, Q., Metaxas, D. N. & Axel, L. in *International Conference on Medical Image Computing and Computer-Assisted Intervention.* 789-797 (Springer).
260 Fischer, S. E., Stuber, M., Scheidegger, M. B. & Boesiger, P. Limitations of stimulated echo acquisition mode (STEAM) techniques in cardiac applications. *Magnetic resonance in medicine* **34**, 80-91 (1995).
261 Zhou, D., Liu, T., Spincemaille, P. & Wang, Y. Background field removal by solving the Laplacian boundary value problem. *NMR in Biomedicine* **27**, 312-319 (2014).
262 Kwon, Y.-W., Yang, H.-M. & Cho, H.-J. Cell Therapy for Myocardial Infarction. *International journal of stem cells* **3**, 8 (2010).
263 Shimizu, T., Yamato, M., Kikuchi, A. & Okano, T. Cell sheet engineering for myocardial tissue reconstruction. *Biomaterials* **24**, 2309-2316 (2003).
264 Leor, J. *et al.* Bioengineered cardiac grafts a new approach to repair the infarcted myocardium? *Circulation* **102**, Iii-56-Iii-61 (2000).
265 Okano, T., Yamada, N., Okuhara, M., Sakai, H. & Sakurai, Y. Mechanism of cell detachment from temperature-modulated, hydrophilic-hydrophobic polymer surfaces. *Biomaterials* **16**, 297-303 (1995).
266 Memon, I. A. *et al.* Repair of impaired myocardium by means of implantation of engineered autologous myoblast sheets. *The Journal of thoracic and cardiovascular surgery* **130**, 1333-1341 (2005).
267 Sakai, T. *et al.* The fate of a tissue-engineered cardiac graft in the right ventricular outflow tract of the rat. *The Journal of thoracic and cardiovascular surgery* **121**, 932-942 (2001).
268 Shimizu, T. *et al.* Electrically communicating three-dimensional cardiac tissue mimic fabricated by layered cultured cardiomyocyte sheets. *Journal of biomedical materials research* **60**, 110-117 (2002).
269 Sekine, H. *et al.* Endothelial cell coculture within tissue-engineered cardiomyocyte sheets enhances neovascularization and improves cardiac function of ischemic hearts. *Circulation* **118**, S145-152, doi:10.1161/circulationaha.107.757286 (2008).
270 Narita, T. *et al.* The use of cell-sheet technique eliminates arrhythmogenicity of skeletal myoblast-based therapy to the heart with enhanced therapeutic effects. *International journal of cardiology* **168**, 261-269 (2013).
271 Miyagawa, S. *et al.* Impaired myocardium regeneration with skeletal cell sheets—a preclinical trial for tissue-engineered regeneration therapy. *Transplantation* **90**, 364-372 (2010).
272 Kakkar, R. & Lee, R. T. Intramyocardial fibroblast myocyte communication. *Circulation research* **106**, 47-57 (2010).
273 Arts, T. *et al.* Mapping displacement and deformation of the heart with local sine-wave modeling. *IEEE Transactions on Medical Imaging* **29**, 1114-1123 (2010).
274 Gage, G. J., Kipke, D. R. & Shain, W. Whole animal perfusion fixation for rodents. *JoVE (Journal of Visualized Experiments)*, e3564-e3564 (2012).
275 Teng, C. J., Luo, J., Chiu, R. C. & Shum-Tim, D. Massive mechanical loss of microspheres with direct intramyocardial injection in the beating heart: implications for cellular

cardiomyoplasty. *The Journal of thoracic and cardiovascular surgery* **132**, 628-632 (2006).
276 Trachtenberg, B. *et al.* Rationale and design of the Transendocardial Injection of Autologous Human Cells (bone marrow or mesenchymal) in Chronic Ischemic Left Ventricular Dysfunction and Heart Failure Secondary to Myocardial Infarction (TAC-HFT) trial: A randomized, double-blind, placebo-controlled study of safety and efficacy. *American heart journal* **161**, 487-493 (2011).
277 Basu, A., Kunduru, K. R., Doppalapudi, S., Domb, A. J. & Khan, W. Poly (lactic acid) based hydrogels. *Advanced Drug Delivery Reviews* (2016).
278 Sun, X. & Nunes, S. S. Overview of hydrogel-based strategies for application in cardiac tissue regeneration. *Biomedical Materials* **10**, 034005 (2015).
279 Roux, R., Ladavière, C., Montembault, A. & Delair, T. Particle assemblies: Toward new tools for regenerative medicine. *Materials Science and Engineering: C* **33**, 997-1007 (2013).
280 Jeong, B., Bae, Y. H. & Kim, S. W. In situ gelation of PEG-PLGA-PEG triblock copolymer aqueous solutions and degradation thereof. *Journal of biomedical materials research* **50**, 171-177 (2000).
281 West, J. L. & Hubbell, J. A. Polymeric biomaterials with degradation sites for proteases involved in cell migration. *Macromolecules* **32**, 241-244 (1999).
282 Zisch, A. H. *et al.* Cell-demanded release of VEGF from synthetic, biointeractive cell ingrowth matrices for vascularized tissue growth. *The FASEB journal* **17**, 2260-2262 (2003).
283 Kloxin, A. M., Tibbitt, M. W., Kasko, A. M., Fairbairn, J. A. & Anseth, K. S. Tunable hydrogels for external manipulation of cellular microenvironments through controlled photodegradation. *Advanced Materials* **22**, 61-66 (2010).
284 Wong, D. Y., Griffin, D. R., Reed, J. & Kasko, A. M. Photodegradable hydrogels to generate positive and negative features over multiple length scales. *Macromolecules* **43**, 2824-2831 (2010).
285 Jiang, X. J. *et al.* Injection of a novel synthetic hydrogel preserves left ventricle function after myocardial infarction. *Journal of biomedical materials research Part A* **90**, 472-477 (2009).
286 Wang, T. *et al.* Bone marrow stem cells implantation with α-cyclodextrin/MPEG–PCL–MPEG hydrogel improves cardiac function after myocardial infarction. *Acta biomaterialia* **5**, 2939-2944 (2009).
287 Rane, A. A. *et al.* Increased infarct wall thickness by a bio-inert material is insufficient to prevent negative left ventricular remodeling after myocardial infarction. *PLoS One* **6**, e21571 (2011).
288 Chow, L. W. *et al.* A bioactive self-assembled membrane to promote angiogenesis. *Biomaterials* **32**, 1574-1582 (2011).
289 Rajangam, K., Arnold, M. S., Rocco, M. A. & Stupp, S. I. Peptide amphiphile nanostructure–heparin interactions and their relationship to bioactivity. *Biomaterials* **29**, 3298-3305 (2008).
290 Zhang, G., Hu, Q., Braunlin, E. A., Suggs, L. J. & Zhang, J. Enhancing efficacy of stem cell transplantation to the heart with a PEGylated fibrin biomatrix. *Tissue Engineering Part A* **14**, 1025-1036 (2008).
291 Martens, T. P. *et al.* Percutaneous cell delivery into the heart using hydrogels polymerizing in situ. *Cell transplantation* **18**, 297-304 (2009).
292 Lu, W.-N. *et al.* Functional improvement of infarcted heart by co-injection of embryonic stem cells with temperature-responsive chitosan hydrogel. *Tissue Engineering Part A* **15**, 1437-1447 (2008).

293 Jendelová, P. *et al.* Magnetic resonance tracking of transplanted bone marrow and embryonic stem cells labeled by iron oxide nanoparticles in rat brain and spinal cord. *Journal of neuroscience research* **76**, 232-243 (2004).
294 Amsalem, Y. *et al.* Iron-oxide labeling and outcome of transplanted mesenchymal stem cells in the infarcted myocardium. *Circulation* **116**, I-38-I-45 (2007).
295 Shapiro, E. M., Skrtic, S. & Koretsky, A. P. Sizing it up: Cellular MRI using micron-sized iron oxide particles. *Magnetic Resonance in Medicine* **53**, 329-338 (2005).
296 Bulte, J. W. & Kraitchman, D. L. Iron oxide MR contrast agents for molecular and cellular imaging. *NMR in Biomedicine* **17**, 484-499 (2004).
297 Liu, J. *et al.* Visualization of in situ hydrogels by MRI in vivo. *Journal of Materials Chemistry B* **4**, 1343-1353 (2016).
298 Dorsey, S. M. *et al.* Visualization of injectable hydrogels using chemical exchange saturation transfer MRI. *ACS Biomaterials Science & Engineering* **1**, 227-237 (2015).
299 Liang, Y. *et al.* Label-free imaging of gelatin-containing hydrogel scaffolds. *Biomaterials* **42**, 144-150 (2015).
300 Noseda, M. *et al.* PDGFR [alpha] demarcates the cardiogenic clonogenic Sca1+ stem/progenitor cell in adult murine myocardium. *Nature communications* **6** (2015).
301 Oh, H. *et al.* Cardiac progenitor cells from adult myocardium: homing, differentiation, and fusion after infarction. *Proceedings of the National Academy of Sciences* **100**, 12313-12318 (2003).
302 Matsuura, K. *et al.* Adult cardiac Sca-1-positive cells differentiate into beating cardiomyocytes. *Journal of Biological Chemistry* **279**, 11384-11391 (2004).
303 Pfister, O. *et al.* CD31− but Not CD31+ cardiac side population cells exhibit functional cardiomyogenic differentiation. *Circulation research* **97**, 52-61 (2005).
304 Liang, S. X., Tan, T. Y., Gaudry, L. & Chong, B. Differentiation and migration of Sca1+/CD31− cardiac side population cells in a murine myocardial ischemic model. *International journal of cardiology* **138**, 40-49 (2010).
305 Makkar, R. R. *et al.* Intracoronary cardiosphere-derived cells for heart regeneration after myocardial infarction (CADUCEUS): a prospective, randomised phase 1 trial. *The Lancet* **379**, 895-904 (2012).
306 Li, R.-K. & Weisel, R. D. *Cardiac Regeneration and Repair: Biomaterials and Tissue Engineering*. (Elsevier, 2014).
307 Kim, K. K. & Pack, D. W. in *BioMEMS and Biomedical Nanotechnology* 19-50 (Springer, 2006).
308 Baimark, Y. & Srisuwan, Y. Preparation of alginate microspheres by water-in-oil emulsion method for drug delivery: effect of Ca 2+ post-cross-linking. *Advanced Powder Technology* **25**, 1541-1546 (2014).
309 Gombotz, W. R., Healy, M. S. & Brown, L. R. (Google Patents, 1991).
310 Determan, A. S., Graham, J. R., Pfeiffer, K. A. & Narasimhan, B. The role of microsphere fabrication methods on the stability and release kinetics of ovalbumin encapsulated in polyanhydride microspheres. *Journal of microencapsulation* **23**, 832-843 (2006).
311 Ghanbar, H., Luo, C., Bakhshi, P., Day, R. & Edirisinghe, M. Preparation of porous microsphere-scaffolds by electrohydrodynamic forming and thermally induced phase separation. *Materials Science and Engineering: C* **33**, 2488-2498 (2013).
312 Hu, C., Zhao, J. & Cui, W. Fabrication and surface characterization of electrosprayed poly (L-lactide) microspheres. *Journal of Applied Polymer Science* **128**, 3177-3183 (2013).
313 Blaker, J. J., Knowles, J. C. & Day, R. M. Novel fabrication techniques to produce microspheres by thermally induced phase separation for tissue engineering and drug delivery. *Acta Biomaterialia* **4**, 264-272 (2008).
314 Anderson, J. M. & Shive, M. S. Biodegradation and biocompatibility of PLA and PLGA microspheres. *Advanced drug delivery reviews* **64**, 72-82 (2012).

315 Eldridge, J. H. *et al.* Biodegradable microspheres as a vaccine delivery system. *Molecular immunology* **28**, 287-294 (1991).
316 Mathiowitz, E. *et al.* Biologically erodable microspheres as potential oral drug delivery systems. *Nature* **386**, 410-414 (1997).
317 Keshaw, H. *et al.* Assessment of polymer/bioactive glass-composite microporous spheres for tissue regeneration applications. *Tissue Engineering Part A* **15**, 1451-1461 (2008).
318 Singh, M., Hemant, K., Ram, M. & Shivakumar, H. Microencapsulation: a promising technique for controlled drug delivery. *Research in pharmaceutical sciences* **5**, 65-77 (2011).
319 Yu, J. *et al.* The use of human mesenchymal stem cells encapsulated in RGD modified alginate microspheres in the repair of myocardial infarction in the rat. *Biomaterials* **31**, 7012-7020 (2010).
320 Gomez-Mauricio, R. G. *et al.* A preliminary approach to the repair of myocardial infarction using adipose tissue-derived stem cells encapsulated in magnetic resonance-labelled alginate microspheres in a porcine model. *European Journal of Pharmaceutics and Biopharmaceutics* **84**, 29-39 (2013).
321 Lee, J. *et al.* Injectable microsphere/hydrogel hybrid system containing heat shock protein as therapy in a murine myocardial infarction model. *Journal of drug targeting* **21**, 822-829 (2013).
322 Sato, M., Kudo, N. & Saito, N. Surface tension reduction of liquid by applied electric field using vibrating jet method. *IEEE Transactions on Industry Applications* **34**, 294-300 (1998).
323 Leor, J., Palevski, D., Amit, U. & Konfino, T. in *Seminars in cell & developmental biology.* (Elsevier).
324 Stefater, J. A., Ren, S., Lang, R. A. & Duffield, J. S. Metchnikoff's policemen: macrophages in development, homeostasis and regeneration. *Trends in molecular medicine* **17**, 743-752 (2011).
325 Das, A. *et al.* Monocyte and macrophage plasticity in tissue repair and regeneration. *The American journal of pathology* **185**, 2596-2606 (2015).
326 Kellman, P., Wilson, J. R., Xue, H., Ugander, M. & Arai, A. E. Extracellular volume fraction mapping in the myocardium, part 1: evaluation of an automated method. *Journal of Cardiovascular Magnetic Resonance* **14**, 1 (2012).
327 Raabe, B. M., Artwohl, J. E., Purcell, J. E., Lovaglio, J. & Fortman, J. D. Effects of weekly blood collection in C57BL/6 mice. *Journal of the American Association for Laboratory Animal Science* **50**, 680-685 (2011).
328 Vincent, J.-L. Understanding cardiac output. *Critical Care* **12**, 1 (2008).
329 Stoeck, C. T. *et al.* In vivo comparison of DENSE and CSPAMM for cardiac motion analysis. *Journal of Cardiovascular Magnetic Resonance* **11**, 1 (2009).
330 Basson, M. Cardiovascular disease. *Nature* **451**, 903-903 (2008).
331 Doppler, S. A., Deutsch, M.-A., Lange, R. & Krane, M. Cardiac regeneration: current therapies—future concepts. *Journal of thoracic disease* **5**, 683-697 (2013).
332 Rangappa, S., Makkar, R. & Forrester, J. Review article: current status of myocardial regeneration: new cell sources and new strategies. *Journal of cardiovascular pharmacology and therapeutics* **15**, 338-343 (2010).
333 Strauer, B. *et al.* [Intracoronary, human autologous stem cell transplantation for myocardial regeneration following myocardial infarction]. *Deutsche medizinische Wochenschrift (1946)* **126**, 932-938 (2001).

Appendix

A1. ‘Muscle Fibres of the Heart’ Image

‘Muscle Fibres of the Heart’ an image I developed using DTI imaging in the ex vivo mouse heart.

This image was acquired in an ex-vivo naïve mouse heart using a 3D fast spin echo diffusion weighted sequence. The tractography image visualises the spiralling myofibre architecture of the heart with a smooth transition from left handed helical fibres at the epicardium to right hand helical fibres at the endocardium. Images such as this help convey the complex microstructure of the heart and describe the magnitude of the task facing regenerative medicine.